



HAL
open science

Multispectral Analysis and spectral Reflectance Reconstruction of Art Paintings

Alejandro Ribes Cortes

► **To cite this version:**

Alejandro Ribes Cortes. Multispectral Analysis and spectral Reflectance Reconstruction of Art Paintings. domain_other. Télécom ParisTech, 2003. English. NNT : . pastel-00000761

HAL Id: pastel-00000761

<https://pastel.hal.science/pastel-00000761>

Submitted on 15 Feb 2005

HAL is a multi-disciplinary open access archive for the deposit and dissemination of scientific research documents, whether they are published or not. The documents may come from teaching and research institutions in France or abroad, or from public or private research centers.

L'archive ouverte pluridisciplinaire **HAL**, est destinée au dépôt et à la diffusion de documents scientifiques de niveau recherche, publiés ou non, émanant des établissements d'enseignement et de recherche français ou étrangers, des laboratoires publics ou privés.



Ecole Doctorale
d'Informatique,
Télécommunications
et Electronique de Paris

Thèse

**Présentée pour obtenir le grade de docteur
de l'Ecole Nationale Supérieure
des Télécommunications**

Spécialité : Signal et Images

Alejandro Ribés Cortés

**Analyse multispectrale et reconstruction de
la réflectance spectrale de tableaux de
maître**

Soutenue le 16 décembre 2003 devant le jury composé de

Jean-Marc Chassery
Bernard Peroche
Philippe Refregier
Haida Liang
Hans Brettel
Christian Lahanier
Francis Schmitt

Rapporteurs
Examineurs
Invité
Directeur de thèse

Ecole Nationale Supérieure des Télécommunications

Ph.D. Thesis

A dissertation submitted in partial fulfillment of the degree of “Docteur de l’Ecole Nationale Supérieure des Télécommunications”

Alejandro Ribés Cortés

Multispectral Analysis and Spectral Reflectance Reconstruction of Art Paintings

Defended on 16 december 2003, Paris, France

Al iaio
In memory of my Grandfather

Acknowledgements

This thesis is dedicated to my grandfather, Manuel Ribés Gozalbo. I suppose that at some point in my life I will fully understand what it is to be proud of my grandson. But I will never feel what it is to have a grandson getting a Ph.D. while I barely went to school. This thesis is dedicated to his memory. Thanks also to my father, my mother and my sister for all their support.

Thanks to Francis Schmitt, my advisor, for all our technical discussions, meetings, conferences and dinners together. Thanks also to Hans Brettel for his support during these years. To the other members of my jury, thanks to the reviewers, Prof. Jean-Marc Chassery and Prof. Bernard Peroche for their very professional and efficient job making the reports, thanks to Prof. Philippe Refregier for his assistance, thanks to Dr. Haida Liang for her corrections and close collaboration and thanks to Dr. Christian Lahanier for representing the world of technology applied to art paintings, and for being at the starting point of the CRISATEL project.

Working in the European project CRISATEL has been a unique experience. I want to thank everybody that collaborated with me. Merci to all the team of *Lumiere Technology*, in particular to Pascal for his energy and to Damien for his kindness and his great *enterrement de jeune garçon*. Special thanks to the Crete tourist team: to Haida for her strong will, to Mohamed for all his extra work and to Space Commander Ruven for being able to change the space-time curvature.

While being at the TSI laboratory of the *Ecole Nationale Supérieure des Télécommunications* I had the opportunity to meet very interesting fauna. Thanks to everybody in the department. I appreciated the human environment, the coffee breaks together and your friendship. Special thanks to: Carlos, Tonii, Celine, Oscar, Gaspar, Fardaous, Svetlanka, Dalila, Olivier, Françoise, Najib, Stéphane, Eve, Gianni, Philippe, Valérie, Séverine, Aline, Gouenou, Yu, Zhang, Daniel, Antonio, Pau, Saeid, Jasmine, David and Isabelle. I enjoyed every single lunch together talking about all the politically incorrect issues possible in the world.

Thanks also to the people I found during my years in Paris, my dinner friends: Nathalie, Yannick and Karim; and the bunch of parisian-Spanish people: Pili, Inigo, Aitor, Cristina, Iñaki, Daniel, Josetxo, Bertha, Oscar, Gerard and all the others I forget. To the friends which I made before starting my Ph.D. I would like to remember some of them here as their contact motivated me to start this job. You are also part of this, from my hometown Castellón: Miguel Angel, Gustavo, Manuel, Ismael, Vicent, Raul, Tony, Gabriel; from Nottingham: Udo and Stefano; from Oxford: Miguel Angel, Alex, Jorge, Blanca, el Dr. Zaragoza, Criel, Gerardo and Ursula; from Sophia-Antipolis: Navid, Paolo, Kahina and Lionel. Finally a big *thank you* to Milena.

Abstract

This thesis is devoted to the analysis of high definition multispectral images of art painting masterpieces and to the reconstruction of the spectral reflectance in each pixel of these images.

To this end, we were mainly interested in:

1. the methods for spectral reflectance reconstruction of the surface of coloured materials in each pixel of an N-channel multispectral image ($N > 3$),
2. the radiometrically controlled acquisition of multispectral images and the automatic calibration of the acquisition system.

The problem of the spectral reconstruction being an ill posed inverse problem, multiple methods of reconstruction were developed in the scientific community. We propose a classification which enables us to better compare these techniques and to improve some of them. The improved methods have been implemented and tested.

The methods usually used for the reconstruction of spectral reflectance from an N-channel image are mainly linear. To improve their precision and noise tolerance we introduced nonlinear techniques based on neural networks. Initially, multi-layer networks mixed with Principal Component Analysis (PCA) obtained good results. From this base we then worked on reconstruction using "Mixture Density Networks". This technique uses neural networks to estimate a probability distribution which is treated a posteriori to obtain a solution of the problem to be solved. The method was adapted to spectral reconstruction and very good results were obtained. This method was then enriched by developing an automatic system of architecture selection. Two strategies, genetic algorithms and random searches, were developed to this end.

The radiometrically controlled acquisition of multispectral images and the automatic calibration of the acquisition system relate to the European project CRISATEL. The goal of this project is the spectral analysis and the virtual removal of varnish of art painting masterpieces. Within the framework of this project, we evaluated the performance of a new high definition multispectral camera. In particular, we studied the influence of the noise on the acquisition parameters and the spatial inhomogeneity of the light sources (two rotating elliptical projectors creating a luminous band synchronized with the movement of the camera CCD). We also characterized spectrally the filters, the CCD and the lamps. We evaluated the elements of the acquisition system. From the results of this evaluation an automatic calibration procedure was conceived and implemented. This automatic system determines the acquisition parameters (exposure time, CCD amplifiers gains and offsets). Its goal is to obtain the best dynamic range possible of the signal, and to gather the necessary data for the correction of the images. The elements to be corrected are dark noise, pixel sensitivity gain and the illuminant inhomogeneity.

We also worked on other aspects related to multispectral imaging, i.e. the selection of the optical filters most adapted to the spectral reconstruction of a specific material, in our case oil pigments. For that we developed an optimisation technique which determines the parameters of a family of Gaussian filters which maximizes a quality criterion on the reconstruction obtained by using these filters.

Finally, the work completed during this thesis was applied to art works. In the results chapter we present two examples: "*Saint-Jacques le mineur*" painted by George de la Tour and "*Le départ pour Jersey*" painted by Guillaume Fouace. The multispectral camera of the CRISATEL project is exploited by the *Centre de Recherche et de Restauration des Musées de France (C2RMF)*. Currently, the camera is located in the Museum of Louvre where it indeed digitises art painting masterpieces.

Résumé

Nos travaux de thèse ont été consacrés à l'analyse multispectrale en haute définition de tableaux de maître et à la reconstruction de la réflectance spectrale en chacun des pixels.

Pour cela nous nous sommes intéressés principalement :

1. aux méthodes de reconstruction de la réflectance spectrale de la surface du matériau imagé en chaque pixel à partir des valeurs des N canaux d'une image multispectrale ($N > 3$),
2. à l'acquisition en situation contrôlée des images multispectrales et au calibrage du système d'acquisition.

Le problème de la reconstruction spectrale étant un problème inverse mal posé, de multiples méthodes de reconstruction ont été développées dans la communauté scientifique. Nous proposons une classification de ces méthodes qui nous permet de mieux les comparer et d'apporter à certaines d'entre elles des améliorations qui ont été implémentées et testées.

Les méthodes couramment utilisées pour la reconstruction spectrale à partir d'une image à N canaux sont principalement linéaires. Pour améliorer la précision et la tolérance au bruit de la reconstruction nous avons introduit des techniques non linéaires à base de réseaux de neurones. Dans un premier temps des réseaux multicouches mélangés avec une approche par analyse en composantes principales ont permis d'obtenir de bons résultats. A partir de cette base nous avons ensuite travaillé sur la reconstruction en utilisant des "Mixture Density Networks". Cette technique s'appuie sur des réseaux de neurones pour estimer une distribution de probabilités qui est traitée à posteriori pour obtenir une solution du problème à résoudre. La méthode a été adaptée à la reconstruction spectrale et de très bons résultats ont été obtenus. Cette méthode a été ensuite enrichie en développant un système automatique de sélection de l'architecture des Mixture Density Networks. Deux stratégies, les algorithmes génétiques et les recherches aléatoires, ont été développées dans ce but.

L'acquisition en situation contrôlée des images multispectrales et le calibrage du système d'acquisition est principalement lié à la problématique du projet européen CRISATEL, le but étant l'analyse spectrale et le dévernissage virtuel de tableaux de maîtres. Dans le cadre de ce projet, nous avons évalué les performances d'une nouvelle caméra multispectrale de haute définition. Nous avons notamment étudié l'influence du bruit sur les paramètres d'acquisition et l'inhomogénéité spatiale de l'éclairage à balayage produit par des projecteurs aux faisceaux lumineux synchronisés avec le mouvement du CCD. Nous avons également caractérisé spectralement les filtres, le CCD et les lampes. Nous avons évalué les éléments du système d'acquisition. A partir des résultats de cette évaluation un système automatique de calibrage a été conçu et implanté. Ce système automatique détermine les paramètres d'acquisition (temps de pause, gains et offsets des amplificateurs liés aux CCD). Son but est d'obtenir la meilleure dynamique possible du signal et de rassembler les données nécessaires pour la correction des images. Les éléments à corriger étant le bruit et le gain par pixel et l'inhomogénéité spatiale de l'illuminant.

Nous avons aussi travaillé sur d'autres aspects liés aux développements de nouvelles technologies de l'imagerie multispectrale, comme la sélection des filtres optiques les plus adaptés à la reconstruction spectrale de matériaux spécifiques comme les pigments à l'huile. Pour cela nous avons développé une technique d'optimisation qui permet de déterminer les paramètres d'une famille de filtres gaussiens qui maximise un critère de qualité sur les reconstructions obtenues en utilisant ces filtres.

Les travaux de recherche réalisés au cours de cette thèse ont été appliqués à l'estimation spectrale de tableaux de maîtres. Nous présentons dans ce document des exemples de traitement de deux tableaux : "*Saint-Jacques le mineur*" de Georges de la Tour et "*Le départ pour Jersey*" de Guillaume Fouace. La caméra multispectrale du projet CRISATEL est à présent exploitée par le *Centre de Recherche et de Restauration des Musées de France* (C2RMF). Actuellement elle se trouve aux Musée du Louvre pour la numérisation d'une collection de tableaux de maîtres.

Contents

INTRODUCTION 1

Part I

NATURE OF DATA..... 9

BASICS OF SPECTRAL RECONSTRUCTION39

IMPROVING SPECTRAL RECONSTRUCTION ACCURACY.....79

SPECTRAL RECONSTRUCTION USING MIXTURE DENSITY NETWORKS91

Part II

THE CRISATEL ACQUISITION SYSTEM129

CHOOSING FILTERS FOR ACCURATE SPECTRAL RECONSTRUCTION.....175

GENERAL RESULTS191

CONCLUSION AND FUTURE WORK213

APPENDICES217

BIBLIOGRAPHY229

Chapter 1: Introduction

Introduction

In digital multispectral imaging images with more than three bands are acquired and analysed. Conventional colour digital cameras producing three-band images appear to be limited when high-fidelity colour reproduction is to be performed. Over the last ten years multispectral imaging has focused on certain fields where colour fidelity is of the greatest importance. Prominent among these applications is that of imaging works of art, where an increasing demand for high-quality reproductions has emerged alongside a traditional scientific interest in multispectral imaging. In this framework, this thesis deals with the acquisition and analysis of multi-band images and it is more specifically concern with images coming from art paintings.

Fundamental to this thesis and to multispectral imaging is the problem of the reconstruction of spectral reflectance curves from multi-band images. The pixel value of a channel in a multispectral image is the result of:

- 1) the spectral interaction of the light radiant distribution with the reflectance of an object surface,
- 2) the spectral sensitivity of the camera combined with the transmittance of the optical path including the filter corresponding to this channel.

Retrieving the spectral reflectance function of the object surface at each pixel is highly desirable. We call this process spectral reflectance reconstruction or simply spectral reconstruction. It allows an intrinsic representation of an object surface property which is independent from light spectral distribution and from the spectral sensitivity of the camera used for the multispectral image acquisition. This representation can be used for many different purposes. A colour management system based on the spectral properties of materials is more general than a classical colour management based on colorimetry. Our main interest in this thesis is high fidelity colour management of fine art paintings. For instance, knowing the spectral reflectances in each pixel allows us to simulate the appearance of a painting under any virtual illuminant. Moreover, it allows virtual varnish removal which can be of great help for conservators in their planning of ancient art painting restoration.

We can conceptually divide this thesis into two main parts. In the first part we study the problem of reconstructing the spectral reflectance of a material from a multispectral image. This problem presents both theoretically and practically interesting aspects. In the second part, this thesis is dedicated to the IST 1999 20163 European project CRISATEL (Conservation Restoration Innovation Systems for Image capture and Digital Archiving to Enhance Training Education and Lifelong Learning). In this European project a multispectral acquisition system taking 13-channel digital images of high spatial resolution (12,000 x 30,000 pixels) has been developed in order to acquire high-fidelity images of art paintings in museums. This second part of our work is intimately related to the CRISATEL acquisition system.

Both parts of this thesis mentioned above fusion properly in a Ph.D. in engineering. General methods of spectral reconstruction not proposed before can be found in this thesis along with their application to a actual acquisition systems. We choose first to start from the theoretical aspects and step by step show their applications in an existing cutting edge system.

In the rest of this introduction we describe briefly the chapters that compose this document. The general ideas of this thesis are then structured here as they will be in the rest of the document.

Chapter 2. Nature of Data.

We introduced in this chapter basic concepts about multispectral imaging including fundamental formulae and the main components of a multispectral system: light sources, filters, CCD and reflectances. Noise sources on multispectral acquisition systems are introduced. But this chapter goes further that an introduction to multispectral imaging. The spectral reflectance databases used on the rest of the thesis are presented and studied. Fourier analysis and Principal Component Analysis (PCA) are the mathematical tools used on their analysis.

We emphasize that a new approach for the comparison of different spectral reflectance databases is also developed. This approach is simple and mathematically well founded. It is based on the Froebius distance between matrices. This distance is used as a measure of comparison of the orthogonal PCA bases associated to the studied spectral reflectance databases. Finally in this chapter, we present and analysed a new colour chart developed on the framework of the CRISATEL European project.

Chapter 3. Basics of Spectral Reconstruction.

This chapter introduces and describes the problem of spectral reconstruction, it also presents a state of the art on existing reconstruction techniques that are illustrated by using computer simulations.

We propose a classification of the reconstruction techniques in three paradigms:

- i) *direct* reconstruction, which is based on the inversion of the camera model and needs the physical characterization of the acquisition system;
- ii) *indirect* reconstruction or *learning-based* reconstruction, where a calibrated colour chart and its multispectral image are used to construct a reconstruction operator;
- iii) reconstruction by interpolation, where the obtained camera responses are interpolated to find an approximation of the corresponding reflectance function.

In our knowledge it is the first time that a survey with this classification is given. We believe it is useful to differentiate methods that have a very different conceptual origin. Our classification is physically and mathematically well founded and helps understanding the limits and requirements of the methods.

Chapter 4. Improving Spectral Reconstruction Accuracy.

In this brief chapter we describe two original ideas that we introduce to improve spectral reconstruction accuracy. These ideas are not themselves new reconstruction techniques but they can be applied to improve most of the existing spectral reconstruction methods. They are independent and they could even be integrated together if desired.

The first idea relates with the generalisation abilities of existing linear reconstruction methods using a priori information about the objects to be imaged. Using the concept of generalisation we propose an algorithm based on intense random resampling that increases the generalisation capabilities of such methods. We present simulation results where an improvement of 50% of accuracy is obtained on the test sets used. This appears as a very promising result.

The second idea relates with the physical constraints to be respected by the reconstructed spectral curves. We have propose a spline projection operator which is simply applied after reconstruction and appears as a straightforward complement to any existing reconstruction technique. It guarantees that the obtained curves are bounded and at the same time smooth.

Chapter 5. Spectral Reconstruction using Mixture Density Networks.

We consider the problem of the reconstruction of spectral reflectance curves from multispectral images using techniques based on neural networks. In our knowledge, this is the first time that this approach is applied to the resolution of the spectral reconstruction problem. Our aim is to find a non-linear learning-based method able to provide noise resistance and good generalization.

In this chapter two new methods are proposed. The first one uses a neural network to estimate, not directly, spectral curves. In fact, it estimates the coefficients associated to the orthogonal vectors obtained from a Principal Components Analysis (PCA) on a reflectance curves database. This method obtains good results on presence of quantification noise but we were not satisfy of its performance, compared to linear methods, when noise is not present.

The second method applies Mixture Density Networks (MDN) to spectral reconstruction. The MDN method is based on the construction of conditional probability distributions between multispectral camera responses and sampled spectral reflectance functions. This approach leads to a reconstruction method obtaining good results when noise is present or not. The method has been tested using simulated and real data, the results being superior to linear methods. Moreover, we describe how the problem of architecture optimisation is solved. This last point makes the final method fully automatic with no parameters to be fixed by hand.

Chapter 6. The CRISATEL Acquisition System.

A high-resolution multispectral color imaging system has been developed for the European project CRISATEL. This system includes a multispectral camera and a dedicated high power lighting system, both developed by LUMIERE TECHNOLOGY, Paris, France. In this chapter we present and characterize the hardware of the CRISATEL camera. Afterwards, we evaluate this acquisition system and using the data obtained on the evaluation we propose and implement a calibration procedure. Finally, a correction system for the calibrated images is described.

This is an experimental chapter where an actual multispectral acquisition system is studied. We have designed and implemented software intimately related to the acquisition system: the calibration and correction systems. These systems aim to acquire images that have not only high visual quality but also a radiometrically controlled signal.

Chapter 7. Choosing Filters for accurate Spectral Reconstruction.

We consider the problem of filter optimisation for increasing spectral reflectance reconstruction quality. The aim is to design camera filters with spectral transmittances which increase spectral reconstruction accuracy.

We introduce a criteria for filter selection and the strategy for its optimisation. This criteria, called the ν -measure, is originally used for colorimetric filter optimisation. We define a space that we call the *Camera Visual SubSpace* (CVSS). We apply the ν -measure to the CVSS. This

allows optimisation of the transmittances without the introduction of a spectral reconstruction stage at each iteration of the optimisation algorithm.

The proposed strategy appears to converge towards an acceptable solution. Moreover, it reveals very time-efficient. At the end of this chapter we apply the proposed algorithm to the optimisation of 10 Gaussian-shaped visible filters for the CRISATEL camera. The optimised set of filters are compared by simulation with the actual ones mounted on the camera.

Chapter 8. General Results.

This chapter presents a first set of spectral reconstruction results obtained by using the techniques already introduced in this thesis. The chapter is dedicated to data acquired on real experimental environments. No simulations appear here. Two different multispectral acquisition systems were used to obtain the data:

- i) A multispectral camera used at the National Gallery of London.
- ii) The CRISATEL multispectral system using HQI lamps.

Both systems have the common point of using the same set of 13 interference filters. The chapter is divided in two main parts: the first one dedicated to the data obtained at the National Gallery and a second part dealing with data from the CRISATEL project.

The present thesis was finished before the CRISATEL project was completely achieved. The phase of art paintings scanning was starting at that time. A general test was first performed on several Georges de la Tour paintings that were scanned at the museum of Albi (France) between November 28th and December 3th, 2003. We show in this chapter one example of calibration, spectral reconstruction and illuminant simulation of one painting of this first test data, *Saint Jacques le mineur*. An intensive scanning stage followed this first test. We also show a painting of Guillaume Fouace, *Le départ pour Jersey*, that belongs to this stage. It was scanned by members of the CRISATEL project at the Musée Thomas Henry in Cherbourg. At this moment, changes are not expected on the CRISATEL system, at least fundamental changes. Data shown here are preliminary but representative enough to be presented.

Chapter 9. Conclusion and Future work.

General conclusions and the future prospects open after this thesis are discussed on this brief chapter.

Part I

Chapter 2:

Nature of Data

Contents

2.1	Introduction	11
2.2	Multispectral imaging	12
2.2.1	Image acquisition system model	13
2.2.1.1	Light sources	14
2.2.1.2	Optical Filters	16
2.2.1.3	CCD sensitivity	17
2.2.2	Noise into the image formation process	18
2.2.2.1	Noise sources associated to a CCD.....	18
2.2.2.2	Quantification Noise.....	20
2.2.2.3	Other noise sources	21
2.3	Nature of spectral reflectance curves	22
2.3.1	Spectral Reflectance Databases.....	22
2.3.2	Fourier Analysis.....	23
2.3.3	Principal Component Analysis.....	28
2.3.4	Noise on the measurements of reflectance.....	32
2.3.5	The CRISATEL chart.....	33
2.4	Conclusion.....	37

2.1 Introduction

In this chapter we introduce fundamental facts about multispectral imaging. The chapter is divided in two sections. Firstly we present basic information about how a multispectral acquisition system works. Secondly, we introduce and give insight into the nature of spectral reflectance curves.

In the first part the concept of multispectral imaging is introduced. Then, formulae of the image formation process are presented. Components involved in the image formation process of multispectral imaging are briefly introduced: usual light sources, filters and CCDs. We finish this part by treating a fundamental problem of any digital acquisition system: the noise sources.

On the second part of the chapter we will focus on the analysis of spectral reflectance curves. This point is basic, before taking any decision concerning design or implementation; we want to understand the nature of spectral curves as much as possible. We first present the Spectral reflectances databases used on this thesis. We analyze them by using various established mathematical techniques and we give insight into their properties. Two sections are dedicated to Fourier analysis and Principal Component Analysis (PCA). In this context we introduce the Froebius norm as a measure of comparison of the orthogonal bases obtained from the PCA. This new approach allows the comparison of different databases. In order to complete the discussion about the nature of spectral reflectance curves we introduce the concept of noise on the measurements of these data. Finally, we present, analyse and compare a new colour chart developed on the framework of the CRISATEL European project.

2.2 Multispectral imaging

We start the discussion about multispectral imaging by the term itself. This name is somehow controversial and its appropriateness is currently being discussed within the scientific community. In general, most people call multispectral camera a device based on a digital greyscale camera, normally using a non-masked CCD (Coupled Charge Device). Several optical filters are interposed in the optical path, and several greyscale images using N filters are obtained. Consequently a multispectral image is a compendium of N images that have been acquired using N different filters. In the case $N = 3$ we do not call the system multispectral, we call it a digital colour camera. When N is big, for instance 100 the system is call hyperspectral. Hyperspectral acquisition systems are typically found in remote sensing. The techniques used on this field are sometimes very similar to the ones used in multispectral imaging. For a brief survey of Remote Sensing made for the multispectral community see [Schott, 2003].

In Figure 2-1 we show a graphical representation of a multispectral acquisition system. In this case an external barrel containing 6 filters is shown. The barrel rotates to automatically change filters between acquisitions. This is a very common mechanical system found in multispectral imaging but not the only one. There exist systems that do not need any mechanical displacement in order to change the filter transmittance. Liquid Crystal Tunable Filters (LCTF) provide this technology. They are basically an accumulation of different layers, each layer containing linear parallel polarisers sandwiching a liquid crystal retarder element [Brettel et al., 2000].

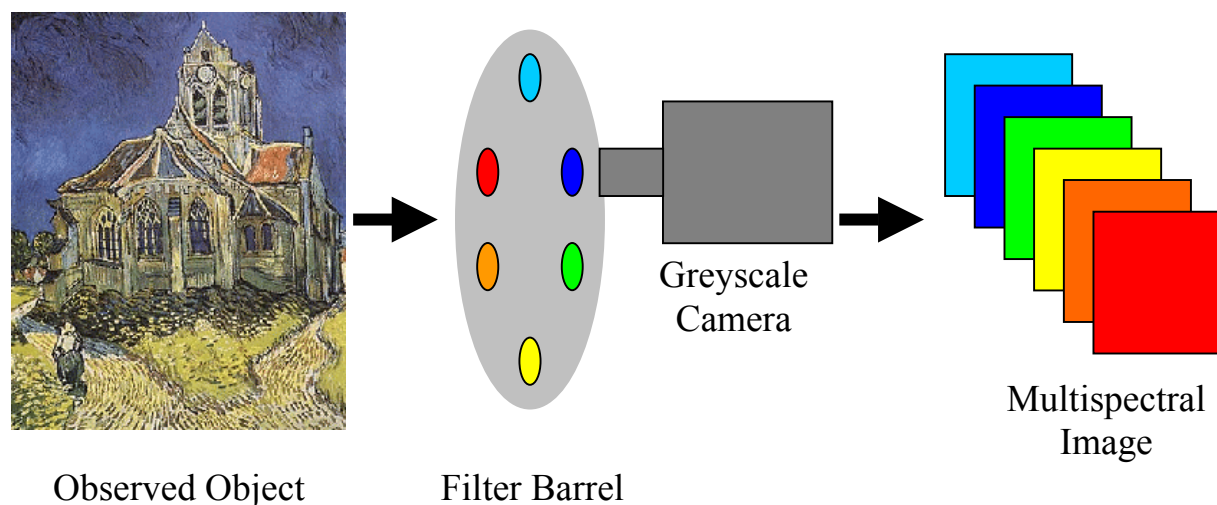


Figure 2-1 Graphical representation of an multispectral acquisition system.

A multispectral camera is then a device using several filters, the exact number used depends on the system and normally varies between 4 and 20. For instance an acquisition system commercialised by *ColorAixperts* in Aachen, Germany, uses 16 filters, [Herzog and Hill, 2003], and on the European project CRISATEL the camera developed by Lumiere Technologie, Paris, France, uses 10 filters on the visible range of the spectrum, [Cotte and Dupouy, 2003]. The older European project VASARI used seven filters, [Saunders and Cupitt, 1993]. The more extended application of multispectral imaging aims to produce high-end colour images. These applications are not in the mass media market at the moment. They are highly specialized. Examples of application can be found in the textile industry [Herzog and Hill, 2003] or on the art-works reproduction [Saunders and Cupitt, 1993]. Recently a

multispectral video camera for accurate colour reproduction has been developed using 6 channels, [Ohsawa et al., 2003]. Due to this prominent high end colour reproduction application most of the filters used in multispectral imaging are *bandpass* filters into the visible range of the electromagnetic spectrum. Currently some researchers consider that the term multispectral imaging is too general. Different names are proposed and used. This wiliness of change is clear in the titles of some recent papers, examples are [Hardeberg, 2003] that uses *Multispectral Colour Imaging* and [Sun and Fairchild, 2003] that propose the interesting term *Visible Spectral Imaging*.

In the rest of this section we introduce the basic concepts found in a multispectral acquisition system.

2.2.1 Image acquisition system model

The main components involved in an image acquisition process are depicted in Figure 2-2. We denote the spectral radiance of the illuminant by $l_R(\lambda)$, the spectral reflectance of the object surface imaged in a pixel by $r(\lambda)$, the spectral transmittance of the optical systems in front of the detector array by $o(\lambda)$, the spectral transmittance of the k -th optical colour filter by $\phi_k(\lambda)$ and the spectral sensitivity of the CCD array by $\alpha(\lambda)$. Note that only one optical colour filter is represented in Figure 2-2. In a multichannel system, a set of filters are used.

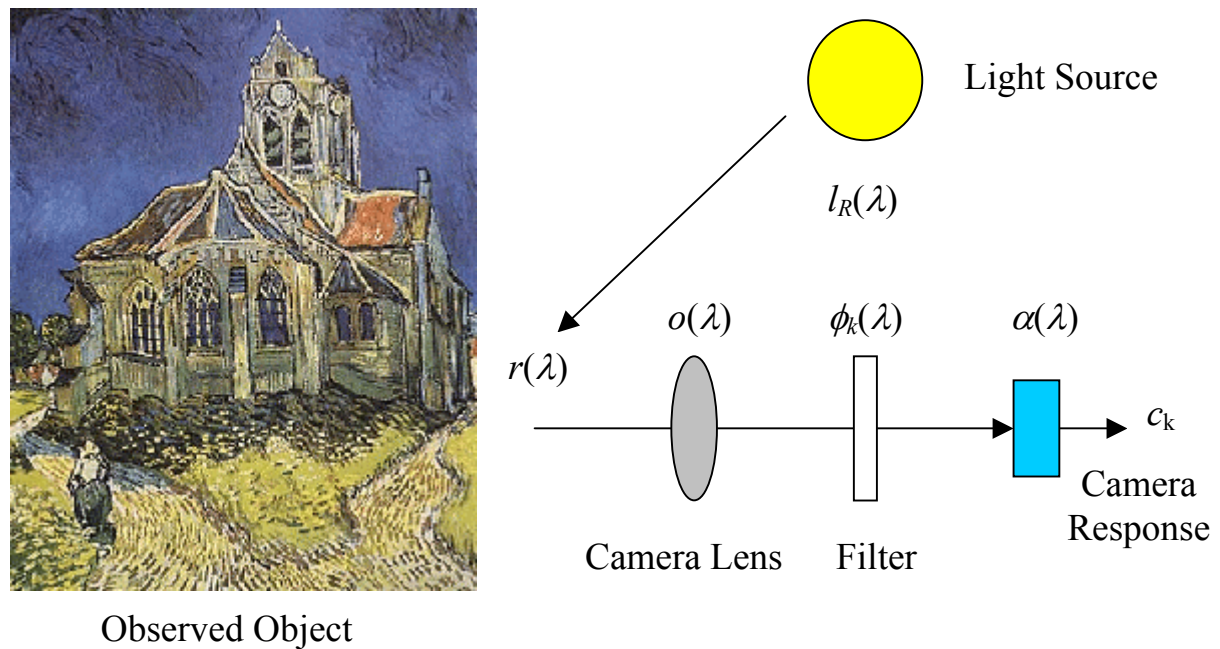


Figure 2-2 Schematic view of the image acquisition process. The camera response depends on the spectral sensitivity of the sensor, the spectral transmittance of the colour filter and camera lens, the spectral reflectance of the objects in the scene, and the spectral radiance of the light source.

Supposing a linear optoelectronic transfer function of the acquisition system, the camera response c_k for an image pixel is then equal to:

$$c_k = \int_{\lambda_{\min}}^{\lambda_{\max}} l_R(\lambda) r(\lambda) o(\lambda) \phi_k(\lambda) \alpha(\lambda) d\lambda + n_k = \int_{\lambda_{\min}}^{\lambda_{\max}} r(\lambda) w_k(\lambda) d\lambda + n_k, \quad (2.1)$$

where $w_k(\lambda) = l_R(\lambda) o(\lambda) \phi_k(\lambda) \alpha(\lambda)$ denotes the spectral sensitivity of the k -th channel, and n_k is the additive noise as it will be described in section 2.2.2. The assumption of system linearity comes from the fact that the CCD sensor is inherently a linear device. However, for real acquisition systems this assumption may not hold, for example due to electronic amplification non-linearities or stray light in the camera, [Farrell and Wandell, 1993], [Maitre et al., 1996]. Stray light may be strongly reduced by appropriate black anodised walls inside the camera. For residual stray light and electronic non-linearities appropriate corrections may be necessary. By modelling the nonlinearities of the camera as:

$$\tilde{c}_k = \Gamma\left(\int_{\lambda_{\min}}^{\lambda_{\max}} r(\lambda) w_k(\lambda) d\lambda + n_k\right), \quad (2.2)$$

we may easily obtain the response:

$$c_k = \Gamma^{-1}(\tilde{c}_k) \quad (2.3)$$

of an ideal linear camera by inverting the function Γ .

By uniformly sampling the spectra at N equal wavelength intervals, we can rewrite equation (2.1) as a scalar product in matrix notation as:

$$c_k = \mathbf{r}^t \mathbf{w}_k + n_k, \quad (2.4)$$

where $\mathbf{r} = [r(\lambda_1) r(\lambda_2) \dots r(\lambda_N)]^t$ and $\mathbf{w}_k = [w_k(\lambda_1) w_k(\lambda_2) \dots w_k(\lambda_N)]^t$ are vectors containing the sampled spectral reflectance function, and the sampled spectral sensitivity of the k -th channel of the acquisition system, respectively. Now, the vector $\mathbf{c}_K = [c_1 c_2 \dots c_K]^t$ representing the responses of all K filters may be described using matrix notation as:

$$\mathbf{c}_K = \mathbf{\Theta} \mathbf{r} + \mathbf{n}, \quad (2.5)$$

where $\mathbf{n} = [n_1 n_2 \dots n_K]^t$, $\mathbf{\Theta}$ is the K -line, N -column matrix of filter transmittances multiplied by the camera characteristics, that is $\mathbf{\Theta} = [w_k(\lambda_n)]^t$. This matrix represents the spectral sensitivity of each k -th channel at each n -th sampled wavelength.

In the following subsections we introduce in more detail three important components that appear as functions on the image formation model of equation (2.1): the light source, the optical filters and the CCD.

2.2.1.1 Light sources

In this subsection we introduce one of the most important components of a multispectral system: light sources. We consider their spectral properties which are characterised by their relative spectral radiant distributions. The spectral range of these distributions is usually confined to the visible. However these distributions extent to the infrared and ultraviolet and can have “side effects” that are out of the scope of this thesis (e.g. fluorescence produced by ultraviolet lighting).

There exists a large variety of light sources obtained either by a natural phenomenon or by a physically created reaction. [Wyszecki and Stiles, 1982] gives the following classification of light sources:

- Daylight
- Thermal radiators
- Electric discharge lamps
- Electroluminescent sources
- Light Emitting Diodes (LED)
- Lasers

Multispectral images are normally taken in laboratories or places where the light source is stable, and can be properly controlled and measured. It is rare to find outdoors multispectral images because of the absence of stability and knowledge about the light source. Daylight is then not very commonly used as light source. Electroluminescent sources and LEDs are also not adapted as they use to have a too low radiant energy. We do not know any application of laser in multispectral imaging, even if possible this kind of light is by definition monochromatic and then it has no sense to use it in conjunction with optical filters.

Finally, only two kinds of light sources are used in multispectral imaging: thermal radiators and electric discharge lamps. Well known thermal radiators are Tungsten and Tungsten-Halogen lamps. Examples of electric discharge lamps are Mercury Vapour lamps, Xenon bulbs, Fluorescent lamps or Flashtubes.

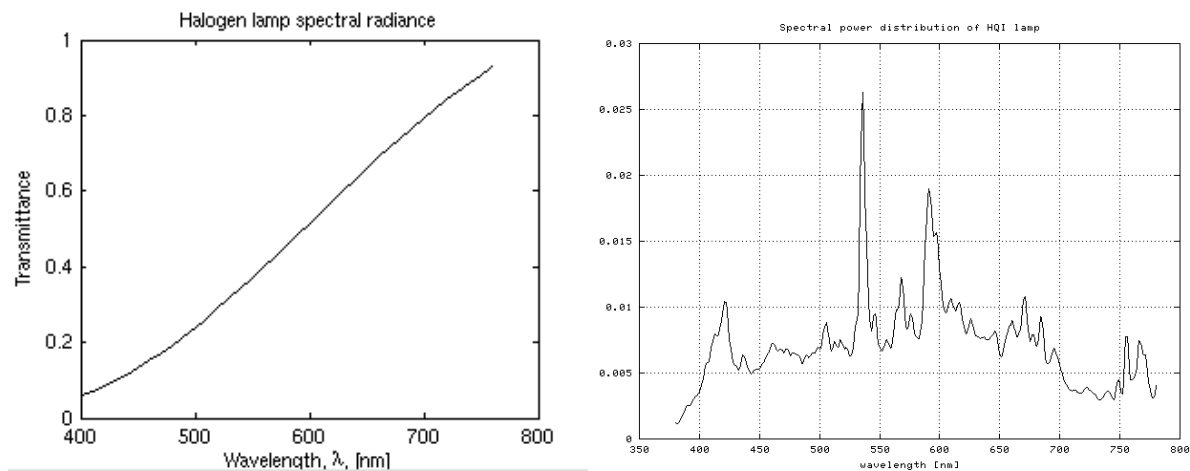


Figure 2-3 Two different emissivity functions of (left panel) an halogen lamp and (right panel) a discharge lamp.

In Figure 2-3 we can see two spectral emissivity functions corresponding to a Tungsten-Halogen and a Xenon discharge lamp. With this figure we illustrate two typical spectral distribution of illuminants which are used in multispectral imaging. We can easily imagine the effect of these different functions on equation(2.1). If all other functions are fixed the camera responses will be very different. We note that in the case of the discharge lamp its spectral emissivity function is not continuous. This fact makes that a discontinuous function appears under the integral sign of equation (2.1). We will come back to this point later in this section but this property can cause serious problems when performing spectral reconstruction. For its continuous shape halogen is one of the most used light sources on multispectral acquisition systems.

2.2.1.2 Optical Filters

In the broadest sense, an optical filter is a device or material that changes selectively or non selectively the spectral distribution of the incident radiant flux, [Wyszecki and Stiles, 1982]. A filter may be designed to select a region of the spectrum within which a portion of the incident radiant flux is transmitted, whereas at all other regions of the spectrum the incident flux is not transmitted. This kind of filters is called *bandpass* and is often used in multispectral imaging. Depending on the size of the band they are classified as *narrow* or *wide* band filters. This classification is fundamental and has important consequences in the properties of the images. In Figure 2-4 we show two Gaussian-shaped filters centred at 600 nm. The area contained under the spectral transmittance of a wideband filter is bigger than for narrowband filters, this implies low spectral resolution but high signal to noise ratio. On the other hand, the nature of the wideband integration performs a low pass filtering. Narrow band filters gives more useful information as they can be seen as an approximation to the Dirac sampling function.

In multispectral acquisition systems we currently find three types of filter technology. We will briefly describe them here for completeness.

- Absorption filters. They are made of glass, gelatine or liquids in which colouring agents are dissolved or suspended. The incident radiant flux on the first surface of the filter propagates through the filter medium and emerges from the second surface. Portions of the radiant flux arriving at the first and second surfaces are lost by reflection, whereas the remaining portions are transmitted but reduced because of absorption within the filter medium.
- Interference filters. They are multilayer thin-film devices. Wavelength selection is based on the property of destructive light interference. Incident light is passed through coated reflecting surfaces. The essential component of these filters is the simplest Fabry-Perot interferometer, two partially reflecting thin-film layers separated by a dielectric spacer. The distance between the reflective coatings determines which wavelengths destructively interfere and which wavelengths are in phase and will ultimately pass through the coatings. If the reflected beams are in phase, the light is passed through two reflective surfaces. If the multiple reflections are not in phase, destructive interference reduces the transmission of these wavelengths through the device to near zero. This principle strongly attenuates the transmitted intensity of light at wavelengths that are higher or lower than the optimal wavelength for which the multiple reflection are in phase.
- Electronically Tuneable Filters (ETF). A tuneable filter is a device whose spectral transmission can be electronically controlled through the application of voltage or an acoustic signal. There are no moving parts and no discontinuity in the spectral transmission range, thus providing finer spectral sampling, and rapid and random switching between bands. A wide variety of different ETFs is commercially available. The majority of them can be classified under three categories: liquid crystal devices based on birefringence, acousto-optical based on diffraction, and Fabry-Perot based on optical interference. We will not give here more details about them, please, refer to [Poger and Angelopoulou, 2001] for an easy to read introduction to their properties.

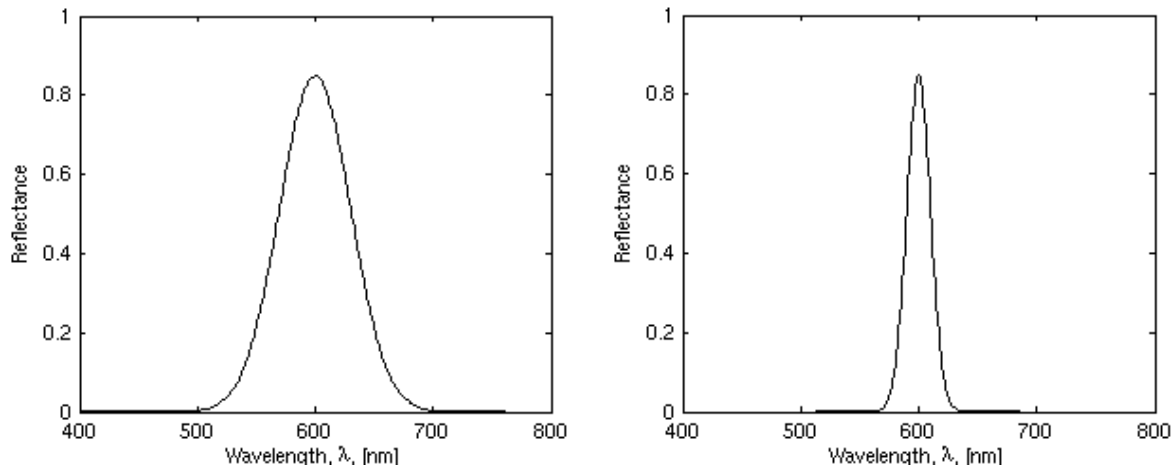


Figure 2-4 Two Gaussian-shaped filters centred at 600 nm, (left panel) a wideband filter, (right panel) a narrowband filter.

2.2.1.3 CCD sensitivity

Existing multispectral cameras are based on Charge Coupled Devices (CCDs). A CCD is a silicon-based integrated circuit consisting of a dense matrix of photodiodes that operate by converting photons into electronic charge. Electrons generated by the interaction of photons with silicon atoms are stored in a potential well and can subsequently be transferred across the chip through registers and output to an amplifier. We will not get into details of the physics of a CCD that are complex and cumbersome. For the design of a multispectral system we need to know the CCD sensitivity as a function of wavelength.

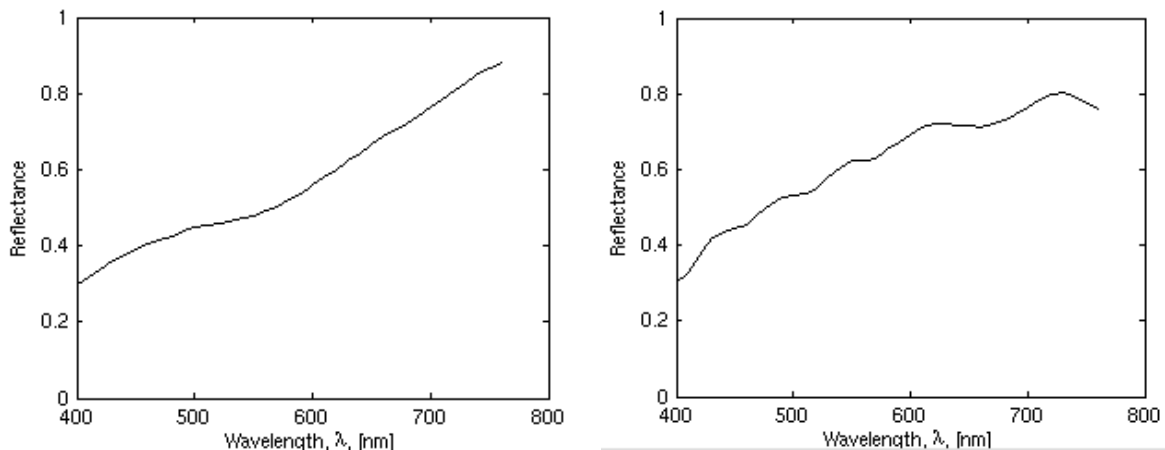


Figure 2-5, Two examples of CCD sensitivity functions: (left panel) Eikonix CCD, (right panel) Thomson linear array CCD.

In Figure 2-5 we show the spectral sensitivity functions of two different CCDs. On the left panel we present the sensitivity of the CCD used in an Eikonix camera and on the right panel the sensitivity of the Thomson linear array that is used in the CRISATEL camera produced by Lumiere Technologie. Both curves are drawn as given by the manufacturers. In this figure we can already see one general feature of CCD sensitivity that is higher on the red part of the visible spectrum than on the blue region. This means, when combined with Tungsten-Halogen lamps, that the resulting imaging system needs to compensate this lack of sensitivity in the blue range by a higher exposure time. The result is that the signal in the blue range is more affected by noise. Currently, CCD manufacturers make efforts to compensate this problem,

latest generation of CCDs for astronomical imaging perform better on the lower side of the visible spectrum.

2.2.2 Noise into the image formation process

We have seen that the image formation process presented in 2.2.1 is noisy. We rewrite here for clearness equation(2.5):

$$\mathbf{c}_K = \Theta \mathbf{r} + \mathbf{n} , \quad (2.6)$$

where \mathbf{n} is the vector of random noise. In this subsection we are interested in the nature of \mathbf{n} . We will see that \mathbf{n} can be decomposed into several components.

Understanding the different sources of noise in a multispectral system can be of great use. In the following we describe the main sources of noise found in this sort of systems.

2.2.2.1 Noise sources related to a CCD.

We can classify noise sources into two types: temporal and spatial. Temporal noise can be reduced by frame averaging, while spatial noise cannot. However, some spatial noise can be removed by frame subtraction or gain/offset correction techniques. Examples of temporal noise that are discussed in this subsection include shot noise, output amplifier noise, and dark current shot noise. Spatial noise sources include photo response non-uniformity and dark current non-uniformity. According to [Eastman Kodak, 2001], we have the following noise sources associated with a CCD:

- Dark Current is the result of imperfections or impurities in the depleted bulk silicon or at the silicon-silicon dioxide interface. These sites introduce electronic states in the forbidden gap which act as steps between the valence and conduction bands, providing a path for valence electrons to sneak into the conduction band, adding to the signal measured in the pixel. The efficiency of a generation centre depends on its energy level, with states near mid-band generating most of the dark current. The generation of dark current is a thermal process wherein electrons use thermal energy to hop to an intermediate state, from which they are emitted into the conduction band. For this reason, the most effective way to reduce dark current is to cool the CCD, decreasing electrons of the thermal energy required to reach an intermediate state.

Dark current generates two types of noise: dark current non uniformity and dark current shot noise. Dark current non-uniformity is a noise that results from the fact that each pixel generates a slightly different amount of dark current. This noise can be eliminated by subtracting a dark reference frame from each image. The dark reference frame should be taken at the same temperature and with the same integration time as the image. This is normally performed at the calibration stage. Although the dark signal can be subtracted out, the shot noise associated with this signal cannot. As in the case of photon shot noise, the amount of dark current shot noise is equal to the square root of the dark signal, D :

$$\sigma_{dark} = \sqrt{D} . \quad (2.7)$$

There exist sources of dark current that do not follow the general dark current equation and cannot be reliably subtracted out. Examples include dark current spikes, generated by

proton-induced cluster damage or by various metallic contaminants, contained in the bulk silicon.

- Shot Noise is the noise associated with the random arrival of photons at any detector. It is the physical fundamental limit of light detection systems in noise performance. Since the time between photon arrivals is governed by Poisson statistics, the uncertainty in the number of photons collected during a given period of time is simply:

$$\sigma_{shot} = \sqrt{S}, \quad (2.8)$$

where σ_{shot} is the shot noise and S is the signal, both expressed in electrons. So a 10,000-electron exposure will have a shot noise of 100 electrons. This implies that the best signal-to-noise ratio possible for a 10,000-electron signal is $10,000/100 = 100$.

- Output Amplifier Noise is composed of two primary sources, white noise and flicker noise. Together, they make up the CCD's "read out noise":
 1. The output amplifier has a resistance that causes thermal noise. The effective resistance in this case is the output impedance of the source follower. This type of thermal noise is sometimes called 'Johnson noise' or simply 'white noise,' since its magnitude is independent of frequency.
 2. Flicker Noise, also called 1/f noise, is a noise that has an approximately inverse dependence on the amplifier frequency. The higher the frequency or pixel rate, the lower the noise. More specifically, the noise power decreases by a factor of 10 for each decade increase in frequency.

In general, white noise increases with amplifier area. Assuming a constant drain current, Flicker noise decreases with amplifier area. The goal of amplifier design is to find the lowest-noise compromise between competing geometries for the desired operating frequency. But read out noise always exists.

- Photo Response Non-Uniformity (PRNU): Due to process variations, not all pixels demonstrate the same sensitivity to light. The result at the pixel-to-pixel level is a faint checkerboard pattern in a flat-field image. Usually this variation is on the order of a percent or two of the average signal, and is linear with average signal. The noise associated with this variation in sensitivity can be removed by 'flat-fielding,' a process by which a previously-captured flat-field image is used to calibrate out the differences between pixels. This is obviously done at calibration step. Although this process removes the photo response non-uniformity, the subtraction of images introduces an increase in shot noise by a factor 2.

Once we know the more important sources of CCD noise we realize that the model in equation (2.6) cannot take into account spatial noise sources. This is because the equation represents the acquisition process of one pixels. There is an underlying assumption: "all pixels in the CCD behave in the same way". As a consequence, PRNU and spatial dark current noise must be treated in a pre-spectral reconstruction stage, let's call it calibration. In any case errors introduced in the calibration are errors that will affect the spectral reconstruction. This source of error is normally not taken into account and we expect the result of the calibration stage to be as good as possible.

The noise sources in a CCD camera normally taken into account in the multispectral community, see [Haneishi et al., 1997] or [Burns, 1997], are dark current \mathbf{N}_{DC} , read-out noise \mathbf{N}_{RO} and shot noise \mathbf{N}_{S} . Dark current and read-out noise are both signal-independent while shot noise \mathbf{N}_{S} is signal-dependent [Healey and Kondepudy, 1994]. Other noise sources are normally ignored. Consequently, CCD noise can be expressed as:

$$\mathbf{n} = \mathbf{N}_{\text{DC}} + \mathbf{N}_{\text{RO}} + \mathbf{N}_{\text{S}}. \quad (2.9)$$

It is known that dark current noise has a positive mean and fluctuates around it, while read out noise and shot noise have zero mean. Representing the dark current noise by a positive mean $\bar{\mathbf{N}}_{\text{DC}}$ plus fluctuation \mathbf{n}_{DC} we have:

$$\mathbf{N}_{\text{DC}} = \bar{\mathbf{N}}_{\text{DC}} + \mathbf{n}_{\text{DC}}. \quad (2.10)$$

Then equation (2.9) can be rewritten as:

$$\mathbf{n} = \bar{\mathbf{N}}_{\text{DC}} + \mathbf{N}_{\text{C}} + \mathbf{N}_{\text{S}}, \quad (2.11)$$

where $\mathbf{N}_{\text{C}} = \mathbf{n}_{\text{DC}} + \mathbf{N}_{\text{R}}$.

$\bar{\mathbf{N}}_{\text{DC}}$ can be estimated at the calibration stage, and subtracted from the obtained image as part of pre-processing. The remainder consists of signal-independent noise \mathbf{N}_{C} and signal-dependent noise \mathbf{N}_{S} . The variance of the remaining noise, σ_n^2 , can be expressed as the sum of the variances of \mathbf{N}_{C} and \mathbf{N}_{S} because the occurrence of each one of these noises is independent of the other:

$$\sigma_n^2 = \sigma_{\text{C}}^2 + \sigma_{\text{S}}^2, \quad (2.12)$$

where σ_{C}^2 and σ_{S}^2 represent the variances of signal-independent noise and signal-dependent noise, respectively.

The characterization of the noise requires some experimentation to obtain actual values of the parameters involve in the noise model. This requires access to dedicated equipment and is time consuming, normally it is done in a laboratory or a controlled environment. The data from this analysis can be exploited at the spectral reconstruction stage. We will see for instance the Wiener filter that integrates such data.

2.2.2.2 Quantification Error

The process of transforming an analog signal into its digital counterpart introduces noise, which is intrinsic to the quantization process and is a consequence of the loss of information that happens when an analog signal is packed into a finite representation. Consequently we are forced to deal with this kind of noise as all digital cameras provide quantized values for the image pixels.

The relationship between the number of bits b used to quantize the camera response, and the signal-to-noise ratio (SNR) is given by:

$$SNR[dB] = 10 \log_{10} \left(\frac{\|\mathbf{c}\|^2}{\|\mathbf{c} - \text{quant}_b(\mathbf{c})\|^2} \right), \quad (2.13)$$

where $\text{quant}_b(\mathbf{c})$ represents the quantisation of \mathbf{c} into b bits. Note that the camera responses are normalised before quantization so that the response of a perfect reflecting diffuser yields to the maximum value $c_{max} = 1$.

2.2.2.3 Other sources of error

In the two preceding subsections we spoke about sources of errors associated with the camera itself but noise errors can exist in other parts of the multispectral acquisition system.

- In a multispectral system we use often calibrated colour charts. These charts are measured by a spectrophotometer. These measurements are not free of noise.
- Differences in viewing/illumination geometry between the image acquisition setup and the reflectance measurements of the colour charts obtained with a spectrophotometer.
- A dedicated illuminant is normally used in multispectral imagery. Any temporal instability of the illuminant introduces errors.
- Deviation from the linear acquisition model due to effects such as *i)* insufficiently corrected non-linear transfer function, *ii)* too coarse spectral sampling, *iii)* residual camera sensitivity outside of the wavelength interval used in the model, and *iv)* fluorescence.

At this moment we understand that noise is significant in multispectral imaging. In the rest of this thesis we will come back to this problem extensively. We will study the noise in the framework of the real CRISATEL acquisition system in Chapter 6.

2.3 Nature of spectral reflectance curves

In this section we are interested in the nature of spectral reflectance because it is a physical characteristic of object surfaces. Knowing the spectral reflectance of a surface is richer than just knowing colour as colour is a psychophysical concept while reflectance is physical. Reflectance is then attached to the imaged object while colour depends on several factors such as the illumination, the spectral sensitivity of the observer or the appearance of surrounding objects. Moreover, colour can easily be deduced from spectral reflectance. Here, we try to give some insight into the nature of spectral reflectances, specially into the ones we will use in the rest of the thesis.

The section is organised as follows. We first present the spectral reflectance databases used on this thesis. Afterwards, we perform a Fourier analysis of these databases. This justifies the smoothness found on the spectral curves and the used sampling ratio. Then, we statistically analyse the databases by Principal Component Analysis (PCA). In this context we introduce the Frobenius norm as a measure of comparison of the orthogonal bases obtained from the PCA. This new approach allows the comparison of different databases. In order to complete the discussion about the nature of spectral reflectance curves we introduce the concept of noise on the measurements of these data. Finally, we present, analyse and compare a new colour chart developed on the framework of the CRISATEL European project.

2.3.1 Spectral Reflectance Databases

We use several databases of spectral reflectances in this thesis. We present them in the following. The first three of them are kindly provided by D. Saunders from The National Gallery, London, the last one is downloaded from the Color Research Laboratory at University of Joensuu [Jaaskelainen, 1994]:

- the “Kremer” database contains 184 spectral curves of pigments produced by Kremer Pigmente, Germany.
- the “Selected Artists” database contains 67 pigments chosen among a collection of artist’s paintings.
- the “Restoration” database contains a selection of 64 pigments used in oil painting restoration.
- the “Munsell” database is not issue from the same canvas painting environment. It contains spectral curves corresponding to 1269 matte Munsell colour chart samples.
- the “MacbethDC” database. We have scanned in our laboratory a GretagMacbeth™ DC color chart using a Minolta CS-100 spectroradiometer. From this experiment we obtained 200 spectral curves from 380 to 780 nm sampled at 1 nm intervals, each curve corresponding to a colour patch of the chart. In Figure 2-6 we can see an image of the scanned chart.
- the “Pine Tree” database. This database contains 370 spectral reflectances of the needles of young (less than 40 years old) individual Scots pines. This is part of an experiment to measure forest reflectances conducted by Vaisala Laboratory, University of Joensuu, Finland. In the same experiment Norway spruce and the leaves of a birch were also measured but we do not use them as dataset.. The data were collected in Finland and Sweden. Measurements using a PR 713/702 AM spectroradiometer were made in clear weather during the growing season in June 1992. Each measurement represents the average spectrum of thousands of leaves of a

growing tree. For further reference on this experiment see [Jaaskelainen, 1994]. We include this database in some of our tests because its nature is fundamentally different from the others we presented above.

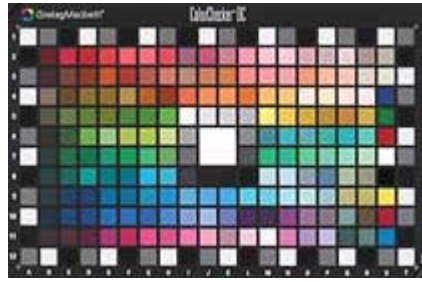


Figure 2-6 Image of the GretagMacbethTM DC color chart.

These databases having been acquired in different laboratories, consequently sampled at different rates and with different wavelength limits, we resampled them in order to represent each spectral reflectance curve as a sequence of regularly sampled values from 400 to 760 nm at 10 nm intervals, which corresponds to 37 values. This is a way of preparing data to be analysed homogeneously.

2.3.2 Fourier Analysis.

Spectral reflectances of pigments being smooth functions, they are band limited as shown by [MacDonald et al., 1999] who performed a Fourier analysis over several spectral reflectance data sets. In this section we apply the discrete Fourier transform (DFT) to our spectral data. We use the fast Fourier transform (FFT) for the analysis, that is a well known quick implementation of the DFT. Our aim is to show which frequencies are included in our particular data sets.

As it is well known, the Fourier transform is based on the assumption that it is possible to take any periodic function of time $x(t)$ and resolve it into an equivalent infinite summation of sine waves and cosine waves with frequencies that start at 0 and increase in integer multiples of a base frequency $f_0 = 1/T$, where T is the period of $x(t)$. The expansion is:

$$x(t) = a_0 + \sum_{k=1}^{\infty} (a_k \cos(2\pi k f_0 t) + b_k \sin(2\pi k f_0 t)). \quad (2.14)$$

An expression of the form of the right hand side of this equation is called a Fourier Series. A Fourier Transform aims to calculate all the a_k and b_k values to produce a Fourier Series, given the base frequency and the function $x(t)$. The a_0 term can be understood as the cosine coefficient for $k=0$. There is no corresponding zero-frequency sine coefficient b_0 because the sine of zero is zero, and therefore such a coefficient would have no effect.

Of course, we cannot do an infinite summation of any kind on a real computer, so we have to settle for a finite set of sines and cosines. Our signals having a finite number of samples they are represented by a vector of 37 numbers as indicated in section 2.3.1. We can pretend that the function $x(t)$ is periodic, and that the period is the same as the length of the elements vector representing the signal. In other words, this vector of 37 coefficients is repeated forever, and we call this periodic function $x(t)$. The duration of the repeated section defines the base frequency f_0 in the equations above. Then, $f_0 = \text{samplingRate} / N$, where N is the number of samples (37).

The output of the Fourier Transform will be the sine and cosine coefficients a_k and b_k for the frequencies $f_0, 2* f_0, 3* f_0$, etc. This pairs a_k and b_k are normally represented as a complex number. The FFT is an algorithm which converts a sampled complex-valued function of time into a sampled complex-valued function of frequency. In our case spectral reflectance curves are real-valued functions, so all the imaginary parts of the input are set to zero (this is done automatically for most FFT implementations).

In order to properly understand the FFT, the following equation shows the relationship between the inputs and outputs that the FFT algorithm tries to approximate:

$$y_p = \sum_{k=0}^{N-1} x_k \left(\cos\left(2\pi \frac{kp}{N}\right) + i \sin\left(2\pi \frac{kp}{N}\right) \right), \quad (2.15)$$

where x_k is the k th complex-valued input (time-domain) sample, y_p is the p th complex-valued output (frequency-domain) sample, and N is the total number of samples. Note that p is in the range $[0..N-1]$. This formula is the discrete version of the Fourier transform or DFT but it is not how the FFT algorithm is implemented. Raw DFT calculation requires $\mathbf{O}(N^2)$ operations, whereas the FFT requires $\mathbf{O}(N*\log_2(N))$. Clearly the FFT is quicker than the raw DFT, but the algorithm loses some precision and impose some conditions. In this sense an important point to take into account is N , the size of the array given as output by the FFT. The value of N in the FFT must be a positive integer power of 2. For example, an array of 1024 is allowed, but one of size 1000 is not. The smallest allowed array size is 2. There is no upper limit to the value of N other than limitations inherent in memory allocation. This limitation is imposed by the FFT algorithm to be able to execute in $O(N*\log_2(N))$. If this limitation does not hold a normal DFT could be computed, but the order of the algorithm becomes $O(N^2)$ as said above. We choose N (FFT output) as the smaller power of two containing the signal to be analysed.

The ordering of the frequencies a_k and b_k in the output of the FFT merit some attention because they contain both positive and negative frequencies. Both of them are necessary for the method to work when the inputs are complex-valued (i.e. when at least one of the inputs has a non-zero imaginary component). Most of the time, the FFT is used for strictly real-valued inputs, as it is the case in our analysis. The FFT, when fed with real-valued inputs, gives outputs whose positive and negative frequencies are redundant. They are *complex conjugates*, meaning that their real parts are equal and their imaginary parts are negatives of each other. Our inputs being real-valued, we can get all the needed frequency information just by looking at the first half of the output arrays. As a consequence just half of our N array is useful and intervals $[0..N/2 - 1]$ and $[N/2..N-1]$ present symmetric values.

At this point, we have described the operation of the FFT in terms of speed and other important considerations to take into account, but in order to proceed with the analysis we need to describe the data obtained in the first half of the output array. The index $N/2$ is a special case: it corresponds to the *Nyquist frequency*, which is always half the sampling rate. Nyquist frequency is in our case $f_0/2$, that is the biggest frequency component of the original input signal that could be recover. FFT inputs being real numbers, the Nyquist frequency index $N/2 - 1$ in the output will always have a real value (meaning the imaginary part will be zero, or something really close to zero due to floating-point roundoff errors). This is due to the symmetry mentioned above, so the Nyquist frequency is its own negative frequency counterpart. Therefore, it must equal its own complex conjugate, which in turn forces it to be a real number.

The first element of the FFT output array, $i=0$ contains the average value of all the input samples. For the output indices $i = 0, 1, 2, \dots, N/2-1$, the value of the frequency expressed in Hz is $f = \text{samplingRate} * i / N$. The negative frequency counterpart of every positive frequency index $i = 0, 1, 2, 3, \dots, N/2-1$, is $i' = N - i$.

In our analysis we are mainly interested in the magnitude of each frequency component, normally called the power spectrum. In fact, this is sensible because one of the aims of our analysis is to see if our signals are bandlimited; for this purpose, only the magnitudes of the frequency components are important. We calculate the power spectrum as follow

$$\text{powerSpectrum} = \text{FFT}_{\text{output}} \times (\text{FFT}_{\text{output}})^* / N, \quad (2.16)$$

where $*$ represents the complex conjugate and operation \times is the multiplication of two vectors element by element. In Figure 2-7 we show some examples of reflectance curves with their calculated power spectrum. Note that because of the division by N in equation (2.16) the used power spectrum is a power spectrum distribution where the areas are normalised. Three important details are to be taken into account when looking at these curves:

- Because Fourier analysis supposes that the curves are periodic, we have periodised the signals. This operation involves two steps: i) we modify the function in order to fit zero on the first at last elements of the signal, ii) we mirror (central symmetry) this modified signal. Due to this process our original of 37 samples curves become periodic signals of 72 samples.
- Because the FFT algorithm just works on signals having number of samples equal to a power of two, we look for the closest power of two that contains our signals. In our case this power is 128, we complete our 72 samples signal with zeros up to 128 and we feed the FFT algorithm with this data.
- Finally, the FFT algorithm outputs a 128 elements complex vector, we apply equation (2.16) on it to obtain the power spectrum. Due to the symmetrical structure of the output data just the first half 64 elements contain significant information going from the so called *DC* (smaller) frequency to the *Nyquist* (highest) frequency.

In the three samples shown in Figure 2-7 we clearly see that most of the power spectrum is nearly zero, note that the vertical axis are different because the curves have the same area but different shapes. Values that can be consider non zero are concentrated in the left hand side of the power spectral graphs. In order to finish our analysis we perform the power spectrum for all the curves contained in our databases. This results are shown together in Figure 2-8. But some further analysis is needed to find a frequency threshold that will summarize numerically that our signals are clearly bandlimited. In order to find such a threshold, after performing the power spectrum for all curves in a database we calculate the mean power spectrum of all of them. As we normalize magnitudes of the frequency components between 0 and 1 we choose a value less than 0.0005 as being an indicator of no presence of these frequency components in the curves. Finally, we sequentially access the FFT output vector from the $N/2-1$ element (corresponding to the *Nyquist frequency*) in decreasing order. The frequency associated to the first element found having a magnitude bigger than 0.0005 is the searched frequency threshold. This threshold is graphically shown in Figure 2-8 as a vertical dashed line.

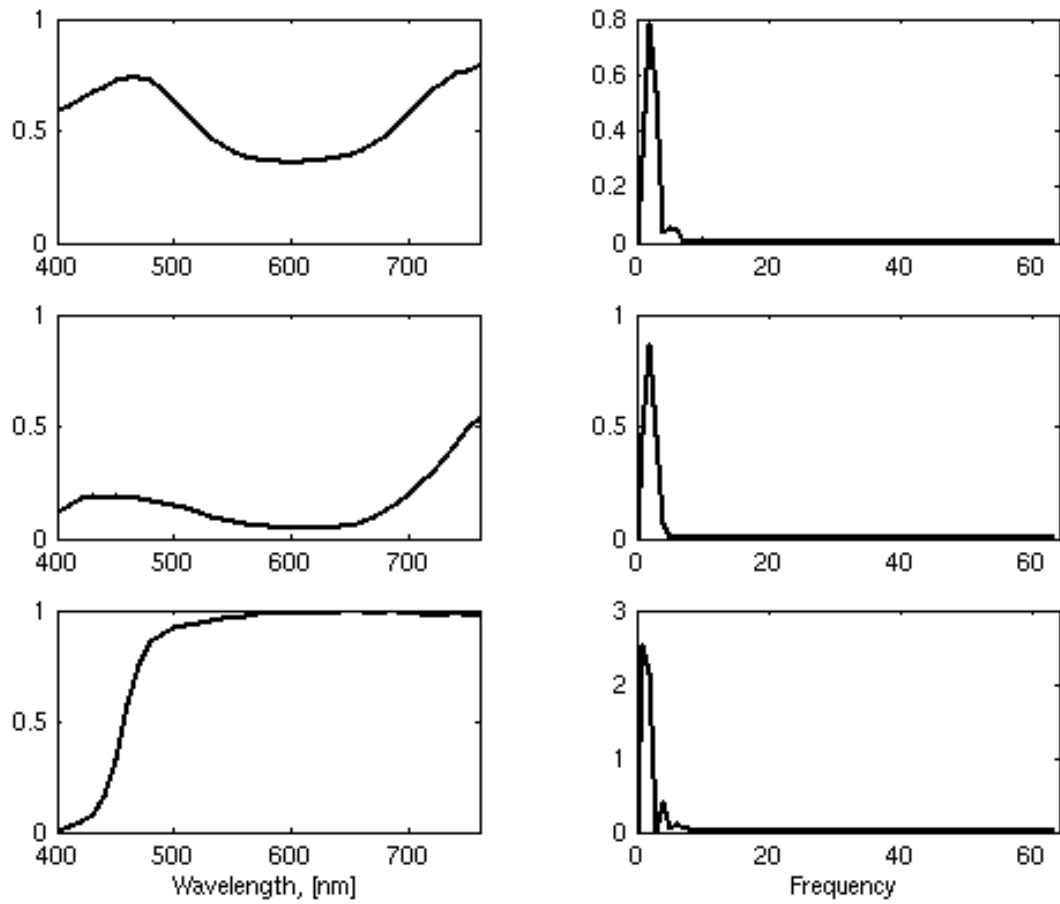


Figure 2-7 (left panels) three spectral reflectance curves coming from the Kremer database, (right panels) corresponding power spectrum distribution.

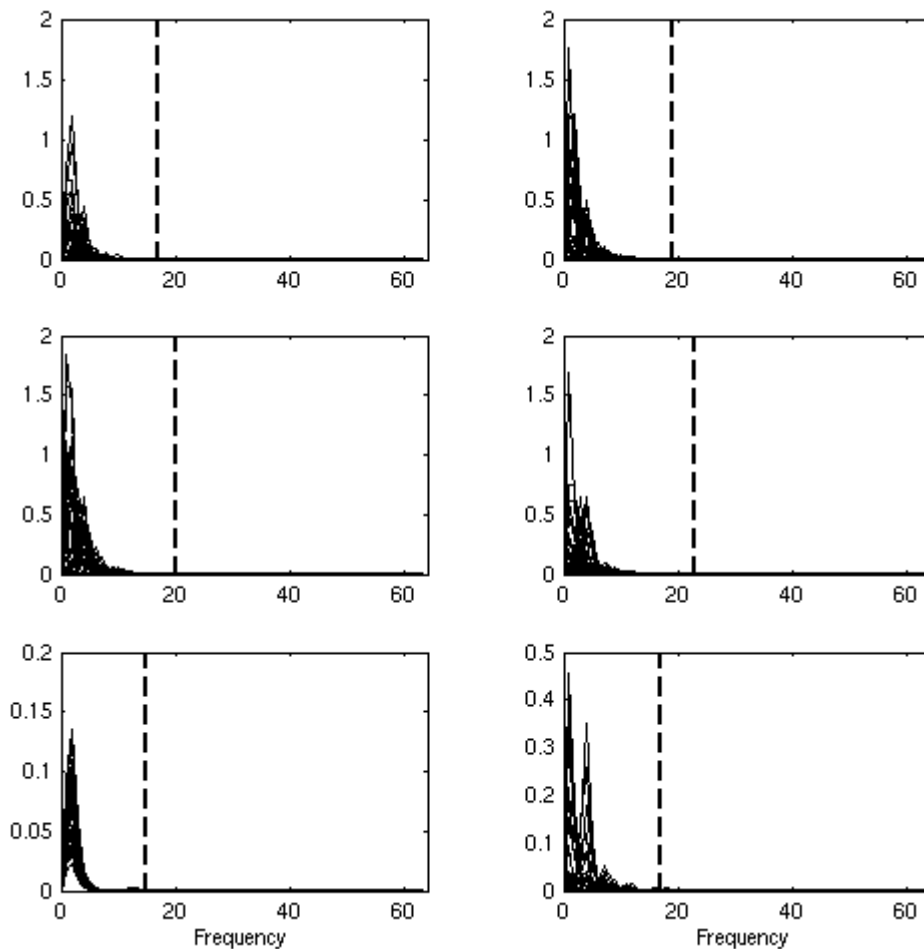


Figure 2-8 Power spectrum of 30 curves in the databases: Restoration (left top panel), Selected Artists (right top panel), Kremer (left central panel), MacbethDC (right central panel), Pine Tree (left bottom panel), Munsell (right bottom panel). Space between dashed lines and left vertical axes indicate the band where signals present frequency components higher than the threshold.

In Table 2-1 we indicate the exact values of the calculated thresholds for all our databases. This threshold can be easily used to compare the databases. As a conclusion we can say that our databases are indeed bandlimited.

Table 2-1: Fourier analysis results.

	frequency threshold
Kremer	<i>17</i>
Selected Artists	<i>19</i>
Restoration	<i>20</i>
Macbeth DC	<i>23</i>
Pine Tree	<i>15</i>
Munsell	<i>17</i>

2.3.3 Principal Component Analysis.

Principal Component Analysis (PCA) is a well known statistical tool that finds an orthogonal basis for the analysed data in which each vector of the basis has an associated energy that indicates the statistical relevance of the vector. PCA is a linear method based on second order moments over data (variance analysis). If the reader is not familiar with PCA he will find suitable introductions to this technique in most introductory textbooks to statistics or linear algebra as [Golub and VanLoan, 1983] or [Lawson and Hanson, 1974].

PCA has been extensively used in the context of multispectral imaging as a technique for compression. See for instance [MacDonald et al, 2001] for a complete paper on this subject. In order to reduce the number of coefficients representing a reflectance curve a few PCA coefficients keeping most energy of the signal are used. As an example, we show on the left panel of Figure 2-9 the accumulated variance per singular value for the Macbeth colour chart. On the right panel of the same figure we can see its normalized singular values plotted against a logarithmic scale. We want to note that keeping only the first singular values keeps most of the variance and consequently this basic fact can be directly used for compressing spectral reflectance functions.

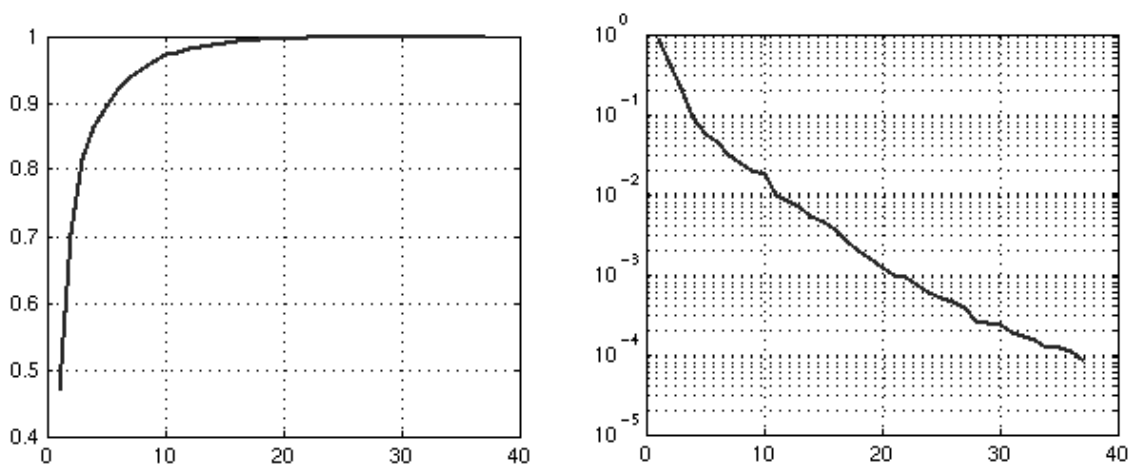


Figure 2-9. (left panel) Accumulated variance per singular values for the Macbeth colour chart, (right panel), normalized singular values plotted against a logarithmic scale

We performed a principal component analysis over all our spectral databases because we want to understand the statistical nature of their spectral reflectance. In Table 2-2 the results of this analysis indicate the dimension of the orthogonal basis needed to keep 90% and 99% of signal variance.

Table 2-2: PCA analysis results.

	90 %	99 %
Kremer	7	22
Selected Artists	6	16
Restoration	6	14
Macbeth DC	6	15
Pine Tree	4	21
Munsell	6	21

With the performed analysis at 99% of signal variance we clearly see that the databases have very different complexity. But at the moment our analysis just deals with the effective dimensionality of data. This kind of results are very useful for compression. For instance, we could decide to use 22 PCA coefficients for representing the spectral curves of the Kremer database. Spectral curves being sampled at 10nm intervals on the visible range from 400 to 760 nm. They are represented by a vector of 37 numbers. Reducing this vector to 22 coefficients supposes a 1.7 compression ratio while keeping a high quality in the curves. For less exigent applications 7 components could be enough, giving a 5,3 compression ratio.

In this chapter we are not directly interested in compression but we would like a way of comparing the spectral curves of different databases. The fact that two databases have equal PCA dimension at 90% or 99% variance does not mean that both databases are similar. In fact, they could contain very different sorts of curves while having similar dimensions. This fact motivated us to go further in the analysis of this datasets and to compare the spaces obtained by the PCA. These spaces are represented by reduced orthogonal basis that keep most energy (e.g. 99%) from the original analysed spaces. Mathematically, we seek for a measure of similarity between two subvectorial spaces of the same vectorial space.

In the quest for this measure we come back to linear algebra and found the *Froebius norm* [Golub and Van Loan, 1983]. We recall its definition and some properties in the following:

Froebius norm definition of a $M \times N$ matrix \mathbf{A} is defined as:

$$\|\mathbf{A}\|_F = \sqrt{\sum_{i=1}^m \sum_{j=1}^n |a_{ij}|^2}, \quad (2.17)$$

where a_{ij} is the i -th row j -th column element of matrix \mathbf{A} . Froebius norm is invariant with respect to orthogonal transformations.

$\|\mathbf{OAZ}\|_F = \|\mathbf{A}\|_F$, where \mathbf{O} , \mathbf{Z} are unitary matrices.

$\|\mathbf{A}\|_F^2 = \sigma_1^2 + \dots + \sigma_p^2$, where σ_i , $i=1, \dots, p$ are the singular values of \mathbf{A} .

It is interesting to see that Froebius norm is like the Euclidian norm applied for matrices or vectorial spaces. However, we are not interested in the norm of a subvectorial space but in comparing two subvectorial spaces. We introduced the Froebius distance, calculated as

$$d_F(\mathbf{U}, \mathbf{V}) = \|\mathbf{U}^t \mathbf{V}\|_F = \sqrt{\sum_i^n \sum_j^m (\mathbf{u}_i^t \mathbf{v}_j)^2}, \quad (2.18)$$

where \mathbf{U} is a $l \times m$ matrix, \mathbf{V} a $l \times n$ matrix, \mathbf{u}_i a column vector of \mathbf{U} and \mathbf{v}_j a column vector of \mathbf{V} . \mathbf{u}_i and \mathbf{v}_j both belonging to the same vectorial space of dimension l . In the case of matrices containing orthogonal vectors in their columns we can clearly see that the measure corresponding to the square of this distance is closely related to the dimension of the intersection of the two subspaces defined by matrices \mathbf{U} and \mathbf{V} : for two orthogonal subspaces d_F^2 is zero and for one subspace with itself the measure is the dimension of this subspace. For two subsets of an orthogonal basis the measure is exactly the dimension of the intersection. In

a general case, the measure relates closely to the dimension of the intersection and the *principal angles* between subspaces.

Principal angles $\theta_1, \theta_2, \dots, \theta_\alpha \in [0, \pi/2]$ between the column vectors of matrices \mathbf{U} and \mathbf{V} , are defined recursively by, [Golub and Van Loan, 1983]:

$$\cos(\theta_k) = \max_{\mathbf{u} \in \mathbf{U}} \max_{\mathbf{v} \in \mathbf{V}} \mathbf{u}^T \mathbf{v} = \mathbf{u}_k^T \mathbf{v}_k, \quad (2.19)$$

subject to:

$$\begin{aligned} \|\mathbf{u}\| &= \|\mathbf{v}\| = 1 \\ \mathbf{u}^T \mathbf{u}_i &= 0 \quad i=1, \dots, k-1 \\ \mathbf{v}^T \mathbf{v}_i &= 0 \quad i=1, \dots, k-1 \end{aligned} \quad (2.20)$$

We calculated the square of the Frobenius distance among the reduced orthogonal set of PCA vectors associated to our spectral databases, keeping signal variance at 90% and 99%. Results are shown in Table 2-3 and Table 2-4 .

Table 2-3: Square of Frobenius distances at 90% of variance.

90%	Kremer	Selected Artists	Restoration	Macbeth DC	Pine Tree	Munsell
Kremer	7	5.95	5.94	5.66	3.16	5.81
Selected Artists	--	6	5.33	5.51	3.12	5.14
Restoration	--	--	6	5.42	3.03	5.59
Macbeth DC	--	--	--	6	2.98	5.55
Pine Tree	--	--	--	--	4	2.85
Munsell	--	--	--	--	--	6

Table 2-4: Square of Frobenius distances at 99% of variance.

99%	Kremer	Selected Artists	Restoration	Macbeth DC	Pine Tree	Munsell
Kremer	22	15.83	13.95	14.92	14.50	19.22
Selected Artists	--	16	13.86	14.56	11.18	15.83
Restoration	--	--	14	13.61	13.61	13.92
Macbeth DC	--	--	--	15	10.81	14.96
Pine Tree	--	--	--	--	21	13.48
Munsell	--	--	--	--	--	21

Our databases are surprisingly related, the above analysis revealing that most signals of these databases are linear combinations of the other databases. In fact, the two small databases are practically included in the Kremer set either at 90 or 99% of signal variance. Kremer database is slightly different because its complexity is greater than the others as shown in Table 2-2.

In Figure 2-10 we show the first 16 vectors of the orthogonal basis provided by the PCA for the Macbeth DC database. We observe that the spectral curves of the basis vectors oscillate more when their corresponding singular values decrease, last singular values being associated to vectors with high frequencies.

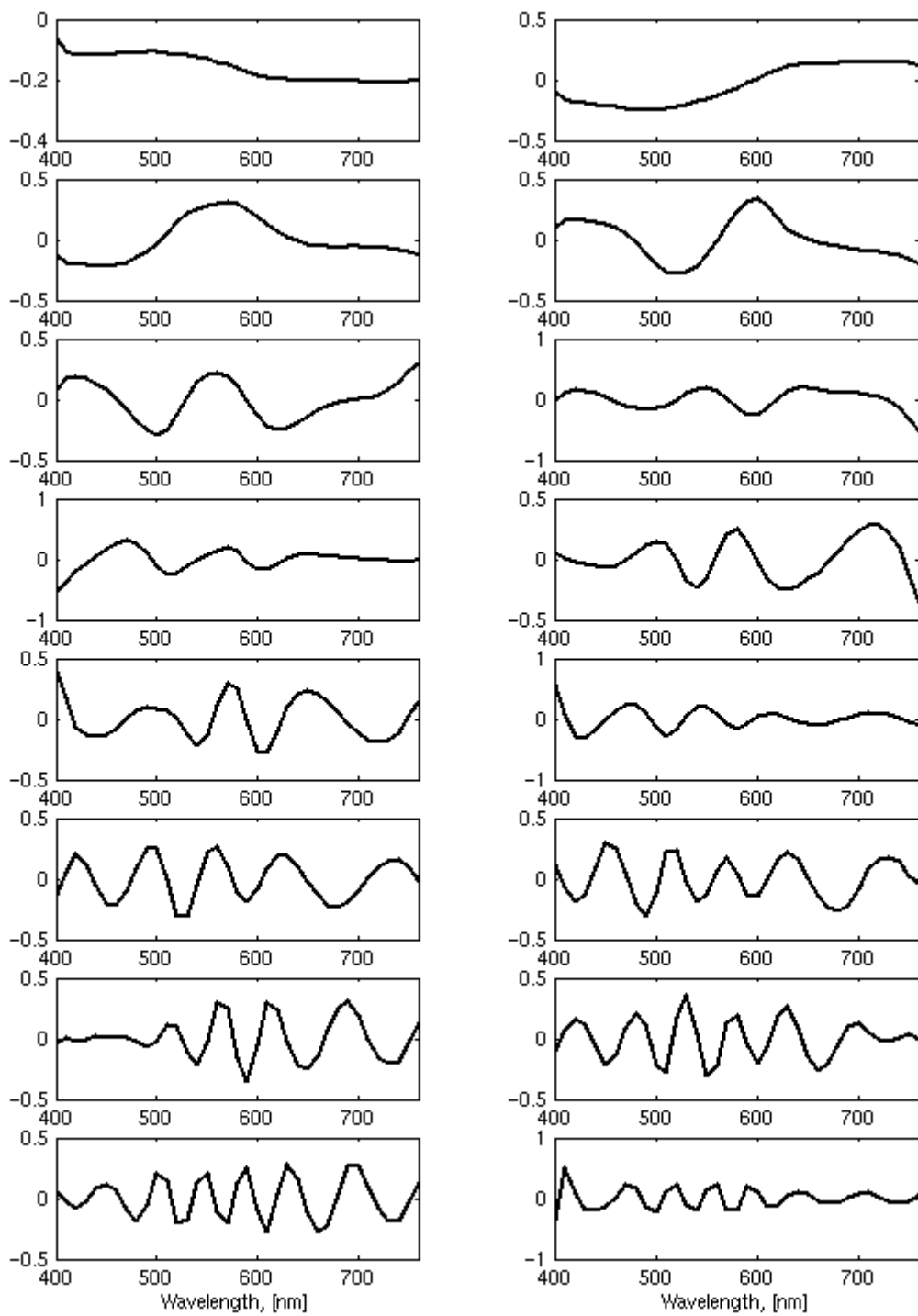


Figure 2-10 First 16th PCA vectors from the Macbeth DC database.

2.3.4 Noise on the measurements of reflectance

The curves of the spectral reflectance databases have been obtained by physical measurements which include different type of noise or errors. As we use these spectral reflectance curves as references the discussion and understanding of errors affecting them are important.

Measurements are done by a *spectrophotometer*, which is an apparatus designed to measure the spectral transmittance and spectral reflectance of objects. It allows us to compare at each wavelength the radiant power leaving an object with that incident to it, [Wyszecki and Stiles, 1982]. In a spectrophotometer there exist two fundamental elements, the light source and the detector. Sometimes the light source can be a monochromator, we will not deal with that case here, we suppose a usual light source having a spectral distribution over a defined spectral range. The measured sample can be placed inside a chamber, a usual form for this chamber, when existing, is a sphere. This sphere is called integrating sphere.

The position of the detector, the light source and the sample to be measured must be fixed. This “spatial setup” is called the measurement geometry and the CIE (Commission Internationale de l’Eclairage) recommends four of them:

- (45/0)
The sample is illuminated by one or more beams whose axes are at an angle of 45° from the normal to the sample surface. The angle between the direction of viewing and the normal to the sample should not exceed 10°. The angle between the illumination axis and any ray of the illuminating beam should not exceed 5°. The same restriction should be observed in the viewing beam.
- (0/45)
This geometry correspond to exchange the position of sensor and light source in the preceding (45/0) geometry.
- (d/0)
The sample is illuminated diffusely by an integrating sphere. The angle between the direction of viewing and the normal to the sample should not exceed 10°, sometimes this angle is known and noted as (d/α), e.g. (d/8) for a 8° angle. The integrating sphere may be of any diameter provided the total area of its apertures does not exceed 10% of the internal reflecting sphere area.
- (0/d)
This geometry corresponds to exchange the locations of sensor and light source in the preceding (d/0) geometry.

From this above description we can already identify some sources of errors on the measurements. Different companies propose spectrophotometers with different sensors, light sources or integrating spheres, then there exists a variation on the measurements depending on the tool being used. But, another important source of variability between different spectrophotometers is their measurement geometry. Consequently, two main factors can generate errors: the inter apparatus variability (specially when produced by different companies) and the measurement geometry variability.

On the CRISATEL project we collaborate with people that studied the importance of both the above described sources of variability on the reflectance measurement. Details are given on [CRISATEL d13, 2003]. In the rest of this section we will summarize some of their results.

A test colour chart was measured at The National Gallery (London) with a spectrophotometer Minolta 2600d consisting of a Silicon photodiode array, an integrating sphere with a d/8 geometry and a xenon flash lamp. Another spectrophotometer was used in Paris, on the laboratory of optics at University Paris 6, to measure the same chart. Both results had small differences. On the other hand, they compared a set of ceramic standards from the National Physical Laboratory (United Kingdom) under two different geometries, 0/45 and 8/d. The conclusion was that the spectral differences obtained with different geometric set ups are not negligible.

As a conclusion we can say that the geometry of the measurements should always be the same. If we deal with measurements taken using the same geometry and desirably the same apparatus, we can consider our measures as comparable.

2.3.5 The CRISATEL chart

In the framework of the European Project CRISATEL a new colour chart has been developed by Pébéo, a company specialised in the production of pigments for fine arts. In this section we present and analyse this chart. An image of this chart is presented on Figure 2-11. The chart is a juxtaposition of three sets of patches. They contain exactly the same patches sorted in the same way. The difference between these sets is the application of varnish over the pigments. The first set has no varnish, the second set has a thin layer of matt varnish and the third set has a layer of brilliant varnish. Each set contains 117 colour patches, 81 are colour patches and 36 forms a greyscale.

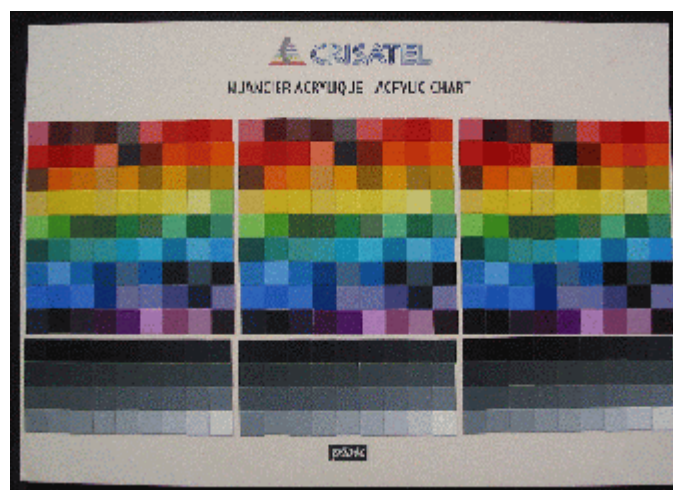


Figure 2-11. Pébéo Chart.

We will just analyse the set of non varnished patches of the chart. The influence of varnish on the appearance of the patches has already been studied on [CRISATEL d13, 2003]. This chart was measured by several spectrophotometers in different laboratories of London and Paris, the measures being performed between 360 and 700 nm at 10 nm intervals. We note that this is different from the sampling interval we normally used on this chapter and on the rest of this thesis.

The first analysis performed on the chart is the Fourier analysis. As the sampling interval is smaller than the one in section 2.3.2 we have fewer samples in our signal. The periodised version of the reflectance functions of this chart can be represented by a 64 dimensions vector instead of 128 for the analysis in section 2.3.2. We show on Figure 2-12 the power spectra of 24 curves uniformly selected from the patches. Using the same criterion as in section 2.3.2 we find a threshold value of 11 for the spectral reflectances. To be comparable with the ones already presented on Table 2-1 an approximate factor of two is applied to the threshold on Figure 2-12 giving a new comparable threshold value of 22.

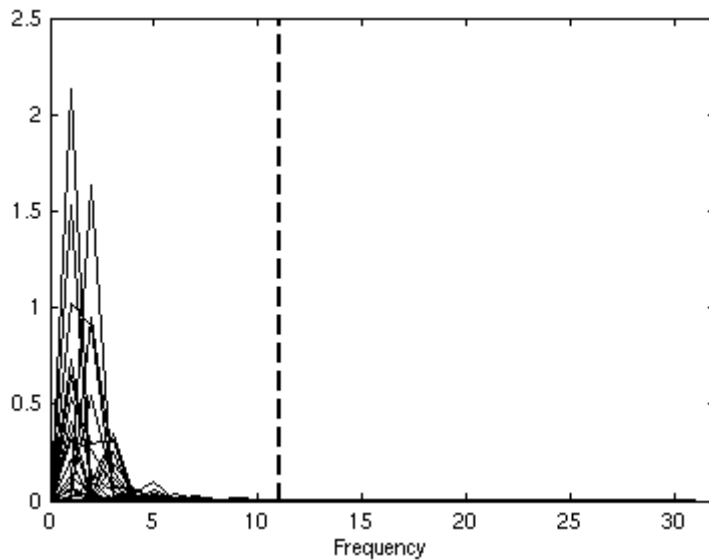


Figure 2-12. Fourier analysis on 30 selected curves of the Pébéo colour chart.

A PCA analysis is also performed on the Pébéo chart reflectances. Results are presented on Table 2-5 . We see that the found dimensions at 90% and 99% variance are similar to the ones found for the Macbeth DC database. This is interesting as both results are coming from commercial colour charts and their comparison can be of great use.

Table 2-5. PCA analysis for the Pébéo Colour Chart

	90%	99%
Pébéo	6	14

On Table 2-6 we use the Froebius norm to compare the Pébéo chart with the databases presented on section 2.3.1. This table provides useful information that can be directly compared to the one presented in Table 2-3 and Table 2-4.

Table 2-6. Comparing the Pébéo colour charts with other reflectances datasets

	90%	99%
Kremer	5.92	13.85
Selected Artists	5.73	12.65
Restoration	5.86	12.23
Macbeth DC	4.87	11.90
Pine Tree	3.29	11.55
Munsell	4.90	13.81

Finally, we compared the Pébéo and the Macbeth DC colour charts. We projected the spectral reflectances of both charts on the CIELAB space using the D50 illuminant. We recall that CIELAB allows the specification of colour perceptions in terms of a three-dimensional space, see Appendix I for a brief introduction to basic colorimetry. The L^* -axis is known as the lightness and extends from 0 (black) to 100 (white). The other two coordinates A^* and B^* represent redness-greenness and yellowness-blueness respectively. Samples for which $a^* = b^* = 0$ are achromatic and thus the L^* -axis represents the achromatic scale of greys from black to white. On Figure 2-13 we show the projections of the reflectances of the CIELAB space on the LA, LB and AB planes. Asterisks represent patches of the Pébéo chart while crosses refer to patches of the Macbeth DC chart. This diagrams visually helps to understand the different distributions of the patches. Clearly, the Macbeth DC chart is based on the regular sampling of the lightness axis for its design. Pébéo chart is not regularly distributed on lightness, presents a larger greyscale, has less colour patches (less dense on the AB plane) and has a different colour gamut. A new Pébéo chart with three times more colour patches is under construction.

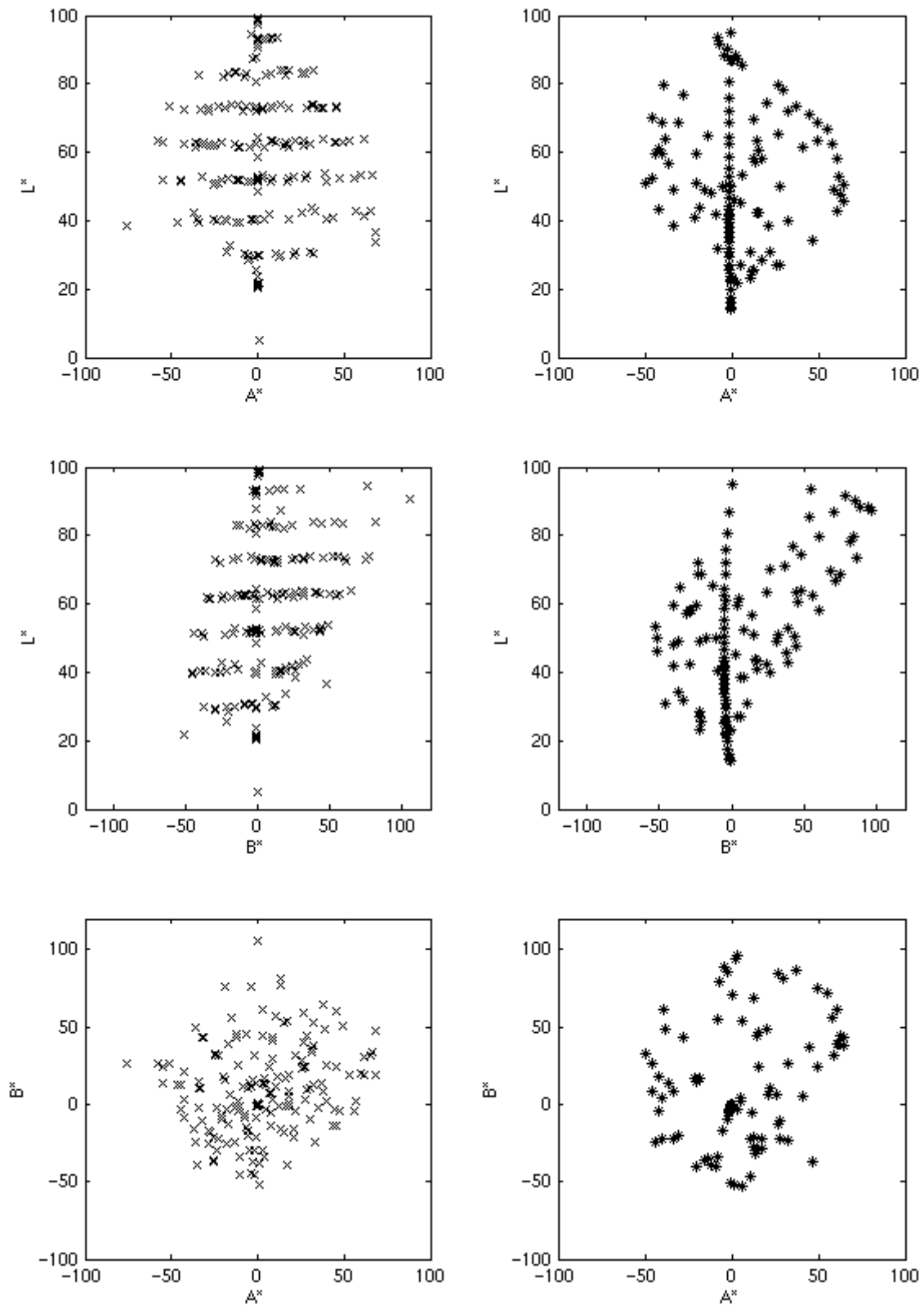


Figure 2-13. Comparing the CIELAB coordinates of the patches of Pèbéo (right panels) and Macbeth (left panels) colour charts.

2.4 Conclusion

In this chapter we have introduced basic concepts about multispectral imaging. Fundamental formulae were described and the main components of a multispectral system (light sources, filters, CCD and reflectances) have been described. Moreover, the spectral reflectance databases used on the rest of this thesis are presented and studied. Fourier analysis and Principal Component Analysis (PCA) are the mathematical tools used on their analysis.

A new approach for the comparison of different databases is also developed. It is based on the Froebius norm as a measure of comparison of the orthogonal bases obtained from the PCA. This approach is simple and mathematically well founded.

Noise sources on multispectral acquisition systems and on the measurements of reflectance are introduced. Their description helps understanding the basic limitations of an imaging system based on the concept of spectral reflectance instead of colour.

Finally, we have presented, analysed and compared a new colour chart developed on the framework of the CRISATEL European project.

Chapter 3:

Basics of Spectral Reconstruction

Contents

3.1	Introduction	41
3.2	Spectral reflectance estimation from camera responses.....	42
3.2.1	Spectral reflectance estimation as an ill-posed problem	43
3.2.2	The two spectral reconstruction problems	44
3.2.3	Spectral reconstruction as interpolation: a third paradigm.....	45
3.2.4	An example of simulation for spectral reconstruction	45
3.3	Least squares and pseudo-inverse	50
3.3.1	Pseudo inverse.....	50
3.3.2	Least square solutions	51
3.3.3	Simulating the ideal spectral reconstruction problem	53
3.4	Taking noise into account.....	58
3.5	Metrics for evaluating reconstruction performance.....	59
3.5.1	Spectral Curve Difference Metrics.....	59
3.5.2	CIE Colour Difference Equations	60
3.6	Existing Reconstruction Techniques	63
3.6.1	Smoothing inverse.....	63
3.6.2	Wiener's filter	65
3.6.3	Hardeberg's modified Pseudo-inverse	66
3.6.4	Pseudo-inverse and SVD.....	67
3.6.5	Non averaged pseudo-inverse	69
3.6.6	Non Negative Least Squares	70
3.6.7	Techniques based on Interpolation.....	73
3.7	Conclusion.....	78

3.1 Introduction

We consider the problem of the reconstruction of spectral reflectance curves from multispectral images. The pixel value of a channel in a multispectral image is the result of:

- 3) the spectral interaction of the light radiant distribution with the reflectance of an object surface and
- 4) the spectral sensitivity of the camera combined with the transmittance of the optical path including the filter corresponding to this channel.

Retrieving the spectral reflectance function of the object surface at each pixel is highly desirable. We call this process spectral reflectance reconstruction or simply spectral reconstruction. It allows an intrinsic representation of an object surface property which is independent from light spectral distribution and from the spectral sensitivity of the camera used for the multispectral image acquisition. This representation can be used for many different purposes. Our interest is in high fidelity colour reproduction of fine art paintings. As an example, knowing the spectral reflectances in each pixel allows us to simulate the appearance of a painting under any virtual illuminant.

The aim of this chapter is to introduce the problem of spectral reconstruction and to present a survey on reconstruction techniques by the introduction of all necessary concepts for their understanding and analysis. We illustrate all the techniques by using computer simulations. These simulations allow us to give some insight to the behaviour of the techniques. Discussions are given along with simulation results.

We propose a classification of the reconstruction techniques in three paradigms: i) *direct* reconstruction, which is based on the inversion of the camera model and needs the physical characterization of the acquisition system; ii) *indirect* reconstruction or *learning-based* reconstruction, where a calibrated colour chart and its multispectral image are used to construct a reconstruction operator; iii) reconstruction by interpolation, where the obtained camera responses are interpolated to find an approximation of the corresponding reflectance function. In our knowledge it is the first time that a survey with this classification is given. We believe it is useful to conceptually differentiate methods that have a very different conceptual origin. Our classification is physically and mathematically well founded and helps understanding the limits and requirements of the methods.

This chapter contains five main sections. In the next section the problem of spectral reflectance estimation from camera responses is presented. Fundamental formulae is given and, based on them, the classification briefly described in the above paragraph is introduced. The following section 3.3 deals with the solution of least squares problems. Afterwards, a brief section 3.4 recalls the role and importance of noise when performing spectral reconstruction. Section 3.5 describes the metrics used in this thesis for the evaluation of spectral reflectance matches. Finally, a survey of the existing reconstruction techniques is presented. This survey is illustrated by computer simulations. The methods are discussed, analysed and compared with others to give a good understanding of their behaviours.

3.2 Spectral reflectance estimation from camera responses

We now consider a multispectral image capture system consisting of a monochrome CCD camera and a set of K filters, for a given illuminant. The spectral sensitivity $w_k(\lambda)$, $k=1 \dots K$, of the k -th channel of the acquisition system including the illuminant radiance, the filter transmittances, and the CCD sensitivity are supposed known. The camera response c_k obtained with the k -th filter, discarding acquisition noise, is given by:

$$c_k = \int_{\lambda_{\min}}^{\lambda_{\max}} r(\lambda) w_k(\lambda) d\lambda_k . \quad (2.21)$$

The vector $\mathbf{c} = [c_1 \ c_2 \ \dots \ c_K]^t$ represents the response to the set of K filters. By uniformly sampling the spectrum at N equal wavelength intervals, we can rewrite equation (2.21) as a scalar product in matrix notation as:

$$c_k = \mathbf{w}_k^t \mathbf{r} , \quad (2.22)$$

where $\mathbf{r} = [r(\lambda_1) \ r(\lambda_2) \ \dots \ r(\lambda_N)]^t$ and $\mathbf{w}_k = [w_k(\lambda_1) \ w_k(\lambda_2) \ \dots \ w_k(\lambda_N)]^t$, are vectors containing the sampled spectral reflectance function, and the sampled spectral sensitivity of the k -th channel of the acquisition system, respectively. Now, the vector \mathbf{c} may be described using matrix notation as:

$$\mathbf{c} = \Theta \mathbf{r} , \quad (2.23)$$

where Θ is the K -line, N -column matrix defining the imaging process, $\Theta = [\mathbf{w}_1 \ , \dots \ , \mathbf{w}_K]^t$. The matrix element $\Theta_{k,n} = w_k(\lambda_n)$ represents the spectral sensitivity of each k -th channel at each n -th sampled wavelength. We note that the transposed N -line, K -column matrix $\Theta_2 = [\mathbf{w}_1 \ , \dots \ , \mathbf{w}_K]$ is also commonly used in the multispectral scientific community, leading to the following equation equivalent to (2.23):

$$\mathbf{c} = \Theta_2^t \mathbf{r} . \quad (2.24)$$

The relationship $\Theta = \Theta_2^t$ is elementary but important to keep in mind when reading the multispectral literature. This is because the formulae of the reconstruction techniques take different forms depending on the choice of notation.

We now address the problem of how to retrieve the spectrophotometric information \mathbf{r} from the camera responses \mathbf{c} . This is different from a direct colorimetric transformation that matches camera responses \mathbf{c} into for example the CIELAB space. This transformation is constrained to a specific illuminant. This approach typically minimises the RMS error in a way similar to what is often done for conventional three-channel image acquisition devices. Given an appropriate regression model, this is found to give quite satisfactory results in terms of colorimetric errors [Burns, 1997]. However, for our applications we are concerned not only with the colorimetry of the imaged scene, but also with the inherent surface spectral reflectance of the viewed objects. Thus the colorimetric approach is not sufficient.

In existing multispectral acquisition systems, the filters often have narrow bandpass shapes and are located at approximately equal wavelength intervals. For the reconstruction of the spectral reflectance numerous techniques have been proposed.

Adopting the linear-model approach of equation (2.23), the problem of the estimation of a spectral reflectance \mathbf{r} from the camera responses \mathbf{c} becomes a quest for an inverse linear operator \mathbf{Q} that reconstructs the spectrum from the K measurements as follows:

$$\hat{\mathbf{r}} = \mathbf{Q} \mathbf{c}. \quad (2.25)$$

Our goal will thus be to determine the matrix \mathbf{Q} that minimises a distance $d(\mathbf{r}, \hat{\mathbf{r}})$, given an appropriate error metric d . Some solutions to this problems are presented and discussed in the following subsections.

3.2.1 Spectral reflectance estimation as an ill-posed problem

The notion of a well-posed problem, “un problème bien pose”, goes back to a famous paper by Jacques Hadamard published in 1902, [Hadamard, 1902]. In an earlier paper in 1901 he already mentioned “questions mal posées”, ill-posed problems. He argued that the problems that are physically important are both possible and determined, i.e., solvable and uniquely solvable. He gave examples of problems that are not well posed; he thought that these problems have no physical meaning. However, he was not right and plenty of important problems in technology, medicine, and natural sciences are ill-posed. In fact, any measurement, except for the most trivial ones, gives rise to an inverse problem that is ill-posed. In our context the problem of spectral reconstruction is ill-posed, this is important to understand when looking for new methods to solve it.

A well-posed problem in the sense of Hadamard is a problem that fulfil the following three conditions:

1. The solution exists.
2. The solution is unique.
3. The solution depends continuously on the problem data.

If any of these conditions is not respected the problem becomes ill-posed. Note that both first and second conditions deal with the feasibility of the problem, the last condition relates with the possible implementation of a stable numerical procedure for its resolution. The solution of a problem is always based on some data, typically obtained from experimentation. If the solution does not depend “smoothly” on the problem data a small variation on the data can create huge variations on the solutions, resulting in strong instability which is not acceptable.

A classical example of ill-posed problems is a Fredholm integral equation of the first kind. They are equations involving a function $f(x)$, and integrals of that function to be solved for $f(x)$. If the limits of the integral are fixed, the equation is called a Fredholm integral equation. If one limit is variable, it is called a Volterra integral equation. If the unknown function is only under the integral sign, the equation is said to be of the *first kind*. If the function is both inside and outside, the equation is called of the *second kind*. If we consider the spectral reconstruction problem we see that equation (2.21) is based on a Fredholm integral equation of the first kind. Consequently, our reconstruction problem is an ill-posed problem.

We can also observe that the problem is ill-posed when taking a look at the discrete system we want to inverse,

$$\mathbf{c} = \mathbf{\Theta} \mathbf{r}. \quad (2.26)$$

The matrix Θ is in general not a square matrix ($K \neq N$) then the system itself is over or underdetermined by definition. This means that either the system has no solution or it has many. Clearly this does not respect conditions 1 or 2 of Hadamard definition: the problem is ill-posed. Third condition is not as easy to see as the others but it must be respected since it is a big issue for numerical solutions. We will come back to this condition latter on this chapter.

When solving ill-posed problems the word *regularization* immediately appears. Regularization is used to make well-posed a problem that is ill-posed. Once the problem is well-posed we can solve it. The so called *Tikhonov regularisation* is one of the oldest and more well-known techniques, see [Tikhonov, 1963] for the original paper of its inventor or [Tikhonov and Arsenin, 1977] for broadest references.

Regularization is then very important for the spectral reconstruction problem. All the reconstruction methods we will describe on this thesis regularize the problem in someway, even when not explicitly said.

3.2.2 The two spectral reconstruction problems

Most people in the multispectral literature speak about spectral reconstruction as a unique problem. In fact, this is an abuse of language and strictly speaking there exist two problems. If we think about the equation (2.23) our aim is to find an inverse operator \mathbf{Q} that will solve the problem, see equation (2.25). But, the direct operator Θ can be known or not. On this section we will explain this point in detail because the difference has important practical and theoretical consequences for the resolution of the problem.

3.2.2.1 Direct reconstruction problem

Knowing the operator Θ means that a physical characterization of the acquisition system has been performed. This characterization requires at least the measurement of the CCD sensitivity, filters transmittances and optics transmittance. The characterization involves the realization of physical experiments in which, typically, a monochromator is used for measuring the CCD sensitivity and a spectroradiometer for measuring transmittances.

Once the characterization has been performed, the operator Θ is known. We can then reach a method to inverse this operator. Θ is a matrix and corresponds to the discretization of the integral operator in equation (2.21) representing the system. But Θ not being a square matrix, its inverse does not exist. This is clearly an ill-posed problem. Furthermore, even if we find a *pseudo-inverse* (we will explain this technique in detail later) the solution cannot be stable. This is basically due to the effect of noise in the system. Knowledge on the model of noise or at least its covariance matrix is very useful. This implies more experiments because the characterization of noise needs in general a model which can be estimated by means of some statistical analysis over a series of images from the CCD taken in a dark room.

3.2.2.2 Indirect or learning-based reconstruction problem

On the other hand, the inverse operator can be constructed without knowing Θ . If we know the spectral reflectance curves of a set of P colour patches and we take an image of these patches with the multispectral camera then we have a set of corresponding pairs $(\mathbf{c}_p, \mathbf{r}_p)$, for $p=1, \dots, P$, where \mathbf{c}_p is a vector of dimension K containing the camera responses and \mathbf{r}_p is a vector of dimension N representing the spectral reflectance of the p -th patch. In this case, we are confronted with a different kind of problem. We want to estimate the inverse operator from a set of known data. As the set of data is obtained experimentally this problem is ill-

posed too. There is an easy way to see that the problem is ill posed. Let's put in the columns of a $N \times P$ matrix \mathbf{R} all the \mathbf{r}_p 's and in the columns of a $K \times P$ matrix \mathbf{C} all their corresponding \mathbf{c}_p 's. The discrete expression of this problem if we do not take into account the presence of noise, becomes:

$$\mathbf{R} = \mathbf{Q} \mathbf{C} , \quad (2.27)$$

where \mathbf{Q} is a $N \times K$ matrix representing the inversion of the unknown matrix Θ . A straightforward solution of this linear system would be:

$$\mathbf{Q} = \mathbf{R} \mathbf{C}^{-1} , \quad (2.28)$$

if \mathbf{C} were a full rank square matrix, but usually $P \gg K$. Moreover, the stability of the solution would not be assured because of the presence of noise. The problem is ill-posed in the sense of Hadamard.

From the above discussion an important fact should be retained: spectral reconstruction can be formulated and treated as two different problems, both of them being ill-posed. This is a source of constant misunderstanding because when searching linear solutions of ill-posed problems the mathematical expressions of the solutions can look very similar even if the underlying problems are different. In practice this often mislead in the literature the comparison of solutions based on different problems.

Practically, it is not always possible to completely characterize a camera. In comparison, taking a multispectral image of a calibrated colour chart is trivial when a multispectral system is operational. The results of the reconstructions obtained when solving one or the other problem should be carefully compared taking into consideration the difference in nature of the two approaches and the experimental conditions.

3.2.3 Spectral reconstruction as interpolation: a third paradigm

There exists a third paradigm for spectral reconstruction. A multispectral system can be seen as sampling spectral reflectance curves. Instead of using delta Dirac functions for the sampling as in the classical framework, the spectral transmittance functions of filters are considered to be the sampling functions. This is conceptually different from the two already presented paradigms. Moreover, it does not require information about the operator Θ or a set of spectral reflectances \mathbf{R} . It just requires the camera response itself, \mathbf{c} .

The methods based on this paradigm interpolate the camera responses acquired by a multispectral camera by using a smooth curve. The smoothness properties of the interpolating curve introduce a natural constraint which regularizes the solutions.

We will describe and give some insight to interpolation methods in subsection 3.6.7 when describing the existing spectral reconstruction techniques.

3.2.4 An example of simulation for spectral reconstruction

In the rest of this chapter we are going to compare linear methods for solving ill-posed problems applied to both direct and indirect spectral reconstruction problems. In order to illustrate these techniques, analyse their behaviours and give insight into their meaning, we have developed a computer simulation of a virtual multispectral system.

This virtual multispectral acquisition system is easy to manipulate and to study with no need of physical experiments. At this stage it reveals itself very useful for understanding, designing and testing the various presented spectral reconstruction techniques. Later on this thesis we will present and compare the results obtained by a selection of reconstruction techniques using data coming from real experiments.

The virtual acquisition system is based on a 10 band multispectral system. The spectral response of the camera is based on the sensitivity function of the CCD array used in the real CRISATEL camera. The filters are simulated by 10 equispaced Gaussian-shaped functions covering the visible domain of the spectrum. We chose 10 because it is also the number of the interference filters used in the CRISATEL camera. This number is a parameter that can be easily modified. The expression used to produce these Gaussian-shape filter transmittances M_k , $k=1, \dots, 10$, is:

$$M_k = 0.85 e^{-\frac{(x-\mu_k)^2}{2\sigma_k^2}}, \quad (2.29)$$

where σ_k controls the half-width of the k -th filter, and μ_k the position of its maximum. The range of μ is 400 to 760 nm, typically the μ 's of 10 equidistributed Gaussian-shaped filters going from $\mu_1 = 416$ to $\mu_{10} = 740$ at constant step of 36 nm. σ represents 30 nm half-bandwidth. The value 0.85 makes the simulated filters not to have perfect transmittance.

The illuminant used in the simulation is a halogen lamp. This choice is justified as it is the light source normally used when performing multispectral image acquisition. Halogen has continuous shape and good physical stability. The virtual spectral reflectance curves are chosen among the databases already analysed in section 2.3 (*Nature of Data*). These databases are regularly sampled from 400 to 760 nm at 10 nm intervals, which corresponds to 37 values.

Basic linear algebra allows us to approximate the virtual camera in the ideal case, when noise is not present, by determining the matrix Θ . The elements of this matrix are perfectly known and are obtained by multiplying the halogen lamp emissivity, the selected Gaussian filters transmittances and the CCD sensitivity. Figure 3-1 show a graphical representation for the construction of Θ . Each curve shown on the bottom panel of Figure 3-1 represents the k -th channel spectral sensitivity of the virtual camera. Each k -th channel is sampled from 400 to 760 nm at 10 nm intervals, which forms a vector of 37 coordinates corresponding to \mathbf{w}_k , the k -th column of matrix Θ .

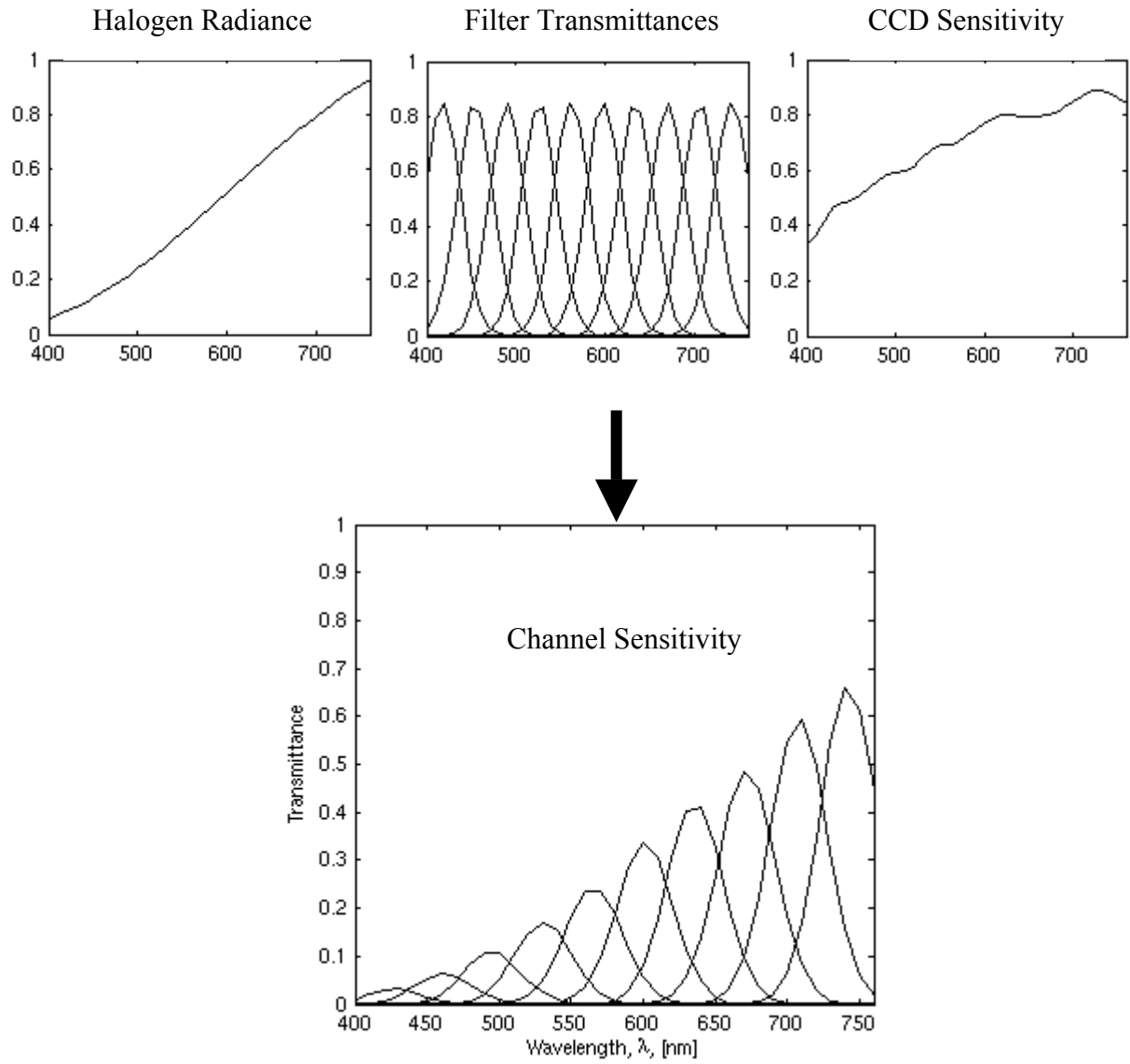


Figure 3-1 Construction of the matrix Θ used in our simulations.

There is another important point to take into account in the simulations. On the bottom panel of Figure 3-1 we can see a graphical representation of the columns of matrix Θ . It is visually evident that the maximum values of the channel sensitivities are not the same. In this case the sensitivity on the red part of the visible spectrum is much higher than on the blue part. This corresponds to the physical reality because the illuminant is not energetic on the *blue* range and the CCD sensitivity is not high in this area. In Figure 3-2 we show a simulation aiming to obtain the virtual camera responses for a perfect reflecting surface, such a spectral reflectance corresponds to an ideal white material that does not exist in nature. As we can see on the obtained camera responses, shown on the right panel of this figure, the result is not satisfactory. We desire to obtain a flat response on the camera responses as the spectral reflectance is flat. A real multispectral camera is also confronted to this problem, a part of a *radiometric calibration* process is normally dedicated to solve it. We will speak further about how to solve this problem on a real camera on Chapter 6.

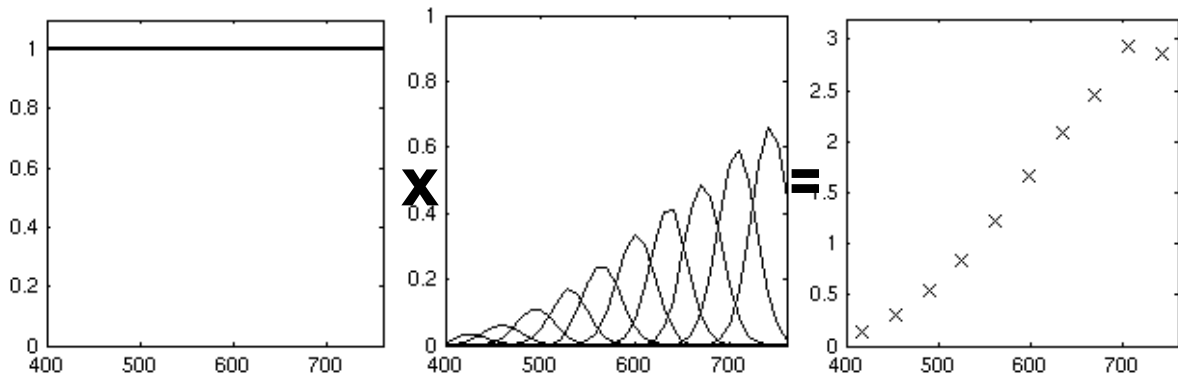


Figure 3-2. Perfect white simulation

The problem observed on Figure 3-2 appears in any spectral reflectance to be virtually imaged. It is avoided by the introduction of a normalisation matrix in the system, mathematically:

$$\Theta_N = \Theta \mathbf{N}, \quad (2.30)$$

where \mathbf{N} is a $K \times K$ diagonal matrix and Θ_N is the normalised matrix Θ . The diagonal elements of \mathbf{N} contain the inverse of the K camera responses corresponding to a perfect white.

Finally, to summarize this section we show in Figure 3-3 a complete diagram of the simulation system. A spectral reflectance curve (top panel) is properly transformed on its camera responses (bottom panel) by the use of the camera model (central panels).

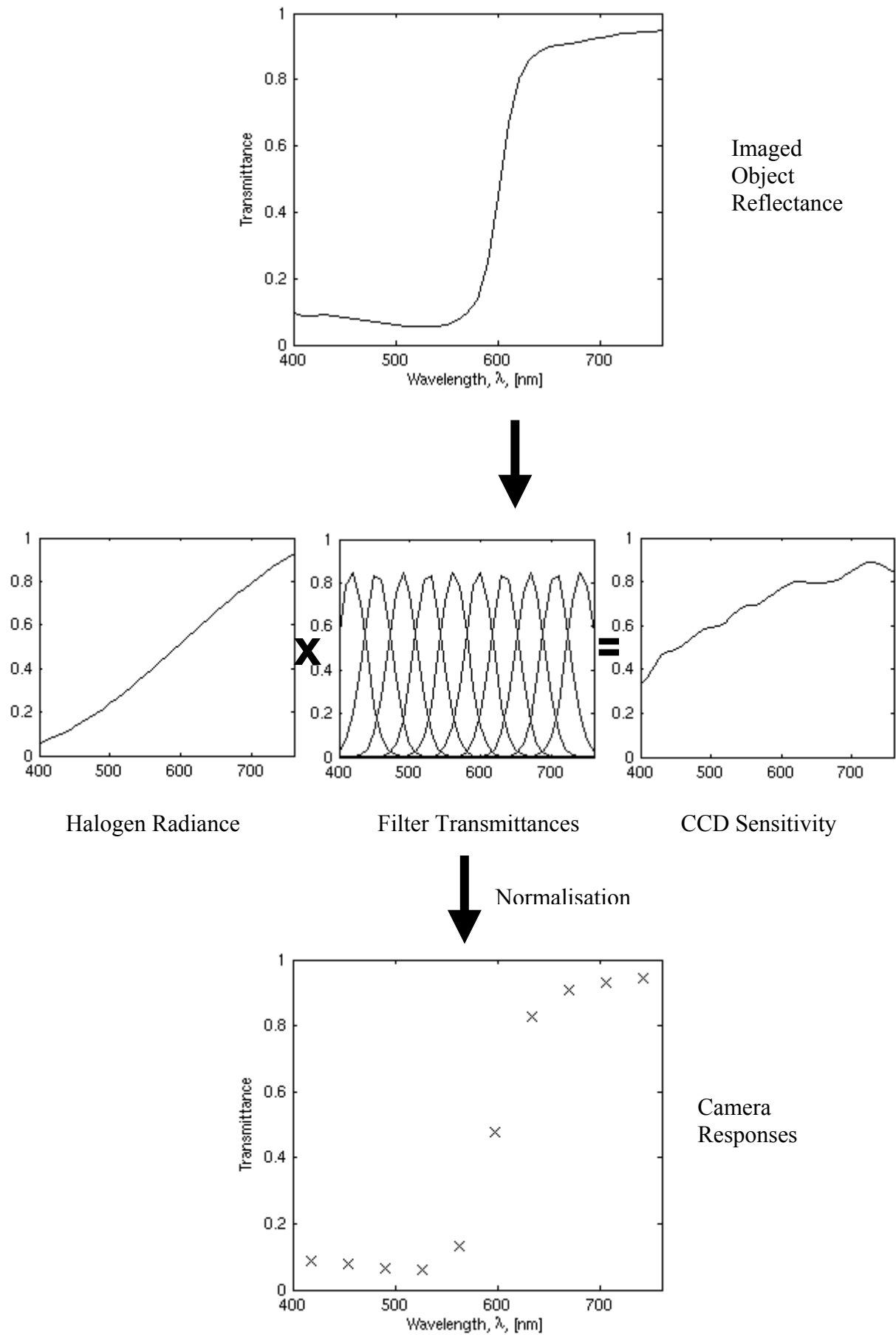


Figure 3-3 Diagram of the virtual multispectral system used in our simulations.

3.3 Least squares and pseudo-inverse

This section aims to describe the pseudo-inverse applied to spectral reconstruction along with its close relation to the solution of the least square problem. We dedicate a section on this subject because the concepts introduced here are used in most existing spectral reconstruction techniques. An exception is given by those based on interpolation (described in section 3.6.7).

3.3.1 Pseudo inverse

We represent a general linear system of equations by

$$\mathbf{b} = \mathbf{A} \mathbf{x} \quad (2.31)$$

where \mathbf{x} and \mathbf{b} are vectors and \mathbf{A} is a matrix not necessarily square. We want to estimate the unknown vector \mathbf{x} knowing \mathbf{b} and \mathbf{A} . This means that we are seeking for an inverse operator \mathbf{A}^- . In this framework we can have three different situations:

- Matrix \mathbf{A} is square and has full rank. \mathbf{A}^{-1} exists and can be calculated and applied to obtain a unique solution. Unfortunately, this situation does not happen very often. In the case of spectral reconstruction it means that the number of filters must be the same as the number of wavelength samples of the spectral curves. Moreover, even in that case \mathbf{A} must be full rank.
- Matrix \mathbf{A} is rectangular, dimension of \mathbf{x} is smaller than \mathbf{b} . There are more observations \mathbf{b} than points \mathbf{x} , the system is called overdetermined. In this case the inversion operator is defined as

$$\mathbf{A}^{-over} = (\mathbf{A}^t \mathbf{A})^{-1} \mathbf{A}^t. \quad (2.32)$$

This operator can be obtained by multiplying on the left by \mathbf{A}^t both sides of equation (2.31), this leads to:

$$\mathbf{A}^t \mathbf{b} = \mathbf{A}^t \mathbf{A} \mathbf{x}. \quad (2.33)$$

If the rank of \mathbf{A} is equal to the dimension of \mathbf{x} , $\mathbf{A}^t \mathbf{A}$ is a square positive defined matrix and it is invertible. We then obtain an estimate of \mathbf{x} as follows:

$$\hat{\mathbf{x}} = (\mathbf{A}^t \mathbf{A})^{-1} \mathbf{A}^t \mathbf{b}. \quad (2.34)$$

- Matrix \mathbf{A} is rectangular, dimension of \mathbf{x} is bigger than \mathbf{b} . There are less observations \mathbf{b} than points \mathbf{x} , the system is called underdetermined. The inversion operator is defined as

$$\mathbf{A}^{-under} = \mathbf{A}^t (\mathbf{A} \mathbf{A}^t)^{-1}. \quad (2.35)$$

Both operators \mathbf{A}^{-over} and \mathbf{A}^{-under} satisfied the so called Moore-Penrose conditions:

$$\begin{aligned} \mathbf{A} \mathbf{A}^- &= (\mathbf{A} \mathbf{A}^-)^t \\ \mathbf{A}^- \mathbf{A} &= (\mathbf{A}^- \mathbf{A})^t \end{aligned}$$

$$\begin{aligned}\mathbf{A} \mathbf{A}^- \mathbf{A} &= \mathbf{A} \\ \mathbf{A}^- \mathbf{A} \mathbf{A}^- &= \mathbf{A}^-\end{aligned}$$

Then, both operators are *generalized inverses* or *pseudo-inverses*. For more details on this subject please refer to *chapter 8* of [Pratt, 1978] or the book of [Albert, 1972].

Consider now the following change of notation where we define the matrix \mathbf{A}_2 such that $\mathbf{A}_2 = \mathbf{A}^t$. Then equation (2.31) is rewritten as:

$$\mathbf{b} = \mathbf{A}_2^t \mathbf{x}. \quad (2.36)$$

In the case of an overdetermined system the inverse operator is rewritten as follows:

$$(\mathbf{A}_2^t)^{-over} = (\mathbf{A}_2 \mathbf{A}_2^t)^{-1} \mathbf{A}_2, \quad (2.37)$$

and in the case of an underdetermined system it is rewritten as:

$$(\mathbf{A}_2^t)^{-under} = \mathbf{A}_2 (\mathbf{A}_2^t \mathbf{A}_2)^{-1}. \quad (2.38)$$

By just changing notation and choosing \mathbf{A}_2 instead of \mathbf{A} ($\mathbf{A}_2 = \mathbf{A}^t$) the literal expressions of the two inversion operators take a different form, when compared to equations (2.32) and (2.35). This is important to keep in mind, as already said, because different authors define the operator Θ differently, but related by a transposition. This fact can sometimes lead to confusion.

In Table 3-1 we present all the forms that the pseudo-inverse can take, according to the two types of equations to be solved, $\mathbf{b} = \mathbf{A} \mathbf{x}$ or $\mathbf{b} = \mathbf{A}_2^t \mathbf{x}$:

Table 3-1 Different forms of the pseudo-inverse.

	$\mathbf{b} = \mathbf{A} \mathbf{x}$	$\mathbf{b} = \mathbf{A}_2^t \mathbf{x}$
Overdetermined	$\mathbf{A}^{-over} = (\mathbf{A}^t \mathbf{A})^{-1} \mathbf{A}^t$	$(\mathbf{A}_2^t)^{-over} = (\mathbf{A}_2 \mathbf{A}_2^t)^{-1} \mathbf{A}_2$
Underdetermined	$\mathbf{A}^{-under} = \mathbf{A}^t (\mathbf{A} \mathbf{A}^t)^{-1}$	$(\mathbf{A}_2^t)^{-under} = \mathbf{A}_2 (\mathbf{A}_2^t \mathbf{A}_2)^{-1}$

3.3.2 Least square solutions

It is important to explain the close relation between the pseudo-inverse and the solution of a least square problem when working linearly. If we take any linear algebra introductory textbook, see for instance *chapter 6* of [Golub and Loan, 1983], we find that the least squares method aims to solve a linear system of the form $\mathbf{A} \mathbf{x} = \mathbf{b}$ where, as in the previous section, \mathbf{A} is a matrix, \mathbf{x} is an unknown vector and \mathbf{b} is the observations vector. The objective of this method is to find an estimation of \mathbf{x} , named $\hat{\mathbf{x}}$, which minimises the square of the Euclidean norm of vector $\mathbf{b} - \mathbf{A} \mathbf{x}$, or equivalently the square of the Euclidean distance $d_E(\mathbf{A} \mathbf{x}, \mathbf{b})$ between vectors $\mathbf{A} \mathbf{x}$ and \mathbf{b} :

$$\hat{\mathbf{x}} = \min_{\mathbf{x}} (\mathbf{A} \mathbf{x} - \mathbf{b})^t (\mathbf{A} \mathbf{x} - \mathbf{b}) \quad (2.39)$$

3.3.2.1 Overdetermined case

This case is very popular in linear algebra as it corresponds physically to having more measures than variables. There is no exact solution, some information being in general not coherent. In this case we seek for a minimal norm solution which can be deduced by calculating the derivatives of $\|\mathbf{Ax} - \mathbf{b}\|^2$ with respect to \mathbf{x} . Writing the derivatives equal to zero we find the expression of the minimum, the so called *normal equations*:

$$\mathbf{A}^t(\mathbf{b} - \mathbf{A}\hat{\mathbf{x}}) = 0 \quad (2.40)$$

which implies: $(\mathbf{b} - \mathbf{A}\hat{\mathbf{x}}) \in \text{nullspace}(\mathbf{A}^t)$. We then directly deduce the following equations:

$$\begin{aligned} \mathbf{A}^t\mathbf{b} &= \mathbf{A}^t\mathbf{A}\hat{\mathbf{x}}, \\ \hat{\mathbf{x}} &= (\mathbf{A}^t\mathbf{A})^{-1}\mathbf{A}^t\mathbf{b}. \end{aligned}$$

That is exactly the definition of the pseudo-inverse. Let's recall that the relationship $\mathbf{Ax} = \mathbf{b}$ does not necessary hold, in this fact resides the interest of the least square techniques. If an exact solution does not exist an approximate one is found. In this sense, we can already see the utility of this kind of methods in the solution of ill-posed problems where the existence of a solution or its uniqueness is not guaranteed.

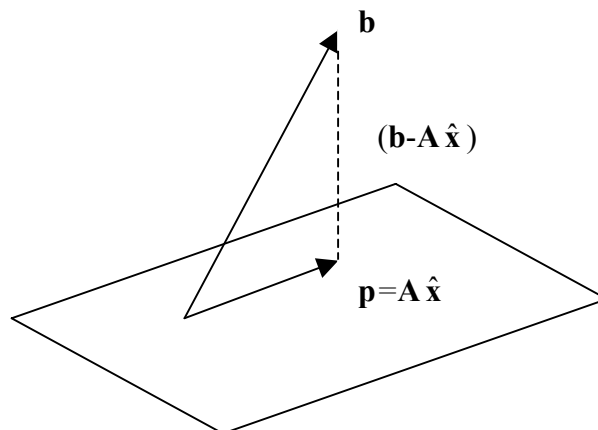


Figure 3-4 Solution of the least squares problem.

In Figure 3-4 we show a graphical interpretation of the linear least square problem. The vector \mathbf{b} is outside the plane representing the acceptable set of solutions and the vector $\mathbf{b} - \mathbf{A}\hat{\mathbf{x}}$ represents the orthogonal difference between \mathbf{b} and the space of solutions. Its projection is

$$\mathbf{p} = \mathbf{A}(\mathbf{A}^t\mathbf{A})^{-1}\mathbf{A}^t\mathbf{b}, \quad (2.41)$$

that gives us an acceptable solution that is considered to be the best in the sense of the least squares.

As a summary we can say that the overdetermined pseudo-inverse is the operator that minimizes the Euclidian distance $d_E(\mathbf{b}, \mathbf{A}\hat{\mathbf{x}})$ between the measures \mathbf{b} and their linear estimate $\mathbf{A}\hat{\mathbf{x}}$. It is then optimal in that sense.

3.3.2.2 Non Euclidian distances

We have just seen that the pseudo-inverse is a solution minimizing the Euclidian norm of the residual vector $\mathbf{b} - \mathbf{A} \mathbf{x}$. This corresponds to the minimization of:

$$(\mathbf{b} - \mathbf{A} \mathbf{x})^t (\mathbf{b} - \mathbf{A} \mathbf{x}). \quad (2.42)$$

But we are also interested in the minimization of other non Euclidean distances. We introduce:

$$(\mathbf{b} - \mathbf{A} \mathbf{x})^t \mathbf{N} (\mathbf{b} - \mathbf{A} \mathbf{x}), \quad (2.43)$$

where \mathbf{N} is a matrix. This family of distances is a generalization of the classical distance where the matrix \mathbf{N} takes a central role while different matrices define different distances. When $\mathbf{N} = \mathbf{I}$ this distance becomes Euclidian.

The optimal least squares operator in the underdetermined case is given by:

$$\mathbf{N}^{-1} \mathbf{A}^t (\mathbf{A} \mathbf{N}^{-1} \mathbf{A}^t)^{-1}. \quad (2.44)$$

Let's note that this operator is a generalization of the pseudo-inverse. For further reference consult *chapter 25* of [Lawson and Hanson, 1974].

3.3.3 Simulating the ideal spectral reconstruction problem

We already explained the different nature of the two spectral reconstruction methods based on equation (2.23). In this section we compare simulated results of two basic methods of spectral reconstruction each one belonging to each paradigm. We suppose that noise is not present and the forward system is perfectly linear. This assumption is not realistic at all but we find interesting to discuss these results here for two reasons: 1) they give insight in the basic behaviour of each method and 2) the comparison itself helps to understand the appropriateness of the methods to a specific engineering problem.

3.3.3.1 Direct method

For the direct reconstruction method we want to determine the unknown \mathbf{r} in equation (2.23), $\mathbf{c} = \mathbf{\Theta} \mathbf{r}$, where $\mathbf{\Theta}$ is a known $K \times N$ matrix the k -row of which represents the sensitivity of the k -th camera channel. Note that $K < N$. An immediate solution for estimating the spectral reflectance consists in applying the underdetermined pseudo-inverse to the matrix $\mathbf{\Theta}$, which provides us with the following minimum norm solution:

$$\hat{\mathbf{r}} = \mathbf{\Theta}^{-under} \mathbf{c} = \mathbf{\Theta}^t (\mathbf{\Theta} \mathbf{\Theta}^t)^{-1} \mathbf{c}. \quad (2.45)$$

This method forms the basis of other more sophisticated methods for spectral reflectance reconstruction. However it is not very well adapted in practical situations. In practice, this solution is very sensitive to noise. In fact, note that we minimise the Euclidian distance $d_E(\mathbf{\Theta} \mathbf{r}, \mathbf{c}_K)$ in the camera response domain. A small distance does not guarantee the spectra \mathbf{r} and $\hat{\mathbf{r}}$ to be close, only that their projections into the camera response space are close. Nevertheless, this approach is used by [Tominaga, 1996] to recover the spectral distribution of an illuminant from a six-channel acquisition. However, he applies a nested regression analysis to choose the

proper number of components in order to better describe the spectrum and to increase the spectral-fit quality.

The pseudo-inverse method provides a unique solution, consequently Hadamard's first and second conditions are respected. Unfortunately, in the presence of noise the constructed operator is not stable. This is the source of its inaccuracy, strongly related with Hadamard's third condition.

3.3.3.2 Indirect method

The indirect method used is based on equation (2.28), $\mathbf{R} = \mathbf{QC}$. This method corresponds to the practical situation where a chart containing colour patches is imaged by a multispectral camera. The colour chart is calibrated, this means the spectral reflectance curves of its colour patches are known. Matrix \mathbf{R} contains these N -sampled spectral reflectances in its columns, and matrix \mathbf{C} contains in its P columns the corresponding K -channel camera responses.

Let now consider the equation to be solved:

$$\mathbf{R} = \mathbf{QC} , \quad (2.46)$$

where \mathbf{Q} is the $N \times K$ unknown matrix, \mathbf{R} and \mathbf{C} are $N \times P$ and $K \times P$ matrices respectively. We see that the unknown is on the left of the right side of the equation. By transposing this equation we obtain:

$$\mathbf{R}^t = \mathbf{C}^t \mathbf{Q}^t , \quad (2.47)$$

Then, for the i -th row of \mathbf{R} , \mathbf{r}_i , and for the i -th row of \mathbf{C} , \mathbf{c}_i , the following equation holds:

$$\mathbf{r}_i^t = \mathbf{C}^t \mathbf{q}_i^t \quad (2.48)$$

This is equivalent to the solution of the following least square problem

$$\min_{\mathbf{q}_i^t} \left\| \mathbf{C}^t \mathbf{q}_i^t - \mathbf{r}_i^t \right\|^2 . \quad (2.49)$$

This corresponds to a conceptually different way of seeing the problem but mathematically equivalent: a least square overdetermined problem. We can then estimate the lines \mathbf{q}_i of the operator \mathbf{Q} using the pseudo-inverse:

$$\mathbf{q}_i^t = (\mathbf{C}^t)^{-over} \mathbf{r}_i^t = (\mathbf{C}^t \mathbf{C})^t \mathbf{C} \mathbf{r}_i^t . \quad (2.50)$$

Applying equation (2.50) to rows of \mathbf{Q} and rows of \mathbf{R} for any index i , $i=1, \dots, N$, we can express the estimation of the whole operator \mathbf{Q} in the following way:

$$\mathbf{Q}^t = (\mathbf{C} \mathbf{C}^t)^{-1} \mathbf{C} \mathbf{R}^t . \quad (2.51)$$

Transposing (2.51) leads to:

$$\mathbf{Q} = \mathbf{R} \mathbf{C}^t (\mathbf{C} \mathbf{C}^t)^{-1}. \quad (2.52)$$

That can be easily computed to solve the problem.

3.3.3.3 Direct and indirect method: a comparison

We start our comparison by a remark on equations (2.45) and (2.52). If we look carefully both equations we see that the pseudo-inverse expression used on both cases is exactly the same. This is a coincidence in this case as equation (2.45) comes from a least square underdetermined problem but (2.52) is the solution of an equation involving matrices that conceptually matches an overdetermined problem. For this reason we choose to modify our notation and to use the term pseudo-inverse, or pinv, in the rest of this thesis for the following expression:

$$\text{pinv}(\mathbf{A}) = \mathbf{A}^t (\mathbf{A} \mathbf{A}^t)^{-1}. \quad (2.53)$$

Now, the direct and indirect problems can be simply solved as follows:

- Direct method:

For the direct inversion we apply the pseudo-inverse to the known operator Θ having

$$\mathbf{Q}_{\text{pinv}\Theta} = \text{pinv}(\Theta). \quad (2.54)$$

This is probably the most evident method of the indirect paradigm we can find. This formula implies that a characterization of the multispectral acquisition system is already performed. We note that the constructed operator can be very sensitive to noise and then ill-posed. As we already said, we use it here just in simulation to give insight in the basics of this and others more complex methods.

- Indirect method:

$$\mathbf{Q}_{\text{pinvRC}} = \mathbf{R} \text{pinv}(\mathbf{C}) \quad (2.55)$$

This method corresponds to the practical situation where a chart containing colour patches is imaged by a multispectral camera. We decide to use this equation (2.55) as a prototype of all indirect methods.

Table 3-2. Mean Squared Spectral Error over different databases.

	$\mathbf{R} \text{pinv}(\mathbf{C})$	$\text{pinv}(\Theta)$
Kremer	0.00029467	0.0024152
Macbeth DC (training)	0.00006719	0.0023151
Selected Artists	0.00023387	0.0024289
Restoration	0.00018397	0.0019890
Munsell	0.00007019	0.0015919

In Table 3-2 we can see the mean errors of these two operators when applied to the reconstruction of pigments of our databases. The matrix \mathbf{R} used in the indirect method contains the spectral curves of the Macbeth DC chart in its columns. We clearly see the superiority of the indirect method using *a priori knowledge* (a colour chart and its multispectral image) over the direct inversion. In order to understand why we obtain such

large differences between both methods we first calculate the condition number (using the Euclidian norm) of the two constructed operators. Being \mathbf{A} a matrix and a_{max} and a_{min} the maximum and minimum of its singular values obtained by a SVD, we remind that the 2-norm condition number of \mathbf{A} can be estimated as the ratio between a_{max} and a_{min} . This number is directly connected to the numerical stability of the solutions. The condition numbers of the operators built from (2.55) and (2.54) are shown in Table 3-3. The condition numbers are similar. The condition number of the indirect method being only a little bigger than for the direct method, then the conditioning of the matrices seems not to be the source of disparity on the results.

Table 3-3. Condition numbers for both linear operators.

	$\mathbf{R} \text{ pinv}(\mathbf{C})$	$\text{pinv}(\Theta)$
Condition Number	3.6312	3.1244

We keep analysing the built operators in order to understand their behaviour. Next step is the graphical representation of the operators themselves. In the case of our simulations the operators are $K \times N = 10 \times 37$ matrices that transform a vector of 10 elements containing the camera responses for each channel into a 37 elements vector containing the samples of a spectral curve. These matrices can be interpreted as a discretization of a three dimensional function and when plotted they provide an interesting representation. Let's see in Figure 3-5 the contour plot of the operators. On the horizontal axis the numbers correspond to the 10 input camera responses and on the vertical ones they represent the samples of the reflectance curves.

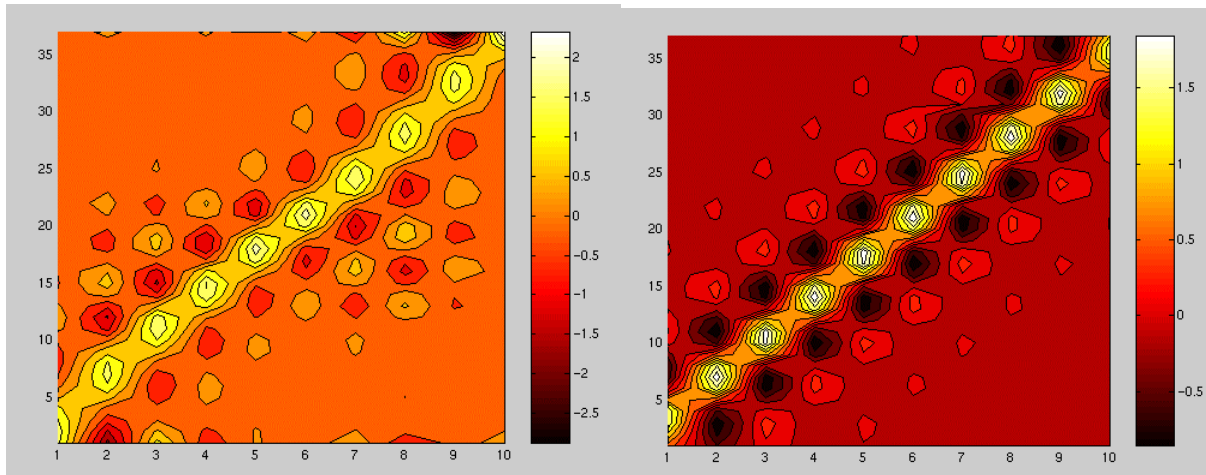


Figure 3-5 Contour plots of the operator $\mathbf{R} \text{ pinv}(\mathbf{C})$ (left panel) and $\text{pinv}(\Theta)$ (right panel)

In this figure we can observe that the operator $\text{pinv}(\Theta)$ has a more regular structure than the operator $\mathbf{R} \text{ pinv}(\mathbf{C})$. This fact is interesting because the symmetry of the operator can be interpreted intuitively as a lack of adaptation to some specific data. Reasoning that way we can say that the operator $\mathbf{R} \text{ pinv}(\mathbf{C})$ shown in the left panel of Figure 3-5 is more adapted to a specific set of data. In our simulation \mathbf{R} contains the Macbeth DC reflectances in its columns, this is the reason why the operator obtains the best results over the Macbeth DC datasets, see Table 3-2. We denote the Macbeth DC set as the *training* set used to build the operator. We should not forget that the other datasets presented in Table 3-3 are in fact coming from spectroradiometric measurements of oil pigments, whereas the painted Munsell patches are not made from oil pigments. As a consequence, it would be interesting to see the effect of both presented operators on a dataset not coming from the “oil pigments” or painting

environment. In Table 3-4 we present the results on the Pine Tree dataset already presented on Chapter 2 (*Nature of Data*).

Table 3-4. Mean Squared Spectral Error for Pine Tree Leaves database.

	$\mathbf{R} \text{pinv}(\mathbf{C})$	$\text{pinv}(\Theta)$.
Pine tree leaves	0.00034866	0.00027975

In this case we see that the direct inversion method is superior to the one using a training set. We note that this dataset is very different in nature to the Macbeth DC one. Clearly we see one general property of both kinds of methods. The direct inversion is general and works for all kind of data. Using a training set helps adapting the method to specific data but losses generality.

3.4 Taking noise into account

If we want to build a robust spectral reconstruction operator, its resistance to noise must be taken into account. In fact, when spectral reconstruction is performed over real data we always deal with noisy data. The noise level can vary for different applications but it always exists. Robust operators are then needed for real applications.

When taking noise into account the direct system model we want to invert is not anymore the one in equation (2.23), it becomes

$$\mathbf{c}_K = \mathbf{G} \mathbf{r} + \mathbf{n} \quad (2.56)$$

where we introduce \mathbf{n} , a vector of additive random noise. This model was justified on Chapter 2. We remind that \mathbf{n} can be decomposed into several components because this noise has not a unique source.

We will see on section 3.6 how some spectral reconstruction methods deal with this noise. For instance, Wiener filtering uses explicitly a model of \mathbf{n} . An a priori requirement for such approach is the characterization of the noise. This needs experimental data and is then attached to the actual acquisition system used. At the moment we do not consider any real acquisition system, then this kind of approach cannot be illustrated with results. By now, we just deal with quantization noise that is not dependent on a specific system.

We introduce several levels of quantization in the simulation. We are interested in quantization at 8, 10 and 12 bits. This is due to a practical reason, currently not cooled technology image systems use typically these range of quantization. In practice, the more bits we want to obtain the lower the CCD sources of noise must be. If we quantize a signal using a 16 bits analog/digital (A/D) converter, but CCD noise is very strong, last bits of the digital signal will be completely corrupted by the noise. For instance, we can imagine a particular case where the last 6 bits are corrupted in a 16 bits signal. In this case, we could use a less expensive 10 bits A/D converter and obtain the same result. Cooled systems exist in high end multispectral applications and in astronomy. These apparatus are very cumbersome but noise is considerably reduced and quantization can be augmented to more than 16 bits.

In a simulation system the quality of the signal is as good as desired, we can simulate any quantization rate. We can consequently study the effect of the quantization itself. Other sources of noise are not as easy to simulate. For instance, if we want to simulate dark current noise, read-out noise and shot noise, three probability distributions of the appropriate form should be used and their parameters must be known. As long as these noise sources depend on a particular CCD, choosing their parameters is somehow arbitrary or too related to a specific hardware. We then prefer not to simulate them and later when studying noise we will use real data.

3.5 Metrics for evaluating reconstruction performance

The choice of the metric used to evaluate the results of spectral reconstruction algorithms is not a trivial subject. In fact, much more attention is generally given to the reconstruction methods themselves than to the metrics involve in them. This is probably because there is no consensus on the metric to be used for spectral match in the multispectral scientific community.

Any reconstruction technique can be generally seen as a method that minimises a criteria. The criteria is either explicit and or inherent to the method. In both cases knowing what we minimise is of great importance and not knowing what we minimise can lead to big application errors. On the other hand there is another question that should be asked when performing spectral reconstruction: for what purpose is the reconstructed spectrum used for? Depending on the application the response of this question can give us a different metric. For instance, if our aim is to fit spectral curves of oil pigments in order to identify pigments a measure based in the space of spectral curves will be used. On the contrary, if the reconstructed reflectance curve will serve for colour reproduction, then it will be better to use a measure of the errors produced in the reproduction of colours.

Lots of metrics are commonly used but it is hard to give a general comparison. In this sense, an effort was made by [Imai et al., 2002, CGIV02] giving, in our knowledge, the only comparative study of metrics in spectral imaging. Their conclusion is that the appropriateness of a metric depends on its application. We consider this assessment to be right and a fundamental lesson can be extracted from it: when general spectral reconstruction is performed different metrics must be used to evaluate its results. In fact, in the same paper they classify the metrics for spectral match quality in four categories:

- Spectral Curves Difference Metrics.
- CIE Colour Difference Equations.
- Metamerism Indices.
- Weighted RMS Metrics.

In the following section we describe the metrics we use for quality evaluation. Even if not said or shown explicitly in the rest of this thesis, all the measures presented here are systematically used in all our experiments.

3.5.1 Spectral Curve Difference Metrics

We call $r_m(\lambda_i)$, $i=1,\dots,N$, a reference spectral reflectance curve where λ_i represents the wavelength, and N is the number of samples used to represent the curve. This curve is typically measured by a spectrophotometer. The function $r_e(\lambda_i)$ is an estimation of $r_m(\lambda_i)$. We use in practice three different metrics:

- The Root Mean Squared (RMS) error. This is the Euclidian or L_2 distance applied to spectral curves, its formal definition is

$$RMS = \frac{1}{N} \sum_{i=1}^N \|r_m(\lambda_i) - r_e(\lambda_i)\|^2. \quad (2.57)$$

- The Absolute Mean Error (ABE). This metric is the L_1 distance applied to spectral curves,

$$ABE = \frac{1}{N} \sum_{i=1}^N |r_m(\lambda_i) - r_e(\lambda_i)|. \quad (2.58)$$

- The Goodness-of-Fit Coefficient (GFC) is a Metric developed in [Hernandez-Andres and Romero, 2001] to test reconstructed daylight spectra. The GFC is based on the inequality of Schwartz and it is calculated by

$$GFC = \frac{\left| \sum_{i=1}^N r_m(\lambda_i) r_e(\lambda_i) \right|}{\sqrt{\left| \sum_{i=1}^N [r_m(\lambda_i)]^2 \right|} \sqrt{\left| \sum_{i=1}^N [r_e(\lambda_i)]^2 \right|}}. \quad (2.59)$$

We find interesting this metric because its value is bounded to the interval $[0,1]$ and it provides a easy interpretation. From [Hernandez-Andres and Romero, 2001], if $GFC \geq 0.999$ the spectral match is consider as good and if $GFC \geq 0.9999$ the match is consider as excellent.

3.5.2 CIE Colour Difference Equations

We will deal in this subsection with metrics based in the CIELAB colour space. Complete understanding of this and other colour spaces requires basic knowledge on colorimetry. Even if the subject of this thesis requires knowledge in this field a chapter in spectral reconstruction is not the place for a introduction to colorimetry. Here we just deal with metrics in the CIELAB space, if the reader is not familiar with basic concepts of colorimetry we have prepared a brief compendium of them in Appendix I. For further information lots of textbooks exists on the subject. For a classical encyclopaedic reference of Colour Science see [Wyszecki, 1982], for a modern and comprehensive introduction we suggest [Berns, 2000] and for introduction and reference in French see [Sève, 1996].

CIELAB space was proposed by the CIE (*Commission Internationale de l'Eclairage*) in 1976. Its origin is related to psychophysical experiments showing that the human eye's sensitivity to light is not linear. Colorimetric colour spaces as RGB or XYZ relate linearly to the spectrum of the coloured light. When changing the tristimulus values of XYZ (or RGB) for a colour stimulus, the observer will perceive a difference in colour for differences greater than the Just Noticeable Difference (JND). In both RGB and XYZ spaces the JND depends on the location in the colour space. The aim of CIELAB is to make JND constant, leading to a uniform colour space where the JND is not depending on the location. In practice, this condition is only fulfilled approximately, thus we normally use the term *pseudo-uniform* for CIELAB. Remark that the notion of JND is observer-dependent and resulting from psychophysical experiments, this makes CIELAB a *psychometric* colour space.

The CIELAB pseudo-uniform colour space is defined by the quantities L^* , a^* and b^* . L^* represents the *lightness* of a colour, known as the CIE 1976 psychometric lightness. The scale of L^* is 0 to 100, 0 being the ideal black, and 100 being the reference white. The chromacity

of a colour can be represented in a two-dimensional (a^* , b^*) diagram, a^* representing the degree of green versus red, and b^* the degree of blue versus yellow.

When comparing two colours, specified by $[L_1^*, a_1^*, b_1^*]$ and $[L_2^*, a_2^*, b_2^*]$, one widely used measure of the colour difference is the *CIE 1976 Lab colour-difference* which is simply calculated as the Euclidean distance in CIELAB space, as follows

$$\Delta E_{ab}^* = \sqrt{(L_1^* - L_2^*)^2 + (a_1^* - a_2^*)^2 + (b_1^* - b_2^*)^2} . \quad (2.60)$$

For more information about this measure see [CIE, 1986]. The interpretation of ΔE_{ab}^* colour differences is not straightforward. A rule for the practical interpretation of ΔE_{ab}^* when two colours are shown side by side is presented in Table 3-5. Another interpretation of ΔE_{ab}^* errors for the evaluation of scanners is proposed by [Abrardo et al., 1996]. They classify mean errors of 0-1 as *limit of perception*, 1-3 as *very good quality*, 3-6 as *good quality*, 6-10 as *sufficient*, and more than 10 as *insufficient*. We note the disagreement between these classifications, this underlining the fact that the evaluation of quality and acceptability is highly subjective, and dependent on the application.

Table 3-5. Rule for the practical interpretation of ΔE_{ab}^ measuring the colour difference between two colour patches viewed side by side*

ΔE_{ab}^*	Effect
<3	Hardly perceptible
[3 .. 6]	Perceptible, but acceptable
>6	Not acceptable

An alternative representation of colours in the CIELAB space appears when using cylindrical coordinates, defining the *CIE 1976 chroma*, as the distance of the colour point from the L^* -axis:

$$C_{ab}^* = \sqrt{a^{*2} + b^{*2}} , \quad (2.61)$$

and the *CIE 1976 hue-angle*, as:

$$h_{ab} = \arctan \left(\frac{b^*}{a^*} \right) . \quad (2.62)$$

The use of these quantities, lightness L^* , chroma C_{ab}^* , and hue angle h_{ab} may facilitate the intuitive comprehension of the CIELAB colour space, by relating them to perceptual attributes of colours. It may also be interesting to evaluate the differences of each of the components of the CIELAB space separately. This is straightforward for L^* , a^* , b^* , and C_{ab}^* , however, for the hue angle h_{ab} this merits some special consideration. Of course, the direct angle difference in degrees may be instructive. However, to achieve that colour differences can be broken up into components of lightness, chroma and hue, whose squares sum to the square of ΔE_{ab}^* , a quantity ΔH^* called the *CIE 1976 hue-difference*, is defined as

$$\Delta H^* = \sqrt{(\Delta E_{ab}^*)^2 - (\Delta L^*)^2 - (\Delta C_{ab}^*)^2} . \quad (2.63)$$

The colour-difference formula of equation (2.60) is supposed to give a measure of colour differences that is perceptually consistent. However, since it has been found that the CIELAB space is not completely uniform, the colour difference ΔE_{ab}^* is not perfect. Several attempts have been conducted to define better colour-difference formulae, e.g. the CMC formula [Clarke et al., 1984], [McLaren, 1986] and the BFD formula [Luo and Rigg, 1987, BFD1], [Luo and Rigg, 1987, BFD2]. A comparison of these and other uniform colour spaces using perceptibility and acceptability criteria is done by [Mahy et al., 1994].

In 1994, the CIE defined the *CIE 1994 colour-difference model* [McDonald and Morovic, 1995], abbreviated CIE94, denoted ΔE_{94}^* , based on the CIELAB space and the previously cited works on colour difference evaluation. They defined reference conditions under which the new metric with default parameters is expected to perform well:

- The specimens are homogeneous in colour.
- The colour difference ΔE_{ab}^* is less than 5 units.
- They are placed in direct edge contact.
- Each specimen subtends an angle of more than 4 degrees to the assessor, whose colour vision is normal.
- They are illuminated at 1000 lux, and viewed against a background of uniform grey, with $L^*=50$, under illumination simulating D65.

The colour difference is calculated as a weighted mean-square sum of the differences in lightness (ΔL^*), chroma (ΔC^*) and hue (ΔH^*):

$$\Delta E_{94}^* = \sqrt{\left(\frac{\Delta L^*}{k_L S_L}\right)^2 + \left(\frac{\Delta C^*}{k_C S_C}\right)^2 + \left(\frac{\Delta H^*}{k_H S_H}\right)^2}. \quad (2.64)$$

For a complete reference about this measure see [CIE, 1995]. The *weighting functions* S_L , S_C , and S_H vary with the chroma of the reference specimen C^* as follows,

$$S_L = 1, S_C = 1 + 0.045 C^* \text{ and } S_H = 1 + 0.015 C^*.$$

The variables k_L , k_C and k_H are called *parametric factors* and are included in the formula to allow for adjustments to be made independently to each colour-difference term to account for any deviations from the reference viewing conditions that cause component specific variations in the visual tolerances. Under the reference conditions explained above, they are set to

$$k_L = k_C = k_H = 1.$$

We note that under reference conditions, ΔE_{94}^* equals ΔE_{ab}^* for neutral colours, while for more saturated colours, ΔE_{94}^* becomes smaller than ΔE_{ab}^* .

As a conclusion the two metrics, ΔE_{ab}^* and ΔE_{94}^* , based on the CIELAB colour space will be used systematically in the rest of this thesis. The reference illuminant for this measure is D⁵⁰.

3.6 Existing Reconstruction Techniques

The aim of this section is to describe and analyse the existing reconstruction techniques. A survey is indeed needed before any new investigations are made.

We start by presenting three direct reconstruction techniques where the spectral characteristics of the imaging system, the matrix Θ , is supposed known. First the smoothing inverse is introduced, this method inverts Θ and reinforces smoothness by the use of a regularizing matrix. Then, we present Wiener's filter, this technique introduce knowledge about the noise on the inversion process to obtain better results. Finally, Hardeberg's method is described which uses a priori information on the imaged objects to regularise the solutions.

After direct methods three indirect or learning-based techniques are presented. The pseudo-inverse and SVD method is a stabilised version of the paradigm presented on equation (2.55). The non-averaged pseudo-inverse is a recent and very promising method naturally introducing noise information in the constructed operator. The Non Negative Least Squares (NNLS) method deals with the problem of not obtaining negative values for the estimated reflectance curves.

Finally, we present the methods based on interpolation, as an example we describe the Modified Discrete Sine Transform (MDST) method. This technique is based on Fourier interpolation and we compare it with a cubic spline interpolation.

3.6.1 Smoothing inverse

Smoothing is a well known way of linear regularization. Its sense is very general as we can see for instance in [Neumaier, 1999]. In fact, smoothing means that the solution we want to find (the vector \mathbf{r} representing the reflectance in our case) can be express as

$$\mathbf{r} = \mathbf{S} \mathbf{w}, \quad (2.65)$$

where \mathbf{w} represents a vector with a reasonable norm and \mathbf{S} is the smoothing matrix. This matrix \mathbf{S} introduces qualitative knowledge on the smoothness to be modelled. Clearly, we can see that this definition is very wide and includes a family of methods.

In the spectral reconstruction literature smoothing inverse is a more restricted term that defines a specific technique used to inverse the known direct system. From our knowledge, this technique was introduced by Mancill and Pratt, for reference see [Pratt and Mancill, 1976] or *chapter 16 section 3* of [Pratt, 1978] where the technique is applied to the similar problem of Spectral Radiance Estimation. Taking the definition given in [König, 1999], directly inspired from both the above cited references, the technique is basically the application of the generalisation of the pseudo-inverse to the non Euclidian distance as seen in (2.43),

$$\text{smoothing_inv}(\mathbf{N}, \Theta) = \mathbf{N}^{-1} \Theta^t (\Theta \mathbf{N}^{-1} \Theta^t)^{-1}, \quad (2.66)$$

where matrix Θ characterizes the direct problem and \mathbf{N} is the following $N \times N$ matrix:

$$\mathbf{N} = \mathbf{N}_\Delta = \begin{bmatrix} 1 & -2 & 1 & 0 & 0 & \dots & 0 & 0 \\ -2 & 5 & -4 & 1 & 0 & \dots & \dots & 0 \\ 1 & -4 & 6 & -4 & 1 & \dots & \dots & \dots \\ 0 & 1 & -4 & 6 & \dots & \dots & 0 & 0 \\ 0 & 0 & 1 & \dots & \dots & -4 & 1 & 0 \\ \dots & \dots & \dots & \dots & -4 & 6 & -4 & 1 \\ 0 & \dots & \dots & 0 & 1 & -4 & 5 & -2 \\ 0 & 0 & \dots & 0 & 0 & 1 & -2 & 1 \end{bmatrix}. \quad (2.67)$$

This makes the built operator to minimize the average squared second differences Δ , where

$$\Delta = [(r(\lambda_{i+1}) - r(\lambda_i)) - (r(\lambda_i) - r(\lambda_{i-1}))]^2. \quad (2.68)$$

We note that Δ is a measure of the curvature of the reflectance functions. Unfortunately, \mathbf{N}_Δ is a singular matrix and consequently it cannot be inverted. The method uses a modification of this matrix that is non singular. This is achieved by using

$$\mathbf{N}'_\Delta = \mathbf{N}_\Delta + \varepsilon \mathbf{I}, \quad (2.69)$$

where \mathbf{I} is the identity matrix and ε is a small positive constant ($\varepsilon \ll 1$). The way of founding this parameter is normally not specified. It is in general fixed a priori or optimised manually. Automatic optimisation is in general not needed.

In the following Table 3-6 we present a comparison between the raw pseudo-inverse method and the smoothing inverse. We recall that this simulation results does not use any kind of noise.

Table 3-6. Mean Squared Spectral Error over different databases.

	smoothing inv(\mathbf{N}, Θ)	pinv(Θ)
Kremer	0.00012944	0.0024152
Macbeth DC (training)	0.00025263	0.0023151
Selected Artists	0.00012348	0.0024289
Restoration	0.00007110	0.0019890
Munsell	0.00010418	0.0015919

In the preceding table we see that the smoothing inverse obtains much better results. This is already a very practical reason to prefer this method but we want to give some insight on why the concept of smoothing is natural when speaking about linear spectral reconstruction. In Figure 3-6 we show two measured spectral curves (on red) along with their reconstructed counterparts using a simple pseudo-inverse (green) and a smoothing inverse (blue), the smoothing matrix being \mathbf{N}'_Δ , where ε is 0.01. Both curves are coming from the Macbeth DC set. We clearly see that the pseudo inverse reconstructed curves oscillate around its target. The idea of smoothing appears then adapted as a priori information to be included in the reconstruction technique.

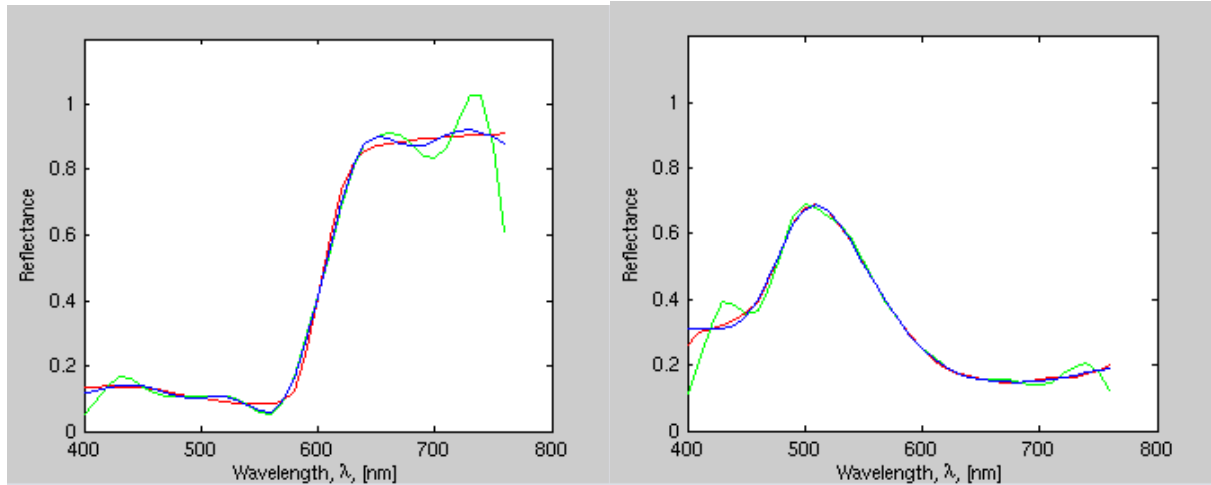


Figure 3-6 Spectral curves from the Macbeth DC set, red, along with their reconstruction using the pseudo-inverse, green, and the smoothing inverse, blue. (left panel) sample number 4 of the Macbeth DC set (right panel) sample number 164.

3.6.2 Wiener's filter

Wiener's filter is probably the oldest technique using regularization. This technique has been applied extensively in signal and image analysis. We found its first application to multispectral image in [Pratt and Mancill, 1976]. Spectral reconstruction not being an exception we can see some simulations in [Konig, 1998] and a good example of application to a real camera in [Haneishi et al., 1997]. Wiener filtering builds a linear operator that is regularized by knowledge about the noise distribution affecting the system. The image formation model we want to invert is the one in equation (2.56),

$$\mathbf{c}_K = \Theta \mathbf{r} + \mathbf{n} \quad (2.70)$$

where \mathbf{n} is a vector of random noise. Wiener filtering is another technique that minimizes the mean average of the square error between the channel responses corresponding to the original and estimated spectral reflectances, respectively. Its main advantage is that it takes noise into account. The resulting operator is then a modification of the pseudo-inverse,

$$\mathbf{Q}_{\text{Wiener}} = \mathbf{R}_{\mathbf{r}\mathbf{r}} \Theta^t (\Theta \mathbf{R}_{\mathbf{r}\mathbf{r}} \Theta^t + \mathbf{R}_{\mathbf{n}\mathbf{n}})^{-1}, \quad (2.71)$$

where $\mathbf{R}_{\mathbf{r}\mathbf{r}}$ is the correlation matrix of the spectral reflectances and $\mathbf{R}_{\mathbf{n}\mathbf{n}}$ is the correlation matrix of the noise. They are given by

$$\mathbf{R}_{\mathbf{r}\mathbf{r}} = \langle \mathbf{r}\mathbf{r}^t \rangle \quad \text{and} \quad \mathbf{R}_{\mathbf{n}\mathbf{n}} = \langle \mathbf{n}\mathbf{n}^t \rangle .$$

As we see the Wiener estimation requires the second-order statistics with respect to the original spectral reflectance and noise, in addition to the system matrix Θ . It belongs to the inversion paradigm. It is important to say that the accuracy of estimation of the spectral reflectance depends on the system matrix Θ , and the correlation matrices $\mathbf{R}_{\mathbf{r}\mathbf{r}}$ and $\mathbf{R}_{\mathbf{n}\mathbf{n}}$. We must estimate the correlation matrices accurately and that implies some experimental work. The correlation matrix of object reflectance, $\mathbf{R}_{\mathbf{r}\mathbf{r}}$, is normally estimated from a patch set. On the other hand, the correlation matrix of noise, $\mathbf{R}_{\mathbf{n}\mathbf{n}}$, is estimated by measuring the noise properties of the CCD camera actually used.

In the early work of [Pratt and Mancill, 1976] they propose some approximations of the covariance matrices. In fact, they model \mathbf{R}_{rr} as a first-order Markov process covariance matrix of the form

$$\mathbf{R}_{rr} = \frac{\sigma_v^2}{Q} \begin{bmatrix} 1 & \rho & \rho^2 & \dots & \dots & \rho^{Q-1} \\ \rho & 1 & \rho & \dots & \dots & \rho^{Q-2} \\ \cdot & \cdot & \cdot & \cdot & \cdot & \cdot \\ \cdot & \cdot & \cdot & \cdot & \cdot & \cdot \\ \cdot & \cdot & \cdot & \cdot & \cdot & \cdot \\ \rho^{Q-1} & \cdot & \cdot & \cdot & \cdot & 1 \end{bmatrix}, \quad (2.72)$$

where $0 \leq \rho \leq 1$ is the adjacent element correlation factor and σ_v^2 represents the variance of vector \mathbf{v} . Pratt and Mancill chose to model observation noise as white noise process with covariance matrix

$$\mathbf{R}_{nn} = \frac{\sigma_n^2}{Q} \mathbf{I}, \quad (2.73)$$

where σ_n^2 is the noise variance and \mathbf{I} is the identity matrix. This choice for the noise model is not justified in their paper and it becomes arbitrary when applied to spectral reconstruction. As we saw in the previous section about noise sources in multispectral images, this noise model can be much more complex in practice. See for instance [Haneishi et al., 1997] that use a more complete approach for modelling \mathbf{R}_{nn} .

3.6.3 Hardeberg's modified Pseudo-inverse

Jon Hardeberg developed a linear reconstruction technique exploiting a priori knowledge of the imaged objects. This technique is based on a pseudo-inverse. Information about the spectral reflectances of the objects that are to be imaged is introduced in the reconstruction operator. Good descriptions of the technique can be founded in [Hardeberg et al., 1999] or [Hardeberg, 1999, Thesis]. The technique belongs to the inversion paradigm, then the characterization of the direct system is necessary.

Hardeberg's operator \mathbf{Q}_{hard} minimises the Euclidian distance $d_E(\mathbf{r}, \hat{\mathbf{r}})$ between the original spectrum \mathbf{r} and the reconstructed spectrum $\hat{\mathbf{r}} = \mathbf{Q}_{\text{hard}} \mathbf{c}$. To achieve this minimisation it takes advantage of a priori knowledge on the spectral reflectances that are to be imaged. Spectral reflectances of typical objects are smooth. This fact is used by assuming that the reflectance in each pixel is a linear combination of a set of smooth basis functions. Typically Hardeberg uses a set of measured spectral reflectances as basis functions, but other sets of functions could be used, e.g. a Fourier basis. Denoting the basis function "reflectances" as the usual matrix \mathbf{R} the assumption implies that, for any observed reflectance \mathbf{r} , a vector of coefficients \mathbf{a} exists such that any reflectance \mathbf{r} may be expressed as:

$$\mathbf{r} = \mathbf{R}\mathbf{a}. \quad (2.74)$$

Hence, we obtain $\hat{\mathbf{r}}$:

$$\hat{\mathbf{r}} = \mathbf{Q}_{\text{hard}} \mathbf{c} = \mathbf{Q}_{\text{hard}} \ominus \mathbf{r} = \mathbf{Q}_{\text{hard}} \ominus \mathbf{R}\mathbf{a}. \quad (2.75)$$

And the ideal expression $\hat{\mathbf{r}} = \mathbf{r}$ becomes:

$$\mathbf{Q}_{\text{hard}} \Theta \mathbf{R} \mathbf{a} = \mathbf{R} \mathbf{a}. \quad (2.76)$$

Assuming that \mathbf{R} is a statistically significant representation of the reflectances that will be encountered for a given application, the above equation should be true for any \mathbf{a} , and hence:

$$\mathbf{Q}_{\text{hard}} \Theta \mathbf{R} = \mathbf{R}. \quad (2.77)$$

This gives then the reconstruction operator minimising the RMS spectral error by an underdetermined pseudo-inverse approach as:

$$\mathbf{Q}_{\text{hard}} = \mathbf{R} \text{pinv}(\Theta \mathbf{R}) = \mathbf{R} \mathbf{R}^t \Theta^t (\Theta \mathbf{R} \mathbf{R}^t \Theta^t)^{-1}. \quad (2.78)$$

The choice of the spectral reflectances in \mathbf{R} should be well representative of the spectral reflectances encountered in the applications. In his experiments on paintings Hardeberg used a set of 64 spectral reflectances of pure pigments utilized in oil painting and provided to him by the National Gallery in London [Maitre et al., 1996].

Some insight on this method can be given from its comparison with the one in equation (2.55) used above in this chapter to illustrate the learning paradigm of reconstruction methods. When noise is not present the equality

$$\mathbf{C} = \Theta \mathbf{R} \quad (2.79)$$

holds, we then deduce:

$$\mathbf{Q}_{\text{hard}} = \mathbf{R} \text{pinv}(\Theta \mathbf{R}) = \mathbf{R} \text{pinv}(\mathbf{C}). \quad (2.80)$$

Both methods are equivalent when noise is not present. We will thus not give any table of results for this method in this section as they are exactly the same as for results found for $\mathbf{R} \text{pinv}(\mathbf{C})$. But, we should not forget that the methods belong to a different paradigm. Hardeberg's method is an inversion technique while the other is a learning technique. It is interesting to see that they converge for the ideal case because in well calibrated high quality multispectral system their performance should be similar. This point is still to be tested. On the other hand, in the presence of noise the methods diverge because their sources of noise are different. One method is affected by the errors performed in the measurements to estimate Θ , while the other suffers from noise associated to a real image acquisition.

Finally, we want to remark the regularizing role played by matrix \mathbf{R} in equation (2.78). Its role is related to Hadamard's third condition, it stabilizes the operator using a set of existing spectral reflectances. As already said, Hardeberg tested its method using a matrix \mathbf{R} containing pure pigments utilized in oil painting, but he proposed for other applications the use of sets such as the object colours of [Vrhel, 1994] or the natural colours of [Jaaskelainen, 1990].

3.6.4 Pseudo-inverse and SVD

This method is based on a principal component analysis method and the pseudo-inverse. The principal components of the spectral reflectances are estimated by a least mean square approach (a pseudo-inverse) from the camera responses.

The method was introduced by Burns, for reference see [Burns, 1997]. A set of spectral reflectances, \mathbf{R} , typically coming from a colour chart are measured and a corresponding set of singular vectors, \mathbf{E} , is calculated by Principal Component Analysis. Note that \mathbf{E} is formally a matrix containing an orthogonal basis on its columns and \mathbf{A}' contains the projection of \mathbf{R} on the vector space spanned by \mathbf{E} . Then, the set of the most representative coefficients of \mathbf{A}' (in the sense of the PCA) form a reduced matrix obtained from \mathbf{A}' that we note \mathbf{A} . A relationship between representative PCA coefficients (or equivalently singular values) and channel responses \mathbf{C} , obtained from multispectral images of a colour chart, can be established by the operator

$$\mathbf{Q}_{\text{pinvPCA}} = \mathbf{A} \mathbf{C}^t (\mathbf{C} \mathbf{C}^t)^{-1} . \quad (2.81)$$

This operator can be used to calculate some (the more representative) of the singular values of the spectral reflectance from the camera responses. Let's note that another operation is needed to obtain the sampled spectral reflectance curve from the set of estimated singular values. This is obtained by a matrix multiplication, a projection from the orthogonal space defined by the PCA to the original reflectance space. If we call this matrix \mathbf{E}_p , we can redefine the operator to estimate directly the spectral reflectance curves as

$$\mathbf{Q}_{\text{pinvPCA}} = \mathbf{E}_p \mathbf{A} \mathbf{C}^t (\mathbf{C} \mathbf{C}^t)^{-1} . \quad (2.82)$$

If we compare this operator to the one used as a prototype of the learning paradigm (2.55) we see that they are very much similar. We repeat here the expression of the operator for better legibility:

$$\mathbf{Q}_{\text{pinvRC}} = \mathbf{R} \mathbf{C}^t (\mathbf{C} \mathbf{C}^t)^{-1} \quad (2.83)$$

In fact the only difference between both above operators is that one uses the matrix \mathbf{R} and the other introduces the product of two matrices $\mathbf{E}_p \mathbf{A}$. It is simple to deduce from the above explanation of the method that this $\mathbf{E}_p \mathbf{A}$ is equivalent to the matrix \mathbf{R} where an SVD has been performed, the "less representative" singular values being set to zero to form a new matrix \mathbf{R}' , then $\mathbf{R}' = \mathbf{E}_p \mathbf{A}$. Of course the concept of "representative singular values" becomes fundamental for this method. We will not enter further into this concept that has been extensively treated in Chapter 2 (*Nature of Data*).

In any case, the quantity of representative singular values should be chosen. One example of the application of this method is [Burns and Berns, 1996], where the authors use five singular values to represent a spectral reflectance curve. In this case the set of reflectance curves is coming from the Munsell Book of Color samples. We think this kind of a priori choice is arbitrary and cannot be claimed as general because the precision of the estimation or the resistance to noise of the reconstruction system depends on this parameter. In general different applications will require different number of singular values. From the same laboratory as [Burns and Berns, 1996], other works have justified their choice for the number of singular values used. [Imai et al., 2002] apply this method using as *training* set the spectral reflectances of a GretagMacbeth Checker DC colour chart. In this case they calculate reconstruction errors using from one to 31 singular values. They choose five as the error starts to stabilize on a plateau for this choice.

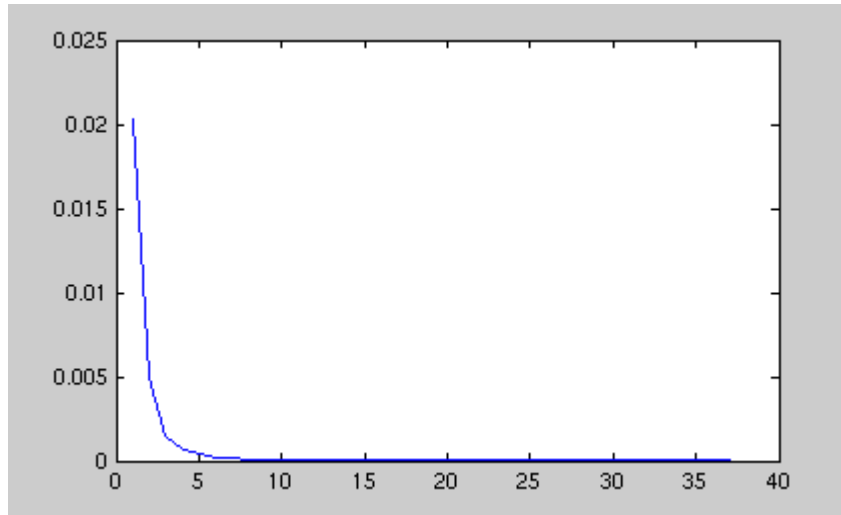


Figure 3-7 RMS reconstruction errors for the Macbeth DC chart using 12 bits quantization. Vertical axis represents the RMS error, horizontal axis contain the number of singular values used.

Using our simulations we calculate optimal number of singular values in that case. In Figure 3-7 we show the RMS reconstruction errors for the Macbeth DC chart using 12 bits quantization. Errors start to reach a plateau when 7 singular values are used. This is of course true in the case of our simulation but this calculation should be repeated when using real data.

Table 3-7. Mean Squared Spectral Error over different databases.

	Q_{pinvPCA}	Q_{pinvR}
Kremer	0.00065728	0.00029467
Macbeth DC	0.00011259	0.00006718
Selected Artists	0.00047047	0.00023387
Restoration	0.00042320	0.00018397
Munsell	0.00009908	0.00007020

It is interesting to compare the results of Q_{pinvPCA} and Q_{pinvRC} in our simulations. In the ideal case when noise is not present operator Q_{pinvRC} should perform better as it contains all singular values. Table 3-7 shows the comparison and confirms these differences. Q_{pinvPCA} has been calculated using the 8 first singular values. Indeed the *learning* strategy not performing any SVD analysis performs approximately twice better on average. We will come back later on this thesis to this discussion but in presence of noise when analysing the performance of reconstruction methods on real data.

3.6.5 Non averaged pseudo-inverse

This technique is a modification of the preceding one. It uses a conceptually easy and very powerful way of introducing noise information in the system. We read its first applications in [Imai et al., 2002] this is the reason why we call it Imai's linear operator.

The key idea behind this technique is simple but an experimental detail must be explained in order to understand how this method works. First of all the method belongs to the learning paradigm where a matrix \mathbf{R} of spectral reflectances and its corresponding matrix \mathbf{C} of camera responses are known. An operator \mathbf{Q} can be built using the pseudo-inverse. Knowing \mathbf{R} and \mathbf{C} implies classically a two steps experiment based on a chart containing colour patches:

1. Measure all the patches of the colour chart using a spectrophotometer. Each measure is stored in a column of the matrix \mathbf{R} .
2. Take a multispectral image of the colour patch. A window (normally squared) is superposed to each patch and its mean value calculated per patch and per channel. The mean values of the window for all the channels form a vector of camera responses. This mean vector is stored in a column of the matrix \mathbf{C} . This column has the same index as the corresponding spectral reflectance column in matrix \mathbf{R} .

The technique is based on taking advantage of the information acquired in the above step two. Instead of calculating a mean value for the windows superposed to the patches, this technique uses all the values contained in the window to build a large \mathbf{C} matrix. Of course matrix \mathbf{R} is expanded to have a corresponding spectral value for every column of \mathbf{C} . This makes the matrices very large. For instance, a typical big colour chart can contain 200 patches. When using the classical mean value approach, if 10 filters are used and the spectral curves have 40 samples, matrix \mathbf{R} has dimensions 40 by 200 while matrix \mathbf{C} is 10 by 200. When using this new approach and a small window of 10 by 10 pixels the sizes of the matrices are multiplied by 100. Matrix \mathbf{C} becomes 10 by 20,000 and matrix \mathbf{R} is 40 by 20,000. We can easily imagine that when the window increases its dimensions the size of the system formed by \mathbf{R} and \mathbf{C} can become huge. This implies much more computation time.

The big advantage of this method is that it captures automatically the acquisition noise model. This holds when the patches of the colours chart used are uniform and the multispectral acquisition system corrected for spatial inhomogeneities of the illuminant and the CCD. In this case, we can consider every pixel of a window as a realization of a random noise process. Then, using all the values in the analysis windows as samples to solve the spectral reconstruction problem means that we implicitly take noise into account. In fact, this approach is interesting because noise is not explicitly modelled, no assumption about its distribution being required. Moreover, if the multispectral images of the colour chart are taken in the same experimental situation as the ones with which the system will be used, then all noise sources are captured implicitly.

3.6.6 Non Negative Least Squares

We found the application of this technique in [Imai et al., 2002]. The Non Negative Least Squares algorithm is used to build a reconstruction operator Q_{NNLS} from a set of spectral reflectances and their corresponding camera responses. For clarity we divide this section in two subsections: first we describe the NNLS algorithm, secondly we explain how it is used for building the reconstruction operator.

3.6.6.1 NNLS algorithm

The NNLS algorithm is due to [Lawson and Hanson, 1974] and it aims to solve the following problem:

$$\min_{\mathbf{x}} \|\mathbf{E}\mathbf{x} - \mathbf{f}\|, \quad (2.84)$$

subject to the constraint

$$\mathbf{x} \geq 0, \quad (2.85)$$

where \mathbf{E} is a K by N matrix, \mathbf{f} a K -vector and \mathbf{x} a N -vector. In the following we will describe practically how the NNLS algorithm find a solution to this problem. For further reference or more theoretical considerations please refer to *chapter 23* of [Lawson and Hanson, 1974].

The solution of the above defined problem is subject to the Kuhn-Tucker theorem, which can be rewritten in this particular case as follows:

Theorem (Kuhn-Tucker conditions for the NNLS problem)

An N -vector $\hat{\mathbf{x}}$ is a solution for the NNLS problem if and only if there exists a M -vector $\hat{\mathbf{y}}$ and a partitioning of the integers $\{1, \dots, M\}$ into two subsets β and H such that

$$\hat{\mathbf{y}} = \mathbf{E}^t (\mathbf{E}\hat{\mathbf{x}} - \mathbf{f}) \quad (2.86)$$

and

$$\hat{x}_i = 0, \hat{y}_i \geq 0 \text{ for } i \in \beta, \quad \hat{x}_i > 0, \hat{y}_i = 0 \text{ for } i \in H \quad (2.87)$$

This theorem has a direct interpretation. The constraint (2.87) defines hyperplanes on the solution space. H is a set of numbers indexing the feasible halfspaces, β a set of indexes the boundaries of these halfspaces.

The NNLS algorithm takes as input the m by n matrix \mathbf{E} and the m -vector \mathbf{f} . This algorithm is based on the evaluation of (2.86) and the manipulation of two sets of indices, P and Z , that are defined and modified at execution time. Variables indexed in the set Z are held at the value zero. Variables indexed in the set P can take values different from zero. If such a value takes a nonpositive value, the algorithm will either move the variable to a positive value or else set the variable to zero and move its index from set P to set Z .

The algorithm is as follows:

Initialisation: set $P := \{NULL\}$, $Z := \{1, 2, \dots, n\}$, and $\mathbf{x} := \mathbf{0}$

Loop 1

Loop 2

Compute the N -vector $w := \mathbf{E}^t (\mathbf{f} - \mathbf{E}\mathbf{x})$

If (Z is empty) OR ($w_j \leq 0$ for all $j \in Z$)

Exit **Loop 1** and **2**

end If

Find index $t \in Z$ such that $w_t = \max \{w_j / j \in Z\}$

Move the index t from set Z to set P

Let \mathbf{E}_P denote the m by n matrix defined by

$$\text{Column } j \text{ of } \mathbf{E}_P := \begin{cases} \text{column } j \text{ of } \mathbf{E} & \text{if } j \in P \\ 0 & \text{if } j \in Z \end{cases}$$

Compute the N -vector \mathbf{z} as a solution of the least square problem $\mathbf{E}_P \mathbf{z} \cong \mathbf{f}$.

If ($z_j > 0$ for all $j \in P$)

$\mathbf{x} := \mathbf{z}$

end If

End Loop 2 If $\exists z_j < 0, j \in P$

Find an index $q \in P$ such that $x_q / (x_q - z_q) = \min \{x_j / (x_j - z_j) : z_j \leq 0, j \in P\}$

Set $\mathbf{x} := \mathbf{x} + \frac{x_q}{x_q - z_q} (\mathbf{z} - \mathbf{x})$

Move from set P to set Z all indices $j \in P$ for which $x_j = 0$

End Loop 1

On termination of this algorithm the vector \mathbf{x} satisfies the positivity constraint and is a solution of the least square problem (2.84). The convergence has been proven, see [Lawson and Hanson, 1974] for details. These authors claim that **Loop 1** of the algorithm requires typically $\frac{1}{2} N$ iterations to find a solution. This is important to note because most reconstruction algorithms used in spectral reconstruction are based on non iterative algorithms.

3.6.6.2 Building operator Q_{NNLS}

Applying the NNLS algorithm directly to reconstruct individual spectral reflectance curves is possible but it would need the full execution of the algorithm for each pixel of the image. As long as NNLS execution time is finite but not bounded that is probably the main reason not to use it that way. In fact, in [Imai et al., 2002], the authors build an operator using the NNLS algorithm and this operator is used in the reconstruction process. They do not specify in this papers how they do it. We have implemented and tested a method using NNLS based in the same assumption as [Imai et al., 2002].

From equation (2.49) we know that the basic learning-based reconstruction operator is equivalent to the solution of the following least square problem:

$$\min_{\mathbf{q}_i^t} \left\| \mathbf{C}^t \mathbf{q}_i^t - \mathbf{r}_i^t \right\|^2. \quad (2.88)$$

where \mathbf{C} is the matrix of camera responses, \mathbf{r}_i is the i -th row of \mathbf{R} containing spectral reflectances on its columns, and \mathbf{q}_i is the i -th row of the desired operator \mathbf{Q} . Once the system is expressed in this way, the constraint $\mathbf{x} \geq 0$ can be imposed by using the NNLS algorithm to solve it. Solving the problems for all the i 's will give us the desired operator \mathbf{Q}_{NNLS} .

The operator \mathbf{Q}_{NNLS} is the result of the application of the NNLS algorithm, consequently no negative values will be found on it. As our input camera responses are always normalised between zero and one, all the samples of the reconstructed spectral reflectance curves are guaranteed to be bigger or equal to zero.

In Figure 3-8 we show a graphical representation of operator \mathbf{Q}_{NNLS} calculated using the simulation presented in 3.2.4. On the left panel we plot a 3d graph while on the right panel a contour plot is shown. By the nature of the method lots of zeros are introduced in the operator.

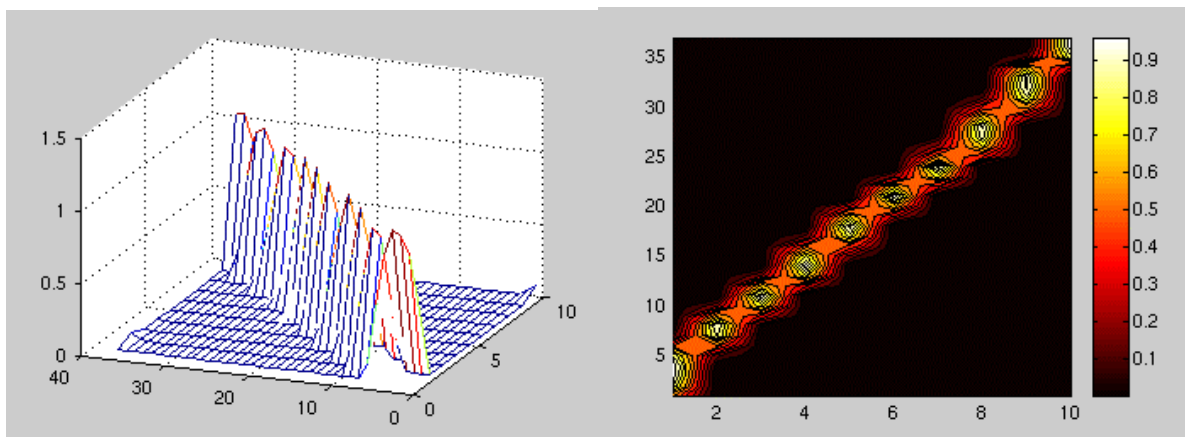


Figure 3-8 3d graph of the reconstruction operator calculated using NNLS on our simulation (left panel), its corresponding contour plot (right panel)

3.6.7 Techniques based on Interpolation

Spectral reconstruction using interpolation is based on the simple assumption that a multispectral system is sampling spectral reflectance curves. Instead of using delta Dirac functions for the sampling as in the classical framework, the spectral transmittance functions of filters are considered to be the sampling functions. In our simulation this fact is easy to see. On the left panel of Figure 3-9 we represent on red some camera responses along with its spectral reflectance curve in the same graph. On the right panel we perform a linear interpolation of the red points to show that simple interpolation roughly approximates the shape of the spectral curve.

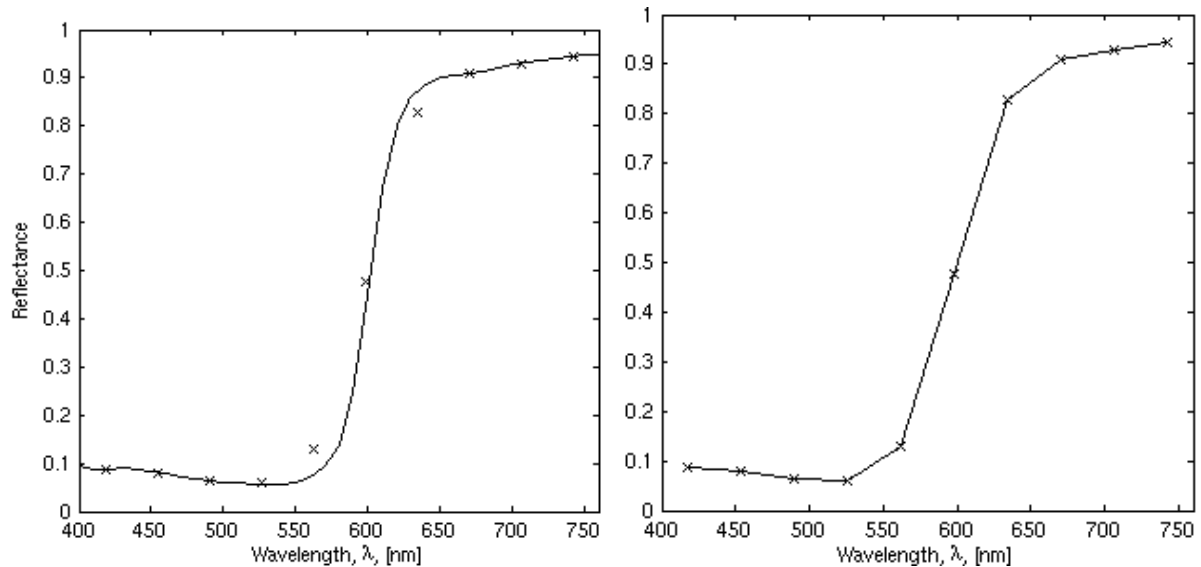


Figure 3-9 A spectral curve along with its camera responses (left panel), linear interpolation of the camera responses (right panel)

There are two underlying problems to take into account before representing the camera responses in the same space as spectral curves:

- The position of the samples in the spectral range. In the case of our simulation the camera responses are drawn at the positions of the centres of the Gaussian filters. Gaussians can be interpreted as basis functions of the spectral curves and their centres are an obvious choice for representing the position of the sample. Real filters are normally not Gaussians. In general, we can say that if a filter is narrow, positioning the camera responses can be done with low uncertainty. Unfortunately, when wide filters are to be used this uncertainty increases with the width of the filter. This is the reason why interpolation methods are used only with multispectral cameras using narrow band pass filters.
- Camera responses must be normalised. In the case of our sample simulation the values of the camera responses belong to the interval $]0,1[$ for all channels. In order to obtain this we multiply the simulated camera responses by a normalization matrix. This normalization matrix is obtained taking into account the responses of the system to the spectral curve of a “perfect white”. In our simulated case this perfect white is a spectral curve with all samples having a maximum unitary value. In a real case, normalising the responses is not so easy. In general, a standard white patch is imaged as a reference for normalisation as part of a calibration procedure.

In the case where camera responses are not normalised any interpolation method would provide very bad results. If we take a look at the \otimes operator used in our simulation we clearly see that the filters on the low side of the spectrum allow less energy to pass through than the filters on the upper side. Interpolation without normalisation would give curves with errors depending on the energy the operator allows to pass trough. In Figure 3-10 we show the same information as in Figure 3-9 when normalisation is missing. On the left panel of Figure 3-10 we see that camera responses (crosses) are not at all an approximation of its spectral reflectance curve. On the right panel we perform a linear interpolation to show how interpolation fails.

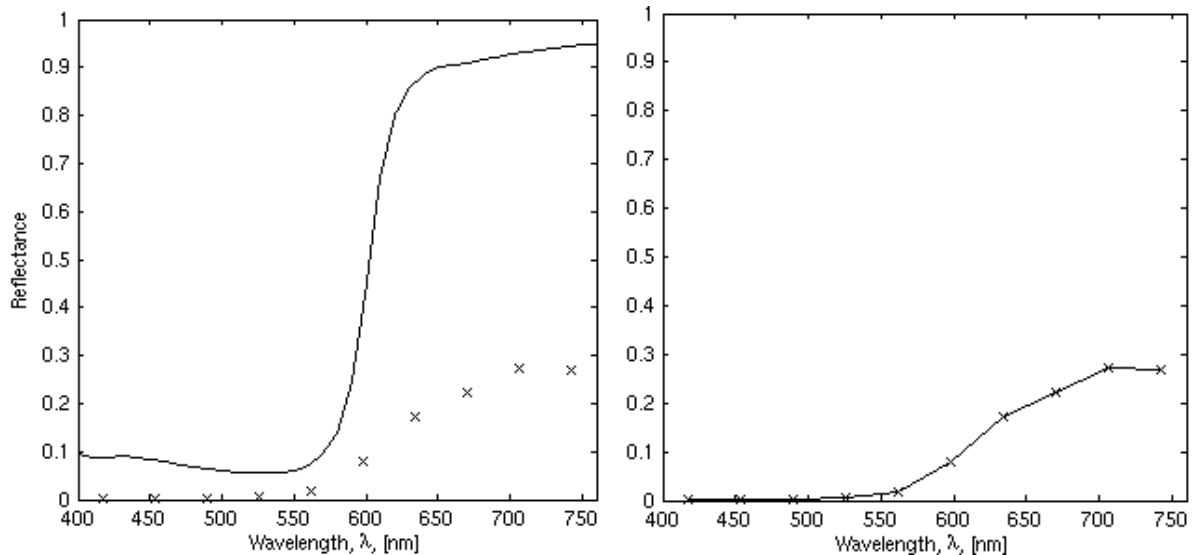


Figure 3-10 A spectral curve along with its non normalised camera responses (left panel), linear interpolation of the camera responses (right panel)

Before giving more details about interpolation based techniques for spectral reconstruction we want to emphasize that even if it seems that this kind of technique is directly applicable to the camera responses without any knowledge of the direct system, this is not true if good results are to be obtained. As we saw above these techniques are adapted to situations where we have a relatively high number of narrow band filters. [Keusen, 1996] mentioned the number of 16 in its simulations. On the other hand a good calibration of the multispectral system is necessary to apply this technique. In general we have seen most practical application of interpolation in cases where the CCD used is cooled and Gaussian like filters are used, see [Herzog and Hill, 2003] for instance. Such methods are reported not to be well adapted to filters having more complex wide-band responses, and suffer from quite severe aliasing errors [Burns 1997, Thesis], [Konig 1999].

In the following we present the existing interpolation techniques that have been applied to the spectral reconstruction problem.

3.6.7.1 Cubic Splines

In their most general form, splines can be considered as a mathematical model that associate a continuous representation of a curve or surface with a discrete set of points in a given space. Spline fitting is an extremely popular form of piecewise approximation using various forms of polynomials of degree n , or more general functions, on an interval in which they are fitted to the function at specified points. The polynomial used can change, but the derivatives of the

polynomials are required to match up to degree $n - 1$ between two intervals, or to meet related interpolatory conditions. Boundary conditions are also imposed on the end points of the intervals. The heart of spline construction resides on how the selected control points are effectively joined using the polynomial function of choice.

Cubic splines are probably the most popular curve representation scheme at the moment. They are piecewise polynomials of degree three, cubic polynomials, with pieces smoothly connected together. In the multispectral community they have been used only for interpolation, not for approximation and they were introduced by [Keusen, 1996]. Splines are well adapted to the representation and reconstruction of spectral reflectance curves because they generate smooth curves, C^2 continuity being assured in a cubic spline.

Giving here an introduction to the mathematics of the splines is out of the scope of this section. The interested reader can find plenty of textbooks and papers on this subject. For a in depth description of this interpolation technique see chapter 9, *Cubic Spline Interpolation*, of [Farin, 1998]. A comprehensive introduction can be found in chapter 3, *Hermite and Cubic Spline Interpolation*, of [Bartels et al., 1987].

3.6.7.2 Modified Discrete Sine Transform (MDST)

The MDST was introduced by [Keusen, 1996]. It is based upon Fourier Interpolation. This technique uses the DFT (Discrete Fourier Transform) to represent the data in the frequency domain. As the Fourier Transform decomposes a signal into an orthogonal basis, this basis can be used as an interpolating function. In the implementation of the technique the FFT (Fast Fourier Transform) is normally used. The key concept that is exploited is that the FFT uses integer positive numbers as indexes. The most usual way of performing the interpolation is based in two steps:

1. a FFT is performed on the original signal,
2. when performing the inverse FFT non-integer indexes are allow in the transformation.

This way of performing Fourier interpolation works by summing together, in the time domain, the frequency components of the interpolation function which is created from the set of sinusoidal basic functions whose magnitudes are specified by the output of the FFT. This is the technique we are using in our implementations of the Fourier interpolation. There exist another way of Fourier interpolation by Frequency Domain Extension. We will not give here more details about these techniques, the interested reader can refer to [Merrit, 2002] for a good introduction to this subject.

A main problem with the application of the DFT or FFT is that initially this transformation delivers good results only if samples of periodic functions are used. The samples considered in spectral reconstruction are typically limited around the range 380 to 780 nm, outside this range no samples are available. If a FFT is applied despite this fact, wrong-frequency components created at the edges of the sampled window produce errors. A pre and post processing method was developed by Keusen to solve this problem. The method works as follows:

- In a first step, a linear function combining the edge values of the samples is subtracted from the sampled values. The result is a smooth function with zero values at the edges. A sample can be seen in left panel of Figure 3-11. On top the original function (solid

line) is shown along with its corresponding linear function. On the bottom we show the function after subtraction (dashed line).

- Afterwards, this function is mirrored periodically with changing sign, as sketched in the right panel of Figure 3-11. This produces a smooth and periodic function, that we can call *modified* function.

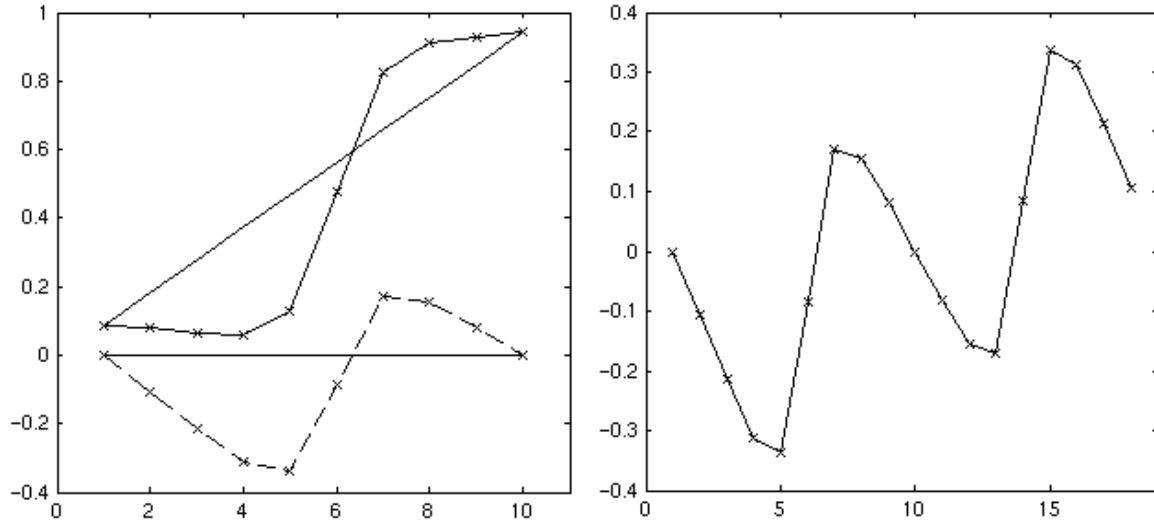


Figure 3-11 (left panel) Original camera responses on red along with its linear function, on the bottom same data after subtraction of the linear function. (right panel) mirrored function

- Now, Fourier interpolation can be applied to derive an approximation of sampled values. We show the result on the left panel of Figure 3-12.
- At last, the first half of the function is kept (bottom of right panel, Figure 3-12) and the linear function computed as first step is added. The final result is shown on the top of the right panel of Figure 3-12.

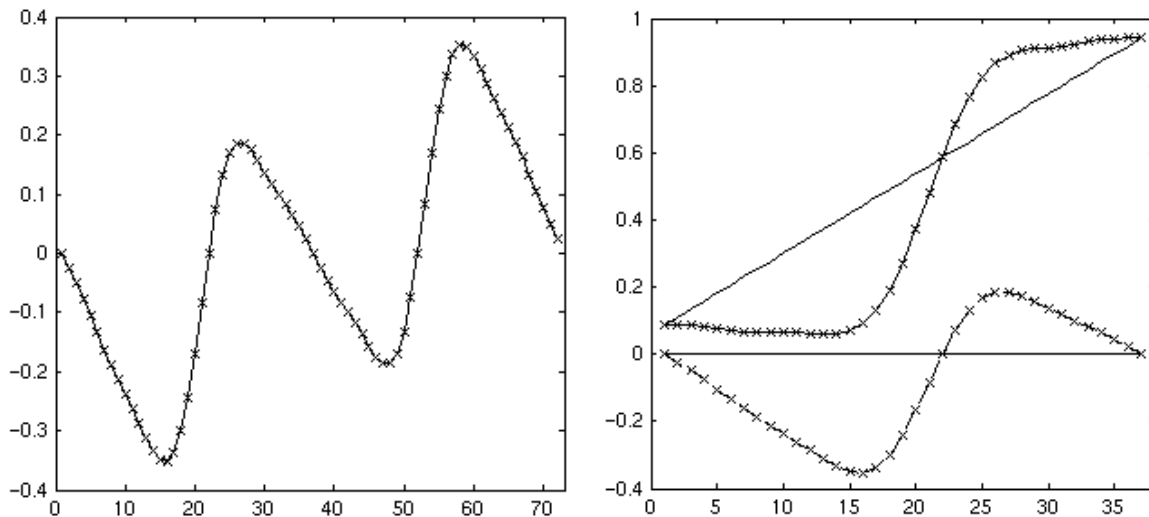


Figure 3-12 (left panel) Modified function after interpolation on the Fourier domain. (right panel) On the bottom, first half of the modified function; on top, final result after addition of the linear function

It is important to note that mirroring and Fourier expansion correspond to a sine transform. The Fourier transform of a real-odd function $f(-x) = -f(x)$ is real-odd. Similar results hold for a

discrete Fourier transform, and thus for these symmetries the need for complex inputs/outputs is entirely eliminated. Moreover, we gain a factor of two in speed/space from the fact that the data are real, and an additional factor of two from the odd symmetry: only the non-redundant (first) half of the *modified* function needs to be stored. The result is the real-odd DFT, also known as the discrete sine transforms (DST). This is the reason why this method is called modified discrete sine transformation (MDST).

3.6.7.3 Interpolation methods simulation results

We show here some results using our simulation for the interpolation methods. Table 3-8 contains a comparison between MDST and the cubic spline.

Table 3-8. Mean Squared Spectral Error over different databases.

	Cubic Splines	MDST
Kremer	0.00095983	0.0020281
Macbeth DC	0.00075815	0.0013742
Selected Artists	0.00084324	0.0016577
Restoration	0.00050814	0.0010732
Munsell	0.00036359	0.0006119

In this case, cubic splines obtain much better results than the MDST method. This is not surprising as MDST was reported by [Keusen, 1996] to obtain good results for 16 filters while we are using 10. In this context the interpolation methods seem no satisfactory. If we look at Table 3-7 we see that results obtained by operators $\mathbf{Q}_{\text{pinvPCA}}$ and $\mathbf{Q}_{\text{pinvRC}}$ are, for all presented databases, clearly superior to interpolation. This fact confirms the idea that reconstructing reflectance curves by interpolation leads to good results only when a high number of narrow band filters is used.

3.7 Conclusion

The problem of spectral reconstruction has been presented and analysed on this chapter. Our analysis and the introduction of fundamental formulae lead to a classification of the methods depending on the type of problem to be solved. The proposed classification of the reconstruction techniques includes three paradigms: i) *direct* reconstruction, which is based on the inversion of the camera model a ii) *indirect* or *learning-based* reconstruction and iii) reconstruction by interpolation. Our classification is physically and mathematically well founded and helps understanding the limits and requirements of the methods.

A survey on the existing reconstruction techniques was also presented. This survey is illustrated by computer simulations, discussions and some algebraic developments. We believe this is useful to give insight on the behaviour of the methods and their possible applications.

The chapter intended to be self-contained. This is why data concerning noise, descriptions about solving least square problems and metrics for the evaluation of reconstructed spectral reflectances are included.

Chapter 4: Improving Spectral Reconstruction Accuracy

Contents

4.1	Introduction	81
4.2	Generalization and linear systems	82
4.2.1	Proposed algorithm	82
4.2.2	Results	83
4.3	Respecting physical constraints	86
4.3.1	A spline-based projection operator	87
4.3.2	Results	88
4.4	Conclusion.....	90

4.1 Introduction

In this chapter we introduce two ideas in order to improve spectral quality reconstruction. These ideas are not themselves new reconstruction techniques but they can be applied to improve most of the existing spectral reconstruction methods. In our knowledge, the proposed improvements have never been applied in the context of spectral reconstruction. Moreover, because they are not specific methods but general improvements they can be broadly used.

The first idea relates with the generalisation abilities of existing linear reconstruction methods using a priori information about the objects to be imaged. As we show on Chapter 3 there are quite a lot of methods belonging to this category. Researchers using this type of methods have characterised and compared their errors over different test sets. But they do not treat the problem of how to increase the results over these test sets. Using the concept of generalisation we propose an algorithm based on intense random resampling that increases the generalisation capabilities of such methods. Even if our simulations are performed on a specific operator chosen as a reference, the algorithm remains general and can be apply to any reconstruction method using a priori information.

The second idea introduced in this chapter relates with the physical constraints to be respected by the reconstructed spectral curves. For instance, a spectral curve cannot be negative because this has no physical meaning. In addition the curves should not contain values bigger than unity (when normalised) and should be continuous and smooth. These physical constraints are generally not taken into account. The only exception we know is in [Imai et al., 2002] where the authors build an operator that assures non-negative values on the reconstructed curves.

We propose a projection operator that is applied after spectral reconstruction to fit the curves on a physically meaningful space. The curves become bounded while keeping their smoothness. The a posterior application of this projection operator makes it an easy and efficient complement to any existing reconstruction technique.

4.2 Generalization and linear systems

In spectral reconstruction we have to deal with the problems of extrapolation, prediction or estimation of spectral curves. A reconstruction method can obtain bad results when confronted to a particular set of imaged objects while obtaining very good results for others. This is a delicate aspect that has not been treated at the moment on the multispectral scientific community. In fact, we have not seen any reference on the multispectral literature about how the existing methods generalise.

When direct or interpolation methods are used, we can apply these methods to different data sets and measure their differences in accuracy. Improvements of the methods which go further than the stabilization of their singular values, [Burns, 1997], are not evident and would introduce new elements in the operators. This is, for instance, the case of [Hardeberg et al., 1999] where a priori information about the objects to be imaged is introduced that modifies the inversion operator. This guarantees a better response over the set of spectral reflectances used as an “a priori information” but it still remains the question of what will happen when using other data sets. Exactly the same question arises when building operators on a set of camera responses and their corresponding spectral reflectances. We expect a good result on the data set used as *training* but the generalisation capabilities of the operators are practically not predictable.

In this section we introduce a method for the improvement of the generalisation accuracy of spectral reconstruction. In order to present the method we choose the operator presented as reference for the learning paradigm, see Chapter 3, we rewrite here its equation for clearness:

$$\mathbf{Q} = \mathbf{R} \text{pinv}(\mathbf{C}) \quad (4.1)$$

where $\text{pinv}(\mathbf{C}) = \mathbf{C}^t (\mathbf{C} \mathbf{C}^t)^{-1}$, \mathbf{C} being the matrix containing the camera responses on its columns, and \mathbf{R} being the matrix containing the corresponding sampled spectral reflectances on its columns.

Our method for generalisation is based on the idea of bootstrap. Bootstrap was introduced by [Efron, 1979]. This paper revolutionized the field of statistics and from there bootstrap has been extensively used. Originally the bootstrap method is a computer based resampling technique for assigning measures of accuracy to statistical estimates. It provides confidence intervals on the estimation of any population statistic.

After more than twenty years from the original paper of Efron the bootstrap now broadly refers to a collection of methodologies in which data are resampled in order to incorporate, into statistical inference, the information contained in the data regarding its probability distribution. The method is conceptually simple yet computationally intense. As computers become faster and more powerful, the bootstrap becomes a more practical tool for data analysis. The method introduced in this section is a bootstrap method in the sense that it uses intense resampling to statistically improve the results of the spectral reconstruction.

4.2.1 Proposed algorithm

The algorithm is based on resampling matrices \mathbf{R} and \mathbf{C} by using a random selection of their columns. The probability distribution used for the selection is uniform. We then call *resample(.)* a function taking a matrix and returning another matrix with randomly resampled

columns. We note that the obtained matrix will contain repeated columns. Consequently, some columns of the original matrix will not be present on its resampled version.

The proposed algorithm consists in building a reconstruction operator using the resampled matrices obtained from \mathbf{R} and \mathbf{C} . A big number of operators can be calculated along with their errors over a test set of data, \mathbf{R}_{test} and \mathbf{C}_{test} . Afterwards the operator showing the lowest RMS error on the test set is chosen.

The algorithm in pseudo-code is as follows:

```

For  $i=1,\dots,I$ 
     $\mathbf{R}_i = \text{resample}(\mathbf{R})$ 
     $\mathbf{C}_i = \text{resample}(\mathbf{C})$ 
     $\mathbf{Q}_i = \mathbf{R}_i \text{ pinv}(\mathbf{C}_i)$ 
     $\text{error}_i = \|\mathbf{Q}_i \mathbf{C}_{\text{test}} - \mathbf{R}_{\text{test}}\|^2$ 
End For
Choose  $\mathbf{Q}_i$  having the smallest  $\text{error}_i$ 

```

where I is the number of iterations. The function *resample(.)* transforms equally \mathbf{R} and \mathbf{C} by using the same random selection in each iteration because these two matrices need to contain corresponding columns.

4.2.2 Results

We applied the algorithm introduced on the preceding section using $I=100$ to some spectral reflectance databases. In this section we choose an example to illustrate the improvements obtained in our experiments. \mathbf{R} in this example contains the spectral reflectances of the MacbethDC dataset. The corresponding matrix \mathbf{C} is calculated by simulation considering a multispectral system with seven equidistributed Gaussian-shaped filters on the visible part of the spectrum. Twelve bits quantization is introduced on the system. The test reflectances used, \mathbf{R}_{test} , are the Kremer dataset. \mathbf{C}_{test} is calculated by simulation exactly as for \mathbf{C} .

Table 4-1. Comparing spectral accuracy results before and after bootstrapping

	MacbethDC	Kremer
Without bootstrap	0.0001884	0.001081
After bootstrap	0.0002069	0.000744

In Table 4-1 we presents the results of the application of the algorithm on the training set of the reconstruction method and on the test set of our algorithm. We found that it indeed reduces the RMS error on the test set but the error is augmented on the set used to build the operator. This increase of the error on \mathbf{R} is not necessarily bad, in fact poor generalisation implies normally high specialisation on a set of data used for training. In fact, by just considering data presented on Table 4-1 we cannot know if the generalisation capabilities of the built operator are increased. We then present on Table 4-2 the same results on the Selected Artists, Restoration, Munsell, and Pine Tree Leaves datasets. The effect on these datasets is very positive, a reduction of the RMS spectral error is clear on all cases. The mean increase in accuracy is 29.6% that can be considered very significant, even more when considering that they are generalisation results and the used datasets come from very different origins.

Table 4-2. Generalisation results before and after bootstrapping

	Selected Artists	Restoration	Munsell	Pine Tree
Without bootstrap	0.0006915	0.0006445	0.0001538	0.0010293
After bootstrap	0.0004822	0.0003969	0.0001326	0.0006592
Improvement	30.3%	38.4%	13.8%	36.0%

Even if the reduction of the RMS errors presented on Table 4-2 is very positive for $I=100$ iterations we wanted to know if it was possible to improve the results further. For this we applied our algorithm iteratively, the best \mathbf{R}_i matrix found after $I=100$ iterations of the algorithm being used as the matrix \mathbf{R} for the next set of $I=100$ iterations. This strategy appears to indeed further reduce the error. Then, we decided to study closer the effect of the iteration of the algorithm. On the left panel of Figure 4-1 we can see the evolution of the error on the test dataset \mathbf{R}_{test} while iterating. Twenty algorithm iterations are enough to see that the error is reduced till a plateau is reached after 5 iterations. On the right panel of Figure 4-1 the evolution of the reconstruction error on \mathbf{R} (the set used to train the reconstruction method) is shown. This error increases on each iteration and also reaches a plateau after 15 iterations. It is important to note that the plateau of error reduction on \mathbf{R}_{test} is reached before the plateau of error increase on \mathbf{R} .

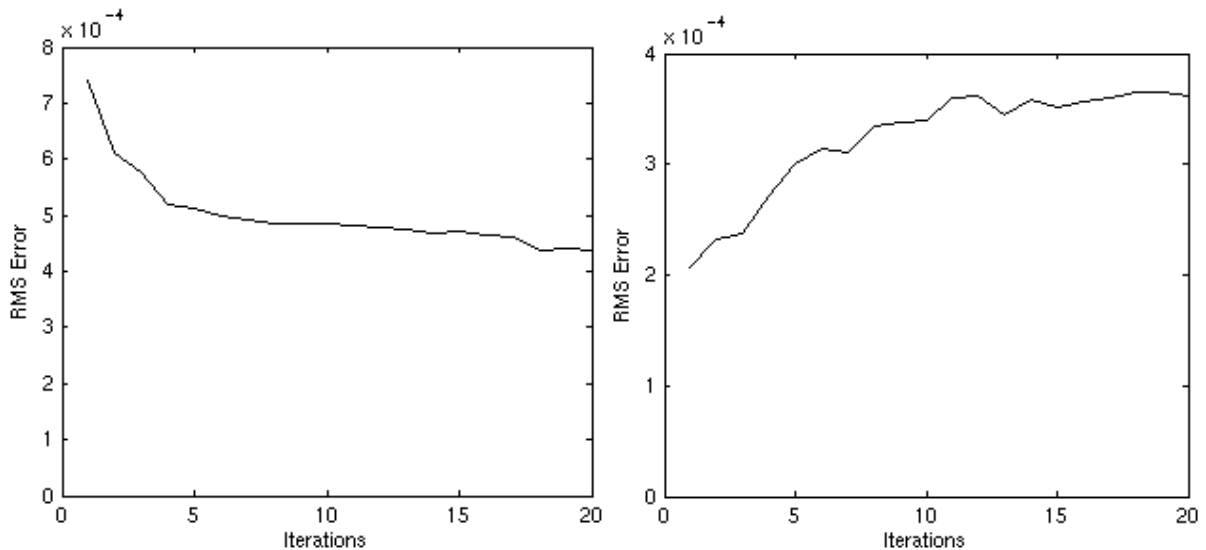


Figure 4-1. RMS error evolution when applying the bootstrap based algorithm several times. (left panel) Data set used as test for the bootstrap, (right panel) data set used as learning set for the reconstruction operator.

On Figure 4-2 we present in a similar graph as on left panel of Figure 4-1 the RMS spectral error on the Selected Artists, Restoration, Munsell, and Pine Tree Leaves datasets. We can see that the iteration of our algorithm also reduces the error on these datasets. A plateau or a minimum is reached around 5 iterations as for \mathbf{R}_{test} , the test set. An exception appears for the Pine Tree dataset that continues decreasing its error. The behaviour of the algorithm observed on these experiments indicates that the optimum number of iterations is five for this case. Iterating more does not decrease the generalisation capabilities of the reconstruction operation. On the contrary too many iterations degrade the reconstruction quality on the training set of the method and also on some datasets used to test the generalisation.

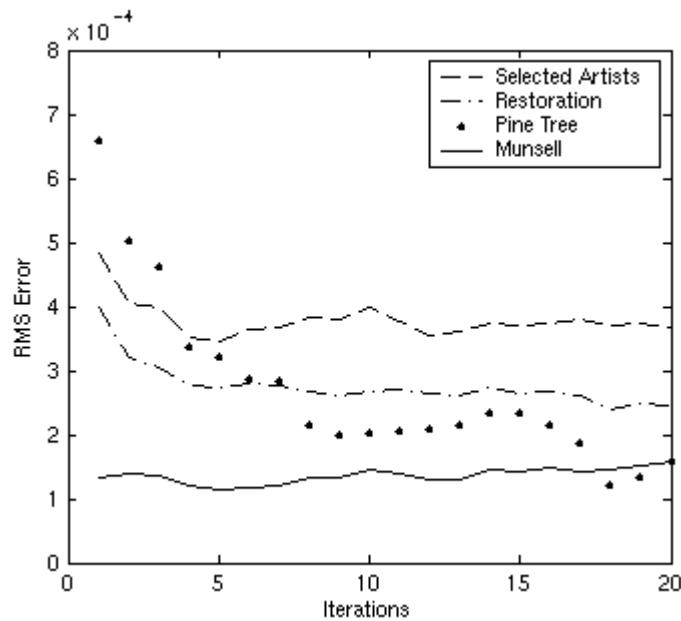


Figure 4-2. RMS error evolution on other data sets.

Before concluding this section we quantify the improvements introduced for the proposed bootstrap based method. If we call rms the RMS reconstruction error without bootstrap and rms_b the RMS error obtained once the bootstrap has been applied, we can then easily calculate the per cent of improvement as:

$$\%_{improvement} = \frac{rms - rms_b}{rms} \times 100. \quad (4.2)$$

On Table 4-3 we present the results obtained after five iterations of the proposed algorithm (with $I=100$). We present for comparison the results when the algorithm is not used and the calculated per cent of improvement using expression (4.2). The results for generalisation appear to be very satisfactory. We also observe that after 5 bootstrap iterations the RMS error is much more equally distributed on the various datasets used for testing generalisation.

Table 4-3. RMS errors before and after bootstrapping (5 iterations) and % of improvement.

	MacbethDC	Kremer	Selected Artists
Without bootstrap	0.0001884	0.0010810	0.0006915
After 5 bootstraps	0.0003009	0.0005168	0.0003467
Improvement	-59.7%	52.2%	49.9%
	Restoration	Munsell	Pine Tree
Without bootstrap	0.0006445	0.0001538	0.0010293
After 5 bootstraps	0.0002742	0.0001141	0.0003194
Improvement	57.5%	25.8%	69.0%

In conclusion, we have proposed a method for improving the generalisation capabilities of linear reconstruction operators by using bootstrap. It is in our knowledge the first time that such an approach is taken on spectral reflectance reconstruction. We have tested the method by simulation and the obtained results are fully satisfactory. Even if the tests have been performed using a specific operator, the algorithm remains general and is applicable to any linear reconstruction method using a priori information over the imaged objects.

4.3 Respecting physical constraints

A spectral reflectance of an object or material is defined as the ratio of its luminance to the luminance of a perfect white diffuser material at the same position. The measure of this physical property satisfies then physical constraints. For instance, there is no physical meaning for a negative reflectance. But when performing spectral reconstruction, negative reflectances can appear in the solutions. This is due to the mathematical formulation of the problem. In general, the reconstruction methods seek to minimise a measure of accuracy which sometimes leads to negative values. In our knowledge, the only effort to deal with this constraint is in [Imai et al., 2002] where the authors apply the Non Negative Least Squares (NNLS) algorithm to build reconstruction operators estimating curves without negative values. As this algorithm is based on the introduction of zeros (instead of negative values) on the constructed operator it is predictable that its accuracy decreases. In any case, the algorithm deals with the problem of non-negative values but not with others constraints.

Three constraints are important on a spectral reflectance curve:

1. the curve cannot be negative,
2. it has an upper bound of 1 (we consider here only diffuse materials without specular reflection),
3. the curve must be continuous and smooth.

The third constraint has been extensively justified on Chapter 2. The reconstruction methods studied on Chapter 3 respect the third condition but not the others (NNLS being an exception).

In the multispectral community there exists another problem that is sometimes solved by similar linear methods as the ones presented on Chapter 3. This is the problem of filter optimisation. In this context [Sharma and Trussell, 1996] introduced an estimation method for spectral sensitivity curves based on the method of Projections Onto Convex Sets (POCS). The method itself was not new, the first image processing application of POCS was on [Youla and Webb, 1982] where the aim was the restoration of images. POCS is a method that allows the use of non-linear maps in simple terms. Every known property of an original signal or image f can be restricted to lie in a well-defined closed convex set. Thus, m such properties place f in the intersection of the corresponding closed convex sets C_1, C_2, \dots, C_m . Given the projector operators P_i onto the individual C_i 's, $i=1 \dots m$, we find f by the recursive application of the operators P_i . The approach is conceptually simple and the major synthesis problem becomes the realization of operators P_i .

[Sharma and Trussell, 1996] used several convex sets for filter transmittance optimisation, they are: the non-negative and upper bounded vector set, the noise variance set, the noise outliers set, the passive response set, the smoothness constraint set, the unimodal set and the set of vectors close to the *Human Visual Space*. Using projection operators onto these sets they solved their problem. As we can see two of this sets are adapted to the constraints of reconstructed spectral curves: the non-negative (and upper bounded) vectors set and the smoothness set.

We can think about the application of POCS to spectral reconstruction. However, the non-negative and upper bounded convex set and the smoothness set are not enough. In fact, they guarantee the reconstruction to be physically feasible but they do not guarantee a good reconstruction accuracy. Consequently, a projection operator minimising an accuracy criterion must be included. Once done, we could apply POCS for spectral reconstruction. But we must

not forget that POCS is an iterative method based on projection operators. Such a method is then not bounded on time and can converge slowly, depending on the case. It is then not adapted for spectral reconstruction where existing methods are bounded and fast.

Even if we cannot consider the use of POCS for spectral reconstruction the underlying idea is still interesting. Based on this idea, in this section we seek for a projection operator that bounds estimated reflectance curves while respecting their smoothness and increasing their estimation accuracy. Such an approach cannot be called POCS because it considers an unique projection, performed in a single step and without any iteration. If the correct projection operator is found it could be apply as a postprocessing step for any reconstruction method.

4.3.1 A spline-based projection operator

Before speaking about the new operator let's take a look at the basic orthogonal projection onto a set of bounded curves. This operator is given by a simple saturation. Be $r(\lambda)$ the reconstructed curve and $r_p(\lambda)$ its orthogonal projection, the operator is defined as:

$$r_p(\lambda) = \begin{cases} 0 & \text{if } r(\lambda) < 0 \\ 1 & \text{if } r(\lambda) > 1 \\ r(\lambda) & \text{elsewhere} \end{cases} \quad (4.3)$$

It is easy to see that $r_p(\lambda)$ is not necessarily continuous, this is due to the two discontinuity points on 0 and 1 on the projection operator. When the projection is performed the smoothness of the resulting curve is not preserved. Our idea is to obtain an operator similar on shape but continuous. Mathematically smoothness is a characteristic of a curve belonging to class C^2 , containing the functions having continuous second derivatives. We remind that the composition of two functions g and h , $h \circ g$, is C^2 when both functions are themselves C^2 . As spectral reflectance function are continuous and smooth if we construct a C^2 projection operator the obtained curve is necessarily C^2 . We take then as a basis to model our operator a cubic spline which assures continuity and smoothness. On Figure 4-3 we can see the overall shape of two operators constructed with cubic splines. We can see that in the upper and bottom regions the operator is a third degree polynomial while on the rest it is a straight-line with unitary slope.

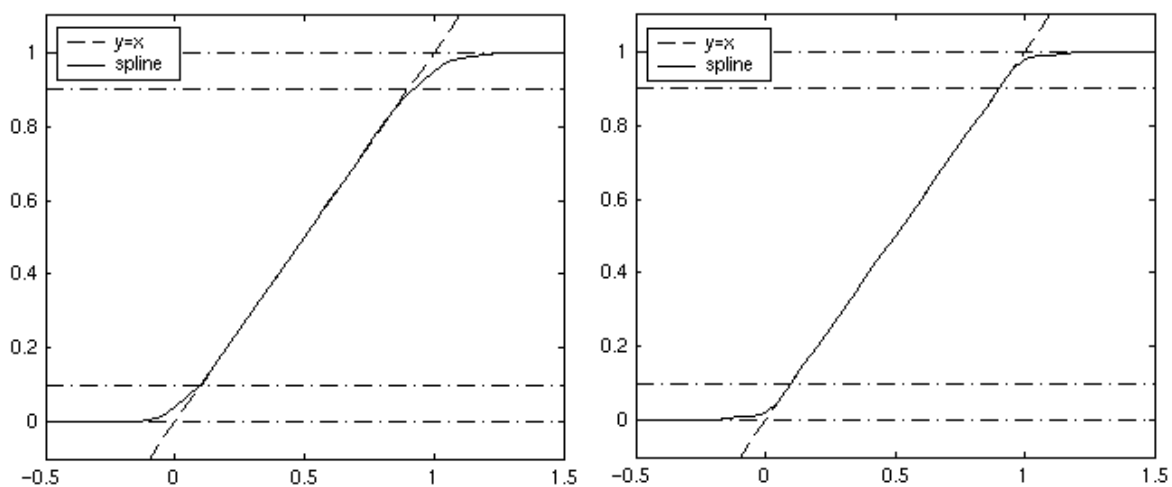


Figure 4-3. (left panel) Proposed projection operator with its parameter fixed at 10%. (right panel) Some operator at 2%.

A question arises on how to define a priori the size of the curved upper and bottom parts of the operator in the regions close to its bounds. We have parameterised the size of these regions by a unique parameter. We express it in per cents (%) because it gives a good intuitive understanding of its effect. The family of operators defined by this parameter is easily obtained by the modification of some of the knots that form the spline. On the left panel of Figure 4-3 we show the resulting operator with parameter 10% while on the left panel we show the one with parameter 2%. In fact, the 10% operator appears not useful as it modifies too much the spectral curves inside the bounded area, this degrades the reconstruction errors. The 2% operator is more realistic. We will see its effects on the next section.

4.3.2 Results

Before presenting data obtained from statistical analysis on different databases we show an example of a projected reflectance curve. A simulation is performed considering a multispectral system with seven equidistributed Gaussian-shaped filters in the visible part of the spectrum. Twelve bits quantization is introduced on the system. In Figure 4-4 we show a measured spectral reflectance from the Kremer dataset (dashed line) and its reconstruction (solid line) using equation (4.1) as in the preceding section. Clearly the reconstructed curve does not respect physical constraints, it contains negative and “bigger than one” values.

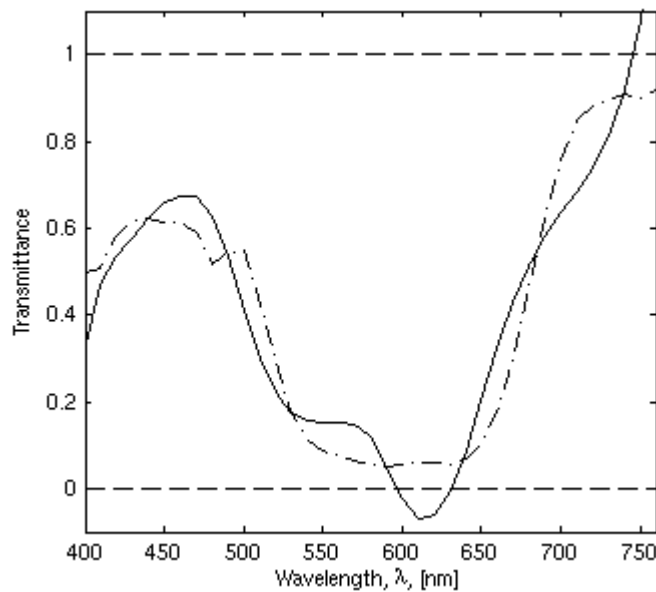


Figure 4-4. Original (dashed line) and reconstructed (solid line) spectral reflectance curves. Clearly the reconstructed curve does not respect physical constraints.

On the left panel of Figure 4-5 we show the projection of the reconstructed curve using expression (4.3). The obtained curve is no more smooth and presents three points in which the curve is not of class C^2 . On the right panel of Figure 4-5 we see the projection using the proposed operator with parameter 2%. The projected curve is bounded and keeps being smooth.

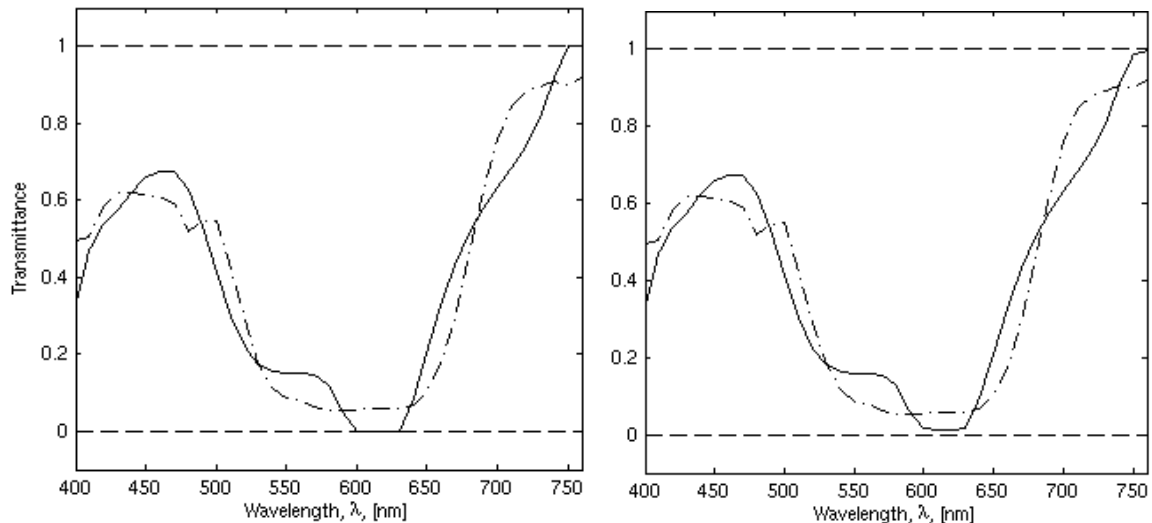


Figure 4-5. Original spectral reflectance curve (dashed line) and projection of its reconstruction (solid line). (Left panel) Projection performed by a raw saturation. (Right panel) Projection operator is the proposed spline with its parameter at 2%.

On the above example we can visually see that the 2% proposed operator is slightly better than the orthogonal projection of expression (4.3). If projection is applied to several databases we can quantify the errors. On Table 4-4 we present simulation results on our different datasets when using raw orthogonal projection and our 1% operator. Note that we do not use 2% anymore, this choice will be justified at the end of this section. We also show the errors without projection for reference. We see that in all cases the best results are obtained by the new proposed projection. The increase of accuracy with respect to the raw projection is not very significant but we should keep in mind that this raw projection should not be used because it does not preserve the smoothness of the curve. Comparing when no projection is performed the proposed operator increases, in this simulation, the accuracy between 1% and 12%. We must also say that this increment will be typically bigger when more noise is introduced on the system. In this simulation, the only source of noise is the quantisation of the signals on 12 bits which is considered as a good signal-to-noise ratio.

Table 4-4. RMS errors using different projection operators

	MacbethDC	Kremer	Selected Artists	Restoration	Munsell
NO projection	0.0001884	0.0010815	0.0006915	0.0006445	0.00015385
Raw projection	0.0001869	0.0008841	0.0006439	0.0005656	0.00015377
Spline (1%)	0.0001858	0.0008697	0.0006365	0.0005555	0.00015365

A last consideration can be done. It concerns the choice of the % parameter on the proposed operator. A priori we do not know if the value 1% is better than 2% or 3%. We know that the parameter cannot be big, 15% for instance would be too strong as the operator would modify 30% of the curve. However, this parameter can be easily optimised using a test dataset. The value of the parameter giving the smallest RMS error on the test dataset can be kept as a solution. In the case of data presented in Table 4-4, 1% was the selected value.

4.4 Conclusion

We have described two original improvements for existing reconstruction techniques which we propose to the multispectral community.

The proposed algorithm to improve generalisation on linear reconstruction techniques using a priori information appears very efficient. The presented simulation results provide an improvement of 50% of accuracy on the test sets used. This is a very good and promising result. The idea of intense random resampling to increase the generalisation capabilities of the reconstruction is well justified by these results. In addition, the idea itself is interesting and opens new research perspectives. For instance, the problem of selecting a subset of important spectral reflectance curves among a set of curves can be studied by this means. The kernel of spectral curves selected by the algorithm is worth to be carefully studied on the future.

Regarding the problem of reconstructing curves that respect physical constraints, we have proposed a spline projection operator. This operator is simply applied after reconstruction and appears as a straightforward complement to any existing reconstruction technique. Its increment of reconstruction accuracy is not very significant, 12% in best cases of our simulations. But it guarantees that the obtained curves are bounded and at the same time smooth.

Chapter 5:

Spectral Reconstruction using Mixture Density Networks

Contents

5.1	Introduction	93
5.2	Spectral Reconstruction with non linear operators	94
5.3	Introduction to Neural Networks.....	96
5.3.1	Feed-forward Backpropagation Neural Networks.	96
5.3.2	A single Neuron.	97
5.3.3	Learning Laws.....	97
5.3.4	Multi-layer feed-forward network.....	101
5.3.5	Generalized Delta Rule.	103
5.3.6	Algebraic description of a multilayer network.....	106
5.4	Neural Networks and Spectral Reconstruction	107
5.5	Mixture Density Networks.....	110
5.5.1	Training a Mixture Density Network.....	112
5.6	Estimating Spectral Reflectances with Mixture Density Networks.....	115
5.6.1	Architecture Optimisation	116
5.6.2	Method Testing	118
5.6.2.1	Testing on Simulated Data	119
5.6.2.2	Testing on Real Data	120
5.7	Spectral Reconstruction Software	124
5.8	Conclusion.....	125

5.1 Introduction

We consider the problem of the reconstruction of spectral reflectance curves from multispectral images using techniques based on neural networks.

In the particular case of colour images the number N of channels is limited to three. Efforts have been made in order to characterize spectral reflectances using just three colour channels. Some authors have proposed linear methods, as [Kotera et al., 1996]. Others have proposed non-linear approaches using neural networks, see for instance [Arai et al., 1996] and [Sato et al., 1999] where spectral characterization is performed from RGB and YMC tristimulus values. On the other hand, neural networks have also been used for other purposes in colorimetry, see for instance [Tominaga, 1999].

In our case, we consider multispectral images with a higher number of channels ($N > 3$) and we aim for a more precise spectral reconstruction than a raw estimation just satisfactory for subjective colour reproduction purposes. Various methods (splines, modified discrete sine transform (MDST), pseudo-inverse, smoothing inverse or Wiener inverse) have already been proposed and are described on Chapter 3.

In this chapter we consider non-linear reconstruction approaches based on neural networks. Our aim is to find a non-linear learning-based method able to provide noise resistance and good generalization. We firstly justify in section 5.2 the use of non-linear operators for spectral reconstruction. A general introduction on the subject of neural networks is presented in section 5.3. Afterwards, section 5.4 describes our first attempt to use neural networks as a spectral reconstruction method, proposed in the paper [Ribés et al., 2002]. We studied the resistance to quantization noise of the spectral reconstruction obtained with different conventional neural networks and compared them with a linear method already used for spectral reconstruction of fine art paintings in [Hardeberg et al., 1999]. Finding not adapted the raw application of neural networks for spectral reconstruction, we developed a new method mixing these techniques with Principal Components Analysis (PCA) that obtains good results on presence of quantization noise.

Aiming to increase the performance of the existing methods we apply Mixture Density Networks in the context of spectral reconstruction. The technique is described in section 5.5. This approach has been initially presented by the authors in a conference [Ribés and Schmitt, 2002], an extended paper was published in [Ribés and Schmitt, 2003]. The application of Mixture Density Networks to the problem of spectral reconstruction is presented in section 5.6, along with a description of how the problem of architecture optimisation has been solved. This last point makes the final method fully automatic with no parameters to be fixed by hand.

5.2 Spectral Reconstruction with non linear operators

Before starting to describe the non-linear methods which we applied to the problem of spectral reconstruction, a fundamental question arises before solving this problem: “why should we use non-linear methods while the nature of the physical underlying problem is mainly linear?”. This section aims to give a justification to this issue.

We recall some basic facts and formulas already introduced on Chapter 2. Supposing a linear optoelectronic transfer function of the acquisition system, the camera response c_k for an image pixel is equal to:

$$c_k = \int_{\lambda_{\min}}^{\lambda_{\max}} r(\lambda) w_k(\lambda) d\lambda + n_k \quad (5.1)$$

where $r(\lambda)$ is the spectral reflectance of the object surface imaged in a pixel, $w_k(\lambda)$ denotes the spectral sensitivity of the k -th channel, and n_k is the additive noise. The assumption of system linearity comes from the fact that the CCD sensor is inherently a linear device. However, as we already said, for real acquisition systems this assumption may not hold, for example due to electronic amplification non-linearities or stray light in the camera. Then, appropriate nonlinear corrections may be necessary. By modelling the nonlinearities of the camera as

$$\tilde{c}_k = \Gamma\left(\int_{\lambda_{\min}}^{\lambda_{\max}} r(\lambda) w_k(\lambda) d\lambda + n_k\right), \quad (5.2)$$

we may obtain the response:

$$c_k = \Gamma^{-1}(\tilde{c}_k) \quad (5.3)$$

of an ideal linear camera by inverting the function Γ . At this point we want to introduce some practical concepts affecting this theoretical representation of the system:

- First of all the modelling of the function Γ implies the characterization and the careful study of the behaviour of the CCD. Moreover, CCDs are not perfectly produced and not all its photosensitive elements have the same response. A characterization is possible in a scientific environment where there exists the time, the necessary tools and knowledge for this to be performed. Of course, any correction always leaves residual errors, on some cases the correction is not performed and the error is assumed.
- There is an important consideration about noise. When the noise level in (5.1) is small compared to the other elements on the equation the linear behaviour can be assumed. When noise starts to be stronger it is not evident if the system can be considered linear. We have already seen linear methods of spectral reconstruction taking noise into account. We could have a different regard on the problem and consider that the introduction of random variables on the system make the system “less linear”.
- We remark that in our description of the camera the time never appears on the equations. We implicitly consider the phenomenon to be not affected by time. But acquiring two multispectral images at two different times leads to different images. Lots of factors are the consequence of this variability that can be bigger or smaller depending on the particular system. For instance, failures in the temporal stability of

light sources on their spectral and/or spatial characteristics are normally a source of errors. But others exist too.

These considerations lead to two different strategies when dealing with any image acquisition system. We can characterize and correct all factors that introduce errors and non-linearities on the system. But we can also increase the resistance of the post-treatment methods to these defaults. It is this approach that we propose in this chapter by the introduction of non-linear techniques.

As we already saw on Chapter 3 the aim of the spectral reconstruction is to find an operator \mathbf{Q} that performs the transformation

$$\hat{\mathbf{r}} = \mathbf{Q} \mathbf{c} \quad (5.4)$$

where $\mathbf{c} = [c_1 \ c_2 \ \dots \ c_K]^t$ is a vector representing the response to all K filters, $\mathbf{r} = [r(\lambda_1) \ r(\lambda_2) \ \dots \ r(\lambda_N)]^t$ is a vector containing the sampled spectral reflectance and $\hat{\mathbf{r}}$ is its estimate. Operator \mathbf{Q} has been always described linearly on the multispectral imaging community, but looking at the above equation (5.4) we can imagine that \mathbf{Q} could be non-linear.

The concept of operator being mathematically broad it refers normally to a mapping between two functional spaces. In our case these spaces are Hilbert spaces. We explore in this chapter the use of neural network as this desired non-linear operator \mathbf{Q} . We will not make considerations about other possible non-linear approaches.

5.3 Introduction to Neural Networks

Neural Networks are fundamental in the new spectral reconstruction methods investigated in this thesis. This section intends to give a brief introduction to the well known backpropagation Neural Network and it is included for completeness. This kind of network is the first and most classical one and abundant documentation can be found in the scientific literature. If the reader is already familiar with Neural Networks we recommend him to skip this whole section.

First of all, when we are talking about a neural network, we should more properly say "artificial neural network" (ANN), biological neural networks are much more complicated than the mathematical models we use for ANNs. In fact, some ANNs are models of biological neural networks and some are not, but historically, much of the inspiration for the field of ANNs came from the desire to produce artificial systems capable of sophisticated, perhaps "intelligent", computations similar to those that the human brain routinely performs, and thereby possibly to enhance our understanding of the brain. In our case, we use ANN just as a tool and the models described in this chapter are very simple compared with others developed in order to understand biological models. Moreover we apply models that have already been studied and that can be easily found in the ANN literature. Our interest is the application of these models to the problem of spectral reflectance reconstruction. In the following of this chapter we will abuse of the term Neural Network and we will use it instead of ANN.

There is no universally accepted definition of a Neural Network. But perhaps a Neural Network could be defined as a network of many simple processors (*neurons*), these neurons are connected by communication channels (*connections*) which usually carry numeric data, encoded by various means. The neurons operate only on the inputs they receive via the connections.

Most Neural Networks have some sort of *training rule* whereby the weights of connections are adjusted on a set of training data. In other words, Neural Networks "learn" from examples and exhibit some capability for generalization beyond the training data. These two characteristics of ANN are useful in the context of our application as we will see later in this chapter.

Neural Networks normally have great potential for parallelism, since the computations of the components are largely independent of each other. The models we will use provide this possibility, but at the moment we do not consider a parallel implementation of our Neural Networks even if remains an open possibility that could provide us with a very fast reconstruction method.

5.3.1 Feed-forward Backpropagation Neural Networks.

In the 1980's after a disappointing period for neural networks [Rumelhart and McClelland, 1986] published their classical book and their new paradigm settled as a new basis for cognitive science. Much cognitive oriented research turned to this new paradigm. One of the main achievements was the analysis of multi-layer networks and their learning capabilities.

A multi-layer feed-forward networks is composed of several layers of neurons. One layer is fully connected with its adjacent layers. It receives input coming from his layer directly below and send his output to the layer directly above. But first of all the reader should understand how a single neuron works.

5.3.2 A single Neuron.

A neuron in a multi-layer feed-forward network is a processing unit that accepts several input signals (a vector of scalar numbers) and produces a single output signal that is a scalar number. Neuron activity can be view as a two steps process:

- First of all, every input signal is multiplied by a weight (scalar number) associated to his channel. Obtained coefficients are summed together afterwards and, in general, there exists a bias term that can be seen as a special channel with a constant input of value 1. If we note w_i the weight of channel i , x_i the signal of channel i , n the number of input channels and θ the bias term. The neuron's net output is defined as:

$$net = \sum_{i=1}^n w_i x_i + \theta . \quad (5.5)$$

- The second step consist in the so called activation function. In fact, we apply a function to the result coming from the first step leading to the neuron's real output. The activation function can be linear or non-linear and that produces important differences in the capabilities of a neural network. In fact, the introduction of non-linear activation functions in the 80's was one of the reasons that lead neural networks to became so popular.

If we note F the activation function the neuron's activity is expressed as:

$$y = F \left(\sum_{i=1}^n w_i x_i + \theta \right) . \quad (5.6)$$

In *Figure 5-1* a graphic representation of a single neuron is shown.

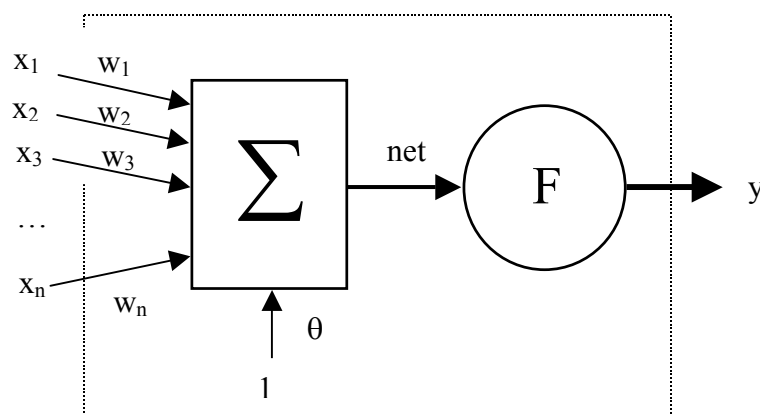


Figure 5-1. Graphic representation of the activity of a single Neuron.

5.3.3 Learning Laws.

This document just deals with *supervised learning* for the problem of spectral reconstruction. Then, no references or information will be mentioned about neural networks and *unsupervised learning* methods. Even if this field is large and very popular, the basic learning paradigm

does not fit the problems we treat, since we have a priori knowledge on the spectral reflectance curves of pigments that we want to reconstruct.

There exist a variety of *supervised learning laws* which are in common use. These laws are mathematical algorithms used to update the connection weights. Most of these laws are variations of the Hebb's Rule. Human understanding of how neural processing actually works is very limited and learning is certainly more complex than the simplification represented by the learning laws currently developed. In any case, they appear useful for practical purposes. A few of the major laws are given as an example below.

- Hebb's Rule.
The first and the best known learning rule was introduced by Donald Hebb, [Hebb, 1949]. This basic rule is: if a neuron receives an input from another neuron, and if both are highly active, the weight between the neurons should be strengthened.
- Hopfield Law.
This law is similar to Hebb's Rule with the exception that it specifies the magnitude of the strengthening or weakening. It states, "if the desired output and the input are both active or both inactive, increment the connection weight by the learning rate, otherwise decrement the weight by the learning rate." Most existing learning functions introduce a learning rate, or a learning constant. Usually this term is positive and between zero and one.
- The Delta Rule.
It is a further variation of Hebb's Rule, and it is one of the most commonly used. This rule is based on the idea of continuously modifying the strengths of the input connections to reduce the difference (the delta) between the desired output value \bar{y} and the actual output y of a neuron. This rule changes the connection weights in the way that minimizes the mean squared error of the neuron.

A single network learns by modifying its weights depending on its objective. This objective can be classifying elements into classes, performing a mapping between two spaces, etc. The learning rules specify how to calculate the modification of the weights based on the objective. The general framework for neuron learning is described in the next paragraphs.

Training a neuron is an iterative procedure based on the modification of its weights and bias (which is a special kind of weight for a constant input), formally:

$$w_i(t+1) = w_i(t) + \Delta w_i(t) \quad (5.7)$$

$$\theta(t+1) = \theta(t) + \Delta \theta(t) \quad (5.8)$$

Suppose we have a set of learning samples consisting of input vectors \mathbf{x} and the corresponding desired output $\bar{y} \in \mathbb{R}$. The general algorithm for supervised training states as follows:

1. Start with random weights for the connections.
2. Select an input vector \mathbf{x} from the set of training samples.
3. Calculate $\Delta w_i(t)$ according to a learning rule. $\Delta \theta(t)$ is considered as a weight and modified in the same way.
4. Go back to 2.

As an example of a simple learning rule we can consider the *Perceptron learning rule*. The Perceptron was proposed by [Rosenblatt F., 1962] and was of great importance for the evolution of neural networks. Even if it is something more complex than the neuron we have presented we can show how it works in a single neuron with a threshold activation function as follows,

$$F(net) = \begin{cases} 1 & \text{if } net > 0 \\ -1 & \text{otherwise} \end{cases} \quad (5.9)$$

In that case this rule calculates the deltas in the following way:

- If $y \neq \bar{y}$ (the Perceptron gives an incorrect response) modify all connections w_i according to $\Delta w_i = \bar{y}x_i$.
- As θ is considered a weight connection with a constant input signal 1, we obtain,

$$\Delta \theta = \begin{cases} 0 & \text{if } y = \bar{y} \\ \bar{y} & \text{otherwise} \end{cases} \quad (5.10)$$

This procedure is basically the application of the Hebb's rule, but when the neuron responds correctly no weights are modified. On the other hand, a convergence theorem exists for such learning rule, which states:

If there exists a set of connection weights w^ which is able to perform the transformation $y = \bar{y}$, the perceptron learning rule will converge to some solution (which may or not be the same as w^*) in a finite number of steps for any initial choice of the weights.*

The Perceptron learning rule is a good historical and easy example of a learning law, but it is not the most used one. In fact, *the delta rule* developed by [Widrow and Hoff, 1960], an application of the Least Mean Square (LMS) method, is probably the most commonly used learning rule. For a given input vector, the output vector is compared to the correct answer. If the difference is zero, no learning takes place; otherwise, the weights are adjusted to reduce this difference. The change in weight from $w_i(t)$ to $w_i(t+1)$ is given by:

$$\Delta w_i = \gamma \delta x_i, \quad (5.11)$$

where γ is the learning rate and δ is the difference between the expected output and the actual output of the neuron, $\delta = \bar{y} - y$.

The delta rule is trivially extended to neural networks with just one layer of neurons with linear activation functions and with no hidden units (hidden units are found in networks with more than two layers). The LMS error when represented versus the weights takes a parabolic form in the weights space. Since the proportionality constant is negative, the graph of such a function is concave upward and has a minimum value. The vertex of this paraboloid represents the point where the error is minimized. The weight vector corresponding to this point is then the ideal weight vector.

This learning rule not only moves the weight vector nearer to the ideal weight vector, it does so in the most efficient way. The delta rule implements a gradient descent by moving the weight vector from the point on the surface of the paraboloid down towards the lowest point, the vertex.

Formally, we can see this gradient descent clearly by considering the following error function to be minimized:

$$E = \sum_p E^p = \frac{1}{2} \sum_p (\bar{y}^p - y^p)^2, \quad (5.12)$$

where E^p represents the error on pattern p , d^p is the desired target output, and y^p is the actual output. We recall that a pattern is a vector of dimension n , its associated delta being $\delta^p = \bar{y}^p - y^p$.

From the expression of the error on pattern p , E^p , we deduce

$$\frac{\partial E^p}{\partial y^p} = -\delta^p. \quad (5.13)$$

The activation function $y^p = \sum_i w_i x_i + \theta$ being linear, we have

$$\frac{\partial y^p}{\partial w_i} = x_i. \quad (5.14)$$

For one pattern p , the delta rule being $\Delta_p w_i = \gamma \delta^p x_i$ equations (5.13) and (5.14) provides to us the following equation

$$\Delta_p w_i = -\gamma \frac{\partial E^p}{\partial y^p} \frac{\partial y^p}{\partial w_i}, \quad (5.15)$$

that is a gradient descent of the error function, E , versus the weights w_i . This clearly appears after applying the chain rule of calculus as follows:

$$\frac{\partial E}{\partial w_i} = \sum_p \frac{\partial E}{\partial y^p} \frac{\partial y^p}{\partial w_i}. \quad (5.16)$$

Each sample being considered as independent, we have $\frac{\partial E}{\partial y^p} = \frac{\partial E^p}{\partial y^p}$. We then deduce the following expression of the gradient of E :

$$\frac{\partial E}{\partial w_i} = \sum_P \frac{\partial E^P}{\partial y^P} \frac{\partial y^P}{\partial w_i} = -\frac{1}{\gamma} \sum_P \Delta_P w_i \quad (5.17)$$

The mean value of the delta rule on the p pattern is then proportional to the gradient of the error function.

As a consequence, in the case of linear activation functions where the network has no hidden layers, the delta rule will always find the best set of weight vectors. However, it is not the case for hidden neurons belonging to a hidden layer: the error surface is no more a paraboloid and generally does not have a unique minimum point. There is no such powerful rule as the delta rule for networks with hidden units. There have been a number of theories in response to this problem. These include the generalized delta rule that we will see later in that section.

5.3.4 Multi-layer feed-forward network.

In a typical multi-layer feed-forward neural network the first level connects the input variables and is not considered as a layer, that is because no operation is performed at this level. The last layer connects the output variables and is called the output layer. Layers in-between the input level and the output layer are called *hidden layers*; there can be more than one hidden layer. All connections are *feed forward*; that is, they allow information transfer only from an earlier layer to the next consecutive layer. The processing units are the neurons as already discussed in previous sections; each of them is connected to the neighboring layer units. The parameters associated to each of these connections are called weights. Neurons within a layer are not interconnected, and neurons in non adjacent layers are not directly connected. Each node j receives incoming signals from every node i in the previous layer and each incoming signal x_i is associated to a weight w_{ij} .

We can see a diagram of a two layers network in Figure 5-2. It consists on three inputs, four neurons on the hidden layer and two neurons in the output layer. In this example the hidden neurons are organized in one single hidden layer, but we could have a neural network with several hidden layers.

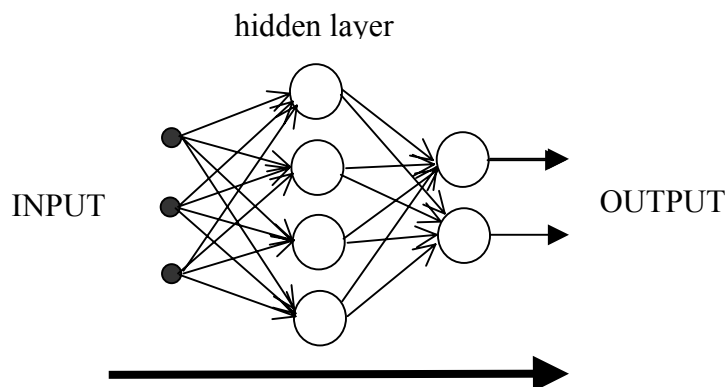


Figure 5-2. Multilayer feed-forward neural network.

The major advantage of multilayer networks is that they can theoretically carve a pattern space into an arbitrary number of decision regions and therefore solve any pattern classification problem. Furthermore, it can be shown that such networks are also universal function approximators; that is, they are able to solve any function approximation problem to an arbitrary degree of precision. It should be noted that although these proofs of function approximation are theoretically powerful, they are not necessarily tractable from a practical sense. The reason for this is two-fold:

- (i) in order to determine the requisite weights for the model, these proofs assume a highly representative sample of the range and domain of the function, and
- (ii) no completely effective procedure is given for arriving at the requisite set of weights.

One of the most appreciated characteristics of multi-layer networks is their ability to learn. Various training techniques have been proposed as the historical one by [Widrow and Hoff, 1960]. We will not enter in cumbersome details but they were all limited to training only one layer of weights while keeping the other layers constant. A general learning rule for networks of arbitrary depth was desired, such that a relatively simple network with a generic learning algorithm could be applied to a wide-range of different tasks.

It must be said that a multi-layer network using linear activation functions is not more powerful than a one-layer linear network. That is because a linear combination of linear systems remains a linear system. Consequently neuronal networks use, in general, non linear activation functions, at least in one hidden layer. One of the most popular non-linear activation function is the sigmoid:

$$\text{sigmoid}(x) = \frac{1}{1 + e^{-kx}} \quad (5.18)$$

where k is a parameter that controls how quick a transition is perform between zero and one. This function closely relates with a threshold function but has the advantages of being non-linear, monotonically increasing and has a smooth first derivative that is easy and quick to calculate. If $k=1$ its gradient (negative first derivative) can be expressed in a recursive form:

$$-\frac{d}{dx} \text{sigmoid}(x) = \text{sigmoid}(x)(1 - \text{sigmoid}(x)) \quad (5.19)$$

or in a numerically stable way as

$$-\frac{d}{dx} \text{sigmoid}(x) = \frac{\text{sigmoid}(x)}{(1 + e^{-x})} \quad (5.20)$$

Figure 5-3 shows a graph of the sigmoid function and its derivative.

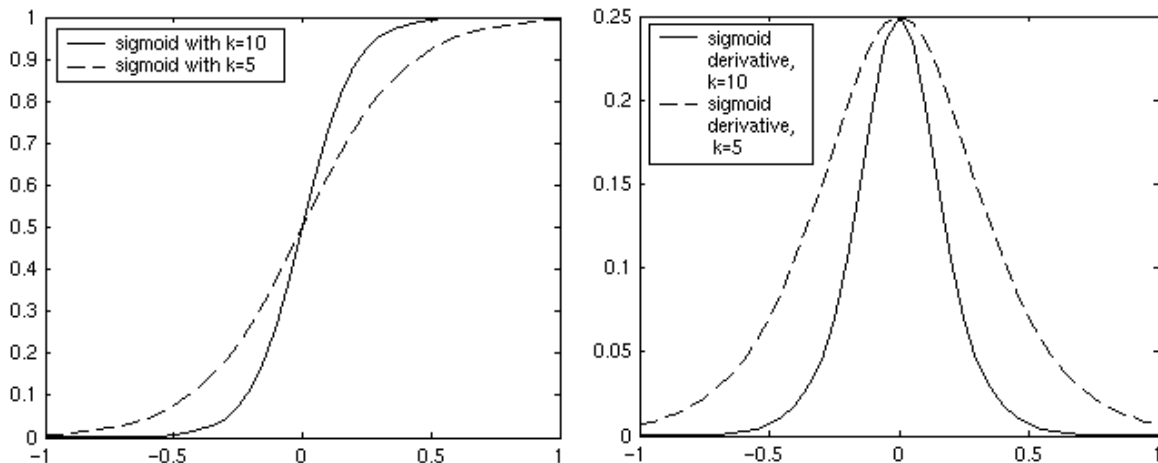


Figure 5-3. Sigmoid function(left panel) and its derivative (right panel).

The next section introduces the Generalized Delta Rule, also known as the standard backpropagation algorithm.

5.3.5 Generalized Delta Rule.

The generalized delta rule can be considered as one of the most significant contributions to the neural networks research. It has allowed the training of multilayer networks. As the name implies, it is a generalization of the Delta Rule for training networks with a total number of layers L greater than one: $L > 1$. The training procedure, however, is commonly referred to as backpropagation of error, or simply backpropagation.

Since we are now considering neurons with non-linear activation functions we must generalize the already presented delta rule. The activation is now a differentiable function, F , of the net input:

$$y_j^p(l) = F(\text{net}_j^p(l)), \quad (5.21)$$

where l is the number of the current layer $l \in \{1, \dots, L\}$, the quantities net_j^p and y_j^p are the outputs before and after activation of the j -th neuron of the l layer. They are converted into functions that depend on the number of layer to explicitly reinforce the concept of layer that is fundamental on the understanding of backpropagation. To correctly generalize the already presented delta rule the variation of the weights is set proportionally to the gradient of E^p :

$$\Delta_p w_{ij}(l) = -\gamma \frac{\partial E^p}{\partial w_{ij}(l)}. \quad (5.22)$$

In (5.22), the error criteria E^p is defined as the total quadratic error for a pattern p at the output layer L :

$$E^p = \frac{1}{2} \sum_{j=1}^{N_L} (\bar{y}_j^p - y_j^p(L))^2, \quad (5.23)$$

where \bar{y}_j^p is the desired output or target for neuron j in the output layer L when pattern p is evaluated, and N_L is the number of neurons in the output layer. At the same time the gradient can be decomposed by the chain rule of calculus giving to:

$$\frac{\partial E^p}{\partial w_{ij}(l)} = \frac{\partial E^p}{\partial \text{net}_j^p(l)} \frac{\partial \text{net}_j^p(l)}{\partial w_{ij}(l)} = \frac{\partial E^p}{\partial y_j^p(l)} \frac{\partial y_j^p(l)}{\partial \text{net}_j^p(l)} \frac{\partial \text{net}_j^p(l)}{\partial w_{ij}(l)}. \quad (5.24)$$

By the formula that calculates the net output of a neuron we deduce:

$$\frac{\partial \text{net}_j^p(l)}{\partial w_{ij}(l)} = y_i^p(l-1), \quad (5.25)$$

and by defining $\delta_j^p(l) = -\frac{\partial E^p}{\partial net_j^p(l)}$ we obtain the delta rule as already found in the case of a single neuron:

$$\Delta_p w_{ij}(l) = \gamma \delta_j^p(l) y_i^p(l-1). \quad (5.26)$$

But the above formula is not new, it is just the delta rule using a slightly different notation that includes a subindex identifying the layer in which we apply this rule. The real innovation is how to calculate the δ 's for every layer. Let's think just about the last layer and suppose that the activation function is linear, the delta rule will be calculated as already seen. But, for the hidden layer immediately below the last layer we cannot apply the delta rule because we do not know the error at the output of this layer, neither the values of δ 's for this layer. This big limitation was solved by propagating error signals backwards through the network in a procedure that is called backpropagation of errors.

Let's see formally how backpropagation works. In order to compute δ_j^p we apply the chain rule as the product of two factors, which reflect the change in error as a function of the output unit and of the input respectively. Thus, we have

$$\delta_j^p(l) = -\frac{\partial E^p}{\partial net_j^p(l)} = -\frac{\partial E^p}{\partial y_j^p(l)} \frac{\partial y_j^p(l)}{\partial net_j^p(l)} \quad (5.27)$$

The second factor correspond to the activation function derivative for the j th neuron:

$$\frac{\partial y_j^p(l)}{\partial net_j^p(l)} = \frac{d}{dx} F(net_j^p(l)) \quad (5.28)$$

For computing the first factor it exists two different cases:

- For the output layer, $l=L$ and for the definition of E^p it follows that

$$\frac{\partial E^p}{\partial y_j^p(L)} = -(\bar{y}_j^p - y_j^p(L)) \quad (5.29)$$

And the δ 's can be calculated as:

$$\delta_j^p(L) = (\bar{y}_j^p - y_j^p(L)) \frac{d}{dx} F(net_j^p(L)) \quad (5.30)$$

- We consider a hidden layer l , $l < L$. We do not directly know the contribution of the layer to the output error of the network. However, the error measure can be written as a function of the net inputs from the hidden layers to the output layer:

$$E^p = E^p(net_i^p(1), i \in \{1..N_1\}, \dots, net_i^p(l), i \in \{1..N_l\}, \dots), \quad (5.31)$$

and we use the chain rule for writing

$$\frac{\partial E^p}{\partial y_i^p(l)} = \sum_{j=1}^{N_{l+1}} \frac{\partial E^p}{\partial net_j^p(l+1)} \frac{\partial net_j^p(l+1)}{\partial y_i^p(l)} \quad (5.32)$$

According to the equations (5.27), and using equations (5.28) and (5.32) the δ 's can be calculated as:

$$\begin{aligned} \delta_i^p(l) &= \frac{\partial E^p}{\partial y_i^p(l)} \frac{\partial y_i^p(l)}{\partial net_i^p(l)} \\ &= \sum_{j=1}^{N_{l+1}} \frac{\partial E^p}{\partial net_j^p(l+1)} \frac{\partial net_j^p(l+1)}{\partial y_i^p(l)} \frac{\partial y_i^p(l)}{\partial net_i^p(l)} \\ &= \sum_{j=1}^{N_{l+1}} \delta_j^p(l+1) w_{ij}^p(l+1) \frac{d}{dx} F(net_i^p(l)) \end{aligned} \quad (5.33)$$

The formulas above give a recursive procedure for calculating the δ 's backwards through the network in the sequence of $L, L-1, \dots, l, \dots, 1$. We can summarize one iteration of the network training in the following algorithm:

For every pair of samples (p, \bar{y}_j^p) in the training set **do**

1. *FORWARD PASS: The weights are fixed and input signals propagate through the network, outputs are calculated. Actual outputs $y_j^p(L)$ are compared with desired outputs \bar{y}_j^p ; the error signal $(\bar{y}_j^p - y_j^p(L))$ is computed.*
2. *BACKWARD PASS: Starting with the output layer recursively computes the local gradient $\Delta_p w_{ij}(l)$ of equation (5.22) for each neuron in each layer. The δ 's are calculated using equation (5.30) for the output layer and equation **Erreur ! Source du renvoi introuvable.** for the hidden layers in descending order. Then the weights are updated using this gradient and equation (5.26).*

End For.

The generalized delta rule allows multi-layer networks to be trained on any information processing problem. However, many limitations still exist with the generic multi-layer feed-forward neuronal network architecture. One problem is that the general delta rule searches through an error space using gradient descent; although gradient descent on average moves towards a minimum it is not guaranteed to move towards a global minimum. There are techniques for trying to improve this. In fact, currently, not many researchers or engineers use neural network backpropagation as described above because these gradient descend limitations. But other more efficient global or local minimization methods are used following the same backpropagation inspiration. We can apply these different methods for calculating the weight increments or/and the δ 's in the backpropagation process. Techniques as conjugate gradient, Levenberg-Marquardt, momentum, simulated annealing, genetic algorithms and in general any function minimization procedure can be used. Describing further these possible

methods applied to multi-layer feed-forward networks is out of the scope of this introduction. But the procedure is highly similar as the one shown for the gradient descend.

5.3.6 Algebraic description of a multilayer network

A feed-forward neural network can be simply described using linear algebra. This change of notation reduces the number of indexes and sum operation and can be used to simplify cumbersome notation. We included here mainly because the vector-matrix expression of a neural network are generally used for implementation and simulation purposes. This gives insight on the method complexity.

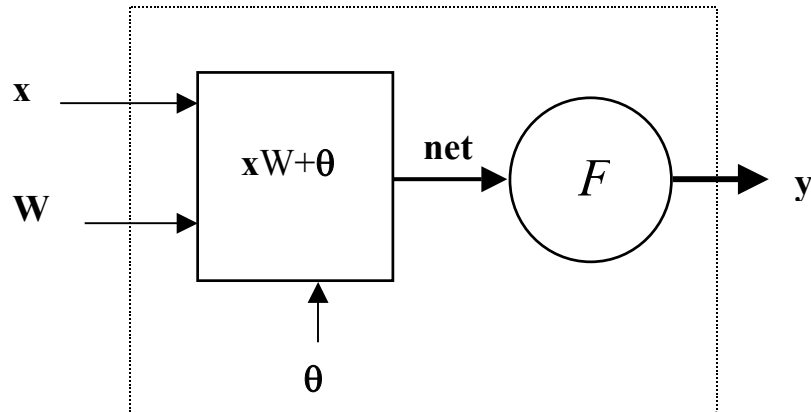


Figure 5-4. Graphic representation of the activity of a layer of a feed-forward neural network using algebraic notation.

In a network the operation of a layer can be expressed in terms of linear algebra in a very similar way as the operation of a neuron. Let's note \mathbf{x} the vector containing all signals arriving to the layer, \mathbf{w}_j is a vector containing all the weights on one neuron where $j=1..N_l$ indexes the neurons on a layer l . If we define \mathbf{W} as a matrix containing vectors \mathbf{w}_j on its columns, $\mathbf{W} = [\mathbf{w}_1 \ \mathbf{w}_2 \ \dots \ \mathbf{w}_{N_l}]$, the net output of the layer is made by:

$$\mathbf{net} = \mathbf{x} \mathbf{W} + \boldsymbol{\theta}, \quad (5.34)$$

where \mathbf{net} is a vector containing the net output, and $\boldsymbol{\theta}$ is the bias vector. In this framework the activation functions is not scalar anymore and becomes a function acting over a vector. Consequently the complete layer activity becomes:

$$\mathbf{y} = F(\mathbf{net}). \quad (5.35)$$

We have at the moment described the operation of a single layer using linear algebra. The operation of the whole neural network is a merely extension of several layers. Introducing l , an index that indicates the number of layer is enough to characterize the network activity.

5.4 Neural Networks and Spectral Reconstruction

Our first approach to the application of non-linear operators for spectral reconstruction was the use of classical backpropagation networks. We tested these approach using simulations as the ones presented on Chapter 3. We started by mapping a virtual 7 channels camera signal to a vector of dimension 37 via a neural network with one hidden layer of neurons. The backpropagation networks used sigmoid functions as activation functions in the hidden and output neuron layers. For simplicity, we chose a linear reconstruction method as a reference for efficiency. We chose the method representing the paradigm of *indirect* reconstruction (Chapter 3, Section 3.2.2) because it belongs to the same approach, both of them mapping a dataset of known camera responses to a corresponding dataset of spectral reflectances. Moreover, this linear method was already introduced as the basic one representing this problem.

Because our aim is the reconstruction of spectral reflectances of pigments, comparisons on this chapter are performed over the following databases: “Kremer” database containing 184 spectral curves of pigments produced by Kremer Pigmente, Germany, “Selected Artists” database containing 67 pigments chosen among a collection of artist’s paintings, “Restoration” database containing a selection of 64 pigments used in oil painting restoration and “Munsell” database containing 1269 matte Munsell colour chart samples.

When using backpropagation neural networks, we found a good reaction over the spectral error, specially in presence of quantization noise, but the reaction over the CIELAB space was not satisfactory compared to the pseudo-inverse based approach.

Radial basis neural networks were tested too. We do not give a description of this kind of neural networks here because it could be cumbersome, if interested the reader can refer to any textbook on neural networks. They have the main advantage of a non iterative and very fast training, but have the drawback of being more sensitive to new data not well represented by the training set. Although the spectral reconstruction results were good without noise the resistance to noise was poor, and we had the same reaction as backpropagation neural networks on the CIELAB space.

This different behaviour of backpropagation and radial basis neural networks over the spectral reconstruction error and the CIELAB error was studied in order to better understand its origin. We found that signed errors in the spectral space are not as centred as in a linear approach, their spectral reconstruction presenting a systematic bias. Consequently, even if the spectral error is small as this error is biased the delta CIELAB error is bigger than in the linear case where the oscillations in the reconstructed curves compensate the error when performing colorimetric calculations. We should not forget that the relationship between spectral curves and CIELAB quantities is not linear.

Because of the systematic bias our first approaches using backpropagation and radial basis neural networks were abandoned. Hence, we will not present any results concerning these initial tests. But we tried to understand why neural networks perform no better than the pseudo-inverse based method over the spectral space. We found the used linear method to have an equally good response over the used spectral databases if noise is not present. As we already saw on Chapter 2 (*Nature of Data*), spectral reflectances of oil pigments are smooth bandlimited functions. It is important to keep in mind the performed principal component analysis (PCA) over the used spectral databases. In Table 2-2 of Chapter 2 we show the results that indicate the dimension of the orthogonal basis needed to keep 90% and 99% of signal variance. This is useful if we want to reduce the number of coefficients representing a

reflectance curve, various linear approaches have been proposed where different specific basis functions are used, see [Sato et al., 1999] or [Eem et al., 1994].

The PCA analysis is not enough by itself to explain the behaviour of the neural networks against the pseudo-inverse method. The already introduced Frobenius distance can give insight on this matter. We remind that it is calculated as:

$$d_F(\mathbf{A}, \mathbf{B}) = \sqrt{\sum_i^n \sum_j^m (a_i^T b_j)^2}, \quad (5.36)$$

where \mathbf{A} is a $l \times m$ matrix, \mathbf{B} a $l \times n$ matrix, a_i a column vector of \mathbf{A} and b_j a column vector of \mathbf{B} , a_i and b_j both belonging to the same vectorial space of dimension l . The calculated square of the Frobenius distance among the reduced orthogonal set of PCA vectors associated to the used spectral databases and keeping signal variance at 90% or 99% are shown in in Table 2-3 and Table 2-4 respectively (in Chapter 2).

The three used oil pigment databases are surprisingly related, most signals of these databases are linear combinations of the other databases. The Munsell database is closely related too. Consequently, we believe the pseudo-inverse reconstruction method works equally well on the different databases because of their highly linear dependencies. Neural networks being non linear methods, their results on a given database are normally worst than those obtained for the training database.

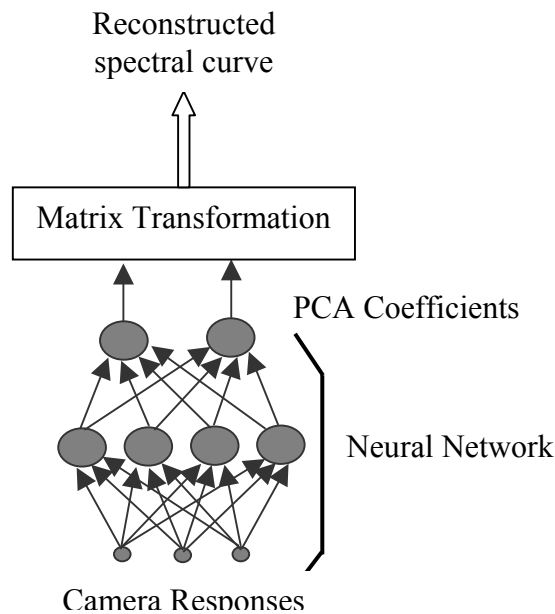


Figure 5-5. PCA Neural Network.

In order to study the robustness of these methods in presence of noise, several levels of quantization on the camera channels have been introduced. We observed that the pseudo-inverse has very bad resistance to quantization noise and conversely a good reaction of neural networks. Looking for a compromise we trained several neural networks not directly over the spectral space but for estimating the coefficients associated to the orthogonal eigenvectors obtained from a PCA analysis keeping 99% of signal variance. A graphical diagram of this method of reconstruction is shown on Figure 5-5. Backpropagation neural networks were

trained much faster using this PCA data reduction (noted PCA NN) because their output layer becomes smaller. They provide also better global results as shown in Table 5-1.

In Table 5-1 we observe that if quantization noise is small the pseudo-inverse performs better except for the database on which the neural network has been trained. In contrast, the PCA neural network provides clearly better results in presence of quantization noise either over the spectrum or over the CIELAB space. The CIELAB errors are shown on Table 5-2. The degradation of the pseudo-inverse in presence of noise is obvious. We note that this modified neural network has equivalent behaviour over the spectral and CIELAB spaces. That is because the orthogonal eigenvectors are smooth oscillating curves. The signed error oscillates around the mean error in a similar way as in the pseudo-inverse method and the bias found for the first neural network approaches is not a problem anymore.

Table 5-1. Spectral Error over different databases.

8 bits quantization	pinv	PCA NN
Kremer	0.0264	0.0195
Selected Artists	0.0222	0.0116
Restoration	0.0218	0.0147
Munsell	0.0188	0.0187
10 bits quantization	pinv	PCA NN
Kremer	0.0142	0.0182
Selected Artists	0.0111	0.0098
Restoration	0.0109	0.0132
Munsell	0.0089	0.0174
12 bits quantization	pinv	PCA NN
Kremer	0.0126	0.0181
Selected Artists	0.0094	0.0097
Restoration	0.0089	0.0130
Munsell	0.0075	0.0173

In summary the PCA neural network reconstruction method could be use on presence of noise. But when noise is not present it is better to use linear methods. In our quest for non-linear spectral reflectance reconstruction methods this results did not satisfy our expectations even if it could be use in case of noise acquisition system. Our aim being a non-linear method able to overcome linear ones on most possible situations we present in the rest of this chapter a better method based on *Mixture Density Networks*.

Table 5-2. CIELAB Error over different databases.

8 bits quantization	pinv	PCA NN
Kremer	6.3127	4.1719
Selected Artists	4.9307	3.5243
Restoration	4.6604	3.2379
Munsell	2.9973	2.1833
10 bits quantization	pinv	PCA NN
Kremer	2.2708	3.6885
Selected Artists	1.8685	1.7292
Restoration	1.6956	1.9488
Munsell	1.0451	1.3826
12 bits quantization	pinv	PCA NN
Kremer	1.8665	3.6331
Selected Artists	1.1356	1.6905
Restoration	1.0107	1.8009
Munsell	0.7073	1.2796

5.5 Mixture Density Networks

A Mixture Density Network (MDN) is a method for solving regression or classification problems that consists in building a conditional probability density function between outputs and inputs of a given problem, [Bishop, 1994]. In the following \mathbf{c} represents an input vector of dimension c , and \mathbf{s} represents an output vector of dimension s .

The desired conditional probability density is modelled by a mixture of basis functions, usually chosen as Gaussians. The parameters of this mixture model are estimated from a set of known data (pairs of \mathbf{c} and \mathbf{s} vectors) using a neural network which can be any conventional neural network with universal approximation capabilities. In our case, the neural network used has a classical feedforward structure, already described on this chapter. The mixture model that represents the conditional probability density is of the form,

$$\text{prob}(\mathbf{s}|\mathbf{c}) = \sum_{i=1}^m \alpha_i(\mathbf{c}) g_i(\mathbf{s}|\mathbf{c}) \quad (5.37)$$

where m is the number of Gaussians used, $\alpha_i(\mathbf{c})$ are mixing coefficients, and $g_i(\mathbf{s}|\mathbf{c})$, $i=1, \dots, m$, represent the following multidimensional Gaussians functions

$$g_i(\mathbf{s}|\mathbf{c}) = \frac{1}{(2\pi)^{s/2} \sigma_i(\mathbf{c})^s} \exp \left\{ -\frac{\|\mathbf{s} - \mu_i(\mathbf{c})\|^2}{2\sigma_i(\mathbf{c})^2} \right\} \quad (5.38)$$

which are parameterized by m scalars σ_i for the standard deviation (all dimensions having the same one) and m vectors μ_i of dimension s representing their centres. Consequently, the vector \mathbf{v} which parameterises the mixture model contains $m(1+1+s)$ elements: α_i , σ_i , μ_i . All these parameters depend on \mathbf{c} because they depend directly on the outputs of the neural networks which takes \mathbf{c} as input. The outputs of the network associated to α_i , σ_i , μ_i are called z_i^α , z_i^σ and z_i^μ respectively. In Figure 5-6 we show a graphic representation of a mixture model.

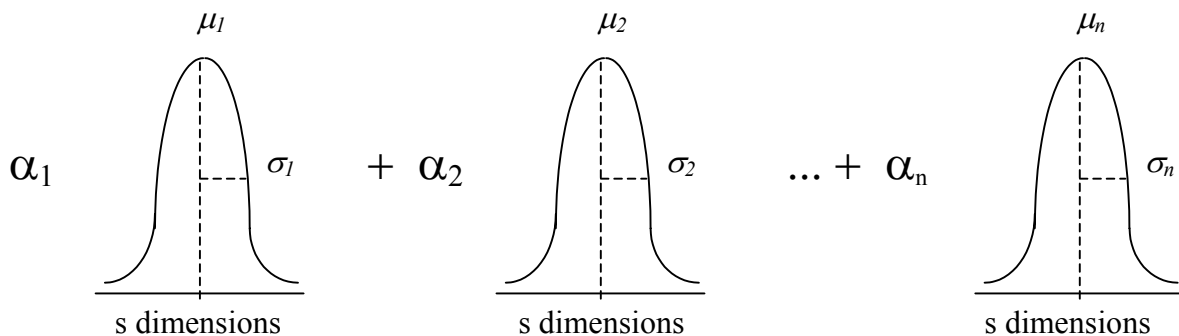


Figure 5-6. Mixture of Gaussians

Expression (5.37) is called a *mixture distribution* and the coefficients α_i are called *mixing coefficients*. Note that as $\text{prob}(\mathbf{s}|\mathbf{c})$ is a probability distribution it must satisfy the constraint:

$$\int \text{prob}(\mathbf{s}|\mathbf{c}) d\mathbf{s} = 1 \quad (5.39)$$

and consequently

$$\sum_{i=1}^m \alpha_i = 1 \quad (5.40)$$

$$0 \leq \alpha_i \leq 1 \quad (5.41)$$

These constraints (5.40) and (5.41) are satisfied by choosing $\alpha_i(\mathbf{c})$ to be related to the corresponding network outputs by a *softmax* function [Bridle, 1990]:

$$\alpha_i = \frac{\exp(z_i^\alpha)}{\sum_{j=1}^m \exp(z_j^\alpha)}. \quad (5.42)$$

The variances represent *scale* parameters and so it is convenient to represent them in terms of the exponentials of the corresponding network outputs

$$\sigma_i = \exp(z_i^\sigma). \quad (5.43)$$

Finally, μ_i is represented simply by the network output z_i^μ :

$$\mu_i = z_i^\mu.$$

A mixture model represents a probability density that is not restricted to its functional form. In general, density estimation approaches are divided into two big families, parametric and non-parametric. Parametric methods assume a specific form for the density distribution. This allows a the function to be evaluated rapidly but its shape can be very different from the true distribution. In contrast, non parametric methods allow very general forms of density distributions but they are slow to evaluate as they depend on the number of training data points. Mixture models can be consider as semi-parametric because its form is not restricted but they do not depend strongly in the data set.

An important property of the used mixture model is that it can approximate any continuous density to arbitrary accuracy provided the model has a sufficiently large number of Gaussians and provided the parameters of the model, $\mathbf{v} = \{\alpha_i, \sigma_i, \mu_i, i=1, \dots, m\}$, are chosen correctly.

We have spoke about the mixture model saying that it represents a probability density function. But we should not forget that the probability density function we want to represent is a conditional density. The fact that the mixing coefficients $\alpha_i(\mathbf{c})$ and the Gussians $g_i(\mathbf{s}|\mathbf{c})$ depend on the input data \mathbf{c} allows the system to estimate conditional probabilities. In Figure 5-7 we show a diagram of a MDN.

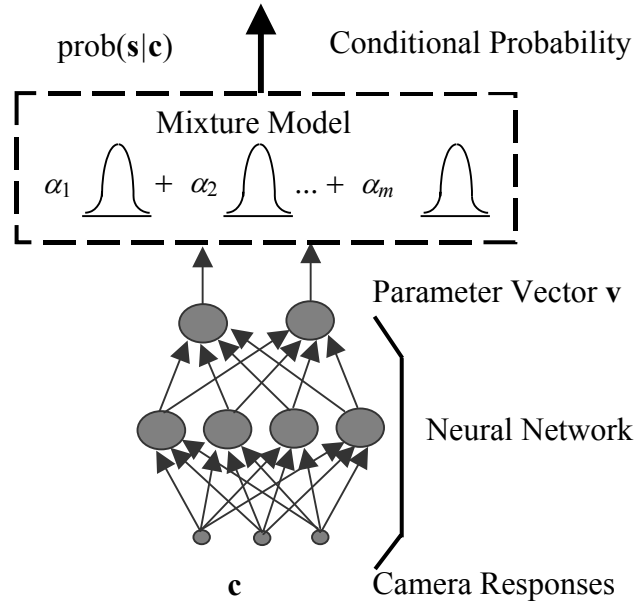


Figure 5-7. Mixture Density Network

5.5.1 Training a Mixture Density Network.

As a Mixture Density Network is based on a neural network, it needs a training phase. In this phase the neural network learns the mapping between each input vectors \mathbf{c} and its associated parameter vector \mathbf{v} defining a conditional probability density function. The learning process is driven by the minimization of the negative logarithm of the likelihood, formally:

$$E = \sum_{p=1}^P -\ln \{ \text{prob}(\mathbf{s}_p | \mathbf{c}_p) \}, \quad (5.44)$$

i.e. maximising $E' = \prod_{p=1}^P \text{prob}(\mathbf{s}_p | \mathbf{c}_p)$ where the index p identifies a training pattern, P being the total number of patterns in the training set. Consequently, we are training the system over a set of P pairs $(\mathbf{c}_p, \mathbf{s}_p)$. In the following section, for simplicity we will avoid the use of P and p .

It is important to say that minimizing equation (5.44) is non-trivial. First of all there exist parameters values for which the likelihood goes to infinity. These arise when one of the Gaussian components collapses onto one of the data points. In addition, small groups of points that are close together can give rise to a local minimum in the error function which may give poor representations of the true distribution.

The error function (5.44) is a smooth differentiable function of the parameters of the mixture model. Then, we can use standard non-linear minimization techniques. But as we said in the preceding paragraph, finding a global maximum is not assured and it depends on the initial estimates used. In any case using non-linear minimization techniques needs gradient information in order to be efficient. In the present case the derivatives of the likelihood can be found analytically.

We must not forget that the parameters of the mixture model are estimated by use of a back-propagation neural network. Consequently, the derivatives of the error E with respect to the weights of this neural network are to be calculated. The neural network can be trained by using a standard back-propagation algorithm, provided we obtain suitable expressions for the derivatives of the error with respect to the outputs of the network. Since E is composed of a

sum of terms $E = \sum_{p=1}^P E^p$, one for each pattern, we can consider the derivatives

$\delta_i^p = \partial E^p / \partial z_i$ for a particular pattern p and then find the derivatives of E by summing over all P patterns. If the neural network has linear activation transfer functions in the output layer, the δ_i^p quantities are the errors already seen in the preceding section about neural networks. These errors can be back-propagated through the network by using a standard back-propagation algorithm.

At this moment of the discussion it is useful to recall the definition of conditional probability:

$$\text{prob}(\mathbf{c}|\mathbf{s}) = \text{prob}(\mathbf{c},\mathbf{s}) / \text{prob}(\mathbf{s})$$

where $\text{prob}(\mathbf{c}|\mathbf{s})$ is the probability of \mathbf{c} conditional to \mathbf{s} , $\text{prob}(\mathbf{c},\mathbf{s})$ is the joint probability of \mathbf{c} and \mathbf{s} , and $\text{prob}(\mathbf{s})$ is the probability of \mathbf{s} . Using a simple transformation we obtain

$$\text{prob}(\mathbf{c},\mathbf{s}) = \text{prob}(\mathbf{s}) \text{prob}(\mathbf{c}|\mathbf{s}). \quad (5.45)$$

There exist a strong analogy between last formula (5.45) and (5.37). In fact, g_i can be regarded as a conditional density function with *prior* probability α_i . Consequently, from (5.45) we obtain

$$\pi_i(\mathbf{c},\mathbf{s}) = \frac{\alpha_i g_i}{\sum_{p=1}^P \alpha_p g_p}. \quad (5.46)$$

Note that the denominator of formula (5.46) is introduced in order to respect a basic theoretical constraint, probabilities must sum to unity:

$$\sum_{i=1}^m \pi_i = 1. \quad (5.47)$$

Considering the derivatives of E^p with respect to those network outputs which correspond to the mixing coefficients α_i ; we obtain from equations (5.44) and (5.46):

$$\frac{\partial E^p}{\partial \alpha_k} = -\frac{\pi_k}{\alpha_k}. \quad (5.48)$$

As a result of the softmax function (5.42), the value of α_k depends on all the network outputs which contribute to the mixing coefficients, so differentiating (5.42) we obtain

$$\frac{\partial \alpha_k}{\partial z_i^\alpha} = \delta_{ik} \alpha_k - \alpha_i \alpha_k, \quad (5.49)$$

where $\delta_{ik} = 1$ if $i=k$ and $\delta_{ik} = 0$ if $i \neq k$. As a consequence, from the chain rule we have:

$$\frac{\partial E^p}{\partial z_i^\alpha} = \sum_k \frac{\partial E^p}{\partial \alpha_k} \frac{\partial \alpha_k}{\partial z_i^\alpha}. \quad (5.50)$$

Combining (5.48), (5.49) and (5.50) we obtain:

$$\frac{\partial E^p}{\partial z_i^\alpha} = \alpha_i - \pi_i. \quad (5.51)$$

Using (5.44), (5.46) and (5.38) we obtain the following expression for the derivatives corresponding to the σ_i parameters [Bishop, 1994]:

$$\frac{\partial E^p}{\partial \sigma_i} = -\pi_i \left\{ \frac{\| \mathbf{s}_p - \mu_i \|^2}{\sigma_i^3} - \frac{s}{\sigma_i} \right\}. \quad (5.52)$$

and knowing (5.43):

$$\frac{\partial \sigma_i}{\partial z_i^\sigma} = \sigma_i, \quad (5.53)$$

we obtain:

$$\frac{\partial E^p}{\partial z_i^\sigma} = -\pi_i \left\{ \frac{\| \mathbf{s}_p - \mu_i \|^2}{\sigma_i^2} - s \right\}. \quad (5.54)$$

Finally, since the parameters μ_{ik} are given directly by the z_{ik}^μ network outputs, using (5.44), (5.46) and (5.38) we have

$$\frac{\partial E^p}{\partial z_i^\mu} = \frac{\partial E^p}{\partial \mu_i} = \pi_i \left\{ \frac{(\mu_i - \mathbf{s}_p)}{\sigma_i^2} \right\}. \quad (5.55)$$

From the above presented equations we have all necessary information to train a Mixture Density Network and to modify its behaviour if necessary.

5.6 Estimating Spectral Reflectances with Mixture Density Networks

Our aim is to estimate the spectral reflectance of pigments from multispectral images of canvas paintings. We are interested in the reconstruction of spectral curves in the visible domain of the spectrum. We consider each curve as a sequence of s regularly sampled values taken from 400 nm to 760 nm at constant d nm intervals.

Our problem consists in the construction of a system that maps a vector \mathbf{c} containing the camera values to a vector \mathbf{s} representing a sampled spectral curve. As long as a sufficient large set of pairs (\mathbf{c}, \mathbf{s}) are known this problem can be solved by the construction of a MDN system from this data.

In this context the probability $\text{prob}(\mathbf{s}|\mathbf{c})$ becomes the conditional probability of a spectral curve \mathbf{s} being obtained from a particular camera response vector \mathbf{c} . That means, we are building a function that assigns probabilities to all possible vectors \mathbf{s} in a s dimensional space. Every point of this space represents the probability of a particular vector \mathbf{s} being the counterpart of the given input \mathbf{c} .

By minimizing the negative logarithm of the likelihood over a database of training pairs (\mathbf{c}, \mathbf{s}) we can fix the weights of the neural network of the MDN. Once the neural network trained, the MDN provides a mapping between a camera response vector \mathbf{c} and a parameter vector \mathbf{v} , $\mathbf{v} = \{\alpha_1, \dots, \alpha_m, \sigma_1, \dots, \sigma_m, \mu_1, \dots, \mu_m\}$. Of course, we are interested in finding a single sampled spectral curve \mathbf{s} that provides the best estimation given a vector \mathbf{c} . For that purpose we need to chose a way to extract this vector \mathbf{s} from the mixture model represented by the parameter vector \mathbf{v} .

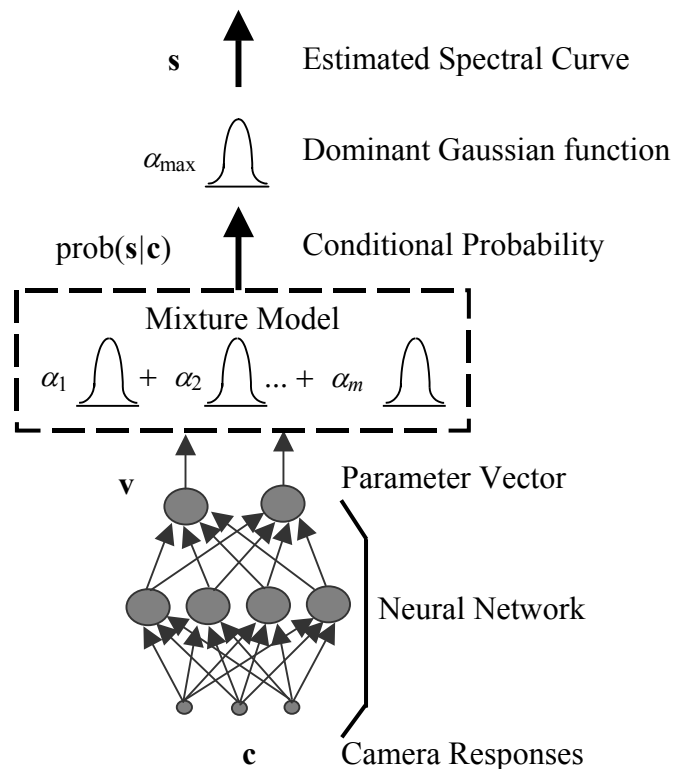


Figure 5-8. MDN spectral reflectance curve estimation.

Maximizing the obtained conditional density would give us the vector \mathbf{s} with highest probability, that is indeed what we are looking for. But maximizing the mixture model is a problem not solved in closed form and implies the application of an iterative optimization procedure that is CPU consuming. We use a much quicker and simpler strategy by keeping as solution the vector \mathbf{s} associated to the Gaussian with bigger mixing coefficient:

$$\max_i \{\alpha_i(\mathbf{c})\}, \quad (5.56)$$

such that $\mathbf{s} = \mu_i(\mathbf{c})$. Then \mathbf{s} corresponds to the centre of the dominant Gaussian function in the Mixture Model. This strategy is justified as long as in our problem we systematically obtain mixture models in which one Gaussian has a much bigger mixing coefficient than the others. In fact, we have compared results coming from different strategies and the one used (max) and the actual optimization of the function provide mostly the same results. This means that, in our case, the maximum of the mixture model is well approximated by the centre of the biggest Gaussian. A graphical summary of the method is shown in Figure 5-8.

5.6.1 Architecture Optimisation

As long as the above described method is based on a Neural Network and a Gaussian Mixture Model there are several important parameters that have to be chosen:

- the number of neurons in the hidden layer of the feed-forward backpropagation neural network,
- the number of iterations of the backpropagation algorithm,
- the number of Gaussians in the Mixture Model.

Clearly these three questions correspond to three parameters that define the architecture of the chosen MDN based method. One MDN with an architecture not adapted to the problem will give very bad results. In fact, the number n_{hn} of neurons ($n_{hn} = N_h$) in a neural network hidden layer has a direct influence in the approximation capabilities of the network; the number n_{ic} of training cycles is related to the generalization abilities of the network; and the number m of Gaussian in the Mixture Model will affect the shape and precision of the reconstructed curves. See Figure 5-9 for a diagram of our MDN architecture.

In order to have a fully automatic training method that gives us an MDN that solves our problem satisfactorily we need to find appropriate values for these three parameters: n_{hn} , n_{ic} and m . We could think about a classical gradient based search over this parameter space but we should not forget that the training algorithm of a Neural Network does not necessarily find a global minimum. Moreover, the solution depends on the random initialisation of the network weights and on the shape of the error criteria that relates closely with the network topology. As a consequence, training twice the same neural network gives, in general, different weight values. On the other hand, training Neural Networks is very time consuming and we cannot afford an exhaustive search. Thus, we are dealing with a problem of combinatorial optimisation and a global optimisation technique is required for the search of a suitable architecture inside this parameter space.

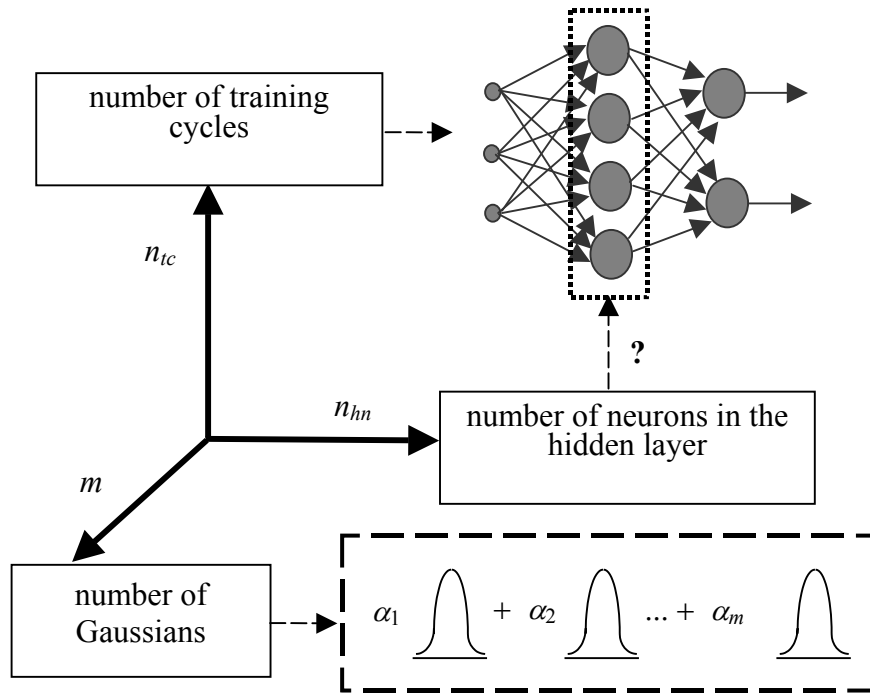


Figure 5-9. Three dimensional parameters space defining the architecture of an MDN.

A further comment must be made on the parameter representing the number of training cycles. In the neural network literature we find a lot of strategies to control this parameter for avoiding overfitting, the most popular one being probably early stopping. Early stopping is based in testing the network over a test set and stopping training when the errors on training and test sets diverge. The implementation of early stopping entails several problems, principally related to the stopping criteria. If this criterion is very strict the training could stop too early providing poor results. If an inertia term is used, stopping too early can be avoided. But if the inertia term is too high, overfitting will occur. Associated parameters are normally tuned to handle these problems.

Even if our implementation of early stopping has provided positive results, we have chosen to avoid it in the training algorithm of the neural network, and have included the number of training cycles as part of the architecture. That means we consider overfitting as a consequence of the whole architecture. Hence, our search criterion is also a test of generalisation. This implies that we use an *architecture optimisation* criterion that is based on an error measure over a test set. In our particular case, this error measure can be either a mean spectral distance or a colorimetric similarity measure between reconstructed curves and their known real counterparts. If an overfitting remedy is to be introduced inside the training algorithm we prefer to consider a periodical test in the training loop and keep the network state corresponding to the minimal error over the test set. This strategy is simple, well-adapted to our problem and does not require the tuning of any extra parameters.

In order to solve the problem of architecture optimisation we have applied two different methods: a random search and a genetic algorithm approach. Both approaches are not new, for instance, the field of optimising neural network architectures using genetic algorithms was already an active field of research in the nineties.

Before applying any optimisation technique we restrict the size of our parameter space in order to deal with a feasible problem. We choose to code the parameter set in 10 bits, that means having a search space of 1024 elements, each element being an MDN. First two bits

are used for coding m , four bits for n_{hn} and the last four bits for the number of training cycles. In the results presented later m takes values in the interval [6-9] for real data and value 1 for simulations, $n_{hn} \in [20-50]$ with samples every 2 neurons and $n_{tc} \in [3500-11000]$ with samples every 500 training cycles.

Global optimisation approaches tested:

- Random search. In this case the 10 bits representing the parameter space are generated randomly a number of times. In all our experiments we found that 60 samples are enough to find an acceptable solution.
- Genetic Algorithm. We used a matlab implementation of a basic genetic algorithm taken from chapter III of the book of [Golberg, 1989], where the chromosomes are just a chain containing characters “1” or “0”. A chromosome represents one MDN. The algorithm uses a single point crossover operator and reproduction is driven by a *roulette wheel* selection.

In our tests, both methods presented above find acceptable solutions. Probably, this is due to the nature of the optimisation problem where different architectures can perform comparably. In order to illustrate this point we have chosen one of our experiments where we apply the genetic algorithm to search for a suitable MDN that trains over a database of spectral curves acquired in our laboratory using the GretagMacbethTM ColorChecker[®] DC chart. This data set was already presented in detail in Chapter 2 (*Nature of Data*). We used, in the genetic algorithm, a crossover probability of 0.6, a mutation probability of 0.03 and populations of 14 chromosomes, afterwards we left the algorithm to evolve for 10 generations. After this time 70 different MDNs were trained. This number is lower than 140 MDNs corresponding to 14 chromosomes x 10 generations because the genetic algorithm keeps alive a part of the population between generations. We have counted the acceptable individuals trained in all generations. As acceptable individual we considered an MDN giving a mean spectral error of approximately 35% less than the linear method used as reference, in that case we chose 0.017. We found 24 MDNs in this category. This means that there is 34% of acceptable MDNs among the 70 trained MDNs. This fact indicates that lots of acceptable solutions exist within our search space. Moreover, the acceptable architectures found can be quite different. As an example one of these 24 best individuals that produces a spectral error of 0.01627 has $m = 9$, $n_{hn} = 28$ and $n_{tc} = 5000$, while another MDN producing an error of 0.16098 presents a different architecture $m = 6$, $n_{hn} = 40$ and $n_{tc} = 3500$.

In summary, we have tested two operational methods for architecture optimisation that are suitable for our application and make our quest for an MDN fully automatic. Both perform similarly because the number of acceptable solutions in our search space is high due to the nature of the problem. In the next section we present experimental results obtained with MDNs. The architectures have been chosen using these methods.

5.6.2 Method Testing

We have tested the proposed reconstruction approach by using both simulated and real data. We compare the results obtained using the mixture density network method with those obtained using the learning-based reconstruction method described on Chapter 3, Section 3.2.2. The testing performed on this section is to be understood as a comprehensive and preliminary analysis on the performance of the MDN based method. Later on this thesis we will present further results and comparison with several other methods. At the moment, the presented results serve to illustrate the adequateness of the designed method to the problem of spectral reconstruction.

5.6.2.1 Testing on Simulated Data

Comparisons are performed over four already well know spectral reflectance databases of pigments: the “Kremer” database contains 184 spectral curves (we use this database for training the MDN and to determine the linear transformation in the pseudo-inverse based method), the “Selected Artists” database contains 67 spectral curves of pigments, the “Restoration” database contains 64 spectral curves of pigments, and the “Munsell” database containing 1269 spectral curves.

These databases are regularly sampled from 400 to 760 nm at $d=10$ nm intervals, which corresponds to $s=37$ values. To obtain the multispectral camera responses we use a simulated seven channel camera with equidistributed Gaussian filters over the range 400 to 760 nm, with 50 nm half-bandwidth. We choose as spectral sensitivity of the camera sensors a typical response of CCD arrays. If no noise is introduced in this simulation process, we remark that the theoretical camera model remains a perfect linear process. This is the reason that justifies the use of a linear based method as a reference method for spectral reconstruction.

In order to study the robustness of these methods in the presence of noise, we simulate acquisitions with quantization noise by using different numbers of bits for representing the camera channels. We present simulation results that show the resistance of a Mixture Density Network for camera responses being quantized at 12, 10 and 8 bits. The choice of these three levels corresponds to the actual quantization levels observed on digital cameras currently available. The small signal to noise ratio (SNR) corresponding to 8 bits quantization is representative of most common digital images. The much larger SNR corresponding to 12 bits is available at the present time only on high-end digital cameras. Simulations performed with 12 bit quantization are indeed close to simulations without noise, and they provide results very similar to a perfect linear theoretical model. On the other hand, for 8 bit quantization the linear relationship is strongly corrupted by noise and the robustness of a reconstruction method against noise becomes predominant, which does not argue in favour of linear reconstruction methods.

Table 5-3. Spectral Error over different databases.

8 bits quantization	pinv	MDN
Kremer (training)	0.0248	0.0138
Selected Artists	0.0230	0.0154
Restoration	0.0219	0.0136
Munsell	0.0202	0.0144
10 bits quantization	pinv	MDN
Kremer (training)	0.0126	0.0094
Selected Artists	0.0119	0.0110
Restoration	0.0113	0.0086
Munsell	0.0114	0.0098
12 bits quantization	pinv	MDN
Kremer (training)	0.0109	0.0089
Selected Artists	0.0105	0.0107
Restoration	0.0093	0.0081
Munsell	0.0103	0.0094

Using a random search for architecture optimisation as described in the previous paragraph we found the best MDN among 60 random trials. This MDN contains just one Gaussian ($m=1$, V -dimension=39). The associated neural network hidden layer contains $n_{hn}=28$ neurons which correspond to a network with 1288 weights.

Table 5-4. CIELAB Error over different databases.

8 bits quantization	pinv	MDN
Kremer (training)	4.6996	2.9995
Selected Artists	4.2582	3.9300
Restoration	3.8773	2.7178
Munsell	2.8551	2.6556
10 bits quantization	pinv	MDN
Kremer (training)	1.6944	1.4398
Selected Artists	1.7265	1.5712
Restoration	1.4521	1.1781
Munsell	1.3179	1.4599
12 bits quantization	pinv	MDN
Kremer (training)	1.3351	1.2227
Selected Artists	1.1909	1.4603
Restoration	1.0956	1.0041
Munsell	1.0944	1.3353

In Table 5-3 we can compare the mean spectral reconstruction errors obtained with the MDN method and with the pseudo-inverse (pinv) method. For a given database they are calculated as the average of the L^1 distance (mean value of the absolute differences) between each real spectral curve and its reconstructed counterpart. We can see that at 8 bits this error is decreased about 40% for all databases tested. This result confirms that the MDN based method used is more robust in presence of noise than the linear reference one. It is also remarkable that the MDN response on 12 bits continues to be slightly better than the reference method, even if at this signal to noise ratio the reconstruction problem is nearly linear. Furthermore, we note that the MDN based method generalizes well over the three databases not used as training set, specially over the Munsell database since this database is not based on oil pigments as it is the case for the training set and the two other testing sets.

In order to compare the colorimetric behaviour of the reconstructed curves with the original ones, Table 5-4 shows the CIELAB errors corresponding to the same experiments as Table 5-3. For each database the CIELAB error is the average of the CIE 1976 CIELAB colour-difference between each real spectral reflectance curve and its reconstruction, D50 being used as reference illuminant. We observe the same general behaviour as in Table 1: the CIELAB error for the MDN method is always better in presence of strong noise than for the reference method and remains comparable when noise is low (12 bits quantization), although this is not so clearly stated as it is for the spectral error.

5.6.2.2 Testing on Real Data

We have scanned a GretagMacbethTM color chart using a Minolta CS-100 spectroradiometer and a PCO SensiCam 370 KL monochrome camera with an electronically tunable liquid crystal spectral filter VariSpec VIS2. From this experiment we obtained 200 spectral curves from 380 to 780 nm sampled at 1 nm intervals, each curve corresponding to a colour patch of the chart. We also acquired 12 images of the GretagMacbethTM chart using the PCO digital camera and 12 band-pass Gaussian-shaped filters using the tuneable filter, their centres being equally distributed from 400 to 740 nm with a mean half-bandwidth of 30 nm.

Table 5-5. Spectral Error over GretagMacbethTM chart.

	pinv	MDN
Training Set	0.0267	0.0162
Test Set	0.0239	0.0134

In *Table 5-5* we compare the spectral reconstruction errors (L^1 distance) obtained by the reference pseudo-inverse based method and a Mixture Density Network using $m=8$ Gaussians in its mixture model and $n_{\text{nn}}=40$ neurons in the hidden layer of its feed-forward neural network (\mathbf{v} -dimension=312). This comparison is performed over two complementary sets of measured patches belonging to the GretagMacbeth™ chart. Set 1 contains 150 patches and is used for training. Set 2 contains 50 patches not included in the training set. We can see that the MDN based method globally decreases the errors about 40% on the training set and about 44% on the test set.

In order to briefly study the effect of the dimension of the training set on the solutions we took 50, 100 and 150 patches as training sets, each set being well distributed inside the colour gamut of the chart. The 50 remaining patches not included in any of the preceding training sets have been used as a test Set 2. We selected the best individuals for a random sampling over 60 MDNs. The best mean errors over the training set were 0.0183, 0.0166 and 0.0153 for 50, 100 and 150 patches, respectively. We see a linear decreasing progression in this error, this is an interesting observation which indicates that the training set is still small and the introduction of more data would decrease the errors even more.

Table 5-6. CIELAB Error over GretagMacbeth™ chart.

	pinv	MDN
Training Set	3.9707	2.6730
Test Set	4.1533	2.3248

Table 5-6 shows the same information as Table 5-5 but for CIELAB errors. We observe that the MDN based method globally decreases CIELAB errors about 33% on the training set and about 44% on the test set.

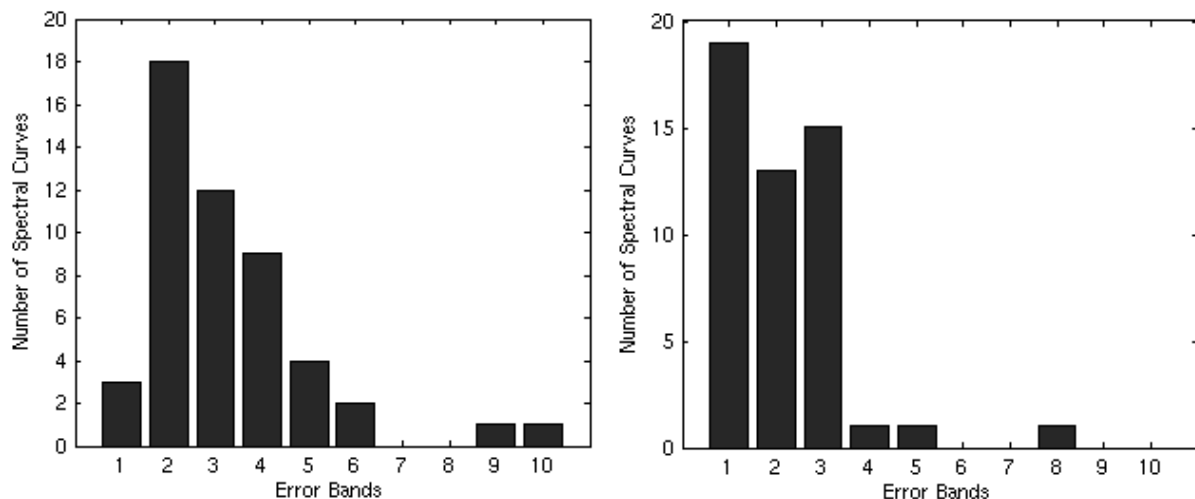


Figure 5-10. Histograms of the error for the pseudo-inverse based method (left panel) and the Mixture Density Network (MDN) based method (right panel). The histograms show 10 error bands going from the minimum (error bar 1) to the maximum error (error bar 10). Maximum error is 0.0972.

In order to better compare the reconstruction behaviour of both methods we show in Figure 5-10 the spectral error histograms for the pseudo-inverse based and the MDN based method. The error has been linearly quantized into ten bands represented by bars. Each bar indicates the number of spectral curves belonging to its error band. We clearly see that the error

distribution is much better for the MDN method, most of the spectral curve reconstruction errors remaining in the first three bands.

In Figure 5-11 we include some examples of spectral curves in order to visually compare both reconstruction methods. Although we have observed that for some rare samples the linear method performs comparably or even better than the MDN method, a large majority of MDN reconstructed curves match the real reflectance curves better. This is understandable as MDN spectral errors are statistically 40% better than the errors obtained by the linear reference method. In Table 5-7 we present the reconstruction errors associated to the curves presented in Figure 5-11.

Table 5-7. Errors associated to curves shown in Figure 5-11.

	pinv	MDN
Example 2	0.0316	0.0131
Example 3	0.0582	0.0238
Example 16	0.0466	0.0213
Example 28	0.0171	0.0114
Example 29	0.0118	0.0089
Example 35	0.0427	0.0257

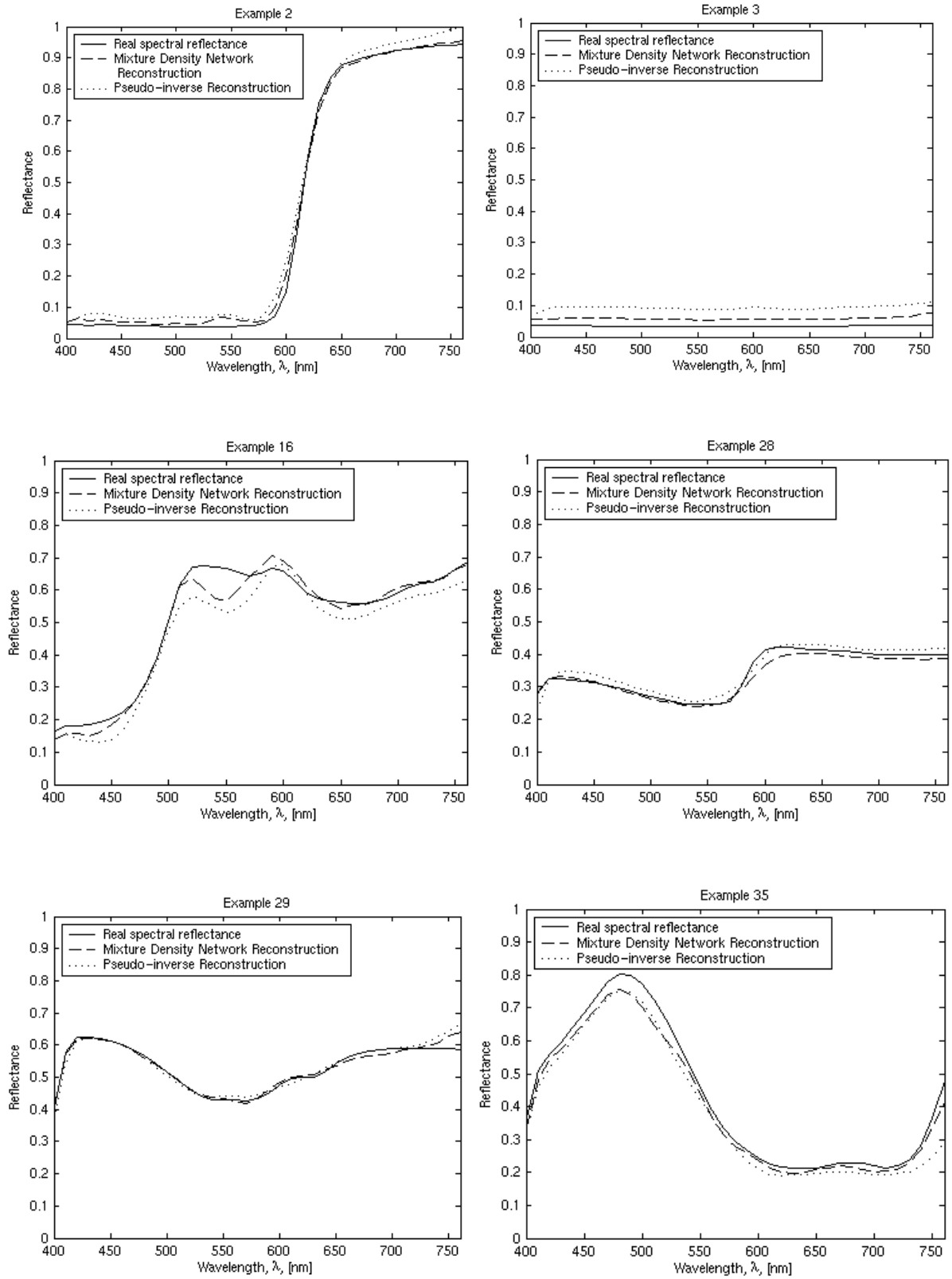


Figure 5-11. Six samples of reconstructed real curves taken from the GretagMacbethTM colour chart not belonging to the training set. Black continuous curves have been obtained by using a Minolta CS-100 spectroradiometer, dotted curves are reconstructed by the linear reference method and half-dotted curves are reconstructed by the MDN based method.

5.7 Spectral Reconstruction Software

We will start this discussion with a practical consideration of Mixture Density Networks. The good results shown in the previous section, whether noise is present or not, may justify the choice of this method. But there is another underlying important factor to consider in this choice. Our work is in the framework of CRISATEL and as part of it we will deal with multispectral images of canvas paintings and we desire the reconstruction of one spectral reflectance curve per pixel. In this project image size will be up to 12,000 by 30,000 pixels, i.e. images of 360 millions of pixels, with 10 channels per pixel in the visible range. For a current imaging system this is a lot of information. Consequently, we need a fast reconstruction method, limited on time and as quick as possible, in other words, with a fixed number of operations. This fact eliminates the choice of time consuming or iterative non bounded methods for our reconstruction system.

Of course, linear methods are the quickest methods because they only require one matrix multiplication per pixel, but they have strong drawbacks as their weak robustness in presence of noise as illustrated in our preliminary results.

Neural Networks are very time consuming in its training stage, specially if an architecture optimisation strategy is also used as we indeed do. Furthermore, using a Gaussian Mixture Model on top of a Neural Network increases the number of outputs, since a plain Neural Network approach needs s output neurons while a MDN with m Gaussians needs $m(2+s)$ output neurons as previously mentioned. But once trained, MDNs are quick at the multispectral image processing stage, for each pixel they require:

- i) Two matrix multiplications. The neural network used in the MDN has two layers, then by equation (5.34) two matrix multiplications must be performed.
- ii) One sigmoid transformation per hidden layer neuron. This is due to equation (5.35). Let's note that the activation function could be efficiently implemented in a look up table. Moreover, just one hidden layer is used in our case and as seen from equation (5.35) the function is the same for all neurons in a layer.
- iii) A max search among m scalars, from (5.56).

In addition to these above presented points, the whole image processing can easily be implemented on parallel computers.

Another important factor when considering time constraints is the choice of the implementation language. Our MDN based system has been implemented using ad hoc Matlab programs for multispectral image analysis, genetic algorithms and random sampling for architecture optimisation, as well as Netlab that is a Matlab toolbox designed at the University of Aston, United Kingdom. It is well known that Matlab is a prototyping tool not suitable for front-end applications. Our current system is acceptable for architecture selection and training of MDNs because time is not a strong requirement at learning stages. The reconstruction stage being simple it can be easily rewritten in C or C++ language in order to be used for processing large multispectral images in a more suitable way.

5.8 Conclusion

We have developed and tested new non-linear methods for the reconstruction of spectral reflectance curves from multispectral images. These new techniques are based on neural networks. On our knowledge it is the first time that this approach is applied to the resolution of the spectral reconstruction problem.

The first developed method uses a neural network to estimate, not directly, spectral curves. In fact, it estimates the coefficients associated to the orthogonal vectors obtained from a Principal Components Analysis (PCA) on a reflectance curves database, keeping 99% of signal variance. This method obtains good results on presence of quantification noise but its performance is worst than linear methods when noise is not present.

Mixture Density Networks are applied in the context of spectral reconstruction. This approach leads to a reconstruction method obtaining good results when noise is present or not. Its performance has been tested using simulations with different levels of quantization noise and it overcomes the learning-based linear method used as reference. Moreover, the method has been tested using real data where the results are also positive.

Part II

Chapter 6:

The CRISATEL Acquisition System

Contents

6.1	Introduction	131
6.2	CRISATEL Multispectral camera description.....	132
6.2.1	Filter characterization.....	132
6.2.2	Lighting system characterization	134
6.2.3	Camera electronic architecture.....	137
6.3	Camera Evaluation	140
6.3.1	CCD linearity	140
6.3.2	Dark Noise Characterization	142
6.3.3	Chromatic Aberration.....	149
6.3.4	Spatial Inhomogeneities	150
6.4	Calibration	153
6.4.1	Fixing camera parameters	153
6.4.2	Characterizing lighting and CCD inhomogeneities	155
6.4.3	Three steps Procedure	155
6.4.3.1	Step 1: Preliminary exposure time adjustment and spatial maps definition 155	
6.4.3.2	The problem of Step 1: complete exposure time optimization.....	158
6.4.3.3	Step 2: Per pixel Dark Current.....	162
6.4.3.4	Step 3: Per pixel gain	163
6.4.3.5	Fully automatic calibration procedure.....	165
6.5	Correction System	167
6.5.1	Performing the corrections	167
6.5.2	Evaluating corrections.....	168
6.5.3	The effects of acquisition geometry	172
6.6	Conclusion.....	173

6.1 Introduction

A high-resolution multispectral color imaging system has been developed for the European project CRISATEL. This system includes a multispectral camera and a dedicated high power lighting system, both developed by LUMIERE TECHNOLOGY, Paris, France. In this chapter we present and characterize the hardware of the CRISATEL camera. Afterwards, we evaluate this acquisition system and using the data obtained on the evaluation we propose and implement a calibration procedure. Finally, a correction system for the calibrated images is described.

On section 6.2 we present the multispectral acquisition system of the CRISATEL European project. The spectral characteristics of its filters and lighting system are described. The electronic architecture of the camera is then introduced. This led us to conduct a set of experiments which are presented in the rest of the chapter.

On section 0 the system is evaluated. Experiments were performed in order to characterize the CCD array. Dark noise being an important matter, a complete characterization quantifying its dependence from the camera parameters has been performed. The problem of chromatic aberration is briefly discussed. Finally, the spatial distribution of the lighting on the image plane is analyzed.

On section 6.4 a calibration process is proposed based on the experiments performed. This calibration process is implemented in three steps: we first determine the parameters controlling the camera and obtain the spatial maps for lighting inhomogeneity correction, then we calculate the per pixel dark current offset, lastly the per pixel gain is determined to correct the differences of sensitivity between the CCD pixels. We show in detail how these operations are performed.

Finally, on section 6.5 we present the correction process which is applied to calibrate the raw acquired images.

6.2 CRISATEL Multispectral camera description

We describe in this section the basic features of the CRISATEL multispectral acquisition system.

The CRISATEL multispectral camera is a digital camera based on a charge coupled device (CCD), a 12 000 pixel linear array. This linear array is mounted vertically and mechanically displaced by a stepper motor. The system is able to scan up to 30 000 horizontal positions. This means that images up to 12 000 by 30 000 pixels can be generated. The current camera is fitted with a system that automatically positions a set of 13 interference filters, ten filters covering the visible spectrum and the other three covering the near infrared. There is an extra position without filter allowing panchromatic acquisitions.

The CRISATEL system is conceived for the digitalization of paintings. It includes a camera and a dedicated lighting system. The lighting system is composed of two elliptical projectors. In Figure 6-1 we show a diagram of the system. The optical axis of the camera should be perpendicular to the painting surface that we approximate as a plane. The two elliptical projectors of light are usually positioned at left and right sides of the camera and closer to the painting. Both projectors rotate synchronously with the CCD displacement and their projected light scans the surface of the painting.

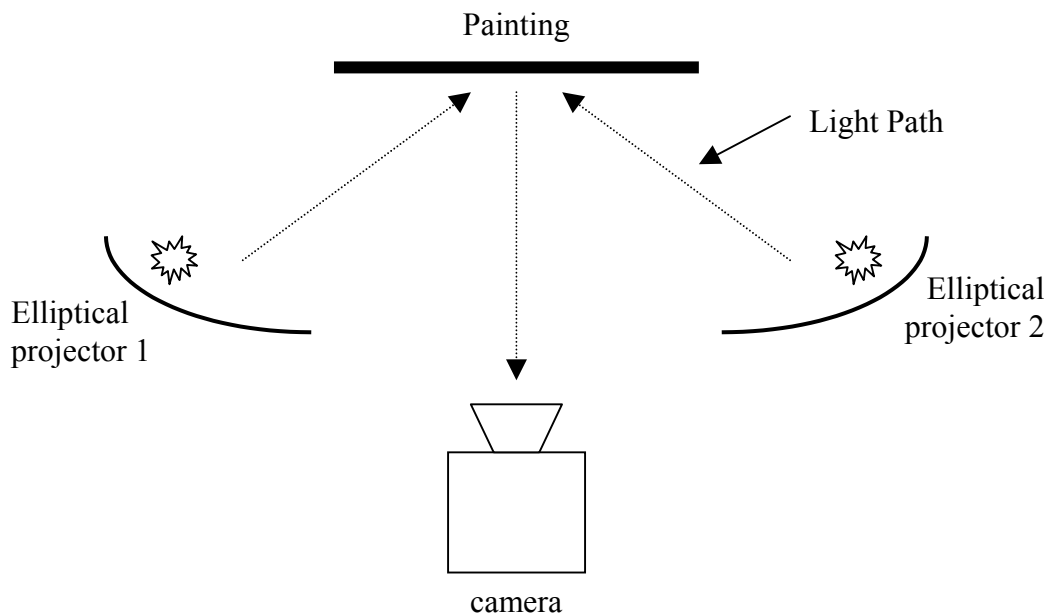


Figure 6-1 Experimental camera configuration.

6.2.1 Filter characterization

The spectral reflectance curves of the 13 filters have been specified within the CRISATEL consortium. In the visible range they have 40 nm bandwidth and are equally spaced from 380 to 780 nm at 40 nm steps. The filters were produced by Melles Griot. The filter transmittance of the 10 filters in the UV to Visible range were measured with a Hitachi U-4000 spectrophotometer at the Victoria and Albert museum in London, see Figure 6-2. The Hitachi double beam spectrophotometer consists of a scanning monochromator, a Spectralon coated integrating sphere, a Tungsten Halogen lamp and a light-tight sample compartment. The system was set up to scan the wavelength range 340-1500nm, using a photomultiplier at short wavelength (<850nm) with a slit-width of 1nm and a scanning speed of 300nm/min, and a PbS detector in the NIR (>850nm) with a slit-width of 10nm and a scanning speed of

750nm/min. First, a baseline calibration was performed by comparing the sample beam (with no filter in the beam) with the reference beam. The transmittance of each filter was then obtained by taking the ratio between the sample and the reference beam. Most of the filters have significant second order response beyond $\sim 1100\text{nm}$, which should not introduce a significant error, since the CCD quantum efficiency cuts off at $\sim 1100\text{nm}$.

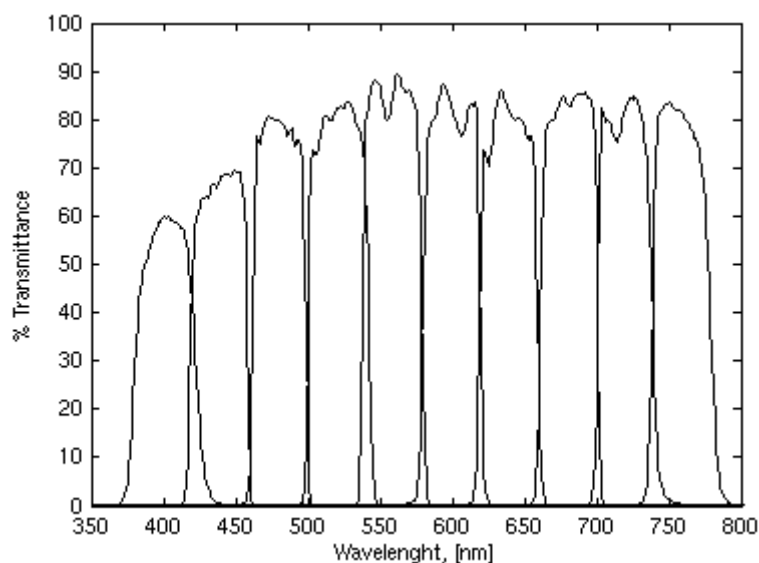


Figure 6-2 Transmittance of the 10 UV-VIS filters measured with the Hitachi spectrophotometer.

The transmittance of the above filters were also measured with a Monolight spectrophotometer at the National Gallery in London. The Monolight system consists of a scanning monochromator, a stabilised Tungsten Halogen light source, a photomultiplier detector for 300-850nm, and a Si detector for 300-1100nm. Both the light source and the detector are connected with a optical fibre light guide and a collimated lens. The calibration procedure consists of a wavelength calibration with a He-Ne laser and a dark level measurement. The transmittance of the 10 filters obtained with the Monolight spectrometer were consistent with the Hitachi measurements within 2%. The transmittance of the 3 IR filters measured with the Si detector of the Monolight system (slit-width 0.45mm) is shown in Figure 6-3.

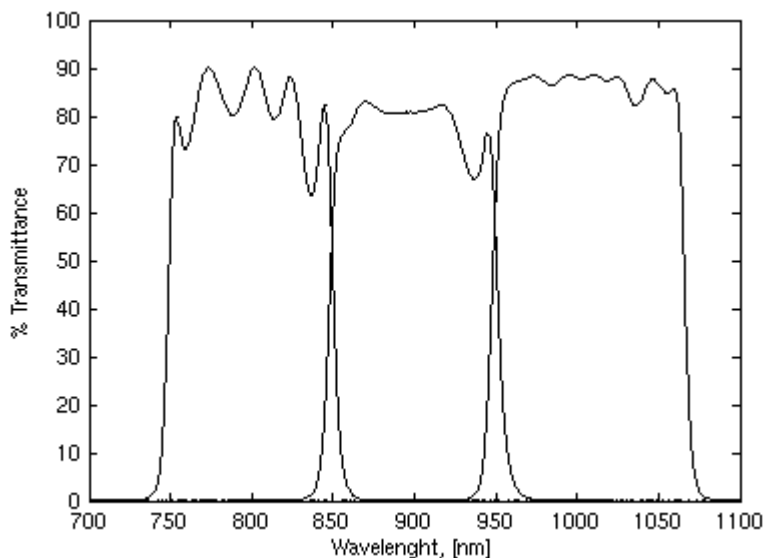


Figure 6-3 Transmittance of the 3 IR filters measured with the Monolight spectrophotometer.

Since the transmittance of interference filters are known to depend on the angle of incidence, we have also measured the angular dependence of selected filters using the Monolight (e.g. Figure 6-4). There is a 1.5nm shift to the blue at 5 degrees and a 4.5nm shift at 10 degrees with no distortion to the spectral shape. Since the maximum angle of incidence for the CRISATEL system is ~7 degrees, the maximum wavelength shift is only ~3nm.

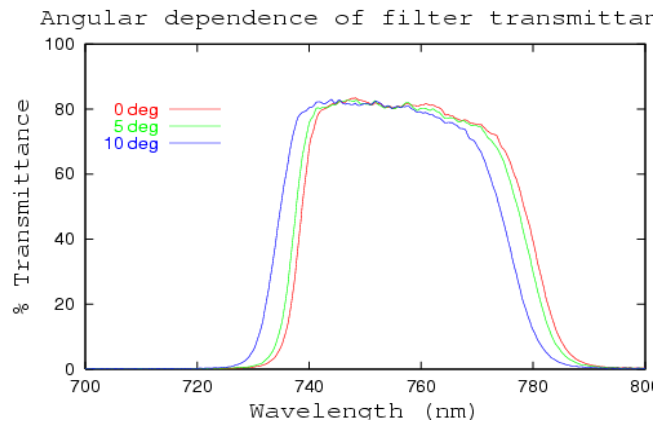


Figure 6-4 Angular dependence of filter transmittance.

The filter thickness and other optical properties being different for each filter, the focal distance for every channel will be different too. This is not a problem as the focus of the lens is precisely controlled by a stepper motor allowing independent focusing distance for every channel. But consequently the 13 channels result in images of slightly different scale. The CRISATEL multispectral camera provides a displacement system of the full camera body that can compensate these differences in scale.

6.2.2 Lighting system characterization

The lighting system is composed of two elliptical projectors positioned at left and right sides of the camera. Both projectors rotate and their projected light scans the surface of the painting. When synchronised, these projectors produce a luminous band that moves on the surface of the imaged plane. A photograph of one of this projectors can be seen in Figure 6-5.



Figure 6-5 Photograph of an elliptical projector part of the CRISATEL system.

The projectors have an elliptical shape. An ellipse has two foci, the lamps are placed in one of these foci and the elliptical mirror concentrates the radiant energy on the other foci that we call focal point. When the projectors rotate their focal points move on the 3d space and not on the plane to be imaged. As a consequence, the band produced by one projector can be more or less thick and intense depending on the position on the plane. As long as there are two projectors, their produced bands are to be synchronised in order to obtain an illumination field as homogeneous as possible. This problem is solved at the moment by a pre-calibration procedure implemented on the camera software. We will not enter here into details about this algorithm. From our experience we found that the synchronisation problem is different when Halogen lamps or HQI bulbs are mounted on the projectors. Halogen lamps being a filament they produce a narrow band because the elliptical mirror projects its shape onto the plane to be illuminated. HQI bulbs produce a wider band. This fact makes the synchronization of the halogen lamps more complex.

In this section, we are mainly interesting in the spectral emittance properties of the light source we can use for scanning paintings. We measured the spectral radiance of the available Halogen lamps and HQI bulbs. The spectral radiant energy distribution functions are shown on Figure 6-6. We show on the left panel the power distribution of the HQI bulbs and on the right panel the same graph for the halogen lamps. These measures were taken by a Minolta CS1000 spectrophotometer positioned normal to a white calibrated patch with a supposed *perfect reflectance*. We then placed the halogen lamps or HQI bulbs at 45 degrees from the normal.

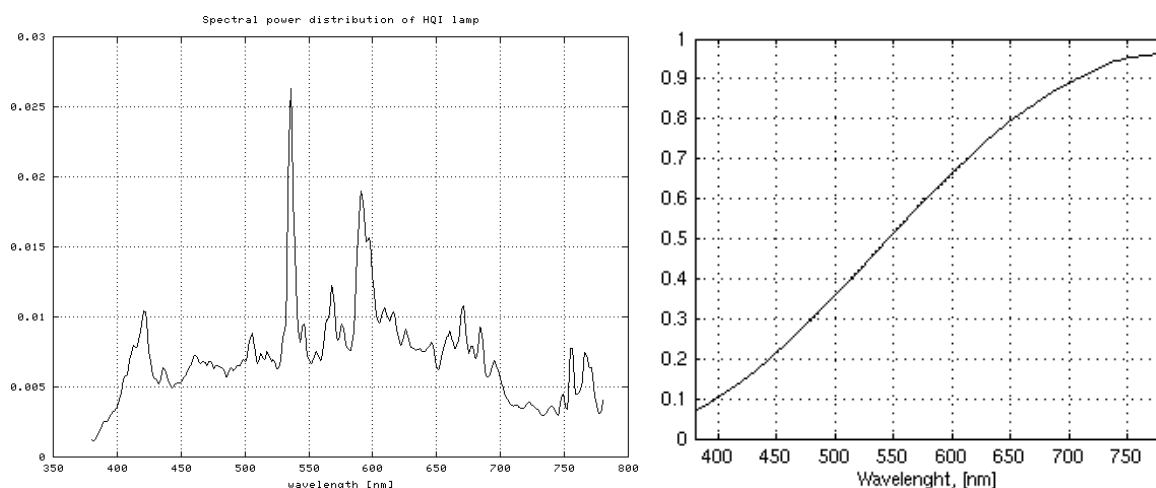


Figure 6-6 Measured spectral distribution of the radiant energy of the HQI bulbs (left panel) and the halogen filaments (right panel) used in the CRISATEL lighting system.

When working with a lamp we expect its radiant energy to be stable with time. For halogen lamps it is well-known that they are stable if the applied electrical power is continuous and controlled. This is the case of the projectors used, but we still need to determine the time it takes to warm up the lamps before a stable image acquisition can be done. In order to answer this question we measured the temporal evolution of one of the CRISATEL projectors using halogen lamps.

A Minolta CS1000 spectrophotometer was used with an acquisition geometry of 45/0. This time the experiment consisted on switching of the lamps and taking measures of the calibrated patch every 3 minutes, starting 30 seconds after the lamps switched on and finishing 30 minutes afterwards. The results are presented on Figure 6-7. On its left panel we present all

the measured spectral curves, that gives an overall impression on the evolution of the radiant energy. We present on the right panel of Figure 6-7 a detail of these curves. This zoom shows the spectral curves identified by different line types. Following the times shown on the legend we see the following evolution:

- the spectral curves initially decrease on absolute value,
- they reach a minimum after around 13 minutes,
- they increase again and stabilize after 20 minutes.

We have drawn the last measure (at 29 minutes and 30 seconds) as a thick black line. As a consequence of these measures we recommend to warm up the lamps for at less 20 minutes.

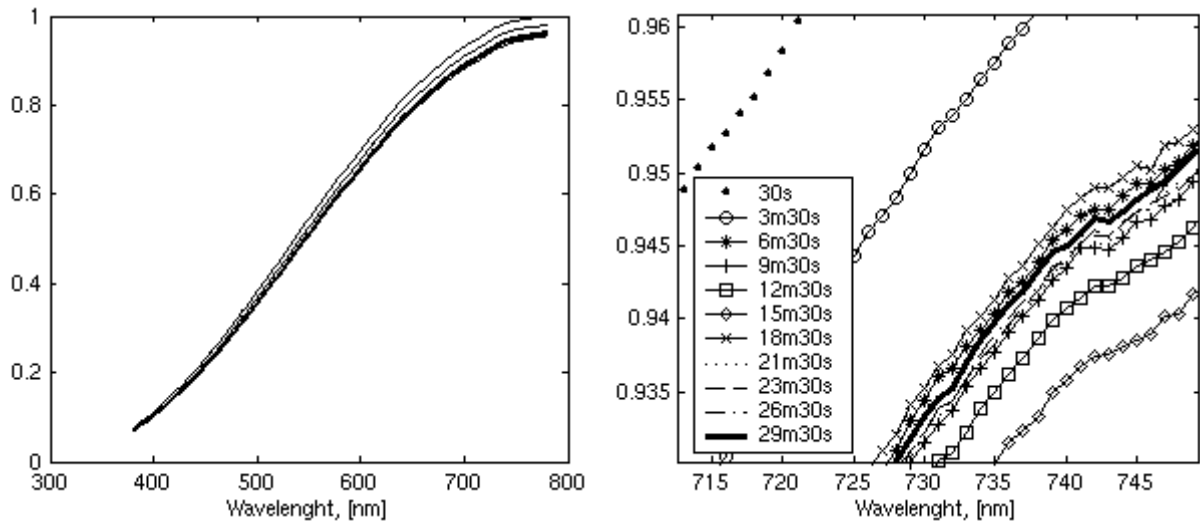


Figure 6-7 Measured spectral distributions of the radiant energy of the halogen filament at different stages of the warming up. (Left panel) Curves showing the evolution of the light source from 30s to 29m30s at 3m intervals. (Right panel) Zoom over a region to better appreciate the evolution.

We will now investigate the nature of the radiant distribution. Halogen lamps are generally known as good approximations of a blackbody radiator. A blackbody radiator is an object the radiance of which depends only on its temperature [Wyszecki and Stiles, 1982]. By Planks formula we can calculate the radiant exitance of a blackbody radiator. Its expression is

$$M_e = c_1 \lambda^{-5} (e^{c_2/T\lambda} - 1)^{-1}, \quad (6.1)$$

where λ is the wavelength and the two radiation constants c_1 and c_2 are obtained from

$$c_1 = 2\pi hc^2, \quad (6.2)$$

and

$$c_2 = \frac{hc}{k}, \quad (6.3)$$

where c is the velocity of light, h is the Planck constant and k is the Boltzmann constant.

Note that the only free parameter on Plank's formula is the temperature. Giving different values to this parameter we can calculate the radiant energy distribution per wavelength of a

blackbody radiator at any temperature. When changing temperature the radiant distribution changes on absolute value and form. We are interested in its form. This is because we can compare the curve of a blackbody radiator with that of a halogen lamp. As long as the absolute values have no possible link between the absolute values for theoretical or real data we just can compare its shape. In any case the shape of a blackbody radiator radiant energy distribution is completely defined by its temperature.

On Figure 6-8 we simulate the curves for blackbody radiators from 3800 Kelvin to 4800 Kelvin at 100 Kelvin intervals. These curves are drawn as black thin lines. The thick black curve represents the experimentally measured spectral emissivity of the halogen lamp used on the CRISATEL system after 30 minutes of warming up. We clamped all the curves at the last wavelength sample (800 nm) in order to better compare the shapes. The measured curve clearly diverges from the theoretical ones. The closest blackbody radiator to this lamp is the one having temperature of 3150 Kelvin.

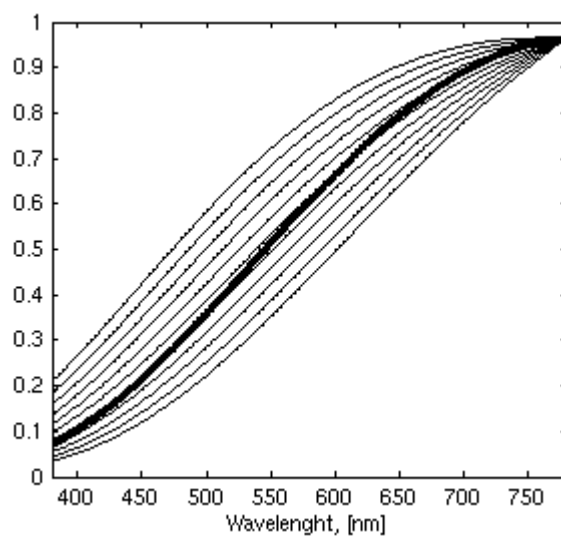


Figure 6-8 The thick black line represents the measured spectral distributions of the radiant energy of the halogen filament after 30 minutes of warming up. Thin curves are the radiant exitance of blackbody radiators at temperatures from 3800 to 4800 Kelvin, drawn at 100 Kelvin intervals.

6.2.3 Camera electronic architecture

The camera electronic architecture is based on the VSP2212 chip produced by Burr-Brown. This is a complete mixed-signal integrated circuit that contains all of the key features associated with the processing of the CCD imager output signal in a digital still camera or similar applications. We will not show any block diagram or precise information not directly relevant to the camera control, for more details see the technical manual of [Burr-Brown, 2000].

The VSP2212 chip allows one, two or four parallel channels for the CCD readout operations. The current system uses two channels which process the pixels on the array occupying even or odd positions respectively. In each channel the raw signal coming from the CCD passes through an analog amplifier. Each amplifier has two control parameters, an offset and a gain. In our case, it is a set of two offsets and two gains which can be fixed for each individual channel before a multispectral acquisition. The analog signal delivered by the amplifier for each pixel is then quantized into 12 bits by an analog to digital converter (ADC). See Figure 6-9 for a diagram of this process.

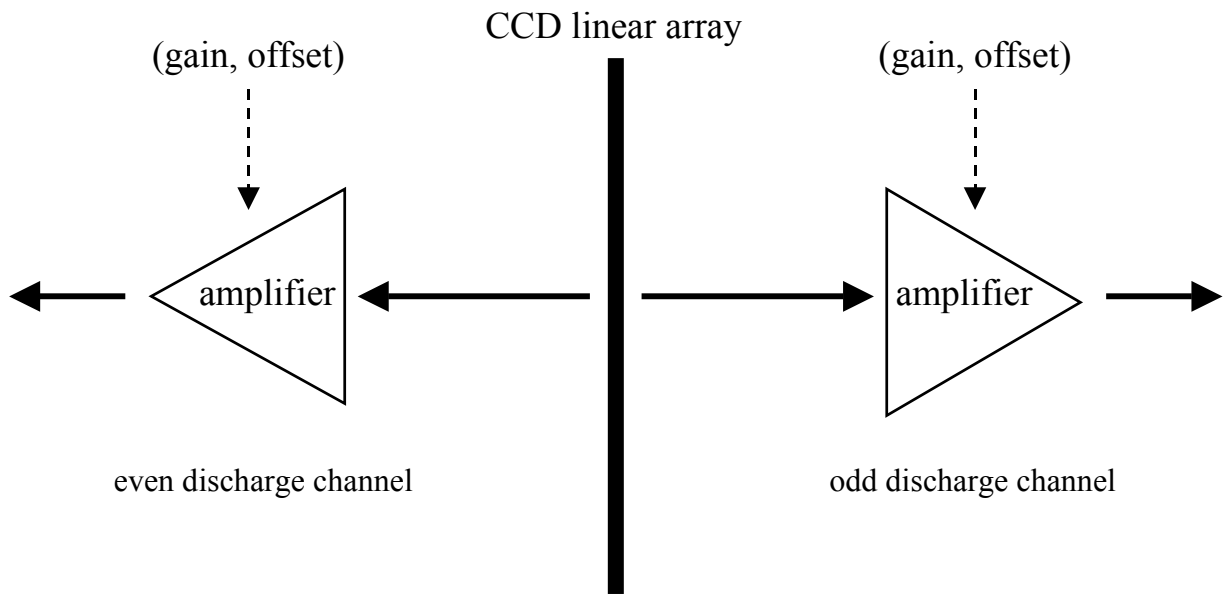


Figure 6-9 Electronic architecture of the VSP2212 chip.

The VSP2212 chip includes the following units: a correlated double sampler (CDS), programmable gain amplifier (PGA), Analog-to-Digital Converter (ADC), input clamp, optical black (OB) level clamp loop, serial interface, timing control, reference voltage generator, and general purpose 8-bit Digital-to-Analog Converters (DAC). The PGA gain control, clock polarity setting, and operation mode selection can be made through the serial interface. In fact, this serial interface allows the camera hardware to be controlled. In particular, the gain and the offset are the parameters of this chip in which we are interested:

- The PGA gain. The PGA provides a gain range of -6dB to $+42\text{dB}$, which is linear in dB. The gain is controlled by a digital code with 10-bit resolution, 1024 input values are then possible running from 0 to 1023. Knowing this we can build the relationship between the amplifier input control gain and the gain in dB, that is:

$$g = (48 / 1023) x - 6 , \tag{6.4}$$

where g is the gain in dB and x is the code accepted by the amplifier interface.

Left panel of Figure 6-10 shows this relationship that was very helpful to express results in this chapter in decibel (dB). We found dB much more comprehensive than a scale of numbers attached to a specific electronic architecture. The dB is a logarithmic unit used to describe a ratio. The dB was first introduced to measure sound level, but it is also widely used in electronics, signals and communication. The ratio may be power, sound pressure, voltage, intensity or many other quantities. In our context we call it *amplification*, that is the factor by which the signal amplitude is increased in the amplification process. Mathematically the relationship is expressed as

$$g = 10 \log_{10}(a) , \tag{6.5}$$

where g is the gain on dB and a is the amplification factor. Right panel of Figure 6-10 shows a graph of this relationship.

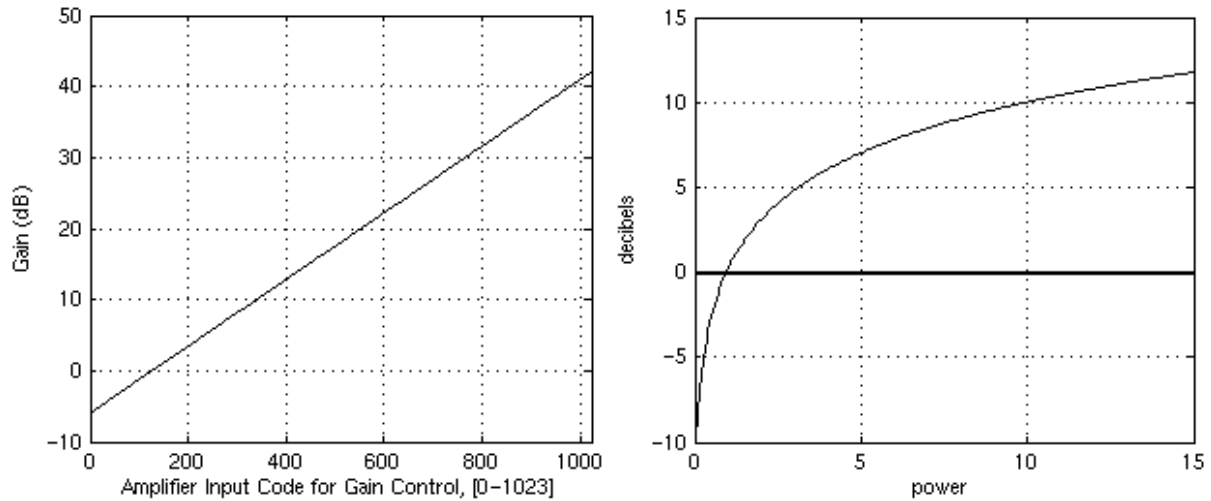


Figure 6-10 (Left panel) Linear relationship between the input code for gain control of the amplifiers and the amplification gain on dB. (Left panel) Logarithmic relationship between amplification factor and decibels.

- The “OB clamp level” (the pedestal level). Instead of the PGA, we are not interested here on the relationship between input code and the OB clamp level. We just need to know that 16 clamp levels can be programmed through the serial interface. The VSP2212 has an auto-calibration loop to establish the OB level using black pixels output from the CCD imager. But this option must be inactive as we will always define by ourselves the OB clamp level. This OB clamp level correspond to the value we called amplifier offset on Figure 6-9.

For a given scene and lighting, there still remain two physical parameters which allow us also to control the amplitude of the signal: the aperture of the optical lens and the exposure time. Both factors can modify the number of incident photons trapped in each individual CCD cell. The aperture of our dedicated optical lens not being controlled electronically, it is kept fixed during an acquisition. The exposure time can be automatically setup and changed from 1.3 ms to 200 ms by steps of 0.1 ms. Since the CCD readout speed is the limiting factor to the rate of acquisition, the minimum time of 1.3 ms could be reduced by using four parallel channels for the CCD readout. But in our case this value is already small enough and appropriate for applications to the scanning of paintings since the lighting irradiance remains limited and necessitates the use of larger exposure times.

6.3 Camera Evaluation

In this section we present a series of tests aiming to characterize the physical aspects of the CRISATEL camera. The studied points relate closely with image quality. This characterization is not a mere description of the system but it provides both a study of the camera performances and a basis for the posterior analysis of the acquired image.

6.3.1 CCD linearity

To control the linearity of the CCD response, we use a calibrated white target under a CRISATEL lighting system equipped of HQI bulbs or halogen filaments. All the camera parameters are kept constant except for the exposure time. The offset of each electronic amplifier is set to its minimum and the gain is kept at 0 dB. The mean output signal corresponding to a white reference target should increase linearly with the exposure time. In Figure 6-11 we show the results of this test of linearity when using HQI bulbs (left panel) and halogen lamps (right panel).

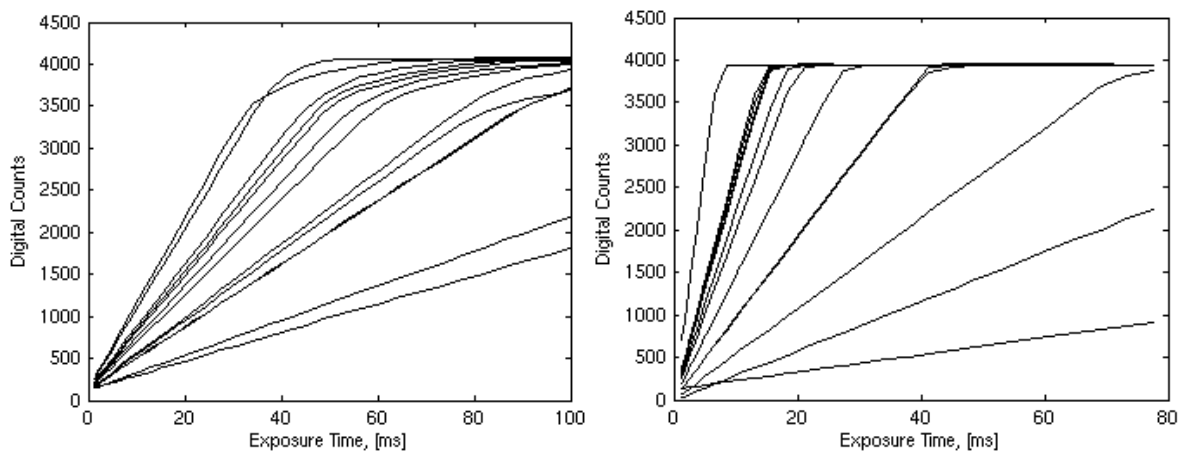


Figure 6-11. Curves showing the linear behaviour of the CCD array for all channels. Amplifier offset is fixed to its minimum level, amplifier gain is 0dB. (left panel) HQI bulbs, (right panel) halogen lamps.

We observe on all the curves a perfect linear response, up to a certain response level where the CCD starts to be saturated and reaches a plateau where the acquired images are overexposed. The transition between the linear behaviour and the plateau is important to characterize in order to determine an optimal exposure time for which the CCD is not saturated and the images are not underexposed. When a channel sensitivity is too low as it is the case of the curves that do not saturate on the limits represented on Figure 6-11, the output response needs to be magnified by increasing the amplifier gain.

We note that the upper limit for the exposure time is different in both graphs presented on Figure 6-11. In general, curves of linearity corresponding to the halogen lamps saturate faster. This is not an intrinsic property of the halogen technology but the design of these projectors that made the luminous flux to be more intense on this particular case. Anyway, this fact is of relevant practical importance because having more luminous flux implies smaller exposure times and consequently faster acquisitions. We have performed a comparison for each channel of the CRISATEL camera between halogen and HQI projectors. For this, we have taken at each channel an exposure time where no curve, neither for halogen nor for HQI, is saturated.

At this exposure time we calculate the signed difference between the digital counts obtained for the halogen lamps against the HQI bulbs expressed in percentage of the halogen lamps. The results are shown on Figure 6-12.

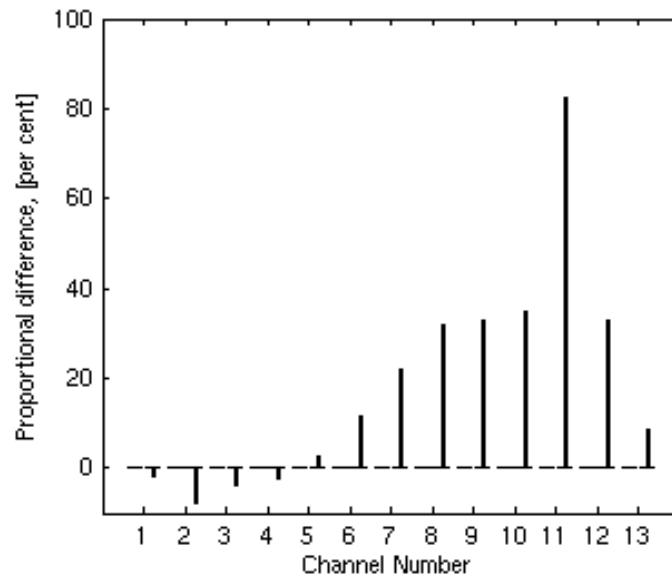


Figure 6-12. Difference on luminous flux per channel between halogen lamps and HQI lamps for the CRISATEL acquisition system. Positive sense for the bars indicates halogen superiority. Channels 1 to 10 correspond to the 10 filters in the visible spectral range, channels 11 to 13 to the three IR filters.

Figure 6-12 shows the difference on luminous flux of both HQI and halogen projectors. A positive value of the bars indicates that halogen has more flux than HQI, the negative sense indicates more flux for HQI. From this analysis we prefer the use of projectors using halogen lamps as it provides much more luminous flux on most channel. HQI seems better for channels on the lower part of the visible spectrum but the difference is less than 10%.

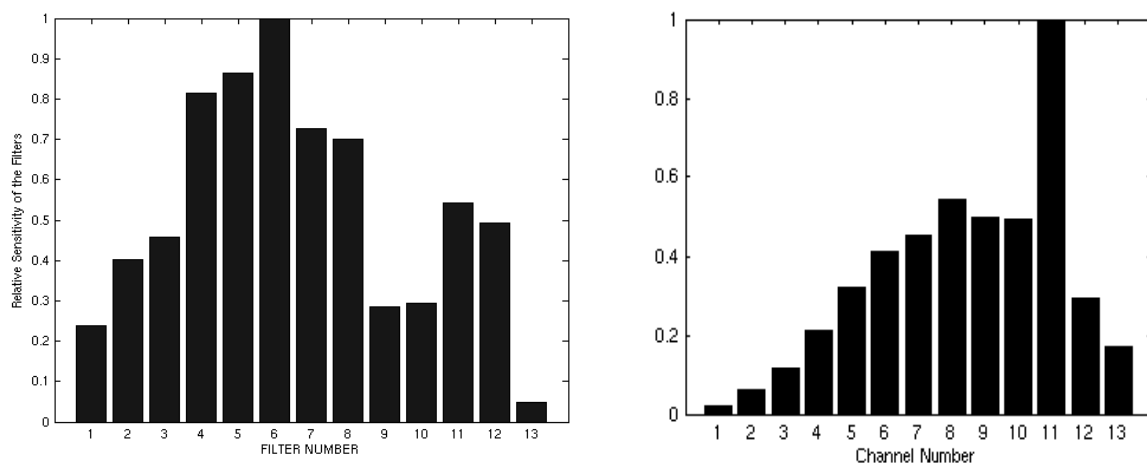


Figure 6-13. Relative channel sensitivity of the CRISATEL camera. Channels 1 to 10 correspond to the 10 filters in the visible spectral range, channels 11 to 13 to the three IR filters. (Left panel) uses HQI bulbs while (right panel) uses halogen lamps.

We can compare the relative sensitivity of the channels represented in Figure 6-13 by measuring their respective responses at a given exposure time where all the curves remain linear (e.g. at 20 ms for the HQI and 5 ms for the halogen). The result of this comparison between the 13 channels of the CRISATEL camera is shown in Figure 6-12. Note that the

relative sensitivity depends strongly on the light source used. On the left panel of this figure we can see the relative sensitivity using HQI bulbs while on the right panel we show the same diagram calculated when using halogen lamps. The differences are visually very significant and the behaviour of the system will change considerably when using different types of light sources.

The measured spectral distribution of the radiant energy of the HQI bulbs and the halogen lamps used in the experiment are shown in Figure 6-6. We comment these two bar diagrams in the following:

- HQI bulbs. In left panel of Figure 6-13, channel 6 is the most sensitive. It corresponds to the filter centred at 600 nm. Channels 1, 9 and 10 are about 4 times less sensitive. They correspond to filters centred at 400 nm, 720 nm and 760 nm, respectively. Channels 11, 12 and 13 correspond to the three infrared filters centred at 800 nm, 900 nm, 1000 nm, respectively. Their larger bandwidth, 100 nm instead of 40 nm, explains the increase in sensitivity of channels 11 and 12 compared to channel 10. Channel 13 is the less sensitive, about 20 times less than channel 6. It is due to a strong decrease of the spectral sensitivity of the linear array in that part of the infrared.
- Halogen filaments. In this case the behaviour is very different, we obtain a bell shaped diagram where the filter centred at 800 nm has a strong pick breaking the smoothness of this shape. The increasing smooth shape on the visible part of the spectrum is justified by the form of the spectral radiance of halogen filaments, see Figure 6-6. The peak on the first infrared channel is due to its wider band, 100 nm instead of 40 nm. The decrease on the 900 nm and 1000 nm channels is explained by the strong decrease of the spectral sensitivity of the linear array in that part of the infrared.

6.3.2 Dark Noise Characterization

One fundamental characteristic of a digital multispectral camera is its level of noise. In this section we present the results of a set of experiments performed to characterize the noise properties of the CRISATEL camera. Noise sources associated to a CCD have already been described on Chapter 2 (*Nature of Data*). In this section we mainly characterize noise encountered on the acquisition system, we call it dark current. In order to measure *dark signals* we block the camera by using a cap and scan “dark images”. We have conducted all our experiments in a dark room in order to avoid any stray light.

Since we have a linear CCD array, we consider each line of a single large dark image as a population of samples of the corresponding CCD pixel and calculate on this line the mean and the variance. Then, the whole CCD array is summarized in one number by using the mean on all the pixels of a selected statistics. This mean is performed separately for even and odd pixels as their amplifiers are different. We recall that the output camera signal is 12 bits quantized in the range [0-4095]. The scales used in the various noise representations are then provided directly in units corresponding to that range, the so called digital counts.

We first present two sets of curves which relate the mean level of dark noise and its standard deviation with the exposure time. In Figure 6-14 we observe clearly that the mean value of the dark noise is linearly dependent on the exposure time. We also observe on Figure 6-14 that the amplifier gain changes the slope of the curve. All these observations agree with simple theoretical expectations. Since the mean dark noise is predictable it is then possible to correct it by applying a negative offset of the same amount on the output signal delivered by the amplifier. In Figure 6-15 we present the standard deviation corresponding to the same

experiment as in Figure 6-14. We observe here that the standard deviation becomes constant for small values of the amplifier gain and for bigger values it is constant after a given amount of exposure time. This constant value increases with the amplifier gain. This indicate to us that it is better to use a longer exposure time in the available range, than to increase the amplifier gain, as far as the precision of the signal is concerned.

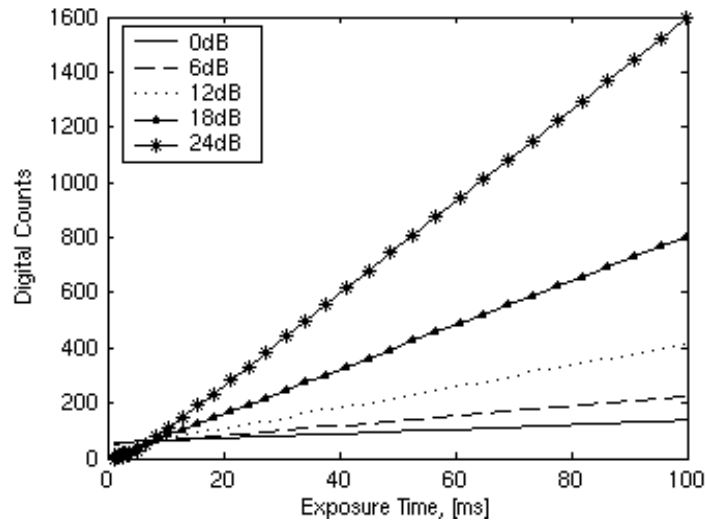


Figure 6-14. Mean value of the CCD dark noise. Each linear curve represents the dark noise mean value versus the exposure time for a fixed amplifier gain. The amplifier gain changes the slope of the lines.

We have calculated the slope of the lines shown on Figure 6-14. The results are presented on the following Table 6-1:

Table 6-1. Slope of lines shown on Figure 6-14.

Gain	Slope
0 dB	0.06173
6 dB	0.12464
12 dB	0.26288
18 dB	0.57404
24 dB	1.22290

In this table we observe that there is approximately a multiplicative factor of 2 on the slope when augmenting the gain by 6 dB. This confirms that the amplification augments practically linearly with the gain expressed in dB.

In order to better understand the information in Figure 6-14 and Figure 6-15 we generate a Signal to Noise graph. This is shown in Figure 6-16. We calculate it by considering the mean of the dark noise as the “signal” and its standard deviation as the “noise”. The graph in Figure 6-16 is the simple division of each standard deviation curve in Figure 6-15 by the corresponding mean curve in Figure 6-14. This new representation helps the visual interpretation of our experiments. In Figure 6-16 we see exponential kind of curves and clearly that the inverse of this “signal to noise ratio” is smaller when the integration time is higher. It is important to see that for small values of the exposure time the noise standard deviation is significant when compared with the mean. In order to better illustrate this point, right panel of Figure 6-16 shows a zoom for small exposure times of the graph presented on the left panel. The relative importance of the standard deviation at these small exposure times

should be studied for applications requiring to perform fast image acquisitions. Knowing that scan velocity is not an issue for art painting applications this graph can be used to fix a minimal exposure time which guaranties a small level of noise.

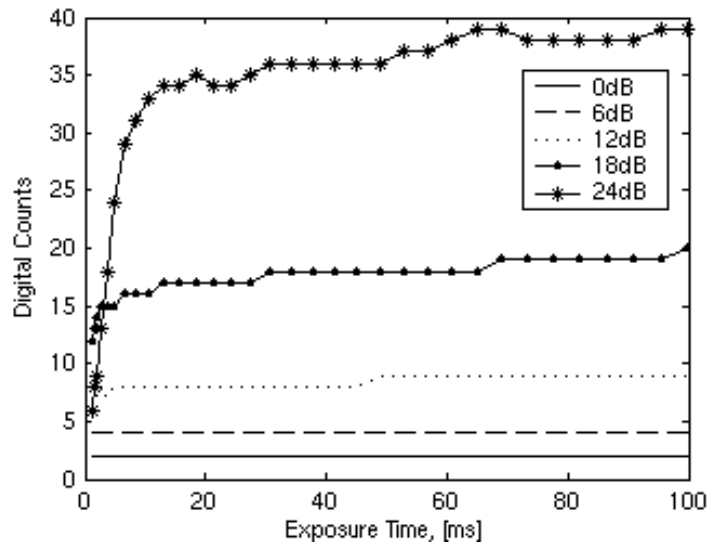


Figure 6-15. Standard deviation of the dark noise. Each curve represents the dark noise standard deviation versus the exposure time for a fixed amplifier gain. The standard deviation reaches a maximum which depends on the gain.

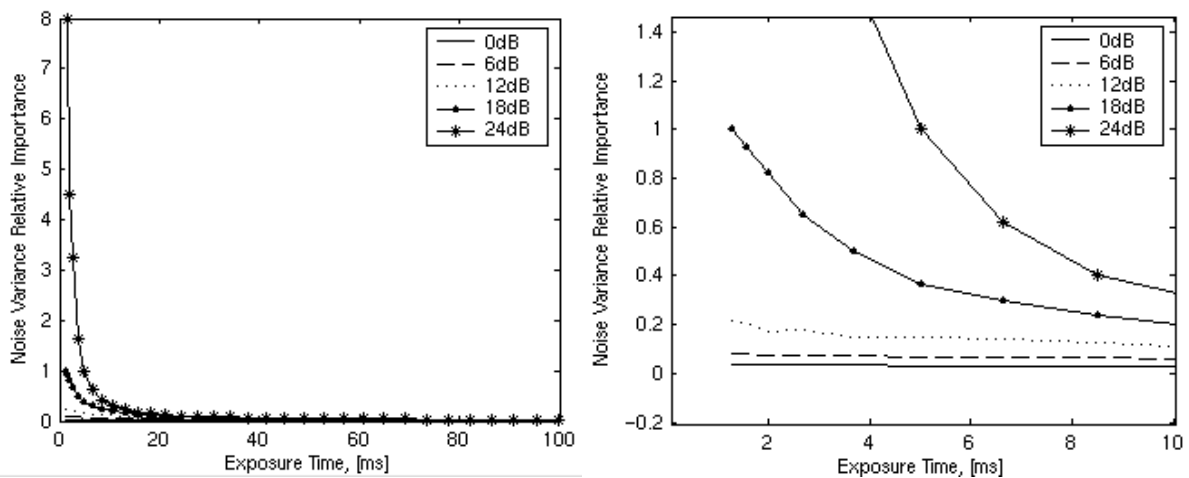


Figure 6-16. (left panel) Division between mean and standard deviation of dark noise versus exposure time. (right panel) Zoom of the left panel graph for small exposure times.

We can further study the mean and standard deviation of the CCD responses, in particular its dependency on the amplifier gain. In Figure 6-17 each curve represents the evolution of the mean (left panel) and standard deviation (right panel) versus the amplifier gain obtained with a fixed exposure time. On the horizontal axis the gain is given in decibels, from -6 dB to 42 dB. Twenty curves are drawn for exposure times going from 1.3 ms to 20.3 ms every 1 ms.

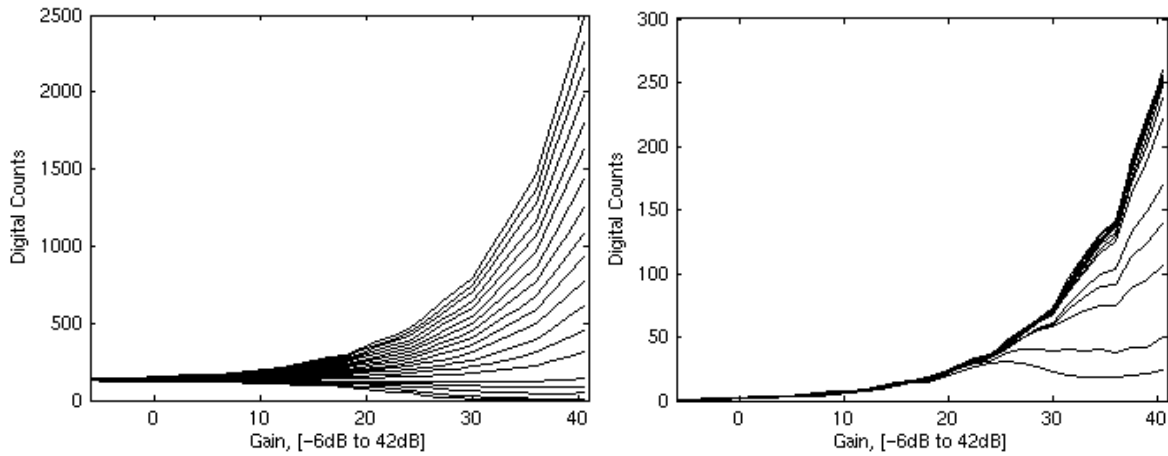


Figure 6-17. Mean (left panel) and standard deviation (right panel) of the CCD dark noise. Each curve represents the dark mean or standard deviation measured on digital counts versus the amplifier gain. Each one is obtained with a fixed exposure time. Twenty curves are drawn going from 1.3 ms (bottom) to 20 ms (top) in 1 ms steps.

From Figure 6-17 we clearly see the change of shape of the curves when augmenting the exposure time. This is justified by the integral nature of the acquisition system. Contrary to the always increasing mean, the standard deviation evolves quicker for small values of the exposure time. We want to illustrate how and why the standard deviation of the dark noise makes the acquisition system lose precision. We take as an example the curve in Figure 6-17 relating standard deviation in digital counts with gain in dB when fixing exposure time at 10 ms. This curve is shown alone on the left panel of Figure 6-18. On its right panel we show the same curve but gain is expressed as an amplification factor. We see that this curve can be approximated by a straight line, even if it does not fit perfectly. On this curve we take three points at 3, 10, 20 and 30 dB, these points correspond to an amplification factor of 2, 10, 100 and 1000 respectively.

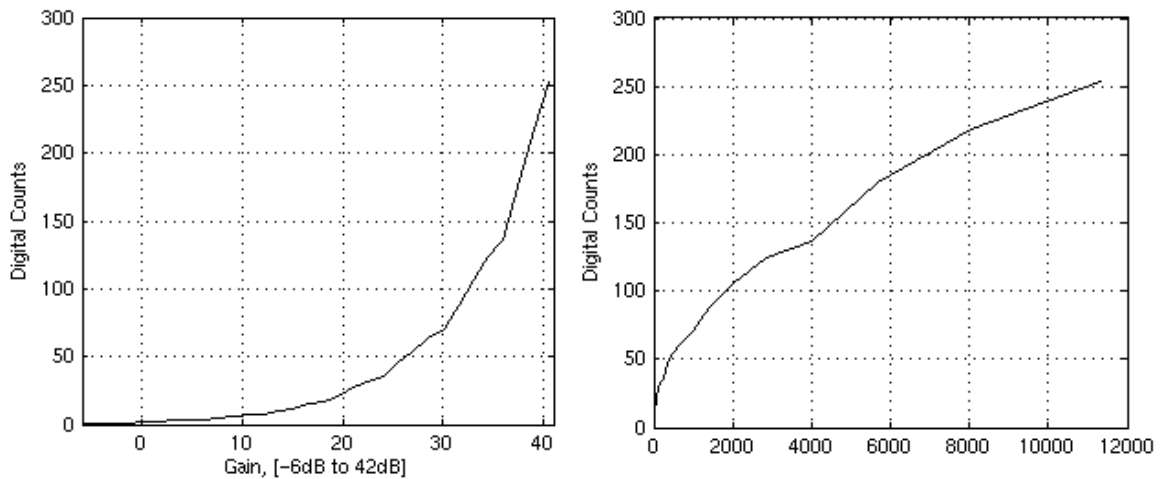


Figure 6-18. (left panel) Standard deviation measured on digital counts versus the amplifier gain for a fixed exposure time of 10ms. (right panel) Same curve using a linear scale to represent the gain.

Let's focus on one of these points, for instance the one with gain = 10 dB. Its standard deviation value being 7 its correspondent mean is 154 (for a CCD offset of 8). If we suppose that the distribution is Gaussian the value of this pixel has 95.45% probably to be found on the interval $[m-2\sigma, m+2\sigma]$, which corresponds to $[140, 168]$. Unfortunately, we have no way to decide which value in this interval is the real one, this fact implies a loose of precision on the signal. As the signal is coded on 12 bits we have 4098 possible values. For the case where

$\sigma = 7$, the *error interval* contains 28 values, $4\sigma=28$, which should be coded on 5 bits and implies the loss of 5 bits of precision. More precisely the loss of bits, q_{bits} , is given by:

$$q_{\text{bits}} = \log_2(4\sigma), \quad (6.6)$$

i.e. 4.8 bits for $\sigma = 7$. We can also measure this error as a relative error, $e_{\%}$, expressed in per cent of the number of possible values (4096), according to the following equation:

$$e_{\%} = (4\sigma / 4096) 100. \quad (6.7)$$

The information about our four sample points at 2, 10, 20 and 30 dB is summarized on Table 6-2. We tabulate for each fixed gain: the corresponding amplification factor, the measured standard deviation and the calculated values for $e_{\%}$ and q_{bits} using the above formulas.

Table 6-2. Noise evolution at 4 different amplifier gain for an exposure time of 10 ms.

Gain	Amplification Factor	Noise Standard Deviation	Error, $e_{\%}$	Lost Bits, q_{bits}
3 dB	2	3	0.15%	3.6
10 dB	10	7	0.34%	4.8
20 dB	100	23	1.12%	6.5
30 dB	1000	70	3.41%	8.1

At the moment we have characterised the noise by considering the amplifier gain and exposure time. We should not forget that the amplifiers have an offset as well. We have then characterized the behaviour of the amplifier offset. In order to do this, we give different values to the offset and measure the dark noise by varying either the exposure time at a fixed gain or the gain at a fixed exposure time. The amplifier control unit allows 16 different levels of offset.

On the left panel of Figure 6-19 we show a graph of dark noise versus exposure time. Four curves are drawn with values 0, 4, 8 and 12 for the offset. We visually observe that the offset increases all the values of a curve by a constant value. Care must be taken when using at the same time small values of the exposure time and offset=0. The curve corresponding to 0 offset shows this point clearly since it becomes zero for values smaller than 10ms. This fact can seem surprising at first glance because signal information can be lost with such parameters. It is due to a design choice for the electronics, the underlying reason being that the *dark offset* of an image is visually related to its contrast. The choice of an offset=0 at exposure times smaller than 10ms loses signal information on dark areas of the images but augments the contrast. If high fidelity reproduction is the aim of an application this choice must be forbidden. We will discuss more this point in the calibration section of this chapter.

On the right panel of Figure 6-19, mean dark current expressed in digital counts is plotted versus amplifier gain. For low values of the gain and for offset values 4, 8 and 12, the dark noise remains constant and behaves as expected. The curves are in fact translated by a constant value along the digital counts axis. But for offset = 0 the curve can no more be considered as a translated one.

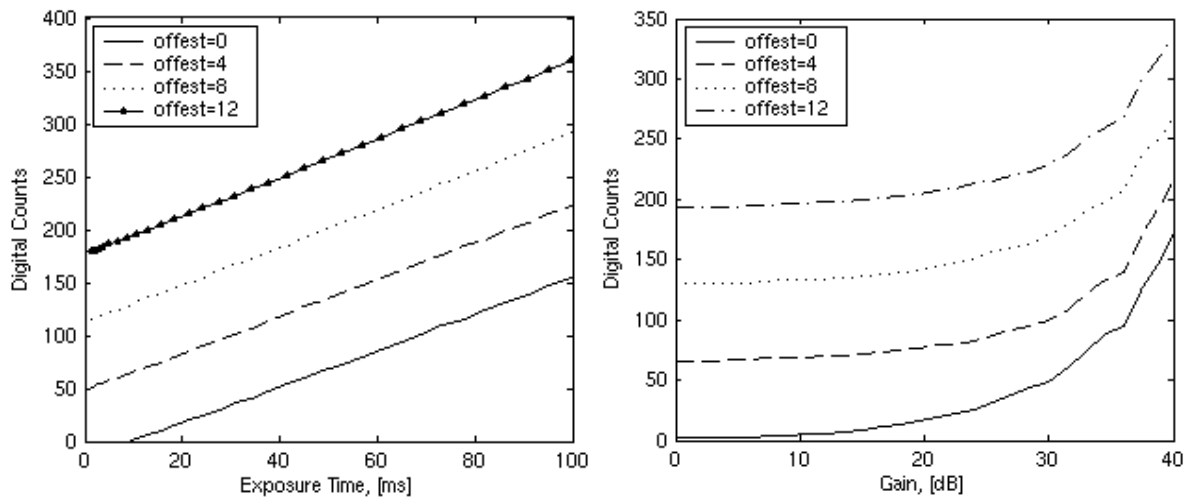


Figure 6-19. Effect of four amplifier offsets on the mean of dark current.

We have presented results based on the mean of dark noise. We have also studied the effect of the offset on the noise standard deviation. We do not present results here because the collected data shows that the offset does not modify the value of the standard deviation. This fact was the expected offset behaviour in well designed amplifiers.

As a conclusion of this section and aiming to better visualize and summarize the data already presented, we show in Figure 6-20 two 3d diagram showing the dependence of dark current noise on exposure time and gain as the same time. The upper plot of this figure presents the noise mean in digital counts while the bottom panel shows the standard deviation of the noise measurements in digital counts. These graphs summarize the behaviour of the camera parameters as far as noise is concerned. The combination of high amplification and big exposure time is seen as giving big levels of noise, both for the mean and the standard deviation.

In this 3d representation we see that exposure time does not affect the standard deviation up to a certain amplifier gain value (~ 10 dB in our case). Dark noise can be considered as an offset that linearly depends on the exposure time. We can either correct this offset in a post-processing stage or integrate part of this correction in the calibration procedure by the use of the electronic offset of the CCD amplifiers.

Three important considerations about the noise can be easily done by the use of these diagrams:

- *Noise offset subtraction.* Even if the mean of the noise can be subtracted from the image signal, this subtraction can affect the quality of the signal. For instance, in the upper panel of Figure 6-20 we see that for 20 ms and a very high amplification (42dB) the mean of the noise is around 2500 digital counts. The range of possible values being 0 to 4095 (12 bits encoded), by systematically subtracting the value 2500 we obtain a practical range of 0 to 1595 values for the useful image signal. This smaller range can be coded on 11 bits. We have then lost one bit of precision.
- *Intrinsic noise.* Looking at the bottom panel of Figure 6-20 we find a characterization of the dark noise of the CRISATEL camera. Indeed, the standard deviation cannot be corrected, but it can be quantify. Consequently this graphs characterizes the remaining level of dark noise that we will obtain from the camera after correction. Decisions

about the free parameters of the system (exposure time and gain) can be made depending on the desired final signal to noise ratio.

- *Amplifier offset.* In general, this offset produces a translation on the Z axis of the diagrams of Figure 6-20. This allows us to produce an easy mental representation of the process. In some particular cases as offset=0 and short time exposures, care should be taken because some deformations are introduced.

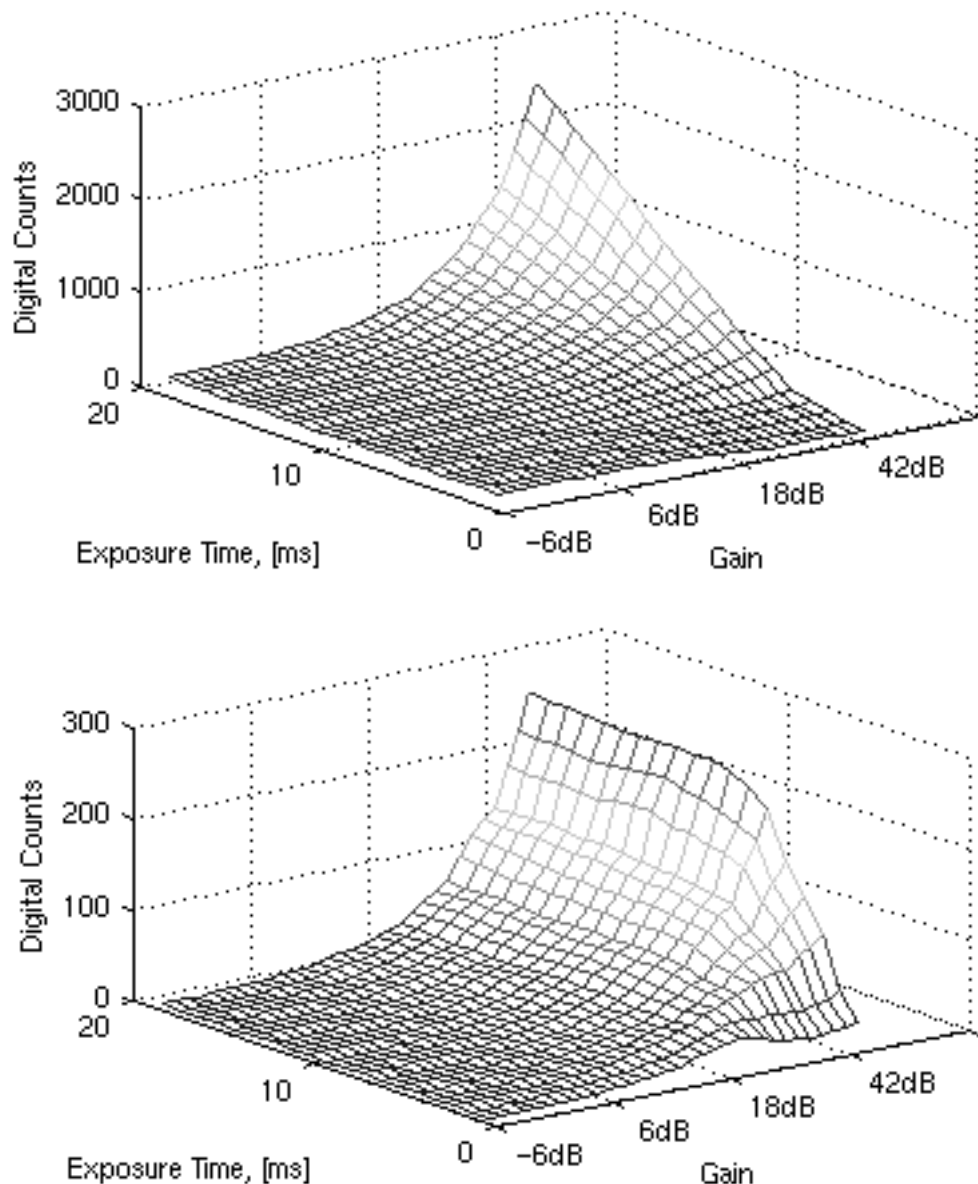


Figure 6-20. (Upper panel) Mean of the CCD dark noise shown as a function of the exposure time and amplifier gain. (Bottom panel) Same graph for the standard deviation.

The results presented on this subsection indicate that it would be better to have a common gain for all the channels, when applicable, in order to keep the dark noise standard deviation per channel constant. We cannot correct the error introduced by the noise standard deviation, a common gain would provide a similar signal to noise ratio for all channels.

6.3.3 Chromatic Aberration

In this section we consider the problem of geometric differences between the images acquired in the different channels induced by chromatic aberrations. The refractive index of glass varies with wavelengths. Furthermore, the interference filters used in our camera have different thickness. This makes the acquisition geometry of the channels slightly different. As a consequence, if the camera is fixed and the images focused individually for each channel, the resulting images will not have the same scale. A characteristic point of the scene may not be imaged in the same pixel in each channel. We illustrate this point by acquiring an image of the simple test chart shown in Figure 6-21 for two different channels. It is composed of a large white band limited by two black bands. The chart was placed vertically and its size chosen such that its image covers the linear array.



Figure 6-21. Test chart used to correct the chromatic aberration.

We chose one filter in the infrared area (centred at 1000 nm) and the other one in the visible spectrum (centred at 680 nm). The lens adjustment being motorised, for each filter the focus is tuned by using a software tool. In the two images we simply note the pixel positions corresponding to the two black/white transitions as shown in Table 6-3.

Table 6-3. Pixel Distance between the black bands.

Filter, [nm]	Pixel position --> Distance
680	10014-1606 = 8408
1000	10041-1573 = 8468

The distance calculated in pixels differs by 60 pixels between the two selected filters. This means that the acquired images need a postprocessing for inter-channel registration. To avoid this, the CRISATEL multispectral camera provides a displacement system that can compensate the differences in geometry for every spectral channel. The system mechanically displaces the whole camera along the optical axis. These displacements can be determined by a calibration process and incorporated in the control software providing the possibility of a fully automatic compensating system. This control software will be developed in the future by the camera constructor.

6.3.4 Spatial Inhomogeneities

A general problem encountered with any imaging system is the spatial inhomogeneity of the lighting. Depending on the position of the lighting system, the camera and the imaged object, the imaged surface presents brighter and darker areas. We performed experiments in order to characterize these spatial inhomogeneities. In this section, we explain how we did it and we present results concerning the CRISATEL camera in a fixed experimental situation.

In order to visualize the differences in energy at different positions of the image plane we proceed with the following experiment:

1. Set up a homogeneous white surface as image plane.
2. Fix the parameters of the system. Note that we will explain in detail how this is made automatically in the “Calibration” section.
3. Take an image per filter of the white homogeneous surface.

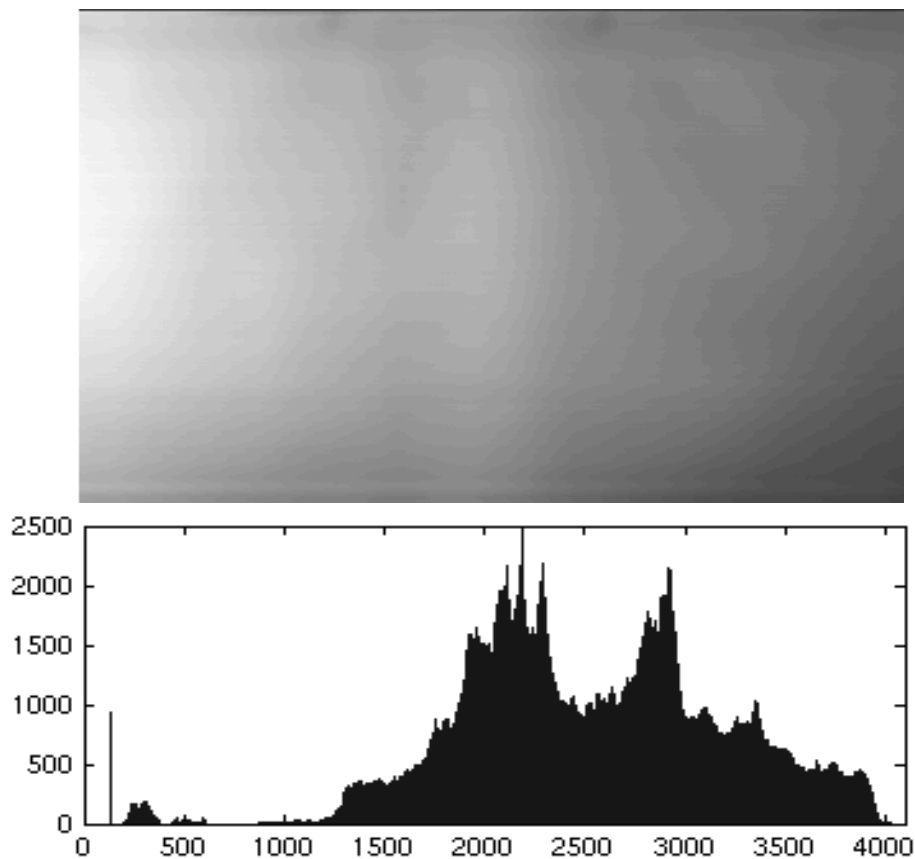


Figure 6-22. (Up) Image of a white homogeneous board using filter at 680nm, (down) its histogram.

After this experiment we obtain a set of $N=13$ images containing information about the spatial distribution of the radiant energy. The images are taken at low resolution to avoid the effects of surface inhomogeneities of the board. We calculate the histograms of the obtained images, this allow the quantification of the error introduced by the irregular spatial distribution of light. In Figure 6-22 we show one of this images corresponding to the 680nm band along with its histogram. In Figure 6-22 we can already see that some areas of the image are brighter than others. If we take an image of a painting this pattern will reduce the quality of the result. Consequently, the identification and analysis of this phenomenon is of major importance for the final quality of the images. Calculating the level contours of the image, see Figure 6-23, we obtain a clearer visual information about the distribution of light over the imaged plane.

By definition a level contour is formed by the points of the image having exactly the same value. In fact, they can be calculated by dividing the histogram in m parts and taking the boundary points between these parts. In Figure 6-23 we chose $m=12$ and we observe that in this particular configuration of the camera and lighting system the energy is stronger on the left part of the image.

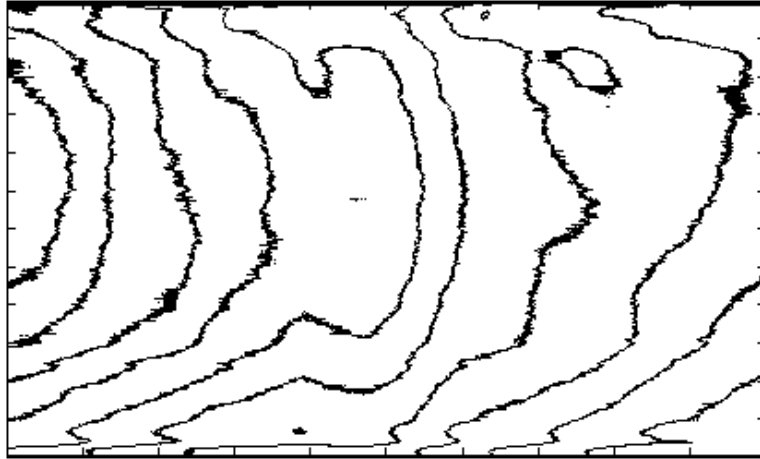


Figure 6-23. Level contours of the image of a white homogeneous board using filter at 680nm.

Of course we expect this “white map” to depend strongly on the position of the lighting system. One question that immediately arises is the dependence of the “white map” on the channel used for the acquisition. If filters are not homogeneous along the different optical paths they can change the spatial distribution of the radiant energy too.

In Figure 6-25 we show the image of a white board, its histogram and its level contours for the 480nm filter. We can directly compare these images with the ones at 680 nm presented in Figure 6-22 and Figure 6-23. We clearly see that the distribution of the level contours is not the same even if the overall image looks similar. In order to better understand this point we calculate the difference image between both the image at 480 and 680nm. This difference map is presented in Figure 6-24. This indicates that the lighting homogeneity must be characterized for each channel in order to correct the spatial inhomogeneities of the lighting.

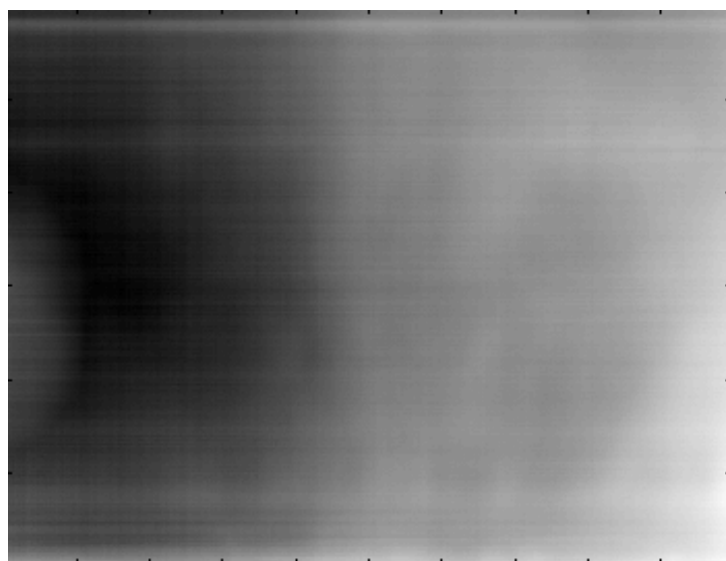


Figure 6-24. Difference map between images of a white panel using filters at 480 and 680 nm. Maximum and minimum values of the 12-bits image difference are white and black respectively. We appreciate that differences can be significant for different channels.

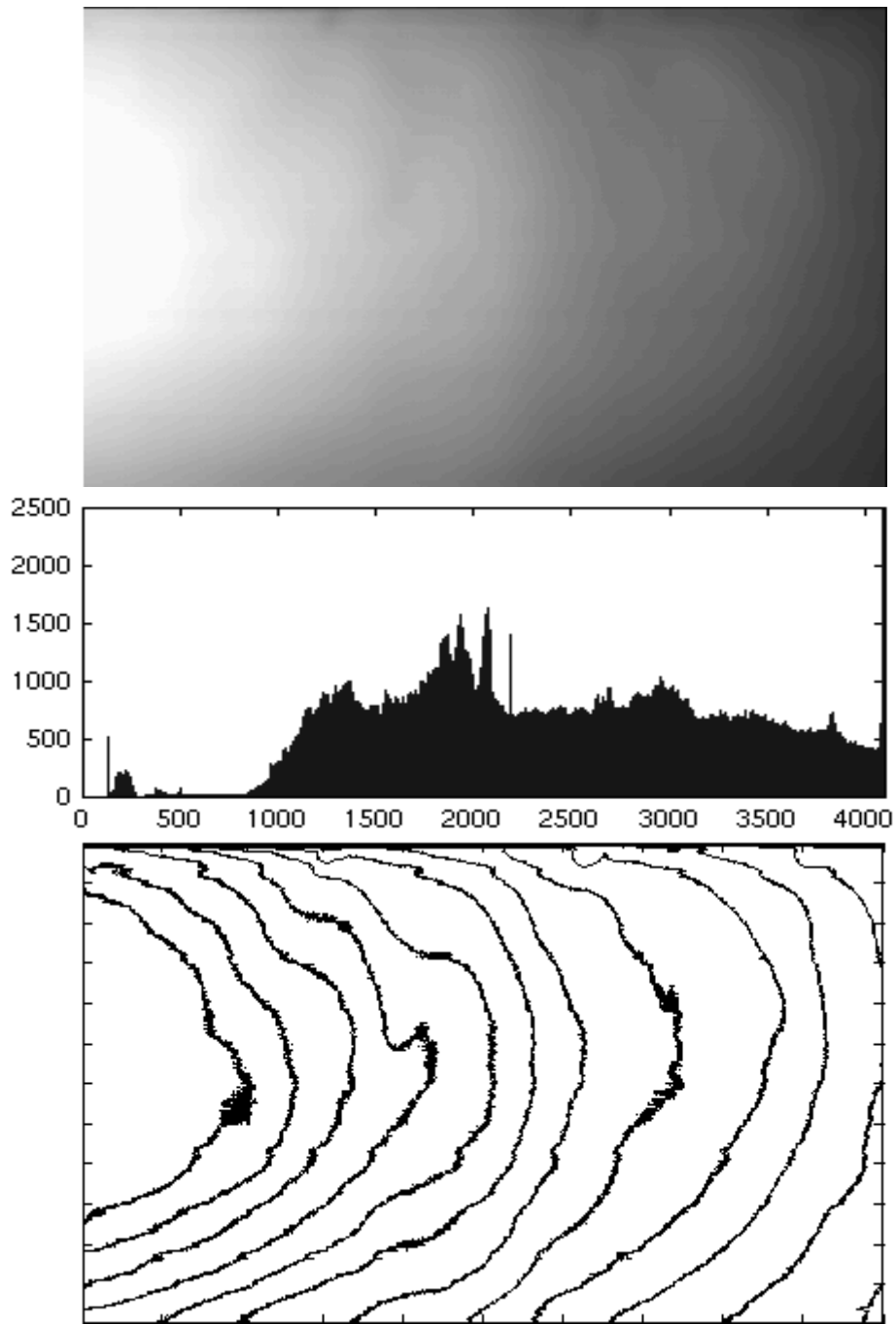


Figure 6-25. (Up) Image of a white homogeneous board using filter at 480nm, (middle) its histogram, (down) corresponding level contours.

6.4 Calibration

Once the system has been studied the definition and implementation of a calibration procedure is the following natural step. Data collected from the performed experiments form the basis for this definition. The calibration consists of a series of experiments which will allow us i) to set up the parameters to be used for the acquisition of images and ii) to collect experimental data for the a posteriori correction of the obtained multispectral images. At the end of the procedure, corrections should be applied and the corrected images are expected to have a high dynamic range and good spatial lighting homogeneity.

In order to attain these objectives we distinguish between two factors:

- Fixing the camera parameters.
- Characterizing lighting and CCD inhomogeneities.

6.4.1 Fixing camera parameters

We start our discussion with the camera parameters. The most fundamental part of the calibration system aims to obtain a high dynamic range by appropriately fixing the camera parameters. These parameters are mainly the exposure time and the amplifier gain and offset. In our case two of these parameters, the amplifier gain and offset, can be fixed a priori.

There are three preliminary steps that should be performed before calibration:

- i) The camera aperture is not electronically controlled. Consequently, this parameter cannot be optimised and should be fixed manually to obtain enough deep of field over the surface we desire to scan.
- ii) The camera should be on focus for all its channels. This is performed by a in-built manual software provided by the camera constructor.
- iii) The hardware correction for inter-channel registration should be done. If this step is not implemented it can be substituted by a postprocessing stage where the registration is performed by software.

The gain can be fixed depending on the quality we want to obtain. Figure 6-20 in section 6.3.2 shows the relationship between this parameter and the dark noise introduced in the signal. There is a direct non-linear relationship between them. Due to our experiment with dark current this relationship is characterized and we know the expected error for every value of the amplifier gain. As a consequence, this parameter can be fixed to a value giving a compromise between low noise and an acceptable acquisition time. We choose this value to be 8dB. We note that this choice is dependent of what our application considers a compromise between acceptable scanning time (i.e. one hour) and good image quality (i.e. 10 representative bits in the obtained digital signal).

If the amplifier gain is fixed its offset can be fixed too. Ideally we should choose the smallest possible offset in order to obtain the maximum dynamic range. In practice this is not possible because the level of noise limits the minimal offset that can be used. Using a smaller offset would produce the lost of one part of the information received by the CCD. We want to keep all noise variability in the image. Considering a Gaussian distribution, the value of a pixel is on the interval $[m-3\sigma, m+3\sigma]$ with 99.74% probability, where m is the mean of the dark noise distribution and σ is its standard deviation. As the level of noise for every value of the gain

has been measured and characterized (see Figure 6-17) the values of m and σ are then known. Consequently, we can directly choose an appropriate offset by the use of this information.

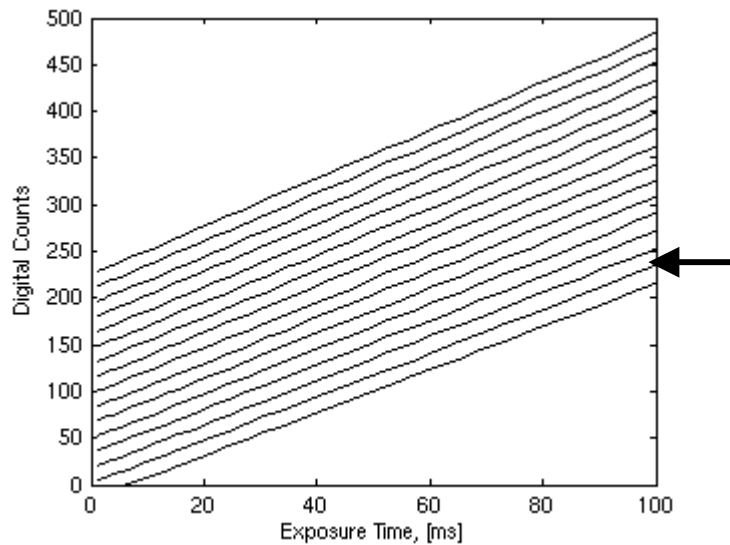


Figure 6-26. Effect of the 16 offsets on the camera dark current experiment. Gain is 8 dB for the selected curve (pointed by the arrow).

In Figure 6-26 we can see the effect on the mean value of the noise of some values of the offset accepted by the amplifier when gain is fixed at 8dB. The arrow indicates the chosen curve that correspond to the offset value 1. This value is the smallest possible, knowing that for a gain of 8dB the standard deviation of the dark noise is around 8 for a dynamic signal range of [0, 4096]. In order to better illustrate this point we show on Figure 6-27 two curves (solid lines) corresponding to the use of offset=0 (left panel) and offset=1 (right panel). Along with these curves we draw dashed lines representing the limits at -3σ and $+3\sigma$ of the noise distribution. In the space between the two dashed lines 99.74% of the noise is included. Offset zero can not be used as noise information is lost for exposure times smaller than 12 ms. For offset=1 information is lost for exposure times less than 3 ms. Since we will normally work at values bigger than 5 ms, that means that the first level of offset can be chosen without loose of information.

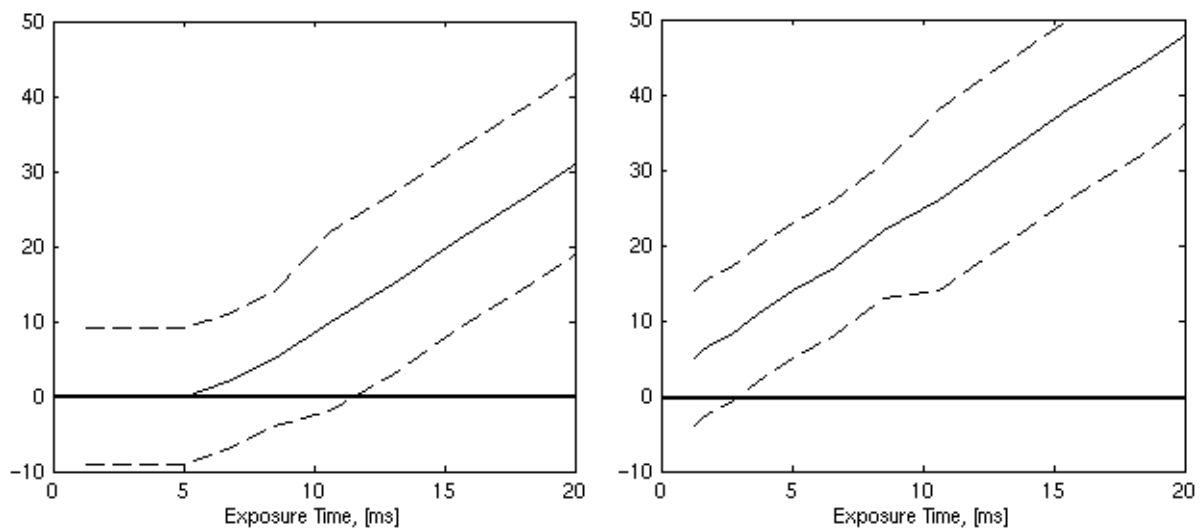


Figure 6-27. (Left panel) Curve for offset=0 showing the camera mean dark current represented by solid lines, with its confidence interval, represented by dashed lines. (Right panel) Same data for offset=1.

Once both the amplifier gain and offset are fixed the only free parameter left is the exposure time. Finding the exposure time that gives the highest dynamic range is to solve a one-dimensional optimization problem. Even if this problem is mathematically affordable, it is unfortunately very delicate in practice. A big part of our calibration system is indeed dedicated to the quest for this parameter.

6.4.2 Characterizing lighting and CCD inhomogeneities

Another part of the calibration procedure is the gathering of data that will be used for the correction of “perturbing” physical phenomena associated to the acquisition process. In the calibration procedure we take into account two important spatial phenomena:

- The inhomogeneous spatial distribution of the lighting.
- The varying behaviour between pixels of the CCD array. In this framework we will study the two following properties:
 1. dark current noise contribution on each individual pixel,
 2. individual pixel responses for the same level of incoming radiant energy.

The way of dealing with these above phenomena is treated in detail in the next section.

6.4.3 Three steps Procedure

The defined calibration procedure consists in three stages. Step 1 is compulsory the first, both Step 2 and Step 3 depend on the parameters obtained from Step 1 and can be done in any order.

6.4.3.1 Step 1: Preliminary exposure time adjustment and spatial maps definition

Experimental configuration: A white homogeneous board must be positioned at the position of the paintings to be scanned and the lighting system should be warmed up.

In this step our aim is to define a first appropriate value of the exposure time for each filter and the map of the spatial inhomogeneities of the lighting per filter. As the procedure is exactly the same for all filters we explain it only for one filter in the following.

Procedure:

1. We select an area, noted G , of the homogeneous white board and we determine by dichotomy the exposure time that does not saturate the CCD. As a basic criteria for the optimization we want the mean value of the area G to attain a certain value s . This s is close to the maximum possible value or saturation of the signal (4096 in the case of 12-bit quantisation) but it is not the maximum because we leave a security area, so called *headroom*. For instance, we use normally a value of 3800 where 296 levels are kept for security. The dichotomy algorithm finds a suitable exposure time whose mean camera response on the area G is equal to the value s . This is made in a reasonable time. The choice of a particular area is not important as we just seek for a first approximation of the exposure time.

2. Using this first approximation we acquire an image of the white board. This is important as we want to calculate the exposure time based on “the biggest and brightest” area of the white image. This, of course, requires some spatial analysis that we perform using the following automatic algorithm:
 - Binarization of the image based on the histogram. We set to one the brighter parts of the image and to zero the rest. This binarization implies the calculation of the gravity centre of the histogram, its maximum and the posterior selection of the brightest band.
 - After the above calculation we could identify the brightest parts of the image, but in a real situation it could happen that two or more very bright areas are found in different positions of the image. This is dependent of the relative position of the camera, the imaged plane and the lighting system. In order to be robust just select the largest of these areas. This is performed by a labelling algorithm that runs over the binarized image. Once the image is labelled we choose its biggest connected component.
 - At the end we determine the bounding box of the selected bright area. We then choose a smaller box inside this bounding box which is considered the biggest and brightest homogeneous area on the image.

In Figure 6-28 we show a diagram of the process just described with results obtained with the 800 nm filter.

3. By performing again a dichotomy search inside the area found in stage 2 we obtain a robust value of the exposure time. Once this value is known for the brighter places of the image we can acquire a full image of the white board using this value, knowing that most pixels of the image will not be saturated. If some of them are saturated this is due to specular reflections that are present on the reflectance surface. The obtained white image is stored for a posteriori image correction.

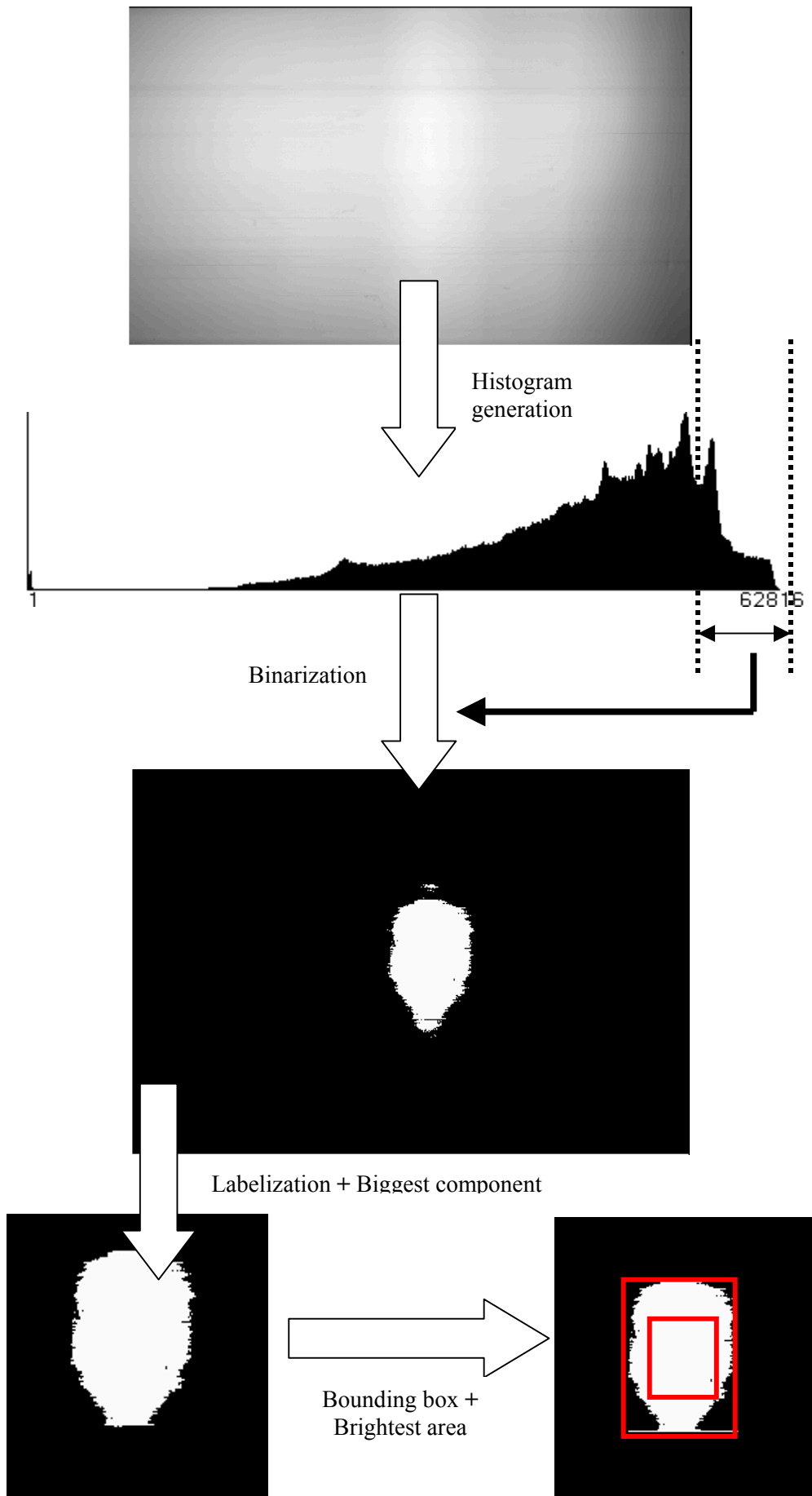


Figure 6-28. Diagram of the automatic calculation of the biggest and brighter area in a white image taken using filter at 800nm.

6.4.3.2 *The problem of Step 1: complete exposure time optimization*

The above procedure which is the main part of Step 1 is robust and finds suitable values for the exposure times. But there is an underlying assumption that should be respected. This assumption is that the white panel positioned in front of the camera is a “perfect white” in the sense that its spectral reflectance function is perfectly flat (all wavelengths have the same reflectance factor) and its constant reflectance value is 100%. This is of course not achieved in reality. There are two kinds of solution to this problem:

1. To introduce a calibrated reflectance patch on the system.
2. To measure the spectral reflectance of the white board material used on the calibration and to introduce this a priori information for correcting the obtained exposure times. In fact, knowing its spectral reflectance and the spectral transmittance of a filter we can know if the imaged white board is going to appear not white but grey. This is the source of error that should be corrected.

The first solution is usually chosen for calibration. In the following of this section we describe a calibration procedure to be added to Step 1 when a calibrated reflectance patch is used. This procedure has been implemented and tested. It is precise but cumbersome and time consuming for the user. This is the reason why our final version of the calibration system uses the second solution based on a priori measures of the white board reflectance. This second solution is presented at the end of the section.

Procedure with a calibrated reflectance white.

Experimental configuration: A black board (or curtain) must be positioned at the position of the paintings to be scanned. A calibrated reference white patch as the one shown in Figure 6-29 is positioned on the board. The position of the reference white patch can be freely chosen by the user as the system automatically will detect its position on the dark board.



Figure 6-29. Photograph of the calibrated white patch used in our experiments.

In this step we look for a precise value of the exposure time. This value will be kept and reuse for the following multispectral image acquisition. This automatic procedure is described in more detail in the following.

Note that, as in Step 1, Step 2 consists in the repetition of the following algorithm for every filter:

1. We take an image of the whole area using the exposure time found in step 1.
2. As the experimental configuration consists in a white patch over a black board, finding the position of the white patch requires simply:
 - A binarization on the image based on a bimodal histogram.
 - The computation of the centre of gravity and of the bounding box of the binarized image. Note that as the histogram of the image should be bimodal we do not need a labelling algorithm as in step 1. However, this algorithm could be easily introduced in our implementation for robustness or if a more complex background needs to be set-up.
 - Knowing the bounding box and the shape of the white patch (a circle), it is trivial to determine an enclosed square box where all pixels belongs to the calibrated white patch.

In Figure 6-30 we show a diagram of the above process.

3. We proceed to a dichotomy search over the area of the included box which leads us to the final value of the exposure time. We calculate the mean intensity of the included box which has a sufficiently large population of pixels.

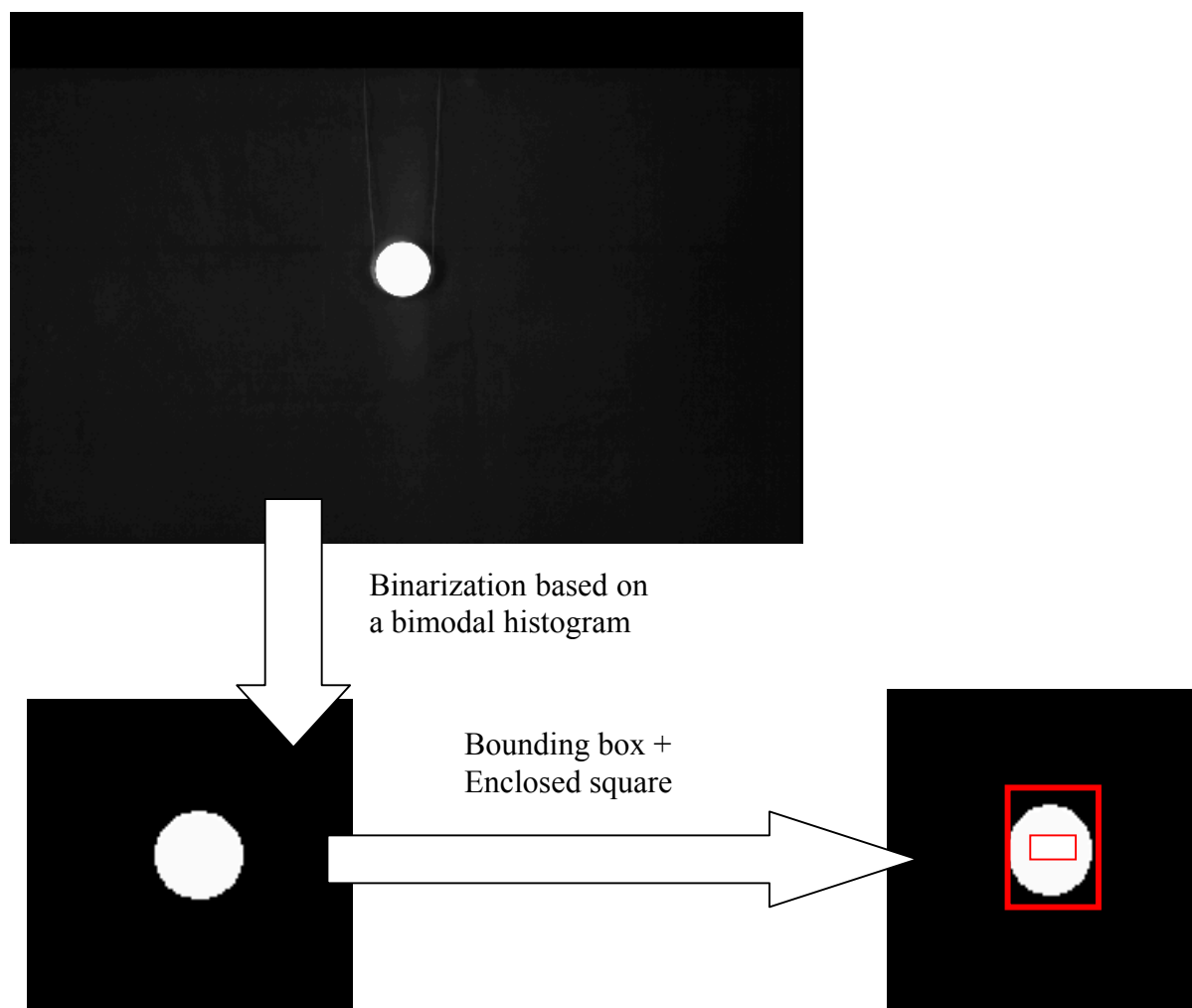


Figure 6-30. Diagram of the automatic determination of the inscribed square from an image of the white patch shown in figure 17 over a black background.

Procedure with known spectrophotometric measurements of the white board

In order to determine the correction factor for each channel exposure time we must know the relationship between the “perfect” white and the white board we are using for calibration, for this specific channel. For that, we measured the spectral reflectance of the plastic white board. We used a Minolta CS-1000 spectrophotometer and an halogen lamp. The geometry of the experiment was 45/0, indicating that the camera view direction is along the normal direction to the surface to be measured and the lamp is at 45 degrees. We proceeded as follows:

- We measured with the spectrophotometer the spectral radiant energy of our reference white patch, the calibrated labsphere shown in Figure 6-29.
- We measured similarly the white board chart. The lamp and the spectrophotometer were kept on the same positions. The board was moved to take five measures in five different places. From these measures we took out the two extreme curves and calculate the spectral radiant energy as the mean of the three remaining curves.
- The white board mean radiant energy has been divided by the measurements obtained on the labsphere. The resulting mean spectral reflectance with values normalized between 0 and 1, is presented on the left panel of Figure 6-31.

On Figure 6-31 we observe that the spectral reflectance of the white board decreases considerably around 400 nm. On the other parts of the spectrum there are smaller differences between the board and the calibrated labsphere. This behaviour is typical of white materials without phosphorescent pigments that enhance the reflectance in the far blue part of the spectrum. Knowing its regular shape this spectral reflectance is acceptable as calibration target. We can mention that producing a large white homogeneous surface made of a material with a flat spectral response would be, at the present time, extremely expensive.

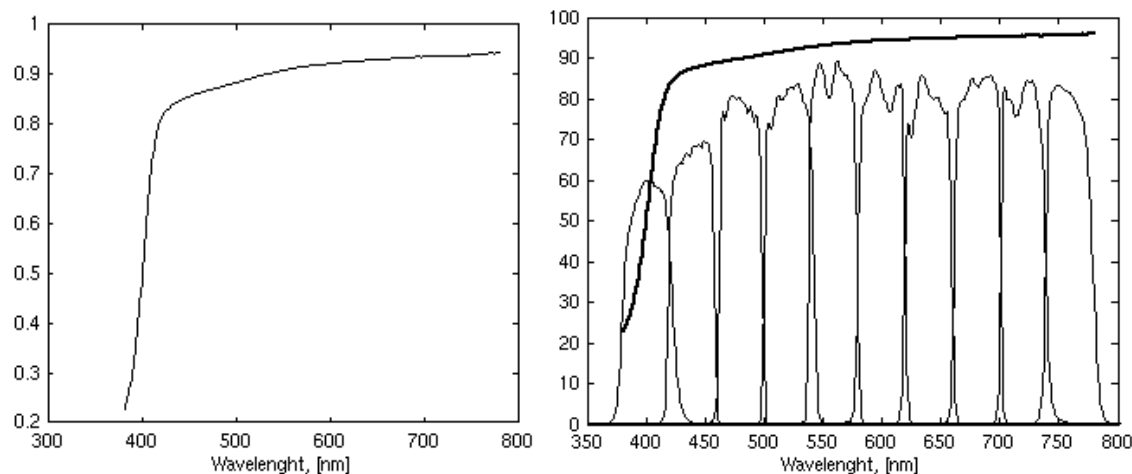


Figure 6-31. (left panel) Mean spectral reflectance of the plastic white board used for calibration. (right panel) Mean spectral reflectance of the white board and filters spectral transmittance on the visible parts of the spectrum.

We must correct the effect of the non flat response of the white board used for calibration. On the right panel of Figure 6-31 are superimposed the spectral transmittance of the ten filters belonging to the visible part of the spectrum with the reflectance of the white board, all expressed in per cents. A multiplicative correction factor has to be applied to the exposure time optimised for the white board for each channel. This takes into account that the white board is darker than a reference white patch. Without this correction factor an image including a reference white would be saturated. The ideal correction factor p_k for channel k , $k=1 \dots K$, would be defined, according to the image formation process modelled in Chapter 2, by:

$$p_k = \frac{\int_{\lambda_{\min}}^{\lambda_{\max}} r_{WB}(\lambda) l_R(\lambda) o(\lambda) \phi_k(\lambda) \alpha(\lambda) d\lambda}{\int_{\lambda_{\min}}^{\lambda_{\max}} l_R(\lambda) o(\lambda) \phi_k(\lambda) \alpha(\lambda) d\lambda}, \quad (6.8)$$

where we denote the spectral transmittance of the k -th optical colour filter by $\phi_k(\lambda)$ and the spectral reflectance of the white board by $r_{WB}(\lambda)$. The lighting spectral distribution, $l_R(\lambda)$, the spectral sensitivity of the CCD array, $\alpha(\lambda)$, and the spectral transmittance of the optical systems in front of the detector, $o(\lambda)$, can be considered constant at first approximation in the bandwidth of filter k . Then, we can estimate p_k as follows:

$$p_k = \frac{\int_{\lambda_{\min}}^{\lambda_{\max}} r_{WB}(\lambda) \phi_k(\lambda) d\lambda}{\int_{\lambda_{\min}}^{\lambda_{\max}} \phi_k(\lambda) d\lambda}. \quad (6.9)$$

When working with discrete signals, the vector $\mathbf{p}_K = [p_1 p_2 \dots p_K]^t$ representing the correction to all K filters may be described using matrix notation as

$$\mathbf{p}_K = \mathbf{\Phi}^t \mathbf{r}_{WB} / \mathbf{\Phi}^t \mathbf{1}, \quad (6.10)$$

where $\mathbf{\Phi}$ is the known matrix of filter transmittances, that is $\mathbf{\Phi} = [\phi_k(\lambda_n)]$, \mathbf{r}_{WB} is the vector containing the sampled spectral reflectance function of the white board and $\mathbf{1}$ is a vector representing perfect reflectance that contains the value 1 on all its elements. Note that operation “/” refers here to the element by element division between two vectors.

The calculated correction factors per visible channel for the plastic white board are presented on Table 6-4. This correction is not a post treatment, it is applied to the exposure times in order to balance all the channels. We note that balancing the channels are more important than finding exposure times that match a perfect white reflectance surface to the maximum of the dynamic range. In effect, a headroom has to be introduced on the 12 bits scale in order to limit the risk of image saturation. This practical fact makes the concept of maximum of dynamic range rather fuzzy. Thus, the concept of balance and equal scaling per channel remains the most important factor and it is well taken into account by the use of the above defined correction factors.

Table 6-4. Per filter correction factors for the plastic white board

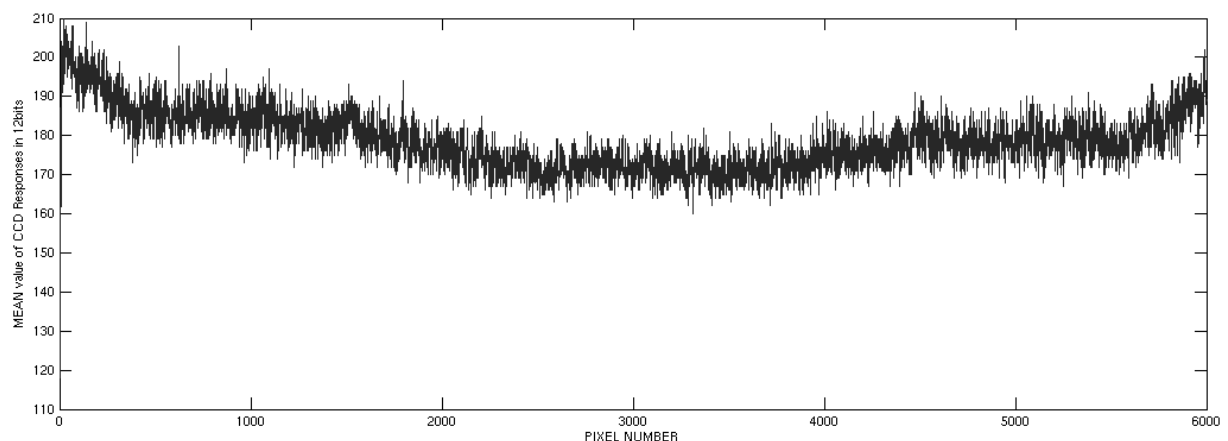
Filter, [nm]	Factor
400	0.5563
440	0.8683
480	0.8973
520	0.9176
560	0.9321
600	0.9415
640	0.9466
680	0.9504
720	0.9532
760	0.9555

The three correction factors for the three channels on the infrared are chosen as equal to the factor obtained by the 760nm filter. This is justify because the reflectance remains very flat for most of the materials in this part of the spectrum. We use this property since the Minolta CS-100 spectrophotometer is not sensitive in the infrared.

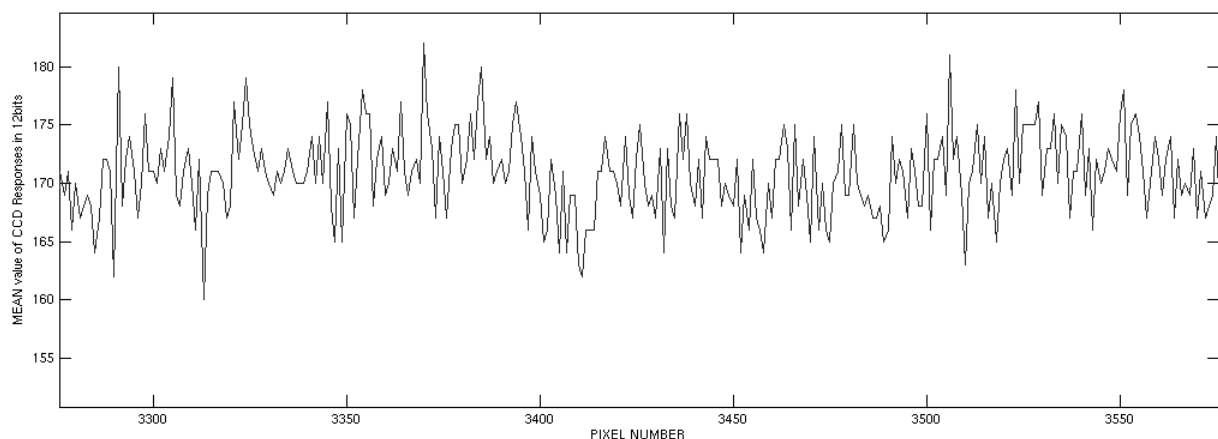
6.4.3.3 Step 2: Per pixel Dark Current

Experimental configuration: The camera lens must be occluded by using an opaque (metallic) cap. In the case of the CRISATEL camera there is a built-in mechanism that allows the occlusion of the camera to be electronically controlled. No direct light reaches the CCD and we can take dark images. The lighting system should not be switched off. This test aims to measure the dark noise contribution per pixel along with the possible stray light getting to the CCD.

This step is much simpler to implement than Step 1. We just need to take a dark image and calculate the mean and standard deviation of the lines of this image, this correspond to the mean and standard deviation of each pixel of the CCD. Afterwards combining this two statistics we build a correction table that will correct every pixel of the CCD in the acquisition stage. In order to illustrate the necessity of this step, we include Figure 6-32 where we represent the mean values of the pixels in even positions on the CCD (they are treated by the same amplifier). We clearly see that the variability of dark noise between pixels must be taken into account.



(a) all even pixels



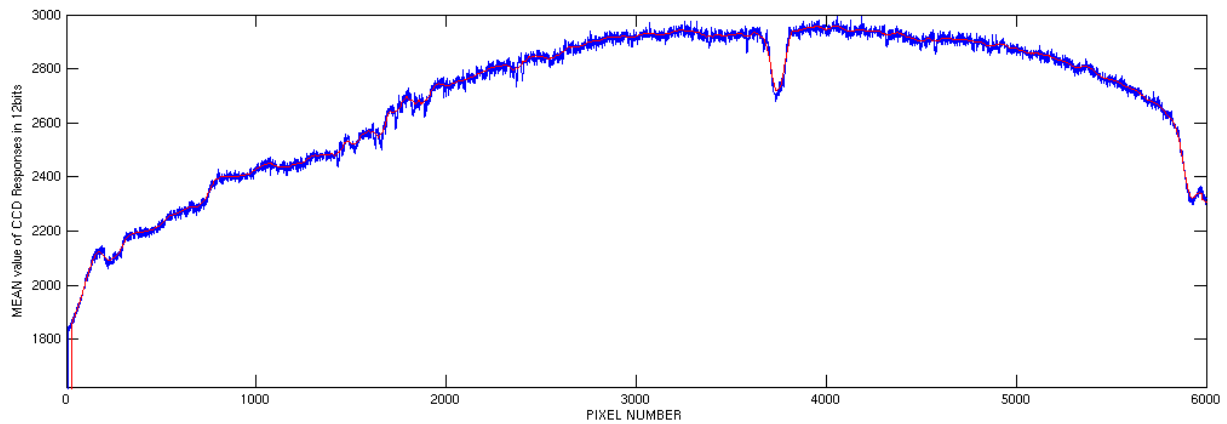
(b) detail of an area of the CCD

Figure 6-32. Mean value of the dark current per even pixel.

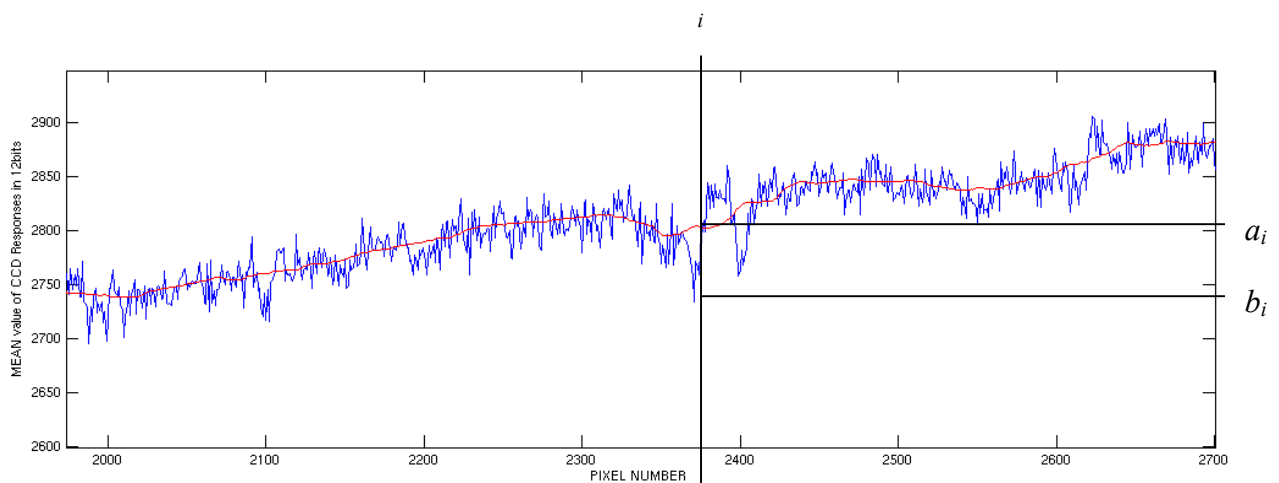
6.4.3.4 Step 3: Per pixel gain

Experimental configuration: The previous white board must be positioned at the position of the paintings to be scanned and a diffuser introduced in the optical path. Using a diffuser we try all pixels of the CCD to locally receive the same amount of radiant energy. The CRISATEL camera has a built-in electronic mechanism that allows the interposition of the diffuser in the optical path.

On the upper panel of Figure 6-33 we show the graph of the mean values of the even pixels of the CCD. Due to the use of a diffuser, this curve should be smooth, presenting only low frequencies. This is not the case. We observe medium frequencies which we assume as resulting of optical inhomogeneities of the diffuser. We also observe high frequencies which are due to pixel sensitivity inhomogeneity. A zoom is performed on the bottom panel of Figure 6-33 to show how the intensity of the pixels changes locally. In order to reinforce this observation we superimpose the same data after being low-pass filtered. In fact, this experiment aims to collect the necessary data to correct this local differences between both curves.



(a) All even pixels



(b) Detail of an area of the CCD, note the differences between a pixel and its filtered value (in red).

Figure 6-33. Mean value of the CCD pixels imaging a white board with a diffuser.

When the diffuser is introduced on the system, part of the light no more reaches the CCD and the exposure times calculated on Step 1 is not valid anymore. This creates the problem of determining which exposure times to use when performing the experiment. One evident solution would be to apply Step 1 again for determining the new exposure time. Step 1 being very time consuming, this would increase significantly the calibration time.

In order to solve this problem we decide to determine an a priori multiplicative factor to be applied to the exposure times issue from Step 1 when using the diffuser. For that we perform the following experiment. We applied Step 1 on a white board without using the diffuser and, afterwards, we applied it again by using the diffuser. From this experiment we can calculate the sensitivity ratio “non diffuser/diffuser” per channel by dividing the two corresponding exposure times determined by Step 1. These ratios are shown in Figure 6-34. As we can see in this figure the channels have about 3 to 6 times more signal without the diffuser. We choose a trade-off value of 3, represented on the figure by a dashed line. This indicates clearly that the spectral transmittance of the diffuser is not flat in the wavelength range of the camera. However, as this transmittance will not change in time, we can tabulate this set of sensitivity ratios. For a given channel we will apply a multiplicative factor to the exposure time equal to the corresponding sensitivity ratio non-diffuser/diffuser.

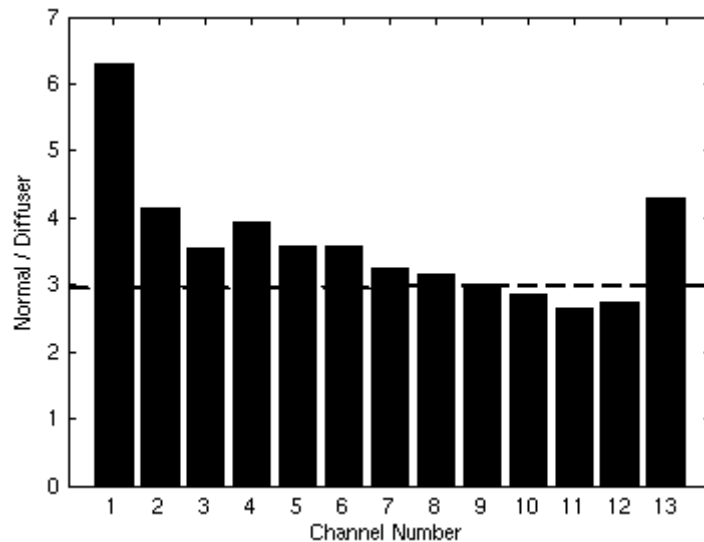


Figure 6-34. Sensitivity ratio “non diffuser/diffuser” per channel. Dashed line represents the multiplicative factor applied to exposure times to work properly with the diffuser.

We assume a good homogeneity of the spectral sensitivity on the linear CCD array. This assumption is justified by physical considerations but it appears very difficult to control experimentally. We can then determine the per pixel gain by performing the diffuser experiment in a single channel.

The gain g_i is to be calculated per pixel i , $i=1, \dots, 12000$, 12000 being the number of pixels of the CCD array. We note b_i the actual i -th pixel value, n_i the dark current noise offset per pixel and v_i the underlying ideal signal. We note that in the case when the CCD array presents no dark noise and the pixels of the cells of the CCD has exactly the same sensitivity we would have $b_i = v_i$. In the real case where these elements are present this relationship becomes:

$$b_i = g_i v_i + n_i . \tag{6.11}$$

Let's note a_i the value resulting from a mean on a window of W pixels centred on the i -th pixel, this leads to

$$a_i = \frac{1}{W} \sum_W g_i v_i + n_i = v_i \frac{1}{W} \sum_W g_i + \frac{1}{W} \sum_W n_i . \quad (6.12)$$

By assuming that the mean of g_i on the W values of the window is equal to 1 we estimate v_i as

$$v_i = a_i - \frac{1}{W} \sum_W n_i . \quad (6.13)$$

The gain is then defined as

$$g_i = \frac{b_i - n_i}{a_i - \frac{1}{W} \sum_W n_i} . \quad (6.14)$$

6.4.3.5 Fully automatic calibration procedure

In this section we emphasize the fully automatic character of our calibration system. In fact, this aspect is not a trivial consequence of our design but it was a prerequisite. The described calibration procedure have been studied carefully in order to require user interaction as minimal as possible. Let's assume that the camera and the projectors have been properly installed to acquire paintings, the lens aperture selected and the focus properly adjusted for all channels. Then, the user has to proceed to the calibration before starting the multispectral image acquisition. Thus, the user is only supposed to warm up the lamps and position a white board in front of the camera before the calibration starts. Afterwards, all the operations performed are automatic.

Occluding the camera optics and introducing a diffuser on the optical path are seemingly easy manual operations but, in practice, they can be delicate and time consuming. Our collaboration with Lumiere Technologie led this company to integrate two mechanical displacement systems on the camera. Figure 6-35 shows a photograph of these mechanisms. They allow occlusion and diffuser introduction to be controlled electronically and make the calibration self-contained

In the design of Step 2 we avoided the use of a white reference patch over a black background, mainly not to introduce the change on scene elements that requires a strong user interaction. This also reduces operation time.

Occlusion System
(metallic plate)

Diffuser

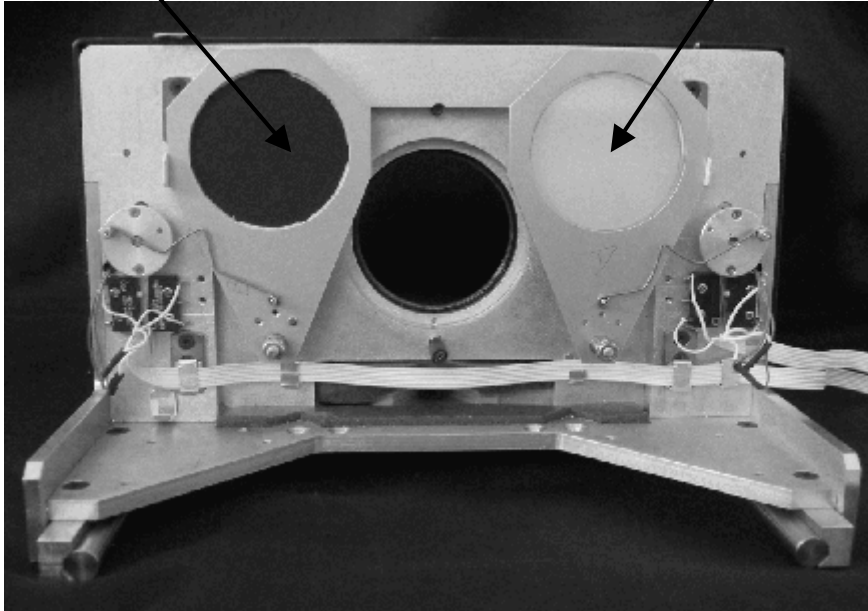


Figure 6-35. Photograph of the camera built-in diffuser and occlusion system.

6.5 Correction System

Once the calibration has been performed in a particular configuration of the CRISATEL acquisition system, we can acquire multispectral images. At this stage the data collected in the three preceding calibration steps are used to correct and enhance the acquired images. This is done by a correction system which is intimately related with the steps of the calibration procedure.

Some care must be taken when dealing with these corrections, even if they seem easy to perform, some details should be taken into account in order not to introduce problems. In this section, we first present these details and afterwards we give some results of the effectiveness of the correction system.

6.5.1 Performing the corrections

In the correction system we have to proceed channel by channel and pixel by pixel to the following sequential operations:

- Correction of the individual behaviour of the CCD pixels by using the two following correction arrays:
 - per pixel dark current offsets (subtraction applied to the raw pixel value),
 - per pixel gains (multiplication by g_i applied to the dark current corrected pixel value).
- Correction of the spatial inhomogeneities.

In Figure 6-36 we show a schema of the operations performed. The first operation being additive we could think that subtracting the mean value of the pixel black current should be enough to remove the noise. But knowing that the standard deviation of the noise distribution is not zero this operation would literary remove from the image one half of the noise variability for dark pixels. If we want to keep all noise variability in the image we should consider that in a Gaussian distribution the value of a pixel is on the interval $[m-3\sigma, m+3\sigma]$ with 99.74% probability, where m is the mean of the distribution and σ is the standard deviation. Approximating dark noise as Gaussian the right subtraction value that keeps 99.74% noise variability in the images is

$$m-3\sigma.$$

Of course, the choice of this value depends on the application. In our case the images will be used for spectral reconstruction and some of the methods that perform this operation take noise into account. If dark patches present erroneous noise distributions due to this cutoff, it could affect the post processing. In other applications the aim can be completely different. Dark noise limits image contrast, then an application aiming at a good visual render of the image could use the value $m+3\sigma$ for the correction. Hence, the dark areas of the images will show no dark noise effects while increasing contrast.

The other delicate correction process is the lighting spatial inhomogeneity compensation, firstly because it has a division nature and secondly because we have to take into account the different resolutions between the inhomogeneity map and the image to be corrected:

- The division is controlled in order to avoid saturation effects due to outliers (erroneous pixels having extreme values) on the uncorrected image. On the other hand outliers on the

map itself are more dangerous. We try to avoid this in two ways, implemented in the calibration stage:

- by taking the maps on low spatial resolution. This introduces a spatial low filtering due to the CCD integration over larger areas of the image. This is because on low resolution the system performs binning of the pixels and a time integration during the linear array motion.
 - by slightly defocusing the camera before taking the map. We consequently introduce an optical low-pass filtering.
- The different resolution level between the map and the image to be corrected is solved by resampling the map. The map is always taken at the smallest resolution. We then use a bilinear interpolation to resample it and correct an higher resolution image. This method respects the low frequency character of the lighting inhomogeneity.

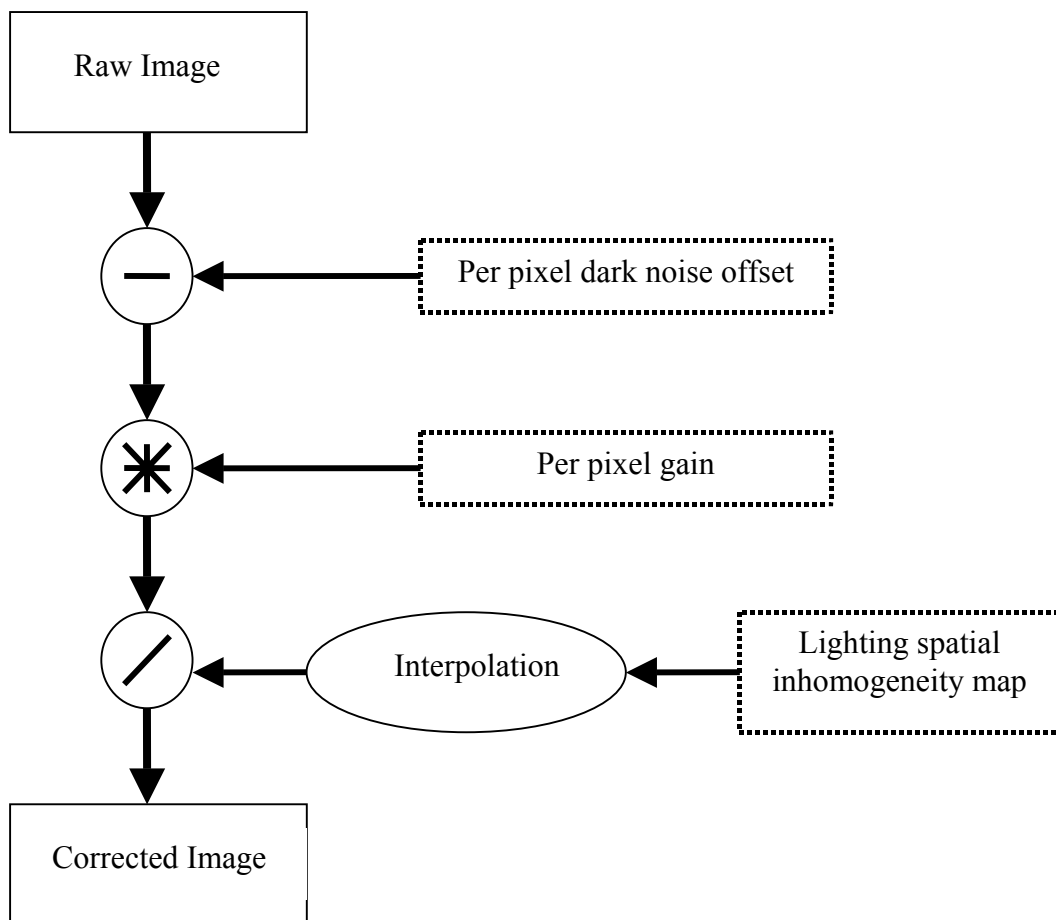


Figure 6-36. Schematic representation of the correction system.

6.5.2 Evaluating corrections.

In this subsection we present a correction example by using an image of the Macbeth chart taken by the CRISATEL camera using the 600nm filter. We can observe in Figure 6-37 the effects of the corrections: (top) raw image obtained by the camera, (bottom) corrected image. We keep on the image the white panel used as a background in order to better show the effects of correction. It is clear that the correction positively increases the visual properties of the image.

To give more insight on the effects of the correction we analyse a particular patch of the imaged chart. We take a 80 by 80 pixels window inside the grey patch we can see on the rightist column and third raw of the chart as positioned on the image of Figure 6-37. In Figure 6-38 we present the histograms of this window before (left panel) and after (right panel) the correction has been performed. We help the visual analysis of these histograms by including in Table 6-5 the mean and standard deviation of the patch after and before correction.

Table 6-5. Statistics over the pixels of a grey patch

	Mean	Standard Deviation
Before correction	1550.3	56.2
After correction	2595.6	59.4

From this table we see that the standard deviation changes slightly. We studied more patches and we found that this variation remains always small and is not necessarily of the same sign. On Figure 6-38 we see that the overall shape of the pixel distribution inside the chosen patch is not significantly changed. This is positive as our correction method does not modify the nature of the images. On the other hand, the mean of the patch is affected, the correction is then mainly performed by the introduction of a correction offset. We also realize that the histogram is slightly less sharp after correction but this difference appears not very significant.

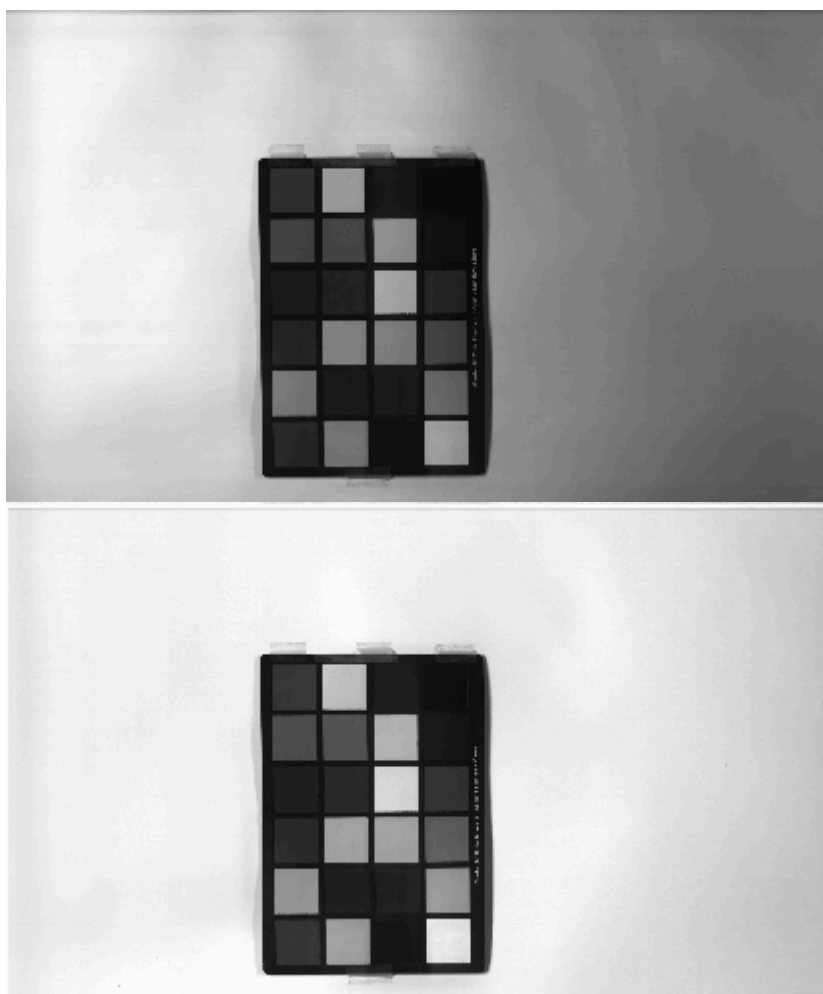


Figure 6-37. (upper panel) Raw image of a Macbeth chart obtained from the CRISATEL camera. (bottom panel) same image after correction performed.

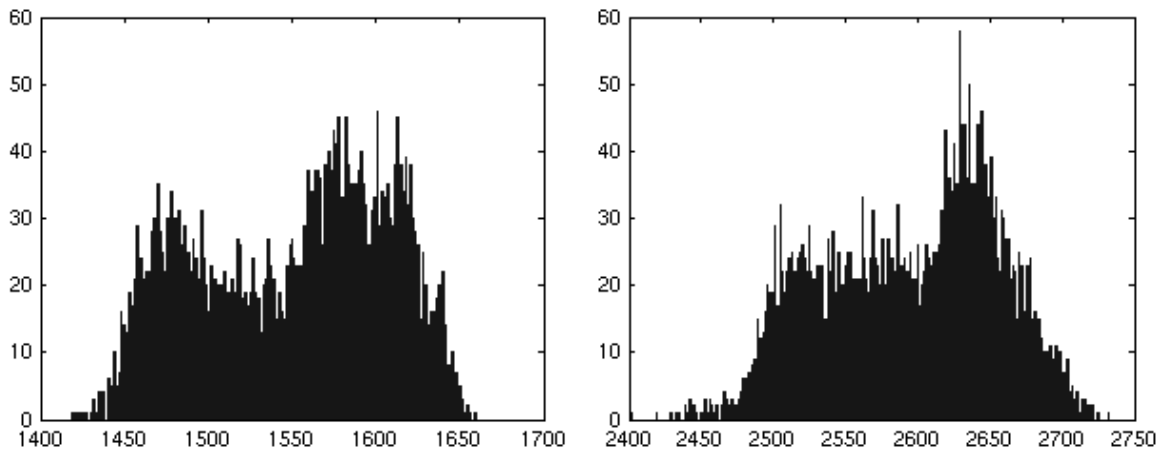


Figure 6-38. (left panel) Histogram of a 80 by 80 window inside a grey path of the Macbeth chart shown on Figure 6-37. (right panel) histogram of the same patch after correction performed.

One particularly interesting test is to see the effects of the correction on a white image. We did this experiment by acquiring a low resolution image of the same white board used for calibration. As a result of the correction we expect to find a white image. To better visualize these results we take two profiles inside the image, one vertical and one horizontal. On the left panel of Figure 6-39 we present the vertical profiles of the raw and corrected images, on the right panel we present their horizontal profiles. Non corrected profiles are the bottom lines on these figures while corrected profiles are the upper curves. It is apparent that the horizontal compensation of lighting inhomogeneities is not complete. This is due to a slow desynchronisation of the lighting system which has been detected by this experiment. The lighting control problem has been recently corrected but not yet completely tested.

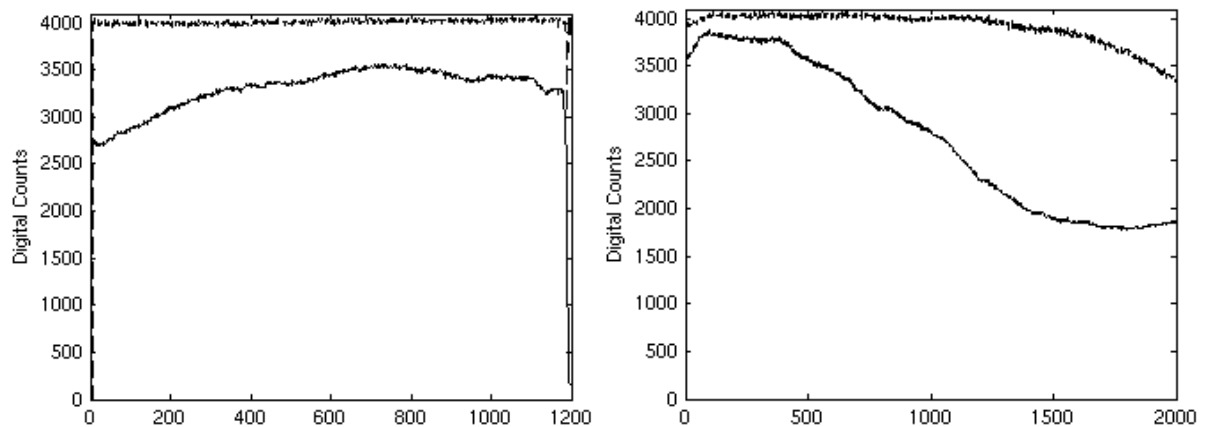


Figure 6-39. (left panel) Vertical profile from a white board image obtained from the CRISATEL. (right panel) Vertical profile. Non corrected profiles are the bottom lines on these figures while corrected profiles are the upper curves.

On Figure 6-40 we show a multispectral calibrated image of the Macbeth chart taken with the CRISATEL camera. Just the ten channels on the visible part of the spectrum are shown. We can appreciate the response in the different channels of the colour patches of this chart.

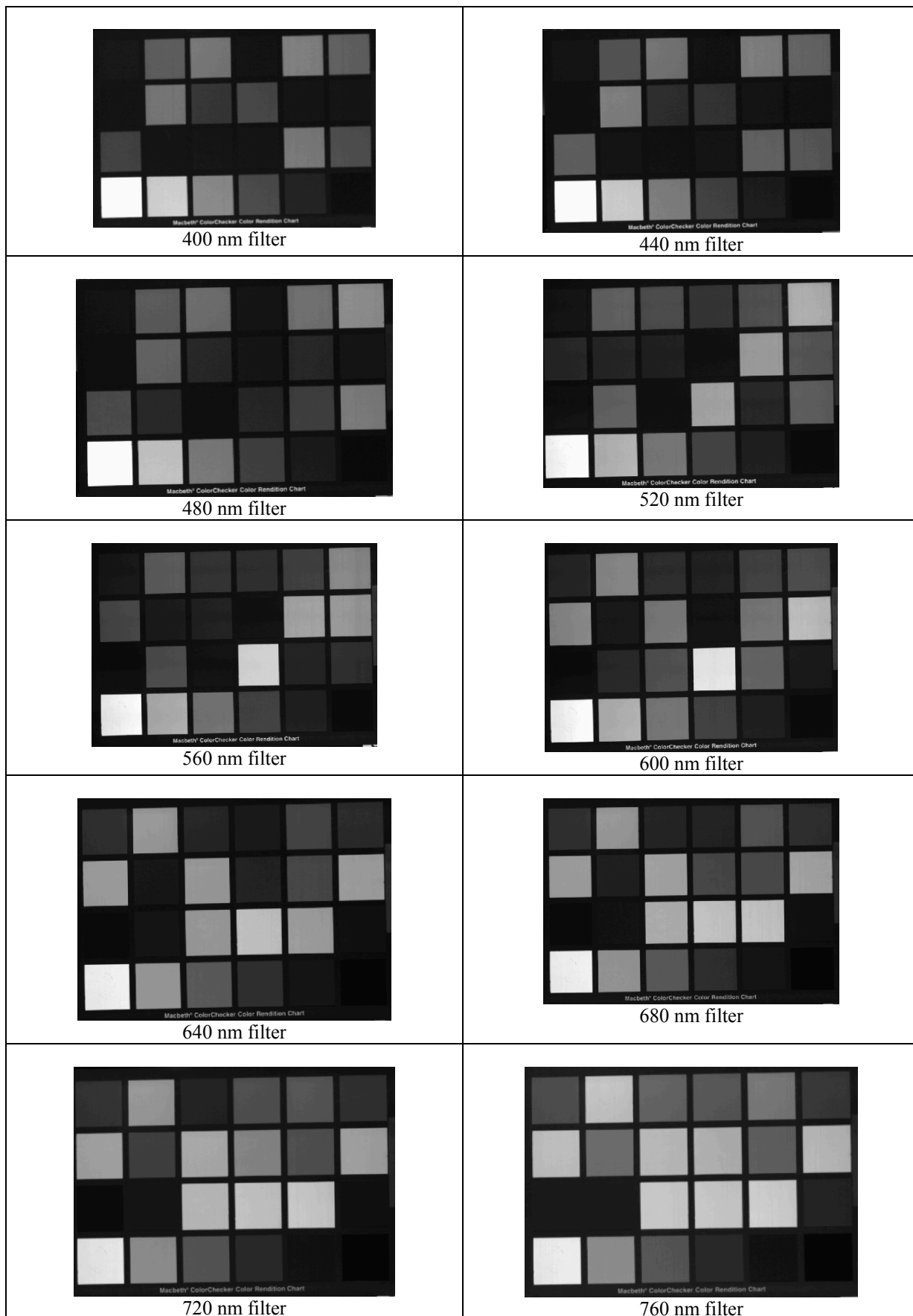


Figure 6-40. A multispectral calibrated image of the Macbeth chart taken with the CRISATEL camera. Just the ten channels on the visible part of the spectrum are shown.

6.5.3 The effects of acquisition geometry

We already discussed in this thesis the effects of the acquisition geometry on the measures performed by a spectrophotometer. A multispectral digital camera can be seen as a measuring tool very similar in nature to a spectrophotometer. Consequently acquiring images using different viewing geometries could lead to different images. In the case of the CRISATEL camera the acquisition geometry differs depending on the pixel location because the elliptical projectors used in the lighting system rotate in synchronisation with the motion of the CCD linear array. This produces a complex situation in which the influence of this variable acquisition geometry is to be evaluated.

We performed a basic experiment consisting of the acquisition of the Macbeth ColorChecker on three different positions in the image: on the left, centre and right sides of the white panel. Images on Figure 6-37 correspond in fact to the centre image of this series. Let's consider the greyscale contained on this chart. This greyscale contains 6 patches, their colour names and brightness (from 0 to 100) are given on the first column of Table 6-6. From the corrected three images of the chart we calculated the mean and standard deviation of the patches using 80 by 80 pixels windows on the obtained images. Intuitively we understand that if one of these statistics is correlated to the acquisition geometry, this statistic should be different on the centre than on both sides. Moreover on the side the statistic should present a similar behaviour due to the symmetry of the camera set up.

Table 6-6. Standard deviation of the greyscale patches as function of their position

	Left	Centre	Right
White (90.0)	58.0	63.8	55.3
Grey (59.1)	45.8	59.4	31.9
Grey (36.2)	22.2	36.2	19.7
Grey (19.8)	10.4	14.6	12.3
Grey (9.0)	6.6	19.1	6.4
Black (3.1)	12.3	14.5	12.1

On Table 6-6 we present the standard deviation calculated on the greyscale patches of the Macbeth ColorChecker depending on its spatial position. We appreciate the behaviour intuitively expected. The central measure is systematically different from the ones on the sides. Moreover, right and left measures show a deviation from the centre of the same sign and of similar amount.

6.6 Conclusion

This chapter has been dedicated to a specific multispectral acquisition system that was developed for the European project CRISATEL. We have performed two main tasks:

- i) the realization of experiments to characterize the components of the system and evaluate their performance,
- ii) the conception, design and implementation of software intimately related to the acquisition system.

The physical experiments and the data analysis performed on sections 6.2 and 0 are of interest for the multispectral community and were presented to an international conference, see [Ribés et al., 2003, PICS]. These results are basic for the evaluation of the camera and are demanded for the European Community in the framework of CRISATEL, a preliminary report being presented to them, [Ribés et al., 2003, CRISATEL]. Moreover, these results are the basic elements for the design of software aiming to obtain high quality images from this acquisition system.

The calibration and correction systems were designed, implemented and tested. These systems aim to acquire images that have not only high visual quality but also a radiometric controlled signal. This fact will allow us to properly perform spectral reconstruction afterwards.

Chapter 7:

Choosing Filters for Accurate Spectral Reconstruction

Contents

7.1	Introduction	177
7.2	Existing approaches to filter optimisation	178
7.2.1	Some properties of the ν -measure	179
7.3	Spectral reconstruction and camera filters.....	181
7.4	Designing Filters.....	182
7.4.1	The first derivative of the ν -measure.....	182
7.4.2	Filters parameterisation.....	183
7.4.2.1	Square-shaped functions.....	183
7.4.2.2	Gaussian-shaped functions.....	183
7.4.3	Optimisation procedure.....	184
7.4.3.1	First step.....	184
7.4.3.2	Second step.....	185
7.4.3.3	Overall method	186
7.5	Results	187
7.6	Conclusion.....	189

7.1 Introduction

We consider the problem of filter selection for increasing spectral reflectance reconstruction quality. The problem of filter optimisation is not new, one of the first remarkable approaches was that of [Neugebauer, 1956]. From there most researches have been interested in choosing filters in the framework of colour applications. The developed methods search, in general, quality colour reproduction, see for instance [Tsumura et al., 1998]. Our approach is different because it aims to design spectral transmittances of filters that will decrease spectral reconstruction errors. Some authors as [Haneishi et al., 1997] or [Imai et al., 2001] have already performed some work on this problem. They minimize a spectral reconstruction accuracy measure which needs spectral reconstructions performed during the optimization process.

In this chapter we first present some existing approaches to filter selection relevant to understanding our contribution. We then introduce the criteria used for filter selection and the strategy developed for its optimisation. The criteria used is originally applied for colorimetric filter optimisation, see [Vora and Trussell, 1993] and [Vora and Trussell, 1997, design] for reference. This criteria is called the ν -measure. We give details about the meaning of this measure on linear algebra. This provides the understanding for the application of this measure on a different context. We define a space that we call the *Camera Visual SubSpace (CVSS)* useful in this new context. The proposed modified criteria allows the design of filters that decrease spectral reconstruction errors without performing spectral reconstruction.

An algorithm for the optimization of the modified ν -measure is presented. This strategy appears to converge towards an acceptable solution. Moreover, it reveals very time-efficient. Finally in this chapter we apply the proposed algorithm to the optimisation of 10 Gaussian-shaped visible filter for the CRISATEL camera. The optimised set of filters are compared by simulation with the actual ones mounted on the camera.

7.2 Existing approaches to filter optimisation

Existing approaches to filter optimisation are normally based on the assumption that we want to produce as best as possible colour reproductions to be seen by a human observer. It is natural then to introduce the concept of the *Human Visual SubSpace* (HVSS). This space is based on the space expanded by the CIE colour matching functions (often referred as $[\bar{x} \ \bar{y} \ \bar{z}]$) but introducing information about the light source. If we call \mathbf{L} the diagonal matrix containing the spectral radiance of the illuminant, the HVSS is expressed as the space expanded by the set of vectors $\{\mathbf{L}\bar{x} \ \mathbf{L}\bar{y} \ \mathbf{L}\bar{z}\}$. The visual tristimulus values $[x \ y \ z]^T$ of a sampled spectral reflectance function \mathbf{r} are determined by the projection values of \mathbf{r} into this subspace: $[x \ y \ z]^T = \mathbf{A}^T \mathbf{r}$, where \mathbf{A} is the $N \times 3$ matrix containing the vectors $\mathbf{L}\bar{x}$, $\mathbf{L}\bar{y}$ and $\mathbf{L}\bar{z}$ in its columns. Therefore, it is important to define the orthogonal projection $P_V(\mathbf{r})$ of the reflectance \mathbf{r} onto the HVSS, as follows:

$$P_V(\mathbf{r}) = \mathbf{A}(\mathbf{A}^T \mathbf{A})^{-1} \mathbf{A}^T \mathbf{r}. \quad (7.1)$$

We verify that the projected reflectance $P_V(\mathbf{r})$ and \mathbf{r} are metameric (same colour):

$$\mathbf{A}^T P_V(\mathbf{r}) = \mathbf{A}^T \mathbf{r} = [x \ y \ z]^T.$$

Using these concepts [Neugebauer, 1956] proposed the so called q factor for filter optimisation, this criteria is defined as

$$q(\mathbf{m}) = \frac{\|P_V(\mathbf{m})\|^2}{\|\mathbf{m}\|^2}, \quad (7.2)$$

where \mathbf{m} represents the sampled spectral transmittance of a filter. But the q factor has some main problems. First of all it measures a single filter independently, it is then not a measure for a set of filters. Moreover, it is not valid for more than three filters. In case of using three filters they must be linearly independent. The q factor presents too much constraints to be used effectively as a design criteria. A criteria should fit some basic requirements to be considered as an effective measure. From [Vora and Trussell, 1993] these requirements are:

- The measure must depend on the space spanned by the filters and not on individual properties. HVSS should be contained in the space spanned by the scanning filters: $R(\mathbf{M}) \supseteq R(\mathbf{A})$, where \mathbf{M} is the $N \times K$ matrix containing vectors \mathbf{m}_i in its columns, \mathbf{m}_i , $i=1..K$, being the sampled spectral transmittances of the filters and $R(\mathbf{X})$ is the space spanned by the vectors composing the columns of \mathbf{X} .
- It should indicate a perfect set of filters. If they are not perfect a measure of goodness should differentiate the best set of filters.
- The criteria must be generalizable to any number of filters. This is evidently important when we deal with multispectral imaging.

These limitations refers to a criteria that measures the *goodness* of a set of filters. They can be overcome by different means. For instance, [Haneishi et al., 1997] used CIELAB differences over a set of reflectances as a measure of goodness. A more recent and very interesting criteria called Universal Measure of Goodness (UMG) presented by [Quan et al., 2000] is also based on the CIELAB space. Noise considerations along with physical constraints on the desired transmittances are taken into account by the authors for the optimisation. We will not

give more details about the UMG because our aim is quite different. As we already said we are looking for a criteria that decreases the reconstruction errors on a particular kind of materials, more specifically pigments in the case of art painting imaging.

[Vora and Trussell, 1993] presented a criteria for filter selection based on the comparison of two subspaces of a same vector space. These authors called the criteria the ν -measure and they define it as

$$\nu(\mathbf{V}, \mathbf{M}) = \frac{\sum_{i=1}^{\alpha} [\lambda_i^2(\mathbf{O}^T \mathbf{N})]}{\alpha}, \quad (7.3)$$

where,

- \mathbf{V} is the $N \times 3$ matrix which represents a base of the Human Visual Subspace (HVSS).
- \mathbf{M} is the $N \times K$ matrix that represents the set of filter transmittances.
- $R(\mathbf{L})$ is the vector space spanned by the columns of matrix \mathbf{L} .
- $\mathbf{N} = [\mathbf{n}_1 \quad \mathbf{n}_2 \quad \dots \quad \mathbf{n}_\alpha]$ is an orthonormal basis such that $R(\mathbf{N})=R(\mathbf{V})$ and $\mathbf{N}^T \mathbf{N} = \mathbf{I}$
- $\mathbf{O} = [\mathbf{o}_1 \quad \mathbf{o}_2 \quad \dots \quad \mathbf{o}_\beta]$ is an orthonormal basis such that $R(\mathbf{O})=R(\mathbf{M})$ and $\mathbf{O}^T \mathbf{O} = \mathbf{I}$, where β is the dimension of $R(\mathbf{M})$, with $\beta \leq N$.
- $\lambda_i(\mathbf{A})$ denotes the i -th singular values of a matrix \mathbf{A} .
- α is the number of singular values and acts as a normalisation factor, $\alpha=3$ because \mathbf{V} represents a base of the HVSS.

This measure is a *normalised measure of the goodness of the filter set*. It is always inside the interval $]0, 1[$ and perfect reproduction implies and is implied by $\nu(\mathbf{V}, \mathbf{M})=1$. This means space $R(\mathbf{V})$ is contained into space $R(\mathbf{M})$. As we can see this criteria does not work on the CIELAB space as the ones cited above but it also takes into account the reference human observer. In this sense, it can seem not to be the kind of measure we are looking for. We give more details about these measure in the following of this subsection to give insight on the real nature of this criteria. This is needed to understand its application in a different context.

Definition (7.3) implies several practical steps in order to obtain the value of the criteria. In fact, we must perform an orthogonalisation of the spaces $R(\mathbf{V})$ and $R(\mathbf{M})$ if we want to calculate the value $\nu(\mathbf{V}, \mathbf{M})$. This implies the use of the QR factorisation (or Gram-Schmidt orthogonalisation procedure). This fact can introduce numerical instabilities, then another form of the measure was defined in [Vora and Trussell, 1997], better adapted for implementation:

$$\nu(\mathbf{V}, \mathbf{M}) = \frac{\text{Trace} \left[\mathbf{V}(\mathbf{V}^T \mathbf{V})^{-1} \mathbf{V}^T \mathbf{M}(\mathbf{M}^T \mathbf{M})^{-1} \mathbf{M}^T \right]}{\alpha}, \quad (7.4)$$

where $\mathbf{V}(\mathbf{V}^T \mathbf{V})^{-1} \mathbf{V}^T$ and $\mathbf{M}(\mathbf{M}^T \mathbf{M})^{-1} \mathbf{M}^T$ are the orthogonal projectors on $R(\mathbf{V})$ and $R(\mathbf{M})$ respectively.

7.2.1 Some properties of the ν -measure

We want to note that the presented measure is just a particular application of the *Froebius norm*. This is not difficult to see by recalling the following definition and properties seen in Chapter 3, [Golub and Van Loan, 1983]:

- Frobenius norm definition:

$$\|\mathbf{A}\|_F = \sqrt{\sum_{i=1}^m \sum_{j=1}^n |a_{ij}|^2} . \quad (7.5)$$

- Noting $\sigma_i, i=1, \dots, p$, the singular values of \mathbf{A} , then:

$$\|\mathbf{A}\|_F^2 = \sigma_1^2 + \dots + \sigma_p^2 . \quad (7.6)$$

- Froebius distance definition:

$$d_F(\mathbf{U}, \mathbf{V}) = \|\mathbf{U}^t \mathbf{V}\|_F = \sqrt{\sum_i^n \sum_j^m (\mathbf{u}_i^t \mathbf{v}_j)^2} . \quad (7.7)$$

Applying (7.6) and (7.7) it is straightforward to see that the ν -measure (7.3) is a simple normalisation of the Froebius distance. Another important relationship [Vora and Trussell, 1993] is:

$$\nu(\mathbf{V}, \mathbf{M}) = \frac{\sum_{i=1}^{\beta} q(o_i)}{\alpha} , \quad (7.8)$$

where it is clear that the ν -measure is a generalization of the q factor. Finally we want to emphasize that the ν -measure is a measure of the difference between two vectorial subspaces. This is clearly seen when introducing the concept of principal angles, see [Golub and Van Loan, 1983] for further reference. Principal angles $\theta_1, \theta_2, \dots, \theta_\alpha \in [0, \pi/2]$ between \mathbf{M} and \mathbf{V} are defined recursively as already seen in Chapter 2 by:

$$\cos(\theta_k) = \max_{\mathbf{m} \in \mathbf{M}} \max_{\mathbf{v} \in \mathbf{V}} \mathbf{m}^T \mathbf{v} = \mathbf{m}_k^T \mathbf{v}_k$$

subject to:

$$\begin{aligned} \|\mathbf{m}\| &= \|\mathbf{v}\| = 1 \\ \mathbf{m}^T \mathbf{m}_i &= 0 \quad i=1, \dots, k-1 \\ \mathbf{v}^T \mathbf{v}_i &= 0 \quad i=1, \dots, k-1 \end{aligned}$$

Due to $\cos(\theta_k) = \lambda_k(\mathbf{O}^T \mathbf{N})$, then relation (7.3) becomes

$$\nu(\mathbf{V}, \mathbf{M}) = \frac{\sum_{i=1}^{\alpha} \cos^2(\theta_i)}{\alpha} . \quad (7.9)$$

As a consequence, the ν -measure is large when the angles between the two subvectorial subspaces are small. It is indeed a measure of similarity.

7.3 Spectral reconstruction and camera filters

In the preceding section we spoke about measures of goodness of a set of filters and we presented in detail one of them, the ν -measure. We explain on this section how we use the basic elements of this measure on the context of filter selection for spectral reconstruction accuracy. But, before a practical consideration must be done to properly understand our approach. Our aim being the increase of accuracy on a specific set of representative reflectances, we propose to minimise a measure of accuracy reconstruction on this set of reflectances. This approach is already taken by [Haneishi et al., 1997] where the measure of accuracy is not directly taken on the reconstructed spectral reflectance but on the CIELAB space. Closer to the approach implicit to our question is the paper of [Imai et al., 2001], where the authors propose a two step optimisation strategy. First they obtain three colorimetric filters and secondly add other filters to this kernel set in order to decrease spectral reconstruction errors.

There exists one important common point between the methods of [Haneishi et al., 1997] and [Imai et al., 2001], in both cases spectral reconstruction is to be performed in order to calculate the criteria. This implies that a particular spectral reconstruction method is included on the optimisation loop.

As we have extensively seen on this thesis, various spectral reconstruction methods with different characteristics exist. The fact of having a reconstruction method on the optimisation loop makes the measure depend on a particular reconstruction method. This choice is at the moment arbitrary and obviously introduces a source of variability. A priori, we do not know how a set of filters optimised using a particular method is going to react when performing spectral reconstruction using a different method. Moreover, in the case of methods requiring training, as the ones presented on Chapter 5, the optimisation loop becomes prohibitively time consuming.

One important aim of this chapter is to find a criteria helping the design of filters for spectral accuracy estimation, but not requiring spectral reconstruction to be performed. This approach is indirectly implicit when performing *progressive filter selection*. One of the oldest examples in our knowledge is proposed by [Mahy et al., 1994] where they make use of the SVD to produce an orthogonal basis of industrial sets of spectral reflectances. They claim that *optimal* filter transmittances will be the vectors representing the orthogonal basis calculated by the SVD. This point is theoretically interesting but the basis vectors can have negative values or, when positive, its physical realisation could be not possible. A more realistic algorithm is proposed by [Hardeberg, 2003]. In this case a set of filters among a database of commercially available ones is *progressively* selected. The criteria is the maximization of the orthogonality of the projections of the real filters onto the space spanned by the considered set of spectral reflectances. In these approaches, the orthogonality criteria is not related to any reconstruction method. In any case, even if mathematically correct, empirically there is no evident reason to choose orthogonality as an optimal criteria, especially when progressive selection is not an issue.

At this point of the discussion we explicitly seek the achievement of two requirements for the desired criteria: i) it should not introduce a spectral reconstruction method on the optimisation loop, ii) it should increase the spectral estimation accuracy on a set of predefined reflectances. In order to obtain this, we propose to look at the fundamental meaning of the ν -measure, a comparison between two subvectorial spaces of the same space. We will not compare anymore a space spanned by filters with the human visual subspace. For us, a space that characterises a set of chosen pigments will be matched with the space spanned by the filters.

7.4 Designing Filters

A measure of goodness can be applied to a set of existing transmittances of filters or it can be used as a criteria for its design. The difference between analysis and design leads to specific consideration for each case. See the twin papers [Vora and Trussell, 1997, analysis] and [Vora and Trussell, 1997, design] for further information on these subjects. In this section we are concern by the problem of filters design. We based our design procedure on two parameterizations of the filters that make the problem feasible and introduce useful constraints on the shape of the filter transmittances. Optimization is based on a gradient descend algorithm, consequently the derivative of the ν -measure is calculated because gradient information is necessary. A consequence of this gradient based method is high sensitivity to initializations and the risk of being trapped by local minima of the criteria. In fact, the ν -criteria is not convex. In order to avoid this problem and build a time-efficient optimization procedure we will present a two step algorithm using two different parameterizations of the filter transmittances. Moreover, random sampling over the space of the parameters that defines the filters is used to ensure convergence to an acceptable solution.

Because the ν -measure is normally used for the optimisation of colorimetric filters, the concept of *Camera Visual SubSpace* (CVSS) is introduced by similitude with the term *Human Visual SubSpace* (HVSS). The CVSS is defined as:

$$\text{CVSS} = \mathbf{L} \mathbf{S} \mathbf{M},$$

where \mathbf{L} and \mathbf{S} are diagonal matrices, \mathbf{L} containing the illuminant and \mathbf{S} the spectral sensitivity on the camera CCD. \mathbf{M} is a matrix containing on its columns the sampled spectral transmittances of the camera filters. The ν -measure then compares the CVSS with an orthogonal basis of a set of spectral reflectances.

7.4.1 The first derivative of the ν -measure

In general, for optimising the criteria (7.4), it is useful to know its first derivatives; this will allow us using numerical methods based under gradient assumptions. We have calculated the first derivatives of $\nu(\mathbf{V}, \mathbf{M})$ with respect to the set of filters, that means with respect to the parameters of the matrix \mathbf{M} . As we can parameterise our filters in multiple ways (for instance using Gaussian functions, sigmoids or splines) we represent by $\frac{\partial}{\partial x}(\mathbf{M})$ the first derivative of \mathbf{M} with respect to a parameter x . At the moment, x can refer to any parameter in any parameterisation.

As \mathbf{V} and α on (7.4) do not depend on the filter parameters they are constants. Knowing that $\frac{\partial}{\partial x}(\text{Trace}[\mathbf{A}]) = \text{Trace}\left[\frac{\partial}{\partial x}\mathbf{A}\right]$ for a $N \times N$ matrix \mathbf{A} and $\frac{\partial}{\partial x}(\mathbf{K}_1 \mathbf{A} \mathbf{K}_2) = \mathbf{K}_1 \left(\frac{\partial}{\partial x}\mathbf{A}\right) \mathbf{K}_2$ where \mathbf{K}_1 and \mathbf{K}_2 are two $N \times N$ matrices not depending on x , then we deduce the following relation:

$$\frac{\partial \nu(\mathbf{V}, \mathbf{M})}{\partial x} = \frac{\text{Trace}\left[\mathbf{V}(\mathbf{V}^T \mathbf{V})^{-1} \mathbf{V}^T \frac{\partial}{\partial x} \mathbf{M} (\mathbf{M}^T \mathbf{M})^{-1} \mathbf{M}^T\right]}{\alpha}. \quad (7.10)$$

The problem reduces then to calculating the derivative of $\mathbf{M}(\mathbf{M}^T \mathbf{M})^{-1} \mathbf{M}^T$. Knowing

$$\frac{\partial}{\partial x}(\mathbf{Y}^{-1}) = -\mathbf{Y}^{-1} \left(\frac{\partial}{\partial x} \mathbf{Y} \right)^{-1} \mathbf{Y}^{-1}, \quad (7.11)$$

where \mathbf{Y} is an $N \times N$ matrix, then we deduce the following equation:

$$\begin{aligned} & \frac{\partial}{\partial x} \left(\mathbf{M}(\mathbf{M}^T \mathbf{M})^{-1} \mathbf{M}^T \right) = \\ & \left(\frac{\partial}{\partial x} \mathbf{M} \right) (\mathbf{M}^T \mathbf{M})^{-1} \mathbf{M}^T - \mathbf{M} (\mathbf{M}^T \mathbf{M})^{-1} \left(\frac{\partial}{\partial x} (\mathbf{M}^T \mathbf{M}) \right)^{-1} (\mathbf{M}^T \mathbf{M})^{-1} \mathbf{M}^T + \mathbf{M} (\mathbf{M}^T \mathbf{M})^{-1} \left(\frac{\partial}{\partial x} \mathbf{M}^T \right) \end{aligned} \quad (7.12)$$

where

$$\frac{\partial}{\partial x} (\mathbf{M}^T \mathbf{M}) = \left(\frac{\partial}{\partial x} \mathbf{M}^T \right) \mathbf{M} + \mathbf{M}^T \left(\frac{\partial}{\partial x} \mathbf{M} \right). \quad (7.13)$$

Knowing the trivial relationship $\frac{\partial}{\partial x} \mathbf{M}^T = \left(\frac{\partial}{\partial x} \mathbf{M} \right)^T$ the only thing we still need to define is the derivative of the matrix \mathbf{M} with respect to x . Once this matrix is defined we could calculate the derivative of the criteria with respect to x . This derivative depends on the parameterisation of the filters. In fact, the matrix \mathbf{M} is a matrix whose columns contain the sampled spectral transmittance functions of the set of filters being used. Consequently, $\frac{\partial}{\partial x} \mathbf{M}$ contains the derivative of the filter transmittances and x is a parameter of the function modelling these transmittances.

Finally, reporting equation (7.13) in equation (7.12) and equation (7.12) in equation (7.10) we can formally define the derivative $\frac{\partial v(\mathbf{V}, \mathbf{M})}{\partial x}$ of the v -criteria with respect to x .

7.4.2 Filter parameterisation

We have used two different parameterisations of a filter spectral transmittance function (STF): a squared-shaped function and a Gaussian function. The spectral transmittance functions are normalised between 0 and 1.

7.4.2.1 Square-shaped functions.

In this case we consider the filter transmittance as perfect (one) on an interval of wavelengths and zero for the rest of them. Of course, no real filter can be constructed with such a transmittance function but it will be useful for our method. We note that this function is not continuous and its derivative is zero when it exists. This fact makes impossible a gradient optimisation procedure based in this parameterisation.

7.4.2.2 Gaussian-shaped functions.

We can parameterise the STF of a filter as a Gaussian function. This approach has several advantages. Firstly, a Gaussian function has easy derivatives, is continue and presents no special numerical problems when implemented in a computer. Secondly, it is possible to construct a real filter with a nearly Gaussian transmittance. The fact that Gaussians have only

one global peak is a net advantage since it is easier to fabricate a single peaked filter than a multi-peaked one. The expression used for this parameterisation is

$$g(\lambda) = e^{-\frac{\|\lambda-\mu\|^2}{2\sigma^2}} \quad (7.14)$$

where λ is the wavelength, σ controls the half-width of the filter and μ the position of its peak. We note that the function is not normalised as for a probability distribution. In fact, we are not interested in having a function with an integral equal to unity. Equation (7.14) allows the two parameters to affect the form of the Gaussian independently.

7.4.3 Optimisation procedure.

Our optimisation method uses the ν -measure presented in equation (7.4). As we already said, the two spaces compared by the ν -measure are: a set of representative spectral reflectances and the CVSS. The optimisation is performed in two steps. The first step uses square-shaped functions to represent the filters and does not make use of derivatives. The second step parameterises the filter transmittances as Gaussians and minimises the same criteria but using a gradient search. Afterwards, several sets of random chosen parameters are used as initialisations of the method. The best solution is kept.

7.4.3.1 First step.

The filters are not parameterised individually. Our parameters are the position of the boundaries between two “perfect transmittance zones” of two filters. We illustrate this point on Figure 7-1. In this figure we can see a set of seven filters. Their “transmittive” zones cover the complete wavelengths range between 400 and 760 nm. We note that if our filters do not cover all spectral samples we would have zero division problems when performing calculations. This justifies selecting the boundaries as parameters and not using two parameters per filter. At the same time, we reduce the number of them. Hence, we have a vector \mathbf{f} of parameters containing these boundaries, each boundary position f_i being a parameter for $i=1, \dots, n$, n being the number of filters to be chosen.

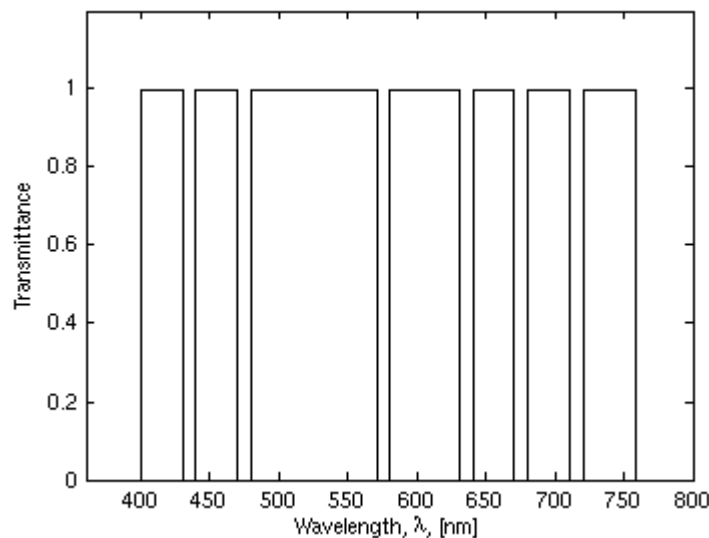


Figure 7-1. Seven square-shaped filters covering the visible range of the spectrum.

In this case we work with a discretization of the variables. We cannot optimise the criteria using gradient based methods because the variables f_i are discrete and we cannot compute the derivatives of \mathbf{M} with respect to f_i . Consequently, we have looked for a method not using this information. We have implemented an optimisation method moving each parameter one sampling step right and one sampling step left and comparing criteria's values on the left, right and original position. The best one is chosen. We can see a scheme of this process in Figure 7-2, for simplicity just two filters cover the spectrum. Of course, superposition of two boundaries are prohibited by the algorithm and the filters are always kept inside the visible range of the spectrum.

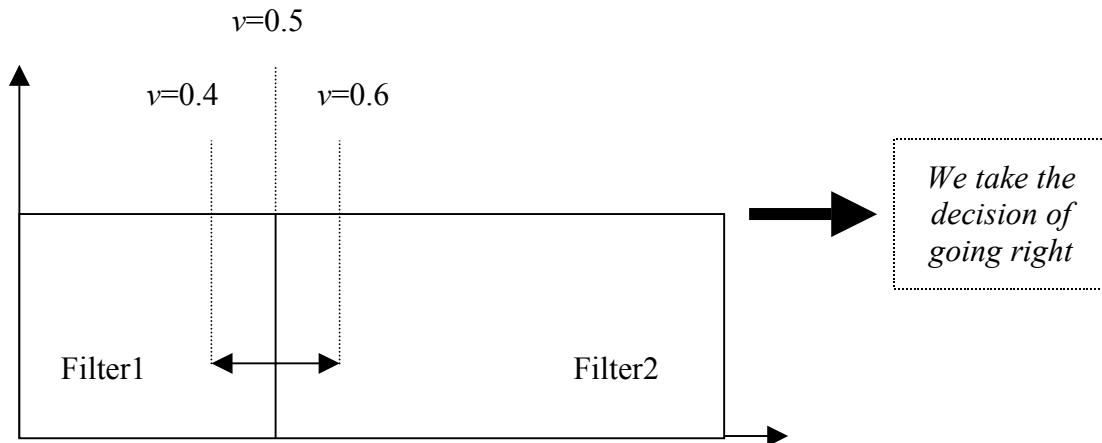


Figure 7-2. Example of discrete optimisation of the boundary position between two square-shaped filters.

7.4.3.2 Second step.

The second step of our method is a gradient descend optimisation algorithm. Our criteria is always the same, (7.4), and our parameterisation consists of a Gaussian function per filter. Then, every filter depends on two parameters μ and σ that controls the position and the half-width of the Gaussian respectively. Matrix \mathbf{M} has n columns containing sampled Gaussian functions, n being the number of filters. $\frac{\partial}{\partial \mu}(\mathbf{M})$ and $\frac{\partial}{\partial \sigma}(\mathbf{M})$ are easy to calculate and contain Gaussians in their columns because the derivative of a Gaussian function is another Gaussian function.

This second step takes the results of the first step and builds the initial matrix \mathbf{M} from them. For this construction, we take every transmittance function obtained from the first step and we transform it in a Gaussian defined as follows: μ is the centre of the perfect transmittance zone and σ is chosen to fit the half-width of this zone. We can see an example of this conversion in Figure 7-3.

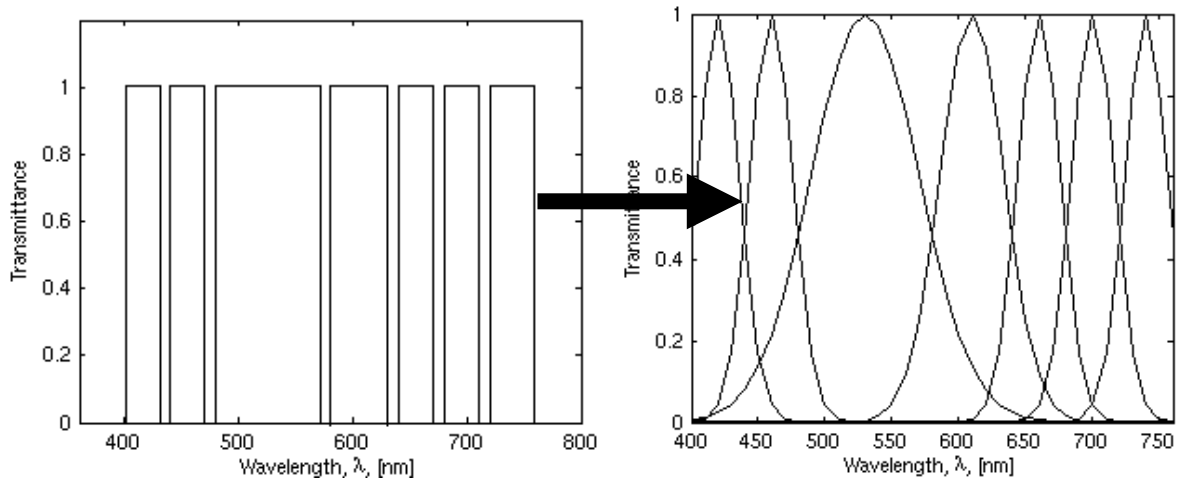


Figure 7-3. Conversion from a set of square-based filter to its Gaussian-shaped counterpart.

Once matrix \mathbf{M} is initialised using the filters created from results of the first step, our method iterates using the gradient for finding the values of the parameters μ_i and σ_i that maximises expression (7.4). This initialisation appears to be suitable and the method converges to values close to 1.

7.4.3.3 Overall method

We tested the method consisting of the sequential application of step 1 and step 2 and we found solutions strongly dependent on the initial configuration of the initial boundaries of step 1. In other words, we can easily find a local minima of the criteria if our parameters initialisation is not close enough to the solution. In order to solve this problem we choose a family of randomly selected vectors f , we use each member of the family as initialisation of our method (Step 1 and Step 2), we compare all solutions and we take the best one.

Other people have optimised Gaussian filters by the used of stochastic methods. [Haneishi et al., 1997] and [Tsumura et al., 1998], using simulated annealing. [Tsumura et al., 1998] deals with the optimisation of colorimetric filters for electronic endoscopes while [Haneishi et al., 1997] applies it to the problem of multispectral imaging of art works. They do not provide details on the application of simulated annealing but it is well know that this method is very time consuming. Our proposed algorithm appears to be time-efficient. For instance the test that will be presented on the results section of this chapter converged on 1 minute 6 seconds on a SunBlade 100 workstation. Moreover the test was implemented on Matlab that is not a time efficient environment.

There are some reasons that make this method efficient:

- The parameterisation of the filter boundaries used on step 1 is compact. This initially reduces the quantity of parameters.
- Step1 is optimised on a discrete and finite space, this implies a fast optimisation.
- Initialisation given to Step2 is already close to a solution, then the gradient based minimisation algorithm normally converges on few iterations.

7.5 Results

The aim of this section is two-fold. On one hand we present positive results of spectral reconstruction after filter optimisation. This justifies the use of the ν -measure for increasing spectral accuracy estimation. On the other hand, we base this section on a particular case. This corresponds to the optimisation of 10 visible filters to image oil pigments under an halogen light source. In fact, we fix our simulation conditions to be as close as possible to the real ones encountered on the already presented CRISATEL camera. Consequently the example presented here will deal with a CVSS composed by: i) the CRISATEL camera CCD, ii) the CRISATEL halogen illuminant and iii) 10 Gaussian-shaped filters. The elements to be optimised are the set of Gaussian filters.

A first consideration must be done about the sampling ratio used on the simulations. Most of our spectral reflectance databases are sampled at 10 nm intervals. This value is at the moment accepted on the multispectral community as normal. In our Fourier analysis on Chapter 2 we presented results confirming this fact. But for filter transmittances nothing is said about the sampling rate. As the CRISATEL system uses narrow band filters its shape is modified by this sampling rate impose by the spectral reflectances. We show on Figure 7-4 the CRISATEL visible filter transmittances subsampled at 10nm intervals. If we compare this figure with the non subsampled one presented on Chapter 6, then we can see that this subsampling has a smoothing effect on the shape of the transmittances. A priori, this smoothing should help to obtain better results, even if we have not quantified this point we accept it as an error and we perform the comparisons under these conditions.

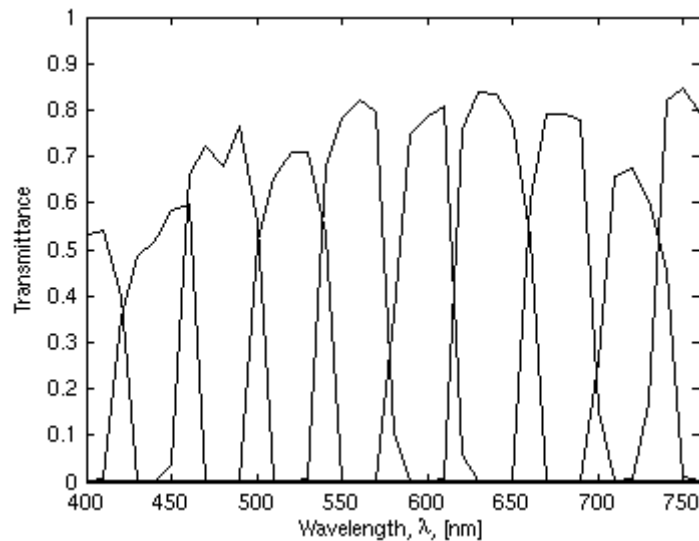


Figure 7-4. CRISATEL visible filter transmittances subsampled at 10nm intervals.

The algorithm presented on the preceding sections of this chapter was used to obtain a set of Gaussian filters optimising the ν -measure between the CVSS and the Kremer database of oil pigments. As this procedure is based on random sampling, repeating the optimisation several times, we could obtain different solutions. We will not give details here but this point is interesting because different acceptable solutions present different distributions of the filters over the spectrum. The visualisation of not only one but a set of the best acceptable solutions of the random sampling gives intuitive information on the nature of the imaging process.

In Figure 7-5 we present the best solution found by the algorithm. In this case the peaks of the Gaussians are close to an equidistant distribution while the half-widths varies more.

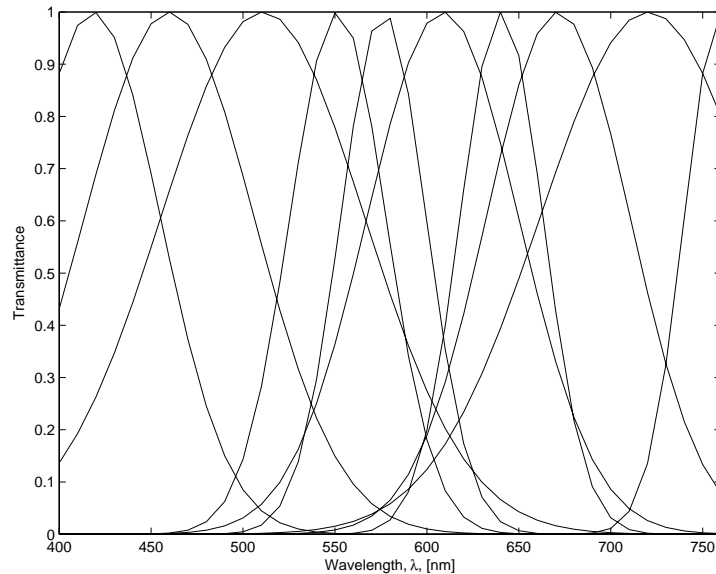


Figure 7-5. 10 optimised Gaussian-shaped filters.

Once optimized, we compare the obtained filters with the ones chosen for the CRISATEL camera. The elements forming the simulation are the same, the only thing that is changed being the filter set used. Moreover, we introduce a new set of Gaussian-shaped equispaced filters for comparison. We believe to be interesting as a reference.

In Table 7-1 we present the results of the comparison. We have introduced 12 bits quantization on the signal to conform with the 12 bits signal of the CRISATEL camera. The spectral reconstruction method used is the one representing linear methods learning from data presented on Chapter 2.

Table 7-1. Spectral Root Mean Squared Error over different databases.

12 bits quantization	CRISATEL	equispaced	optimised
Kremer (training)	0.00009637	0.00012492	0.00008045
Selected Artists	0.00011133	0.00014384	0.00011797
Restoration	0.00007539	0.00012333	0.00008473
Munsell	0.00009052	0.00012559	0.000094379

The optimized filters obtain a smaller spectral root mean squared error for the Kremer database as we desired. The reconstruction error is about 16% less on this case than when using the CRISATEL filters. For other databases the error is similar or worse to the one obtained by the CRISATEL filters. Knowing that the cost of producing a set of interference filters with a particular shape is at the moment very expensive, the commercial filters used on the CRISATEL camera appears to be a reasonable choice. Even if work can be done to optimize more the 16% obtained in our simulations, an increase of this order of magnitude in a particular set of reflectances does not justify the cost. Moreover, we can clearly see that when specializing the filters for a particular set of reflectances we lose generality. Once the filters would be physically built this choice will make the CRISATEL camera less adaptable to applications not related with the imaging of art paintings.

7.6 Conclusion

We developed an algorithm for the optimization of Gaussian-shaped filter transmittances. The aim of the optimization is the accurate spectral reconstruction of a given set of reflectances. An existing criteria, the ν -measure, is adapted to this new aim. The criteria applied to this new context allows the optimisation of the transmittances without the introduction on the algorithm of a spectral reconstruction stage at each iteration of the optimisation algorithm. Because the ν -measure is normally used for the optimisation of colorimetric filters, the concept of *Camera Visual SubSpace* (CVSS) is introduced in a similar sense as the term *Human Visual SubSpace* (HVSS).

The optimisation is very time-efficient. This is due to a two stages structure, each of them based on a different parameterisation of the filter transmittances. First, square-shaped filters are used, they are compactly parameterised and optimised on a discrete space. This is very time efficient and provides a good initial approximation for a gradient based optimisation procedure. We calculate the gradient of the ν -measure analytically to increase the efficiency. This two-stage procedure can be trapped on local minima as the criteria is not convex. Application of this optimisation strategy to different initial sets of randomly selected filters appears to be a good solution of this problem.

The developed method has been applied to choose 10 Gaussian-shaped filters for the CRISATEL camera, its aim being to increase the accuracy of the spectral reconstruction on a set of oil pigment reflectances. Using simulations we have compared the results obtained with optimized filters with the ones obtained using the actual CRISATEL filters. These results show that the optimised filters provide reconstructions of better accuracy on the selected set of reflectances. But this increase of accuracy remains small, 16%, and is accompanied by a lose of generality. As an important conclusion, the difficult construction of optimised Gaussian-shaped interference filters is not justify by the obtained results.

The work developed on this chapter could easily be applied to the optimisation of electronically tuneable filters. In fact, the approach seems very adapted. For this kind of filters, the transmittance functions can be electronically changed and their shape belongs to a family of curves very close to Gaussians.

Chapter 8:

General Results

Contents

8.1	Introduction	193
8.2	Multispectral system at the National Gallery of London	194
8.2.1	Description of the system	194
8.2.2	Calibration.....	195
8.2.3	CRISATEL chart experiment.....	195
8.3	CRISATEL multispectral system	197
8.3.1	Calibration Results	198
8.3.2	CRISATEL chart experiment.....	198
8.3.3	Art work paintings spectral reconstruction	204
8.3.3.1	Saint-Jacques le mineur.....	204
8.3.3.2	Le départ pour Jersey	206
8.3.4	Illuminant Simulation.....	208
8.4	Conclusion.....	211

8.1 Introduction

This chapter presents a first set of spectral reconstruction results obtained by using the techniques already introduced in this thesis. The chapter is dedicated to data acquired on real experimental environments. No simulations appear here. Two different multispectral acquisition systems were used to obtain the data:

- i) A multispectral camera used at the National Gallery of London.
- ii) The CRISATEL multispectral system using HQI lamps.

Both systems have the common point of using the same set of 13 interference filters. The chapter is divided in two main parts: the first one dedicated to the data obtained at the National Gallery and a second part dealing with data from the CRISATEL project.

The present thesis was finished before the CRISATEL project was completely achieved. The phase of art paintings scanning was starting at that time. A general test was first performed on several Georges de la Tour paintings that were scanned at the museum of Albi (France) between November 28th and December 3th, 2003. We show in this chapter one example of calibration, spectral reconstruction and illuminant simulation of one painting of this first test data, *Saint Jacques le mineur*. An intensive scanning stage followed this first test. We also show a painting of Guillaume Fouace, *Le départ pour Jersey*, that belongs to this stage. It was scanned by members of the CRISATEL project at the Musée Thomas Henry in Cherbourg. At this moment, changes are not expected on the CRISATEL system, at least fundamental changes. Data shown here are preliminary but representative enough to be presented.

8.2 Multispectral system at the National Gallery of London

In this section we present results obtained with a multispectral camera currently used at the National Gallery of London.

8.2.1 Description of the system

The multispectral system used at the National Gallery is formed by a greyscale 12 bits cooled camera and a filter wheel containing the CRISATEL filters presented in Chapter 2. Normally halogen lamps are used on the acquisition images. The only not known component of this system is the CCD sensitivity. Haida Liang from the National Gallery scientific department kindly provided us some estimated quantum efficiency samples of the CCD. We show this data on the left panel of Figure 8-1 and we convert them into sensitivity. The conversion from quantum efficiency to sensitivity implies the multiplication of each sample by its wavelength and the posterior normalisation of the results. We show the converted curve on the right panel of Figure 8-1.

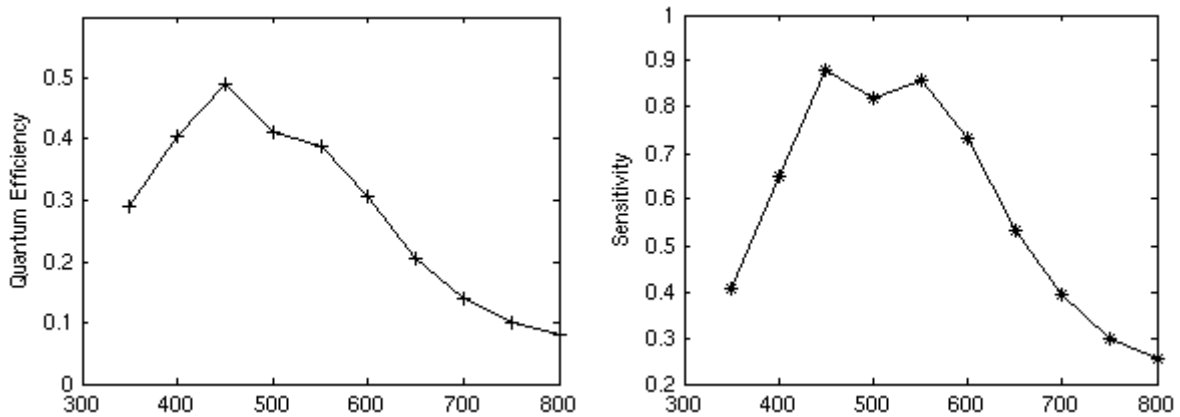


Figure 8-1. (Left panel) quantum efficiency samples provided by the National Gallery of London, (right panel) quantum efficiency converted to sensitivity.

There is a practical problem that must be taken into account if an inverse operator is to be build based on this data. Sampling rate of the original quantum efficiency is 50 nm and we need at least 10 nm. We perform a cubic spline interpolation of the sensitivity curve show on the right panel of Figure 8-1 and we resample it to 10 nm intervals. The result is shown in Figure 4-1. We note that this curve being an approximation of the real sensitivity this is a source of inaccuracy when building an inverse operator.

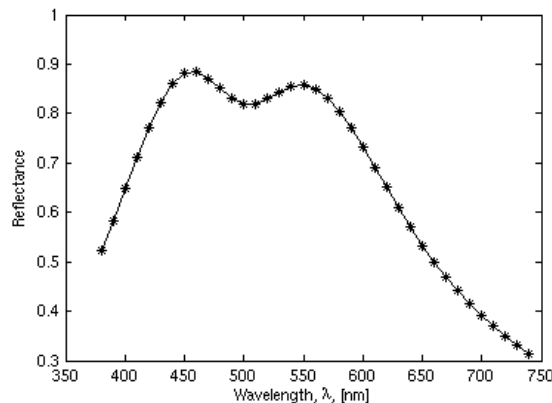


Figure 8-2. Interpolated spectral sensitivity of the CCD at the National Gallery.

8.2.2 Calibration

The National Gallery acquisition system have not an automatic calibration procedure as the one we designed and implemented for the CRISATEL system. The images we received are off-line corrected by several means, please refer to [Liang et al., 2004] for details:

- Dark noise was obtained by taking a median frame from a set of 20-30 dark frames
- A flatfield frame that includes the combined effect of spatial lighting inhomogeneity and pixel to pixel gain variation was used to correct all the dark subtracted frames. The flatfield was obtained by taking images of different sections of a whiteboard and taking a median frame of these images so that we can “filter” out the small scale spatial inhomogeneities of the surface of the whiteboard but retaining the effects of the lighting inhomogeneity and CCD pixel to pixel gain variation.
- A reference white was taken per filter to correct for the spectral response of the system.

8.2.3 CRISATEL chart experiment

For this experiment an image of the CRISATEL chart was taken at the National Gallery. We recall that this chart was presented at the end of Chapter 2. The chart was measured by a different spectrophotometers at London and Paris, see report [CRISATEL, 2003] for more details. This experiment is based on the first test data obtained with the NG system in Aug/Sept. 2003, for details of the system and calibration refer to [Liang et al., 2004].

We take the 117 non varnish patches of the chart and we analyse them to obtain two different kinds of data:

1. A matrix containing 117 columns with the mean camera responses of each colour patch.
2. A matrix containing $117 \times S$ columns containing non averaged camera responses, S being the quantity of pixels analysed into each colour patch.

Part of the methods presented on this thesis are based on learning over a training set of spectral reflectances and their corresponding camera responses. We then divide the CRISATEL chart into two sets, one will be used for training and the other for test. This leads to four different sets: averaged train set, non-averaged train set, averaged test set and non-averaged test set. Train and test sets have the same size. The original matrix have been divided into two non intersecting sets by taking even elements for one set and odd for the other. We note that the averaged camera responses sets can be considered as less influenced by noise than the non-averaged ones that present a more realistic situation.

In Table 8-1 we present spectral reconstruction errors, L_1 , obtained by using different spectral reconstruction techniques. We first note that direct inversion methods as smoothing inverse and Hardeberg inverse perform badly compared to the rest of the methods. This is justified by the lack of precision on the physical measurements and the factors not taken into account into the modelisation of the system. This illustrates the difficulties and great effort necessary to reach good spectral accuracy with direct methods. We also see that methods based on interpolation (MDST and cubic spline) perform worst than the leaning-based ones but much better than the direct inversion.

Table 8-1. Spectral reconstruction errors for the CRISATEL chart experiment

	Train set	Mean test set	Non averaged test set
Smoothing Inverse	0.051270	0.052479	0.052479
Hardeberg Inverse	0.054312	0.055944	0.056674
Learning Pseudo-inverse	0.008960	0.010854	0.012662
Non-averaged Learning Pseudo-inverse (NAPinv)	0.009183	0.010721	0.012198
Bootstrapped Learning Pseudo-inverse	0.010068	0.011369	0.013344
NNLS	0.012590	0.013354	0.014247
SVD Pseudo-inverse	0.009306	0.011264	0.012951
MDST Interpolation	0.022951	0.024837	0.025992
Cubic Spline Interpolation	0.027512	0.029885	0.031269
Mixture Density Network	0.004308	0.009316	0.011214

Methods based on pseudo-inverse have a degradation of the error in the non-averaged test set, which is not positive as this set is considered as the more realistic one. Even for the pseudo-inverse learning method trained using non-averaged data (NAPinv). In any case, this degradation is not very strong; this is most probably due to the good quality of the CCD that is cooled in order to reduce the level of noise.

Finally, the Mixture Density Network (MDN) used on this comparison presents the best performance. This MDN has 22 neurons in its hidden layer and presents 7 Gaussians in its mixture model. It is interesting to note that the MDN has been trained over the averaged samples (a non averaged train set has been used for early stopping test) but it slightly outperforms the Napinv method trained directly on the non averaged train set.

In Table 8-2 we present the same results as Table 8-1 but using CIELAB colorimetric errors. The overall behaviour is similar but using this metric we obtain the same results on the non-averaged test set for the Napinv method than for the MDN, those appear to be the best methods in this context. All the other methods perform not so well as Napinv and MDN.

Table 8-2. CIELAB94 reconstruction errors for the CRISATEL chart experiment

	Train set	Mean test set	Non averaged test set
Smoothing Inverse	6.77	6.60	6.90
Hardeberg Inverse	6.58	6.49	6.81
Learning Pseudo-inverse	2.37	2.60	3.18
Non-averaged Learning Pseudo-inverse	2.22	2.29	2.84
Bootstrapped Learning Pseudo-inverse	2.68	2.72	3.33
NNLS	3.07	3.05	3.41
SVD Pseudo-inverse	2.35	2.62	3.22
MDST Interpolation	2.77	2.71	3.34
Cubic Spline Interpolation	5.41	5.52	5.99
Mixture Density Network	1.02	2.04	2.84

8.3 CRISATEL multispectral system

In this section we present comparisons of spectral reflectance curves reconstructed using images acquired by the CRISATEL multispectral system. We have already shown in detail in Chapter 6 how this system is calibrated. Now, calibrated and corrected images are used to reconstruct spectral reflectances.

Before starting the comparisons, we show in the right panel of Figure 8-3 the spectral sensitivity curve of the CCD used on the CRISATEL camera. This curve is necessary for the implementation of any direct reconstruction method. This data is obtained from an experiment using a monochromator performed at University of Paris VI. An integrated sphere was connected at the output of a monochromator. The wavelength of the monochromatic light was increased at 5 nm steps from 400 nm to 800 nm, its energy being controlled by a calibrated radiometric sensor. At each 5 nm increment an image of the aperture of the integrating sphere was taken, an extra dark image was also acquired for dark current correction. Afterward dark current correction and a mean value calculation over the imaged sphere aperture is performed. Representing every mean value against wavelength we obtain the sensitivity curve presented in the left panel of Figure 8-3.

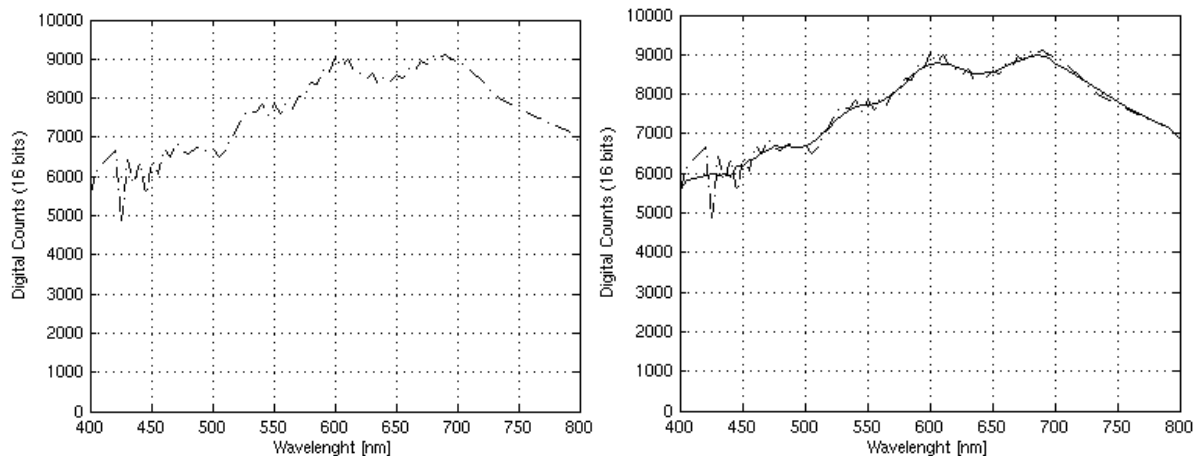


Figure 8-3. (Left panel) noisy CRISATEL camera CCD sensitivity curve measured by the use of a monochromator, (right panel) smoothed sensitivity.

As we can see the curve obtained from the monochromator experiment (left panel of Figure 8-3) is not smooth. This is physically not acceptable. In fact, the curve is noisy due to the low radiant energy of the light source used on the experiment. Moreover, the light source was an halogen lamp. As we already saw in Chapter 2 this kind of lamps presents much less energy on the low part of the visible spectrum than on the upper part. This is the reason why we see strong oscillations of the sensitivity curve on the left side of the curve presented on the left panel of Figure 8-3 while on the right side the curve is smooth.

In practice we need a smooth curve if this information is used for building inverse operators. We then smooth the curve by a 7 elements window that performs a mean operation on the signal. We take care of the correct application of the mean on the limits of the signal and we do not apply this window on the right side of the curve as it is already smooth. We see the result on the right panel of Figure 8-3.

8.3.1 Calibration Results

In this section we show a visual example of the effects of our calibration and correction systems in the framework of CRISATEL. On the right panel of Figure 8-4 we present a calibrated but non corrected image of a Georges de la Tour “Saint Jacques le mineur” painting. On the left panel of the same figure calibrated and corrected version is presented. The image is taken by the 1000 nm centred filter (infrared). The visual quality and contrast is clearly improve when visualising the images in a calibrated display. We note that Georges de la Tour produced very dark paintings where dynamic range is very small. We expect this calibration procedure to be even more effective when digitising colourful paintings.



Figure 8-4. (Left panel) calibrated and corrected image of a Georges de la Tour “Saint Jacques le mineur” painting, (right panel)calibrated but non corrected version.

8.3.2 CRISATEL chart experiment

We repeat the experiment performed for the National Gallery system in section 8.2.3 but using data obtained with the CRISATEL acquisition system. In this case the Mixture Density Networks clearly outperforms the rest of methods, see Table 8-3. Non-averaged pseudo-inverse does not perform better than a simple averaged pseudo-inverse. This is most probably due to the inter-pixel sensitivity correction applied to the CRISATEL images that makes the pixels less noisy.

We note that as in section 8.2.3 the estimation accuracy of direct methods is worst than the one obtained by learning based methods. Now, the difference is not as big as in the National Gallery experiment. This is due to the reliable measures of the CCD and filters used to characterize the system. We recall that the transmittances of the CRISATEL filters were carefully measured using a spectrophotometer and the sensitivity curve is the result of an independent experiment using a monochromator. We believe that this lack of accuracy is justified by the fact that our trainings and tests sets all belong to a painting environment while the direct solution stays general.

Table 8-3. Spectral reconstruction mean absolute errors for the CRISATEL chart experiment

	Train set	Mean test set	Non averaged test set
Smoothing Inverse	0.030948	0.034021	0.034203
Hardeberg Inverse	0.021479	0.024172	0.024437
Learning Pseudo-inverse	0.010225	0.01487	0.015390
Non-averaged Learning Pseudo-inverse	0.010225	0.014741	0.015258
Bootstrapped Learning Pseudo-inverse	0.010878	0.014594	0.015176
NLS	0.016108	0.018059	0.018454
SVD Pseudo-inverse	0.010770	0.015380	0.015878
MDST Interpolation	0.024060	0.027588	0.027842
Cubic Spline Interpolation	0.020306	0.023558	0.023805
Mixture Density Network	0.007171	0.011385	0.012161

In order to give more insight in the behaviour of the method we calculate their error histograms (using test noisy data). We take the maximum error obtained in the worst case for all the methods and use it as a maximum for the histograms. We then divide the errors in 40 zones and represent them by bars in a plot, bar number one represents the minimum error while bar number 40 represents the maximum. In Figure 8-5 we present the error histograms of the non-averaged pseudo-inverse and Mixture Density Networks. In Figure 8-6 we present the histograms of the other tested methods. The Mixture Density Network based method is the one that performs the best in this experiment.

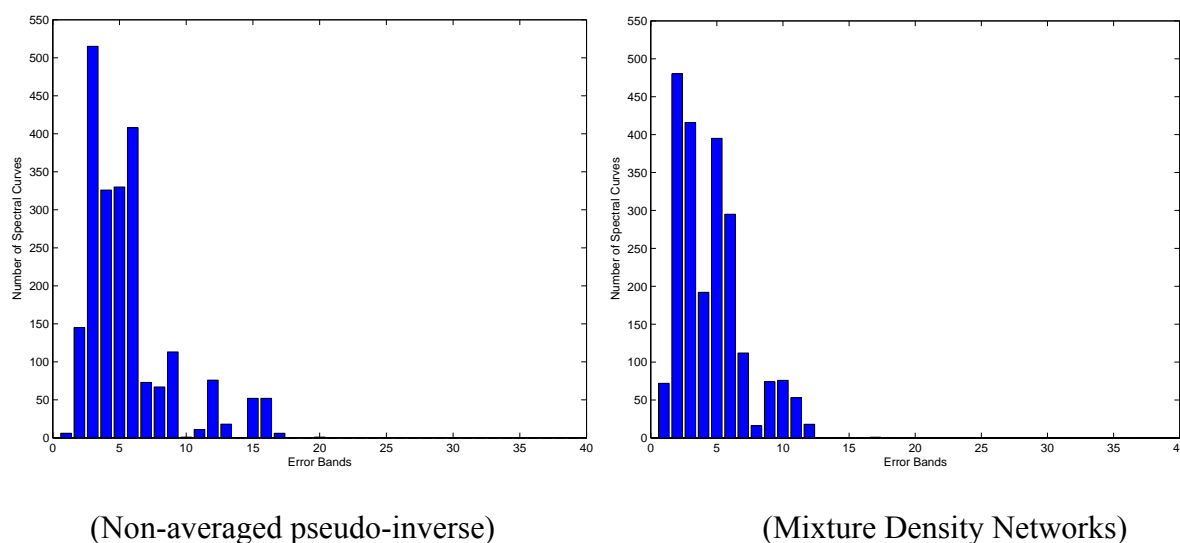


Figure 8-5. Error histograms of the two spectral reconstruction methods obtaining the best results.

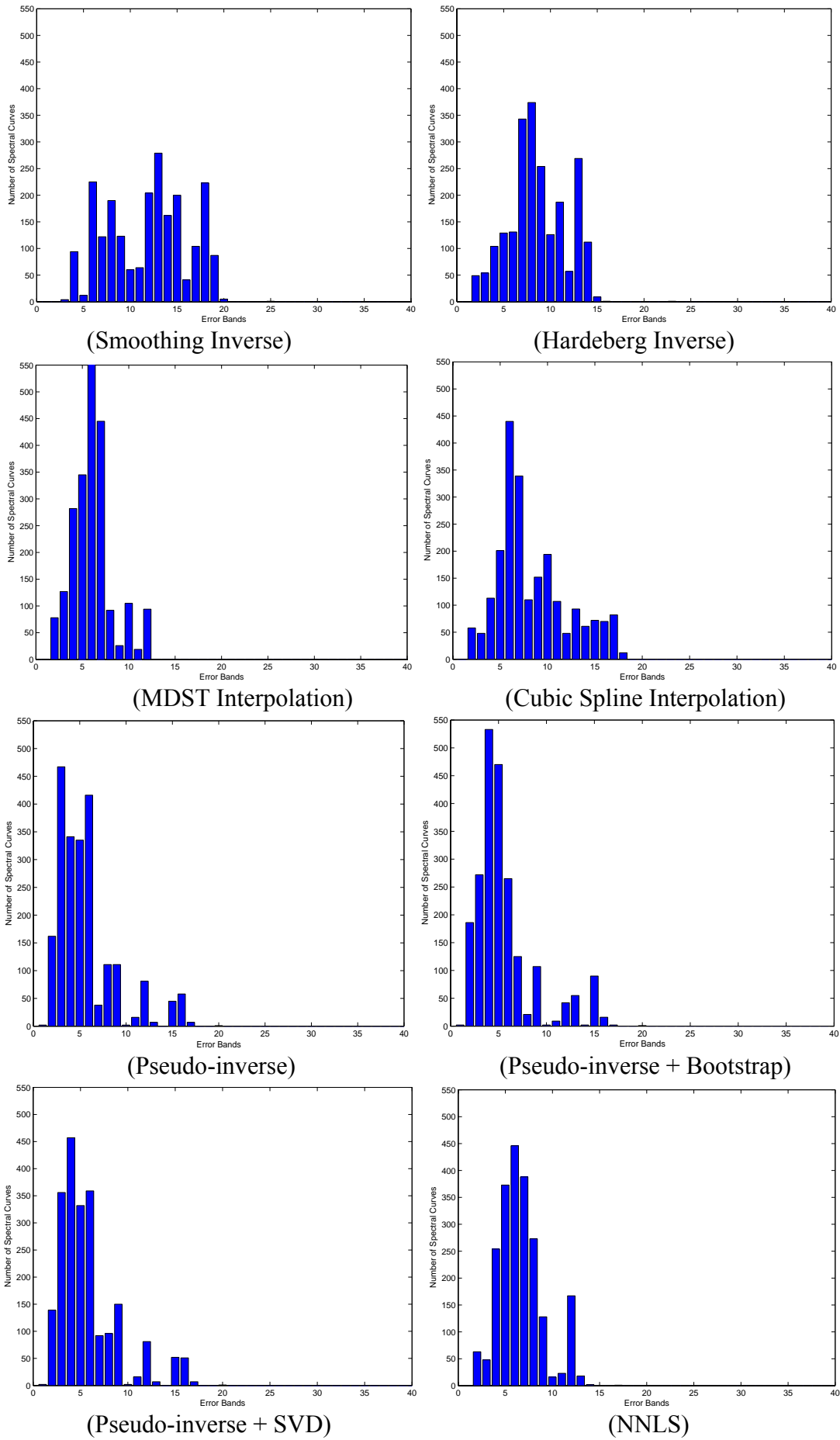


Figure 8-6. Error histograms of different spectral reconstruction methods.

All methods based in a pseudo-inverse present more or less the same performance, this is justified by the fact that the data obtained by the CRISATEL system after calibration is of good quality and present low noise. Consequently a simple pseudo-inverse obtains approximately the same errors as more complex methods. Note that the SVD Pseudo-inverse degrades the error; this means that all the singular values are needed for a good reconstruction, consequently the smallest ones are not corrupted by noise. We believe that Non-averaged Learning Pseudo-inverse increases just slightly the accuracy because the calibration system is efficient removing interpixel sensitivity inhomogeneities. Bootstrapped Learning Pseudo-inverse also slightly increases the error and NNLS obtains a clear degradation. We consider the results of the interpolation methods very interesting, the cubic spline interpolation obtain worst results compared to the learning-based methods but acceptable enough to perform acceptable spectral reconstruction (2.4% of error). As interpolation needs a strict calibration we think this acceptable error is a consequence of the success of the calibration system.

In Table 8-4 we see the CIELAB94 errors associated to each method. We note that in this error space the Mixture Density Network performs the best. The results follow a very similar behaviour than the ones calculated for the absolute errors and shown in Table 8-3.

Table 8-4. CIELAB94 reconstruction errors for the CRISATEL chart experiment

	Train set	Mean test set	Non averaged test set
Smoothing Inverse	4.69	4.42	4.51
Hardeberg Inverse	4.74	4.33	4.44
Learning Pseudo-inverse	2.48	3.33	3.38
Non-averaged Learning Pseudo-inverse	2.45	3.28	3.33
Bootstrapped Learning Pseudo-inverse	2.59	2.84	3.49
NNLS	3.82	3.44	3.53
SVD Pseudo-inverse	2.58	3.43	3.50
MDST Interpolation	4.79	4.84	4.86
Cubic Spline Interpolation	4.02	3.46	3.59
Mixture Density Network	1.88	2.41	2.48

In order to conclude this section we show in Figure 8-7 and Figure 8-8 two examples of spectral reflectance reconstruction. We choose two colour patches of the CRISATEL chart belonging to the mean test set. Spectral reflectance (solid line) is known as it has been measured by a spectroradiometer, we present the estimated curves (dashed lines) using the different reconstruction methods.

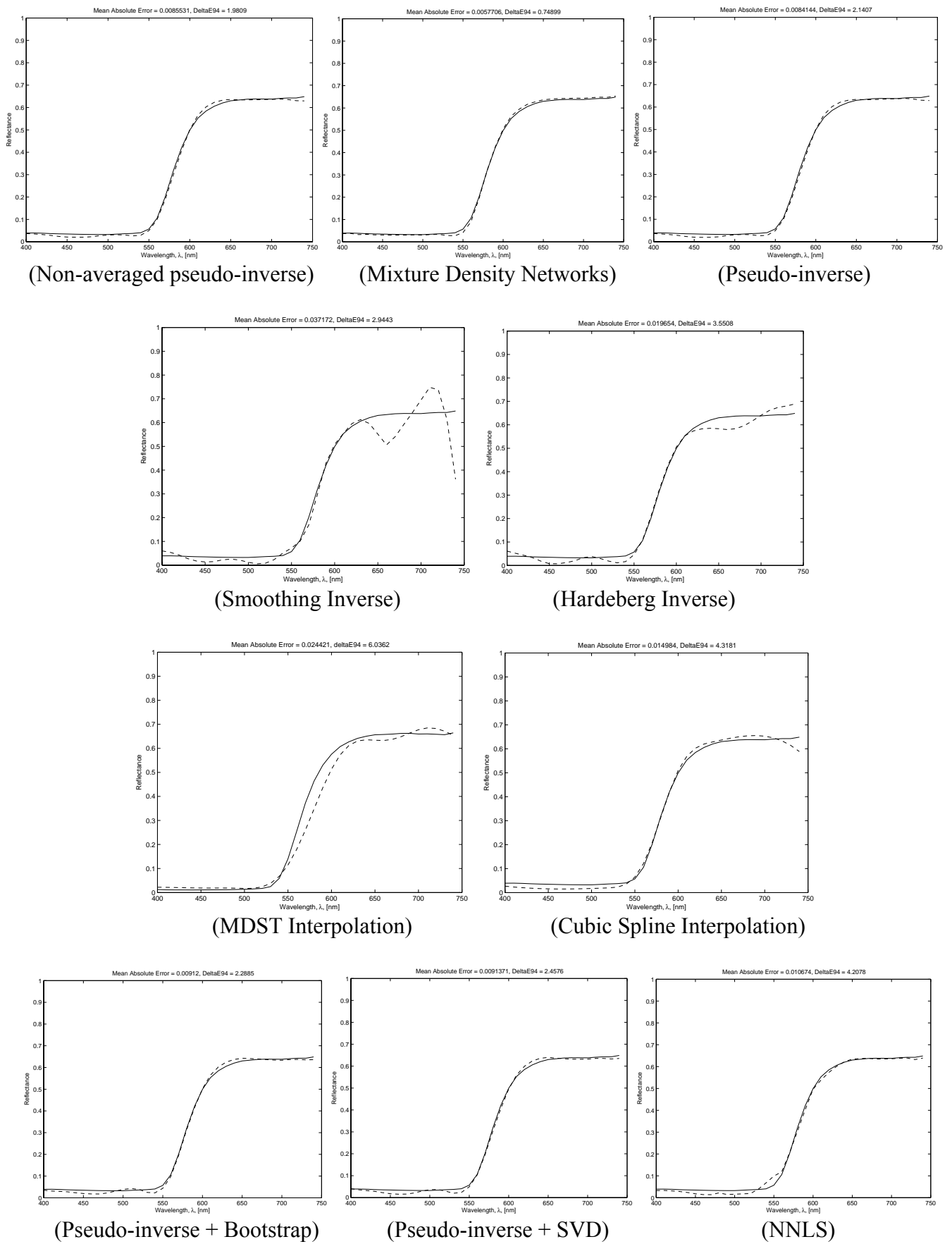


Figure 8-7. CRISATEL chart colour patch spectral reflectance (solid line) and its estimations(dashed lines) using different reconstruction methods.

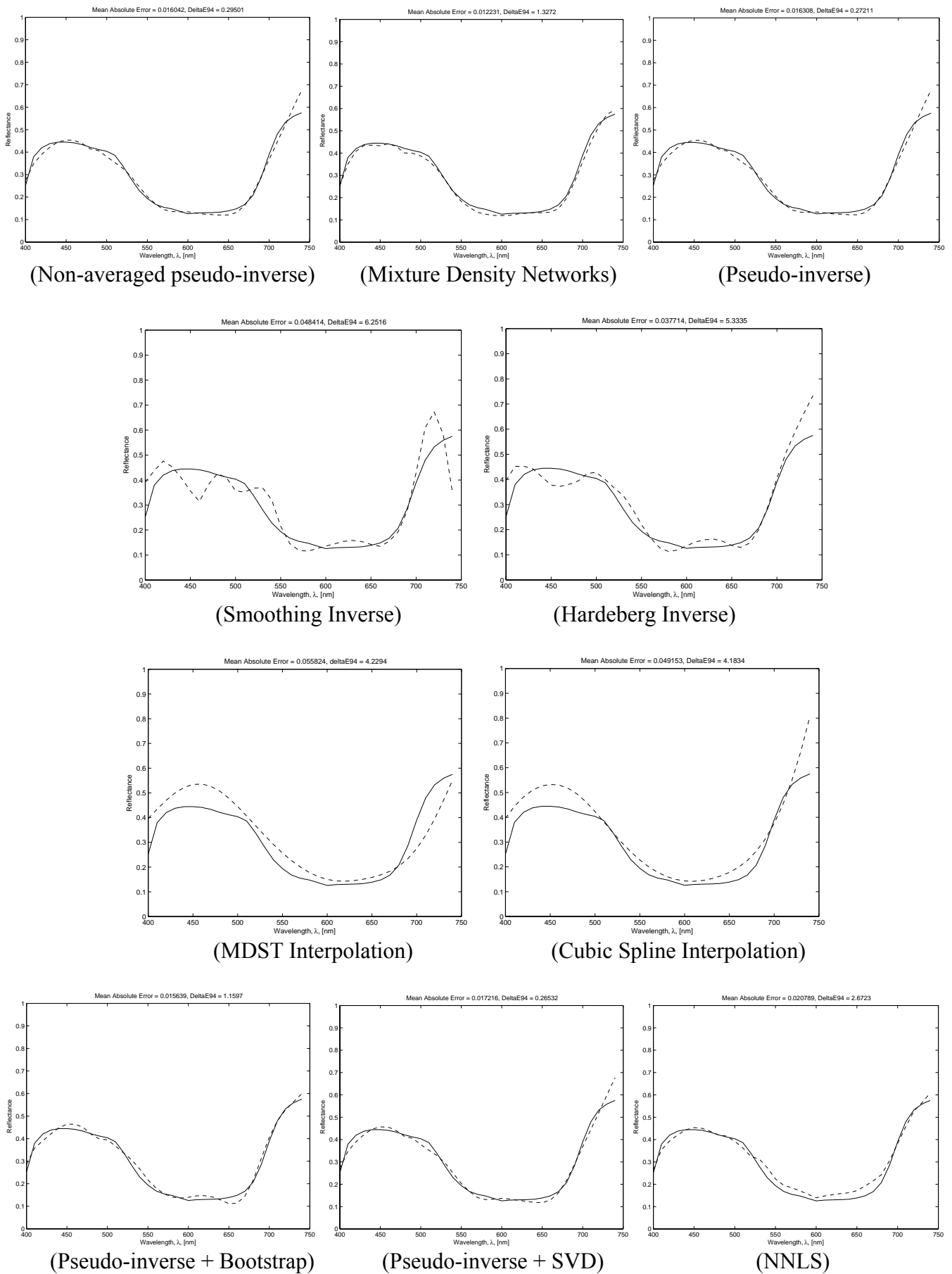


Figure 8-8. CRISATEL chart colour patch spectral reflectance (solid line) and its estimations(dashed lines) using different reconstruction methods.

8.3.3 Art work paintings spectral reconstruction

In this subsection we show two illustrative examples of spectral reflectance reconstruction on real art work paintings: one art work painted by Georges de la Tour and another by Guillaume Fouace.

8.3.3.1 *Saint-Jacques le mineur*

Images of a painting of Georges de la Tour, “Saint-Jacques le mineur” were acquired at *Musée Toulouse Lautrec*, Albi, France, on December 2003 by a team of experts of the CRISATEL project. A colour reconstruction of this multispectral image is shown in Figure 8-10. We note that the shown image is a highly subsampled version of the original one that is obtained at full resolution of the CRISATEL system (20,000x12,000 pixels). We also note that the colours are not realistic as the visualisation medium you see is not calibrated. The original multispectral image has been reconstructed and each spectral reflectance curve projected into sRGB using the d65 illuminant (daylight).

From the image shown in Figure 8-10 we extract a crop of the hand of Saint-Jacques holding the stick. This crop is not extracted in high resolution as we wanted to keep a recognizable shape in the presented image. Much better zooms of the image can be obtained when working at high definition. We performed spectral reflectance reconstruction on two pixels of the extracted crop image. The two spectral curves are shown on Figure 8-9 along with the crop itself. The reconstruction method used was a Mixture Density Network with 12 neurons in its hidden layer and 7 gaussians composing the mixture model.

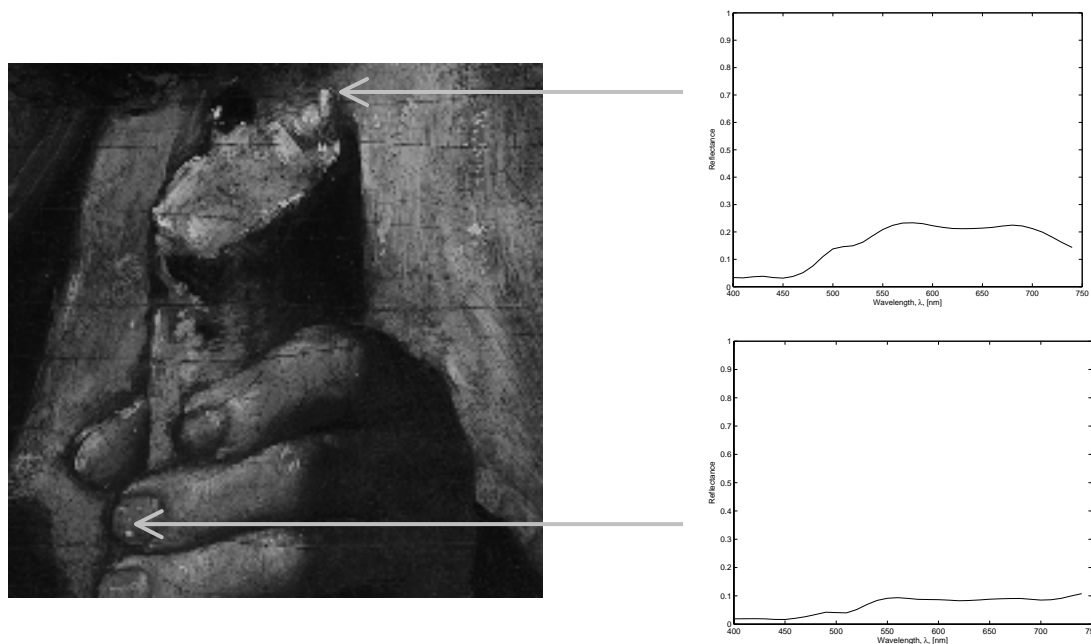


Figure 8-9. Left panel: Crop of the hand of Saint-Jacques holding the stick, greyscale image using a filter centered at 720 nm. Right top and bottom panels: reconstructed reflectance curves on two pixels of the image. The spectral reflectance curves have been estimated using a Mixture Density Network.

The upper graph of Figure 8-9 shows a reconstruction on a pixel belonging to a “light” zone of the image. At a first glance it can seem that the reconstructed curve is not correct because the pixels shown in the crop image are very clear. We note that the image intensity levels have been modified to enhance contrast and better illustrate this document. The original images and the painting itself are very dark, this forms part of Georges de la Tour style. The reconstructed curve is conform to the original painting.



Figure 8-10. Painting Saint Jacques le mineur from Georges de la Tour acquired with the CRISATEL system. The spectral image has been projected into sRGB using the d65 illuminant (daylight).

8.3.3.2 *Le départ pour Jersey*

Le départ pour Jersey was painted by Guillaume Fouace around 1883. It was scanned by members of the CRISATEL project at the Musée Thomas Henry in Cherbourg, France. Its dimensions are 60 x 73.5 cm. As with the previous example it was scanned at 20000x12000 pixels. The image shown in Figure 8-12 is the projection of the reconstructed spectra into the sRGB colour space using daylight D65 illuminant.

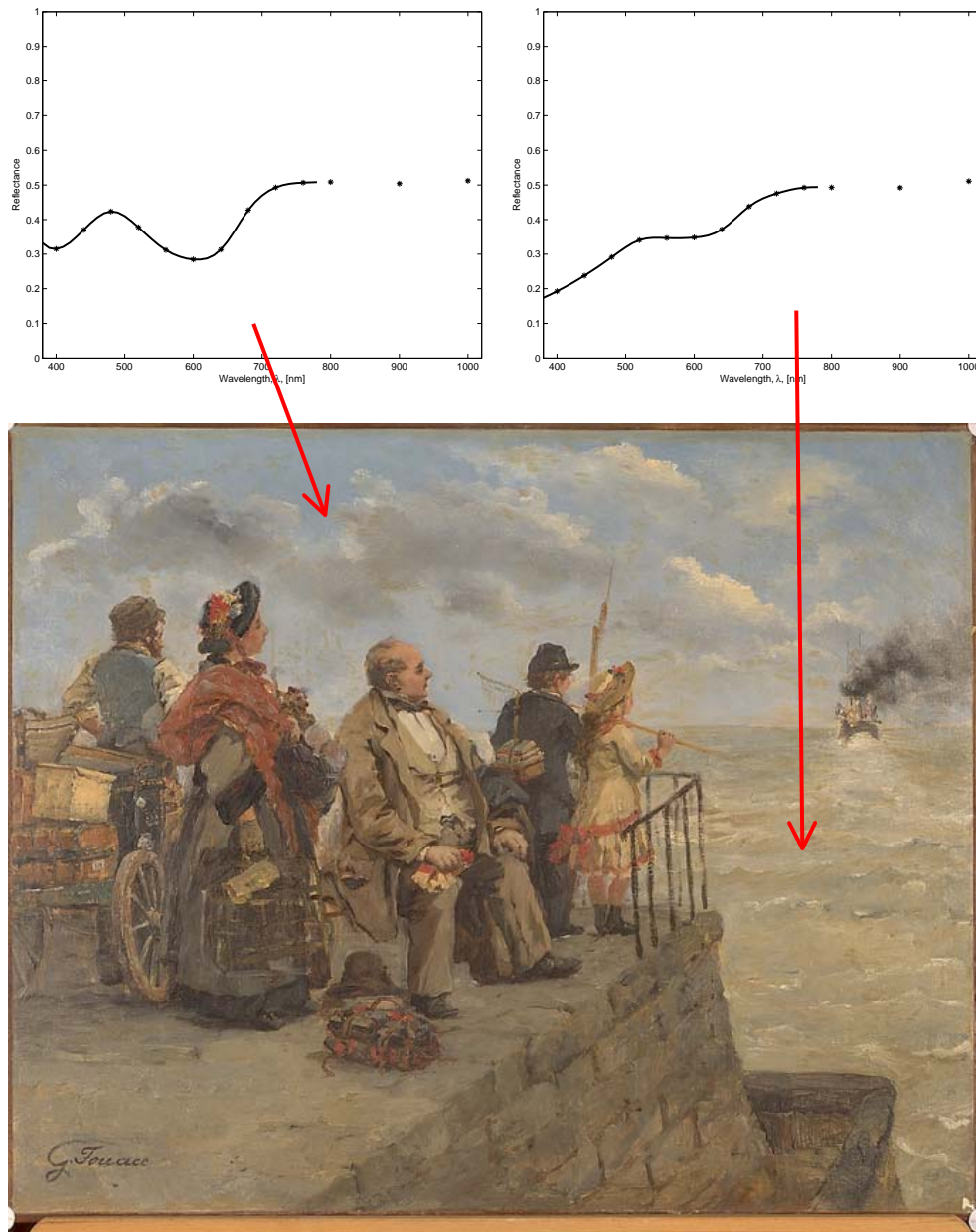


Figure 8-11. Bottom: colour sRGB image of “*Le départ pour Jersey*” painted by Guillaume Fouace (Musée Thomas Henry in Cherbourg, France). Top: reconstructed reflectance curves on two pixels of the image. The spectral reflectance curves have been interpolated from the camera responses using a cubic spline. The camera responses themselves are shown as black stars, the three infrared channels are included even they are not used for spectral reconstruction in the visible spectrum.

The images of this painting were fully processed at the C2RMF where the Space Commander Ruven Pillay implemented in VIPS several of the reconstruction methods described in this thesis. VIPS, see [Cupitt and Martinez, 1996], is Open Source image processing software developed by the National Gallery in London for the efficient manipulation of very large images as those acquired on paintings. The image in Figure 8-12 has been produced using this software that will be the user interface for the museum photographers using the CRISATEL system.

In Figure 8-11 we show the responses of all the thirteen camera channels in two pixels of the painting, one on the lady's face (her cheek) and the other on the blue river to the right of her. The camera responses on the visible range of the spectrum where interpolated (a cubic spline was fitted) and the ones on the infrared are shown without reconstruction. This is to emphasize that only the 10 visible channels are used for colorimetric reconstruction.



Figure 8-12. Colour sRGB image of “Le départ pour Jersey” painted by Guillaume Fouace around 1883. The spectral image has been projected into sRGB using the d65 illuminant (daylight).

8.3.4 Illuminant Simulation

The appearance of an object or a scene may change considerably when the illuminant changes. This is due to a combination of physical and psychophysical effects that we will not consider here. These effects are taken into account in most colour appearance models in somewhat heuristic manner. However, such models cannot predict correctly changes for arbitrary illuminants, one important reason for this being metamerism. In fact, to make quantitative predictions about the physical phenomena involved when the illuminant is changed, a complete spectral description of the illuminants and the scene is required. Working with multispectral imaging and a spectral reflectance reconstruction system provides a complete spectral description of the scene. Light sources can be measured simply by the use of a spectrophotometer and a reference white patch. Moreover, most common illuminants are already measured and standardized by the CIE. All these facts made illuminant simulation a straightforward application of the systems presented in the present thesis.

In the framework of art paintings, a computer tool implementing illuminant simulation is of great aid. A curator having to decide the appropriate light sources for an art exhibition will be pleased to use such a tool. Illuminant simulation can become a central issue, for instance, when a high quality printed reproduction of a painting is to be produced. If the reproduction is to be seen on the streets for advertising purposes the illuminant will be daylight but if the reproduction is in a book on a library it will be probably seen with an halogen lamp.

Simulating the illuminant from the spectral reflectance curve is mathematically simple. First of all a spectral reflectance curve $\tilde{\mathbf{r}}$ is reconstructed from a multispectral image by any of the existing methods. We then calculated colorimetrically the estimated XYZ tristimulus values of the surface imaged in this pixel and lit by illuminant \mathbf{L}_{sim} . Then:

$$\begin{bmatrix} \tilde{X}_{sim} \\ \tilde{Y}_{sim} \\ \tilde{Z}_{sim} \end{bmatrix}^t = \mathbf{A}^t \mathbf{L}_{sim} \tilde{\mathbf{r}} \quad (4.1)$$

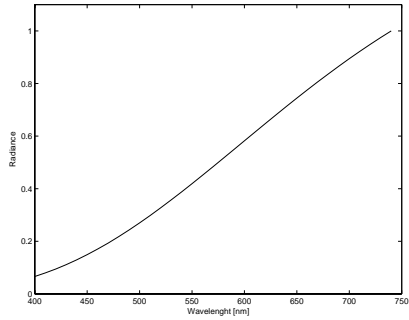
where \mathbf{L}_{sim} is the diagonal matrix corresponding to the spectral radiance of the simulated illuminant, $\mathbf{A} = [\bar{x} \ \bar{y} \ \bar{z}]$ represents the colour matching functions (see Appendix I), \tilde{X}_{sim} , \tilde{Y}_{sim} and \tilde{Z}_{sim} are the estimated XYZ tristimulus values. In our case the estimated XYZ tristimulus values are used to calculate their sRGB corresponding values. This is achieved by a simple linear transformation based on phosphor chromaticities and the white point corresponding to illuminant D_{65} :

$$\begin{bmatrix} R_{sRGB} \\ G_{sRGB} \\ B_{sRGB} \end{bmatrix} = \begin{bmatrix} 3.2406 & -1.5372 & -0.4986 \\ -0.9689 & 1.8758 & 0.0415 \\ 0.0557 & -0.2040 & 1.0570 \end{bmatrix} \begin{bmatrix} X \\ Y \\ Z \end{bmatrix} \quad (4.2)$$

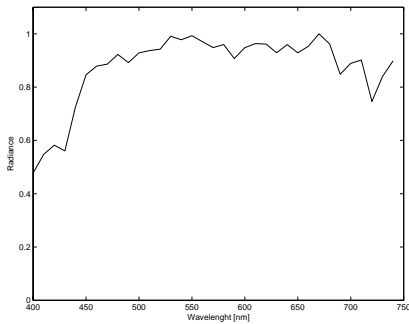
Then the Gamma-corrected sR'G'B' values are defined as

$$R'_{sRGB} = \begin{cases} 12.92R_{sRGB}, & R_{sRGB} \leq 0.00304 \\ 1.055R_{sRGB}^{1.0/2.4} - 0.055, & elsewhere \end{cases} \quad (4.3)$$

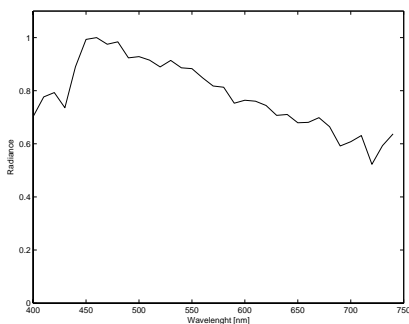
and likewise for G'_{sRGB} and B'_{sRGB} . The 8-bit digital values that should be transmitted to the display are finally calculated as $R_{8bits} = 255.0R'_{sRGB}$. In Figure 8-13 and Figure 8-14 we show examples of illuminant simulation.



Illuminant A



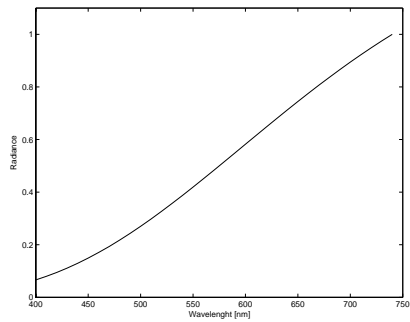
Illuminant d50



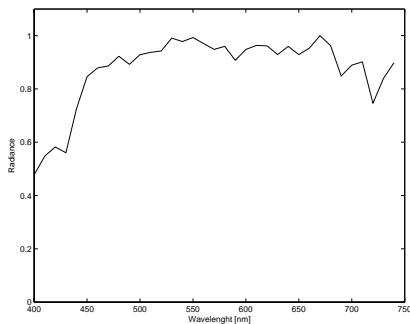
Illuminant d65



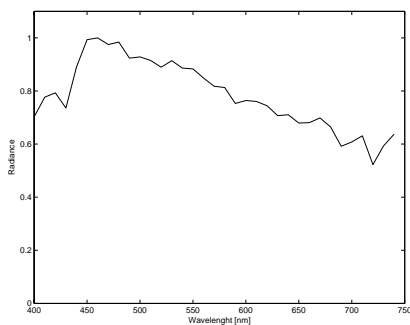
Figure 8-13 Illuminant simulation to produce a sRGB colour image of the hand of Saint-Jacques le mineur. A Mixture Density Network was used for spectral reflectance reconstruction. The three images does not present big visual differences because of the red-yellowish nature of the pigments.



Illuminant A



Illuminant d50



Illuminant d65

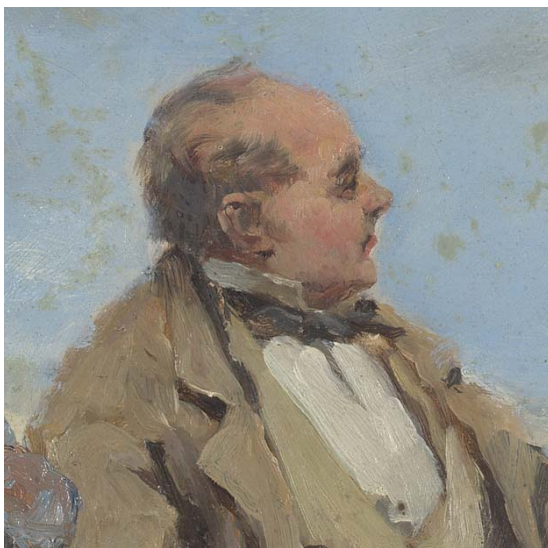


Figure 8-14. Illuminant simulation to produce a sRGB colour image of the head of the sitting fat man in “Le départ pour Jersey”. A cubic spline interpolation was used for spectral reflectance reconstruction. Note that blue being a prominent element in this painting, the visual appearance is seriously altered by the change of illuminant.

8.4 Conclusion

This chapter finishes the experimental part of this thesis. The methods developed or studied in the first part have been applied to existing multispectral acquisition systems. The two used multispectral acquisition systems (National Gallery of London and CRISATEL) are cutting-edge systems designed for a high-quality demanding application as it is the digitalization of art paintings.

We have been involved in the CRISATEL project from the beginning of this thesis. The colour reproductions being performed at the moment for this system show that our efforts have a direct application. At the present time, the CRISATEL project is not completely achieved. The first results shown in this thesis using Georges de la Tour and Guillaume Fouace paintings will be followed by much more analysis and acquisitions. The CRISATEL system is currently operational at the Museum of Louvre (Paris).

The performed work opens new perspectives, in fact, the CRISATEL multispectral system is now used by the C2RMF (*Centre de Recherche et de Restauration des Musées de France*) for the digital acquisition of paintings from different periods and styles on a large scale in several museums in France, [Lahanier et al., 2003]. The main aims are to characterise the palette of the artists and, if possible, to identify the pigments by comparison of their spectral reflectance curves with a reference of pure and mixed pigments used by artists. The digital results are verified by measuring several areas on the paint surface with a spectrophotometer. Analysis by X Ray micro-fluorescence is additionally used to identify the chemical composition of the pigment.

Further research on high fidelity colour reproduction and pigment identification will follow this work.

Chapter 9:

Conclusion and Future Work

The idea to create a high-fidelity colour acquisition system for imaging art paintings is central in this thesis. The application of multispectral imaging to works of art is a consequence of the very demanding representation and reproduction standards involved in this field. This driven force has moved us to perform methodological investigations in one hand and experimental testing and developments on the other hand. Probably, the most fundamental result of this thesis is that new methods for spectral reconstruction have been investigated and applied to existing cutting-edge multispectral acquisition systems. The present document has been divided into two main parts and both of them converge together into the results chapter where we showed examples of art paintings acquired and processed by methods developed by us during these past years.

We note that a new classification of existing techniques for spectral reconstruction has been proposed. This new classification is physically and mathematically well founded. It is indeed use to give insight on the behaviour of the methods presented in our detailed survey.

Concerning the methodological investigations performed we remark the introduction of non-linear techniques for spectral reflectance reconstruction. We developed a fully-automatic technique based on Mixture Density Networks that is performing very satisfactorily at this moment when is being applied to real data. When tested on simulated data this approach leads to a reconstruction method obtaining good results when quantisation noise is present or not. This method appears suitable for any kind of multispectral camera and is not designed for a specific camera.

We also developed techniques to improve the estimation accuracy of existing methods. In this sense, a bootstrap strategy has been introduced to increase the generalisation capabilities of existing linear reconstruction techniques. In the future, this strategy can be applied to other purposes as subset selection, the selection of representative spectral curves among a database. A spline projection operator has also been developed to force the reconstructed spectral curves respecting physical constraints.

A large part of this thesis is dedicated to the CRISATEL system. Some methodological and theoretical work about the selection of filters for the CRISATEL camera has been done presenting an original approach to this issue. But, most of the work concerning the acquisition system has been experimental. One of our main tasks in this European project has been to obtain the best quality of image as possible from the hardware system designed by Lumiere Technology. We firstly characterised all the elements involved in the acquisition system, this characterization implied systematic and time consuming experimental work. Based on this precise characterization an autocalibration procedure and correction software were designed and implemented. They allow high quality images to be obtained and are being used at the moment as part of the CRISATEL system.

The work developed for the CRISATEL system opens new axes of research and application. It is important to note that the system was designed to be used by the C2RMF (*Centre de Restauration des Musées de France*) for the scanning of fine art paintings in French Museums. This objective has been accomplished, currently the acquisition system is physically installed at the *Musée du Louvre* (Paris). There, it is used for the digitisation of fine art works. The results chapter of this thesis shows images of paintings (by Georges de la Tour and Guillaume Fouace) already acquired and some tests performed over the CRISATEL chart.

The obtained images will be of great use in museological research due to their high spatial resolution and high-fidelity colour representation. The spectral reconstruction can be exploited in many ways:

- Illuminant simulation can be performed for realistic visualisation under any given light sources.
- Pigment identification and classification can be based in a good spectral reconstruction. This point needs to be investigated as a consequence of the work already performed.
- Spectral printing becomes possible once the image is represented by spectral reflectances and not in a colour space. This involves the use of the spectral reflectance and not a colour space to produce the printing. Trying to match a spectral reflectance by using combinations of dyes is at the moment an open field of research.
- All the colour management system can, indeed, be based on the concept of spectral reflectance instead of tristimulus colour values. This allows a more general and powerful system where the calibration of the devices and transfer of data becomes easier and scientifically controlled.
- Devarnishing means getting the spectral reflectances of the pigments under the varnish layer of a painting. It aims to simulate the effect of a partial or full removal of the varnish under any lighting conditions. This is very important for restoration as most of the times restoring a painting involves the manual removal of old deteriorate varnish and the application of new one. This process is performed manually by specialist and is very expensive and time consuming. Virtual devarnishing of a painting being based on spectral reconstruction, it would be a very useful tool for conservators to decide which paintings are worth to be restored.
- As a consequence of having a computerised system for storing works of art realistically, "printing on demand" becomes a straightforward application. Visitors of a museum can generate their own choice of prints. They will be able to specify a picture from the collection and use calibrated (eventually spectral) printing technology to carry home their own copy. This is already done at the National Gallery of London where its Sainsbury's Wing shop proposes prints on demand at Standard sizes (A4, A3 and A2).

Finally, we would like to remark that both theoretical and experimental developments performed in this Ph.D. have fused in an actual system. Moreover, the CRISATEL system is currently operational and the performed developments open new perspectives for museological and technological research.

Appendix I:

Colorimetry in a Nutshell

The retina of the human eye has two categories of light receptor: rods, which are active in dim light and have no colour sensitivity, and cones, which are active in bright light and provide us with the ability to discriminate colour. This fact was experimentally demonstrated in 1965 and the response curves for three different kinds of cones in the retina of the human eye were measured. The relative sensitivity of the three receptors for the "average" human eye, designated by letters S (short), M (medium) and L (long) are shown in Figure AI-1. The shapes of the curves are obtained by measurement of the absorption by the cones, but the relative heights for the three presented curves are normally set equal for lack of detailed data. The S and M sensors correspond closely to blue and green. An ink with the same spectral reflectance curve than the L sensor would appear yellow-orange. The eye/brain discriminates colour by processing the relative stimuli in the three sensors.

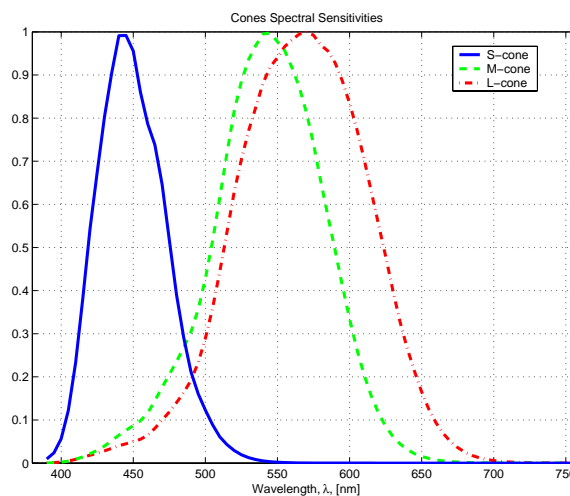


Figure AI-1. Spectral Sensitivities of the cones.

In order to quantify human colour vision, the CIE (*Commission Internationale de l'Éclairage*) has established a set of imaginary primary colours that, when combined, cover the full range (*gamut*) of human colour vision. These primaries (shown on the left panel of Figure AI-2) present negative energy in portions of their spectra, consequently they are not physically realizable. This is because these curves are determined experimentally by performing mathematical matrix transformations of the results of a split screen matching experiment. These experiments, carried out in the 1920s, showed that three primaries (RGB) could indeed match all visual colours within a certain range called a *gamut*, but that they could not match all the spectral colours, particularly in the green range. It was found that if a certain amount of red light was added to the colour being matched, then all colours could be matched. The quantitative results were expressed in terms of tristimulus values for the RGB primaries, but it was necessary to allow negative values for the red tristimulus values in order to match all colours.

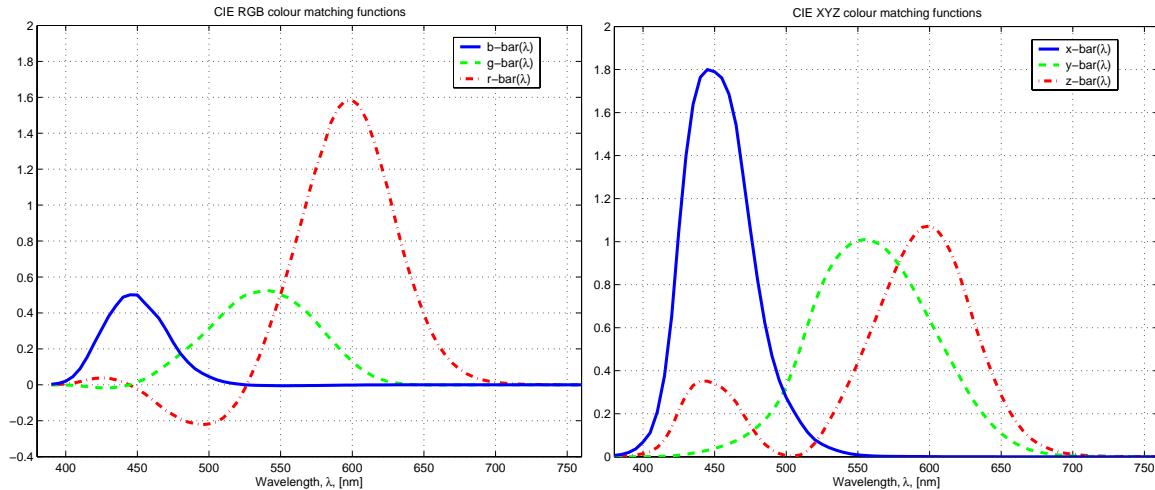


Figure AI-2. (Left panel) CIE RGB colour matching functions presenting negative energy in some parts of the curves, (right panel) CIE XYZ colour matching functions not presenting negative values.

Due to the problems presented by the RGB primaries the CIE derived a new set of primaries. This new set, called X, Y, and Z, have the following properties:

1. They always produce positive tristimulus values.
2. It is possible to represent any colour in terms of these primaries.
3. They were derived so that equal values of X, Y, and Z produce white.
4. They were arranged so that a single parameter Y determines the luminance of the colour.
5. They are related to the sensitivity of the human eye by the use of colour matching functions which match to the CIE 1931 Standard Observer.

On the right panel of Figure AI-2 we show these Colour Matching Functions for the Standard Colorimetric Observer. They are designated \bar{x} , \bar{y} , and \bar{z} , and they never have negative values. The Colour Matching Functions are used to derive the XYZ tristimulus values that form the basis of CIE colorimetry; two objects with the same tristimulus values have identical colour appearance when viewed under the same conditions. The X, Y, and Z tristimulus values are calculated by integrating the product of the spectral reflectance $r(\lambda)$, the illuminant $l(\lambda)$, and the corresponding colour matching function normally from $\lambda_{\min} = 380$ to $\lambda_{\max} = 760$ nm:

$$X = \int_{\lambda_{\min}}^{\lambda_{\max}} r(\lambda) l(\lambda) \bar{x}(\lambda) d\lambda ,$$

$$Y = \int_{\lambda_{\min}}^{\lambda_{\max}} r(\lambda) l(\lambda) \bar{y}(\lambda) d\lambda ,$$

$$Z = \int_{\lambda_{\min}}^{\lambda_{\max}} r(\lambda) l(\lambda) \bar{z}(\lambda) d\lambda ,$$

Although the tristimulus values uniquely define an object colour, they do not define the eye's response to the colour, which depends on the environment and the eye's adaptation.

Colour spaces as XYZ (or RGB) relate linearly to the spectrum of the coloured light but psychophysical experiments showed that the human eye's sensitivity to light is not linear.

When changing the tristimulus values of XYZ (or RGB) for a colour stimulus, the observer will perceive a difference in colour for differences greater than the Just Noticeable Difference (JND). In both RGB and XYZ spaces the JND depends on the location in the colour space.

CIELAB space was proposed by the CIE in 1976. The aim of CIELAB is to make JND constant, leading to a uniform colour space where the JND is not depending on the location. In practice, this condition is only fulfilled approximately, thus we normally use the term *pseudo-uniform* for CIELAB. Remark that the notion of JND is observer-dependent and resulting from psychophysical experiments, this makes CIELAB a *psychometric* colour space. The CIELAB pseudo-uniform colour space is defined by the quantities L^* , a^* and b^* . They are calculated from X, Y, Z using:

$$\begin{aligned} L^* &= 116f\left(\frac{Y}{Y_n}\right) - 16, \\ a^* &= 500\left[f\left(\frac{X}{X_n}\right) - f\left(\frac{Y}{Y_n}\right)\right], \\ b^* &= 200\left[f\left(\frac{Y}{Y_n}\right) - f\left(\frac{Z}{Z_n}\right)\right], \end{aligned}$$

where

$$f(\alpha) = \begin{cases} \alpha^{1/3} & , \alpha \geq 0.008856 \\ 7.787\alpha + \frac{16}{116} & , \text{otherwise} \end{cases} .$$

The tristimulus values X_n , Y_n and Z_n are those of the nominally white stimulus. For a given illuminant $l(\lambda)$, they are defined:

$$\begin{aligned} X_n &= \int_{\lambda_{\min}}^{\lambda_{\max}} l(\lambda) \bar{x}(\lambda) d\lambda, \\ Y_n &= \int_{\lambda_{\min}}^{\lambda_{\max}} l(\lambda) \bar{y}(\lambda) d\lambda, \\ Z_n &= \int_{\lambda_{\min}}^{\lambda_{\max}} l(\lambda) \bar{z}(\lambda) d\lambda. \end{aligned}$$

In the CIELAB space, L^* represents the *lightness* of a colour and it is known as the CIE 1976 psychometric lightness. The scale of L^* is 0 to 100, 0 being the ideal black, and 100 being the reference white. The chromacity of a colour can be represented in a two-dimensional (a^* , b^*) diagram, a^* representing the degree of green versus red, and b^* the degree of blue versus yellow.

Appendix II:

Résumé Long en Français

L'imagerie numérique couleur multispectrale est une discipline de l'ingénierie où des images avec plus de trois bandes dans le domaine visible sont acquises et analysées. Les appareils photo-numériques couleur conventionnels produisent des images de trois bandes et sont limités pour la reproduction haute fidélité de la couleur. Ils ne permettent pas notamment de reproduire correctement une scène sous différents types d'éclairage. Au cours des dix dernières années l'image couleur multispectrale s'est concentrée sur certains domaines où la fidélité de la couleur est d'un grand intérêt scientifique, en particulier celui de l'analyse et de la reproduction des oeuvres d'art. Cette thèse s'inscrit dans cette continuité et traite de l'acquisition et de l'analyse des images couleur multispectrales haute résolution appliquées aux toiles de maître.

Un des problèmes fondamentaux liés à l'imagerie multispectrale est la reconstruction des courbes de réflectance spectrale à partir des valeurs mesurées dans chacune des bandes multispectrales. Cette thèse aborde en profondeur ce sujet. La valeur d'un pixel d'un canal dans une image multispectrale est le résultat de :

- 1) l'interaction de la distribution spectrale d'énergie radiante générée par la source de lumière avec la réflectance de la surface de l'objet éclairé,
- 2) la sensibilité spectrale de l'appareil photo-numérique combinée à la transmittance spectrale du chemin optique comprenant l'objectif de l'appareil et le filtre correspondant à ce canal.

La détermination de la fonction de réflectance spectrale de la surface de l'objet en chaque pixel de son image est primordiale. Nous appelons ce processus *reconstruction de la réflectance spectrale* ou simplement *reconstruction spectrale*. Celle-ci permet une représentation intrinsèque des propriétés visuelles de la surface d'un objet qui est indépendante de la distribution spectrale d'énergie de la source lumineuse et de la sensibilité spectrale de l'appareil photo-numérique utilisé pour l'acquisition de l'image. Cette représentation peut être employée dans de nombreuses applications. On peut ainsi concevoir un système de gestion de la couleur basé sur les propriétés spectrales des matériaux. Un tel système serait beaucoup plus général qu'un système de gestion classique basée sur la colorimétrie. Dans cette thèse, notre principal intérêt est la gestion haute fidélité de la couleur des toiles de maître. Par exemple, connaître la réflectance spectrale en chaque pixel de l'image d'une peinture nous permet de simuler l'aspect de cette peinture sous n'importe quel illuminant virtuel. Il permet également de simuler l'enlèvement virtuel d'un vernis âgé, ce qui peut être d'un grand intérêt pour les conservateurs dans leur tâche de planification de la restauration de toiles de maître anciennes.

Nous pouvons conceptuellement diviser cette thèse en deux grandes parties distinctes. Dans la première partie nous étudions le problème de la reconstruction de la réflectance spectrale en un pixel d'une image multispectrale. Ce problème présente des aspects théoriques et pratiques intéressants et qui restent de portée générale. La deuxième partie est consacrée au projet européen IST-20163-1999 CRISATEL (*Conservation Restoration Innovation Systems for Image capture and Digital Archiving to Enhance Training Education and Lifelong Learning*). Dans ce projet un système multispectral d'acquisition d'images numériques à haute fidélité et à haute résolution spatiale (12.000 x 30.000) a été développé pour la numérisation des toiles de maître dans les musées. Il est composé d'une caméra multispectrale comportant 13 canaux (10 dans le visible et 3 dans l'infrarouge), et d'un système d'éclairage dédié qui balaye le tableau en synchronisation avec le mouvement de la barrette CCD équipant la caméra. La deuxième partie de notre travail est donc plus expérimentale et intimement liée au système d'acquisition développé par CRISATEL. Les deux parties de cette thèse se complètent de façon naturelle : les méthodes générales de reconstruction spectrale proposées dans un premier temps sont ensuite appliqués à un système réel d'acquisition.

Dans la suite de ce résumé nous décrivons brièvement les chapitres qui composent ce document. Les idées générales de cette thèse sont alors structurées ici en français de la même façon qu'elles le sont en anglais dans le reste du document.

Chapitre 1. Introduction.

Ce bref chapitre donne une vision générale du contenu de cette thèse. Il introduit le sujet traité et présente, chapitre par chapitre, les informations plus remarquables que le lecteur va trouver dans le reste du document.

Chapitre 2. La nature des données.

Nous présentons dans ce chapitre les concepts de base sur la formation d'une image multispectrale, comprenant les formules fondamentales et une description des principaux composants d'un système d'acquisition multispectral : sources lumineuses, filtres, CCD et réflectances spectrales. Les sources de bruit entachant les systèmes d'acquisition et les mesures de la réflectance sont présentées. Leur description aide à comprendre les limitations d'un système de formation d'image basé sur le concept de réflectance spectrale au lieu de la couleur.

Ce chapitre se veut plus qu'une simple introduction à la formation de l'image multispectrale. Dans sa deuxième partie nous nous concentrons en effet sur l'analyse des courbes de réflectance spectrale. Ce point est fondamental avant de prendre toute décision sur la conception d'un système d'acquisition ou d'une méthode de reconstruction spectrale. Nous voulons comprendre la nature des courbes spectrales autant que possible. Les bases de données de réflectances utilisées dans le reste de la thèse sont présentées et étudiées. L'analyse de Fourier et l'Analyse en Composantes Principales (ACP) sont les outils mathématiques utilisés pour leur analyse.

Nous soulignons qu'une nouvelle approche pour la comparaison entre différentes bases de données de réflectances spectrales a été également développée. Cette approche est simple et mathématiquement bien fondée. Elle est basée sur la distance de Froebius entre matrices. Cette distance est employée comme une mesure de similarité pour des bases orthogonales

issues d'une ACP associée aux bases de données des réflectances spectrales étudiées. Enfin, nous présentons et analysons une nouvelle mire développée dans le cadre du projet européen CRISATEL.

Chapitre 3. Bases de la reconstruction spectrale.

Ce chapitre décrit le problème de la reconstruction spectrale et présente un état de l'art actualisé des techniques existantes de reconstruction illustrées en employant des simulations par ordinateur. Nous proposons une classification des techniques de reconstruction en trois paradigmes :

- i) *la reconstruction directe*, qui est basée sur l'inversion du modèle du système d'acquisition et qui a besoin de la caractérisation du système;
- ii) *la reconstruction indirecte* ou reconstruction par apprentissage, où une mire calibrée et son image multispectrale sont employées pour construire un opérateur de reconstruction ;
- iii) la reconstruction par interpolation, où les réponses obtenues par la caméra multispectrale sont interpolées pour trouver une approximation de la fonction de réflectance spectrale correspondante.

A notre connaissance c'est la première fois qu'une telle classification est donnée. Nous croyons qu'il est utile de différencier des méthodes qui ont une origine conceptuelle très différente. Cette classification est physiquement et mathématiquement bien fondée et aide à comprendre les besoins intrinsèques et les limites à chaque méthode.

Chapitre 4. Amélioration de la précision de la reconstruction spectrale.

Dans ce bref chapitre nous décrivons deux idées originales que nous proposons pour améliorer la précision de la reconstruction spectrale. Ces idées ne sont pas en elles-mêmes de nouvelles techniques de reconstruction et peuvent être appliquées pour améliorer la plupart des méthodes de reconstruction spectrale existantes. Elles sont indépendantes et pourraient être intégrées ensemble.

La première idée consiste à améliorer les capacités de généralisation des méthodes linéaires de reconstruction existantes en utilisant des informations a priori sur la réflectance des objets imagés. L'algorithme proposé utilise le concept de généralisation, il se base sur un rééchantillonnage aléatoire intense des données utilisées pour construire les opérateurs. Nous présentons des résultats de simulation où une amélioration de 50% de la précision est obtenue sur les ensembles d'essai utilisés. Ceci apparaît comme un résultat très prometteur. De plus, l'idée en elle-même est intéressante et ouvre de nouvelles perspectives de recherche. Par exemple, le problème du choix d'un sous-ensemble de courbes de réflectance spectrale représentatif d'un ensemble de courbes peut être étudié par ce moyen. Le sous-ensemble des courbes spectrales choisies par l'algorithme vaut la peine d'être soigneusement étudié dans le futur.

La deuxième idée est liée aux contraintes physiques à respecter par les courbes spectrales reconstruites. Nous avons proposé un opérateur de projection *spline* qui est simplement appliqué après reconstruction, il apparaît comme un complément à n'importe quelle technique existante de reconstruction. Il garantit que les courbes obtenues sont continues et lisses en même temps.

Chapitre 5. Reconstruction spectrale en utilisant des *Mixture Density Networks*.

Nous considérons à présent le problème de la reconstruction des courbes de réflectance spectrale à partir d'images multispectrales en utilisant des techniques basées sur les réseaux de neurones. A notre connaissance, c'est la première fois que ce type d'approche est appliqué à la résolution du problème de reconstruction spectrale. Notre but est ici de trouver une méthode non linéaire basée sur l'apprentissage, capable de fournir une bonne résistance au bruit et ayant également une bonne capacité de généralisation.

Dans ce chapitre nous commençons par justifier l'utilisation des opérateurs non linéaires pour la reconstruction spectrale. Une introduction générale aux réseaux de neurones est d'abord présentée. Ensuite nous décrivons notre première tentative d'employer des réseaux de neurones comme méthode de reconstruction spectrale, [Ribés et al., 2002]. Nous avons étudié la résistance au bruit de quantification de la reconstruction spectrale obtenue avec différents réseaux de neurones conventionnels et les avons comparés à une méthode linéaire déjà utilisée pour la reconstruction spectrale des toiles de maître [Hardeberg et al., 1999]. Trouvant non adapté l'application directe des réseaux de neurones à la reconstruction spectrale, nous avons développé une nouvelle méthode mélangeant cette technique et l'Analyse en Composantes Principales (ACP). La méthode résultante fournit de bons résultats en présence d'un bruit de quantification mais elle n'est pas satisfaisante, comparée aux méthodes linéaires, quand le bruit n'est pas présent.

Pour augmenter la précision des méthodes existantes nous appliquons des *Mixture Density Networks* (MDN) dans le contexte de la reconstruction spectrale. Cette approche a fait l'objet de plusieurs publications [Ribés et Schmitt, 2002, Ribés et Schmitt, 2003]. La méthode MDN est basée sur la construction de la fonction de distribution de la probabilité conditionnelle entre les réponses multispectrales de la caméra et les fonctions de réflectance spectrale associées. Cette approche mène à une méthode de reconstruction fournissant de bons résultats, que le bruit soit présent ou non. La méthode a été testée en utilisant des données simulées et des données expérimentales, les résultats étant supérieurs à ceux obtenus avec les méthodes linéaires. Pour terminer nous décrivons comment le problème de l'optimisation de l'architecture du MDN a été résolu. Ce dernier point rend la méthode finale entièrement automatique sans la nécessité de fixer des paramètres à la main.

Chapitre 6. Expérimentation : le système d'acquisition CRISATEL.

Un système d'acquisition multispectral à haute résolution a été développé pour le projet européen CRISATEL. Ce système inclut une caméra multispectrale et un système d'éclairage dédié d'une puissance élevée, les deux systèmes ayant été développés par Lumière Technology, Paris, France.

Nous présentons d'abord le système d'acquisition multispectral du projet européen CRISATEL en décrivant les caractéristiques spectrales de ses filtres, son système de d'éclairage et l'architecture électronique de la caméra . Cette présentation générale est nécessaire pour comprendre l'ensemble des expériences présentées dans le reste du chapitre.

Ensuite nous procédons à l'évaluation du système. Des expériences physiques ont été élaborées et implémentées afin de caractériser la linéarité de la réponse du CCD et son bruit au noir. Le bruit au noir étant un aspect très important, sa caractérisation complète et sa dépendance avec les paramètres de la caméra ont été étudiées en profondeur. Le problème de l'aberration chromatique est brièvement présentée. Finalement, la distribution spatiale non

homogène de l'éclairage sur l'image est analysée. Les expériences physiques et l'analyse des données obtenues se sont avérées d'intérêt pour la communauté multispectrale et ont été présentées à une conférence internationale [Ribés et al., 2003, PICS]. L'ensemble de ces résultats forme la base de l'évaluation du système d'acquisition et est contractuel pour la communauté européenne dans le cadre du projet CRISATEL. Ce sujet a fait l'objet d'un rapport technique préliminaire [Ribés et al., 2003, CRISATEL].

Suite à l'évaluation réalisée nous avons proposé une procédure de calibrage. Cette procédure est composée de trois étapes : nous déterminons d'abord les paramètres liés au contrôle de la caméra multispectrale et obtenons les cartes spatiales pour la correction de l'inhomogénéité de l'éclairage, ensuite nous procédons à l'étude du bruit au noir en chaque pixel (ou photo site) du CCD et finalement le gain en chaque pixel est déterminé afin de corriger les différences de sensibilité entre les pixels du CCD. Nous montrons en détail comment ces opérations sont effectuées.

En résumé, nous avons effectué deux types de tâches dans ce chapitre expérimental consacré à l'étude du système d'acquisition multispectral réel développé dans le cadre du projet européen CRISATEL:

- i) la réalisation des expériences physiques pour caractériser les composants du système et pour évaluer leurs performances,
- ii) la conception et la mise en oeuvre logicielle des systèmes de calibrage et de correction intimement liés à l'acquisition.

Ce travail expérimental effectué sur le système d'acquisition CRISATEL permet d'acquérir des images multispectrales qui ont non seulement une qualité visuelle élevée mais également un signal contrôlé radiométriquement.

Chapitre 7. Choix des filtres pour une reconstruction spectrale précise.

Nous considérons à présent le problème de l'optimisation du choix d'un ensemble de filtres pour une caméra multispectrale. Le but est de déterminer les transmittances spectrales d'un jeu de filtre de filtres permettant d'augmenter la précision de la reconstruction spectrale de manière optimale.

Nous présentons d'abord les quelques approches qui ont été proposées pour le choix d'un ensemble de filtres. Nous présentons alors le critère utilisé pour le choix des filtres et la stratégie développée pour son optimisation. Le critère utilisé (la *v-mesure*) a été à l'origine appliquée pour l'optimisation colorimétrique. Nous donnons des détails pour comprendre la signification de cette mesure en termes d'algèbre linéaire. Ceci fournit des éléments supplémentaires pour la compréhension de cette mesure et pour son application dans un contexte différent. Nous définissons alors un espace que nous appelons le *sous-espace visuel de la caméra* qui s'avère très utile dans ce nouveau contexte.

Le critère modifié proposé (*v-mesure* modifiée) permet la conception de filtres diminuant les erreurs de reconstruction spectrale sans avoir besoin d'effectuer explicitement une reconstruction spectrale. Un algorithme pour l'optimisation de la *v-mesure* modifiée est présenté. Cette stratégie converge vers une solution acceptable qui s'avère également très rapide. Son efficacité en temps de calcul est due à une structure en deux étapes, chacune d'elles étant basée sur une paramétrisation différente de la transmittance spectrale des filtres. D'abord, des filtres représentés par des fonctions rectangulaires sont utilisés. Cette

paramétrisation compacte est optimisée sur un espace discret. Cette première étape, très rapide, fournit une bonne approximation initiale pour la seconde étape où les transmittances spectrales sont modélisées par des fonctions gaussiennes et où un procédé d'optimisation par gradient est utilisé. Nous avons calculé analytiquement le gradient de la *v-mesure* afin d'augmenter l'efficacité dans la descente du gradient. Il faut préciser que ce procédé en deux étapes peut tomber sur des minimums locaux car le critère qui le guide n'est pas convexe. Mais l'application de cette stratégie d'optimisation à différents ensembles initiaux de filtres aléatoirement choisis a permis d'atteindre une bonne solution à ce problème.

Nous avons appliqué l'algorithme proposé à l'optimisation de 10 filtres de forme gaussienne pour la caméra CRISATEL, le but étant d'augmenter la précision de la reconstruction spectrale sur un ensemble de réflectances correspondant à des pigments à l'huile. Par simulation nous avons comparé les résultats obtenus avec les filtres optimisés avec ceux obtenus à l'aide des filtres réels de la caméra CRISATEL. Ces résultats prouvent que les filtres optimisés fournissent des reconstructions d'une meilleure précision pour l'ensemble des réflectances choisies. Mais, cette augmentation de qualité demeure petite, 16%, et s'accompagne d'une diminution de la généralité puisque restreinte à des pigments à l'huile. La conclusion importante qui découle finalement de ces résultats est que la construction difficile et coûteuse de filtres interférentiels de forme gaussienne optimisés n'est pas justifiée.

L'approche développée dans ce chapitre peut facilement être appliquée à l'optimisation de filtres électroniquement réglables. Elle est en fait très adaptée pour ce genre de filtres car les fonctions de transmittance peuvent être électroniquement sélectionnées, leur forme appartenant à une famille de courbes très similaires aux gaussiennes.

Chapitre 8. Résultats Généraux.

Ce chapitre présente un ensemble de résultats de reconstructions spectrales obtenus en employant les techniques présentées dans cette thèse sur des données acquises dans de vrais environnements expérimentaux. Aucune simulation n'apparaît donc ici. Deux systèmes différents d'acquisition multispectral ont été utilisés pour obtenir les données :

- i) Une caméra multispectrale appartenant à la *National Gallery* de Londres.
- ii) Le système multispectral CRISATEL avec les projecteurs équipés de lampes HQI.

Ces deux systèmes ont pour point commun d'utiliser le même ensemble de 13 filtres interférentiels.

Le chapitre est divisé en deux parties principales : la première est consacrée aux données obtenues à la *National Gallery* et la deuxième partie traite les données du projet CRISATEL. Nous signalons que cette thèse vient de se terminer avant que le projet de CRISATEL ait été complètement réalisé. La phase d'acquisition de toiles de maître ne fait que juste commencer. Nous présentons les premières acquisitions numériques sur un ensemble de tableaux de Georges de la Tour qui ont été scannés au Musée d'Albi (France) entre le 28 novembre et le 3 décembre 2003. Après ce premier test une étape intensive d'acquisition a commencé au Musée du Louvre par le *Centre de Conservation et de Restauration des Musées de France (C2RMF)*. Nous montrons également des images d'une toile de Guillaume Fouace, *Le départ pour Jersey*, qui appartient à cette étape d'acquisition.

Même si des modifications vont être apportées au système CRISATEL, celui-ci est dans une phase mature et des changements fondamentaux ne sont pas prévus. Les données utilisées ici sont donc encore préliminaires mais elles sont cependant suffisamment représentatives pour bien permettre d'illustrer les performances obtenues avec les différentes approches proposées dans le cadre de cette thèse.

Chapitre 9. Conclusion et travaux futurs.

Des conclusions générales sont présentées et les perspectives de travail qui s'ouvrent après cette thèse sont discutées dans ce chapitre.

Bibliography

- Abrardo A., Cappellini V., Cappellini M., and Mecocci A. 1996. Art-works colour calibration using the VASARI scanner. In proceedings of *Fourth Color Imaging Conference Color Science, Systems, and Applications*. pp. 94-97. Scottsdale, Arizona, USA.
- Albert, A. 1972. *Regression and the Moore-Penrose pseudoinverse*. Academic Press.
- Arai Y., Nakauchi S. and Usui S. 1996. Color Correction Method Based on the Spectral Reflectance Estimation using a Neural Network. In proceedings of *Fourth Color Imaging Conference Color Science, Systems, and Applications*. pp. 5-9. Scottsdale, Arizona, USA.
- Bartels R. H., Beatty J. C., and Barsky B. A.. 1987. *An Introduction to Splines for Use in Computer Graphics & Geometric Modeling*. Edited by Morgan Kaufmann Publishers, Inc.
- Berns R. S. 2000. *Principles of Color Technology*. Third Edition. John Wiley & Sons, Inc.
- Bishop C. M. 1996. Mixture Density Networks. Neural Computing Research Group Report NCRG/4288. Aston University, United Kingdom.
- Bridle J.S. 1990. Probabilistic interpretation of feedforward classification network outputs, with relationships to statistical pattern recognition. Chapter in *Neurocomputing: Algorithms, Architectures and Applications*. pp. 227-236. New-York: Springer-Verlag.
- Burns P. D. 1997. Analysis of image noise in multitraitement color acquisition. Ph.D. thesis, Center for Imaging Science, Rochester Institute of Technology, USA.
- Burns P. D. and Berns R. S. 1996. Analysis Multispectral Image Capture. In proceedings of *Fourth Color Imaging Conference Color Science, Systems, and Applications*. pp. 19-22. Scottsdale, Arizona, USA.
- Burr-Brown. 2000. VSP2212: CCD signal processor for digital cameras. *Company data sheet*. USA.
- Brettel H., Hardeberg J. Y., and Schmitt F. 2000. WebCam for Interactive Multispectral Measurements. In proceedings of the *Colour Image Science CIS 2000 Conference*, pp. 160-168. Derby, UK.
- Clarke F. J. J., McDonald R., Rigg B. 1984. Modification to the jpc79 colour-difference formula. *Journal Soc. Dyers & Colorists* **100** pp. 128-132.
- CIE Publication15.2. 1986. *Colorimetry*. Second Edition. Commission International de l'Eclairage. Vienna, Austria.
- CIE Publication116. 1995. *Industrial Colour-Difference Evaluation*. Commission International de l'Eclairage. Vienna, Austria.

- Cotte P. and Dupouy M. 2003. Crisatel High Resolution Multispectral System, *PICS03 The Digital Photography Conference*, pp. 161-165. Rochester, USA.
- CRISATEL Progress Report, deliverable d13. 2003. *Prediction of Original Colours*. European project IST-1999-20163.
- Cupitt J. and Martinez K., 1996. VIPS: an image processing system for large images. In proceedings of *SPIE conference on Imaging Science and Technology*, San Jose, Vol 1663.
- Eastman Kodak Company, 2001. CCD Image Sensor Noise Sources. Application Note MTD/PS-0233. Rochester, New York, USA.
- Eem J. K, Shin H. D., and Park S. O.. 1994. Reconstruction of Surface Spectral Reflectances Using Characteristic Vectors of Munsell Colors. In proceedings of *Second Color Imaging Conference Color Science, Systems, and Applications*, pp. 127-131.
- Efron, B. 1979 Bootstrap Methods: Another Look at the Jackknife. *Annals of Statistics*, 7, pp. 1-26.
- Farrell J. E., and Wandell B. A. 1993. Scanner Linearity. *Journal of Electronic Imaging and Color*. 3 pp. 147-161.
- Farrell J. E., Cupitt J., Saunders D. and Wandell B. A. 1999. Estimating Spectral Reflectances of Digital Images of Art. In proceedings of *International Symposium on Multispectral Imaging and Color Reproduction for Digital Archives*. pp. 58-64. Chiba, Japan.
- Farin G. 1988. Curves and Surfaces for Computer Aided Geometric Design. Edited by Academic Press Inc.
- Golberg D. E. 1989. Algorithms in Search, Optimisation, and Machine Learning. Addison-Wiley Publishing Company, Inc.
- Golub G. H., Van Loan C. F. 1983. Matrix Computations. The Johns Hopkins University Press.
- Hadamard J. 1902. *Sur les problèmes aux dérivées partielles et leur signification physique*. Bull. University of Princeton, pages 49-52.
- Hardeberg J. Y. 2003. Filter Selection for Multispectral Color Image Acquisition. In proceedings of *PICS03: The Digital Photography Conference*. pp. 177-182. Rochester, USA.
- Hardeberg J. Y. 1999 Acquisition and reproduction of colour images: colorimetric and multispectral approaches. Ph.D. dissertation. Ecole Nationale Supérieure des Télécommunications. Paris, France.
- Hardeberg J.Y., Schmitt F., Brettel H., Crettez J., Maître H.. 1999 Multispectral image acquisition and simulation of illuminant changes. Chapter in MacDonald and Luo, pp. 145-164.

- Haneishi H., Hasegawa T., Tsumura N., and Miyake Y. 1997. Design of Color Filters for recording Art Works. In proceedings of *IS&T 50th Annual Conference*, pp. 369-372. Cambridge, Massachusetts, USA.
- Hebb, D. O. 1949. *The Organization of Behaviour*. Wiley, New York, USA.
- Healey G. E., Kondepudy R. 1994 Radiometric CCD camera calibration and noise estimation. *IEEE Patt. Anal. Mach. Intell.* **16** pp. 267-276.
- Hernandez-Andres and Romero, 2001. Colorimetric and spectroradiometric characteristics of narrow-field-of-view clear skylight in Granada. *Journal of the Optical Society of America*, 18 pp. 412-420.
- Herzog G. P., and Hill B. 2003. Multispectral Imaging and its Applications in the Textile Industry and Related Fields. In proceedings of *PICS03: The Digital Photography Conference*. pp. 258-263. Rochester, USA.
- Herzog P. G., Knipp D., Stiebig H. and König F. 1999. Characterization of novel three and six channel color moiré free sensors. In proceedings of SPIE, *Color Imaging: Device Independent Color, Color Hardcopy, and Graphic Arts IV*. pp. 48-59. San Jose, California, USA.
- Herzog P. G., Knipp D., Stiebig H. and König F. 1999. Characterization of novel three and six channel color moiré free sensors. In proceedings of SPIE, *Color Imaging: Device Independent Color, Color Hardcopy, and Graphic Arts IV*. pp. 48-59. San Jose, California, USA.
- Imai F. H. and Berns R. S. 1999. Spectral Estimation Using Trichromatic Digital Cameras. In proceedings of *International Symposium on Multispectral Imaging and Color Reproduction for Digital Archives*. pp. 42-49. Chiba, Japan.
- Imai F. H., Quan S., Rosen M. R., and Berns R. S. 2001 Digital camera filter design for colorimetric and spectral accuracy. In proceedings of *Third International Conference on Multispectral Color Science*. pp. 13-16. Joensuu, Finland.
- Imai F. H., Rosen M. R., and Berns R. S. 2002. Comparative Study of Metrics for Spectral Match Quality. In proceedings of *CGIV 2002: The First European Conference on Colour in Graphics, Image and Vision*. Poitiers, France.
- Imai F. H., Taplin L. A. and E. A. Day. 2002. Comparison of the accuracy of various transformations from multi-band image to spectral reflectance. *Technical Report of the Rochester Institute of Technology*. Rochester, USA.
- Jaaskelainen, T., Silvennoinen, R., Hiltunen, J. and Parkkinen, J. P. S. 1994. Classification of the reflectance spectra of pine, spruce, and birch. *Applied Optics*, Vol. 33, No. 12, 20 , pp. 2356-2362.
- Jaaskelainen T., Parkkinen J., and Toyooka 1990. Vector-subspace model for color representation. *Journal of the Optical Society of America*, 7(4) pp. 725-730.

- Keusen T. 1996. Multispectral color system with an encoding format compatible with the conventional tristimulus model. *Journal of Imaging Science and Technology*, 40(0), pp. 510-515.
- König F. and Praefcke W. 1999. A multispectral scanner. Chapter in MacDonald and Luo. pp. 129-144.
- Kotera H., Motomura H. and Fumoto T. 1999. Recovery of Fundamental Spectrum from Color Signals. In proceedings of *International Symposium on Multispectral Imaging and Color Reproduction for Digital Archives*. pp. 141-144. Chiba, Japan.
- Lahanier C., Schmitt F., Le Bœuf P., and Aitken G. 2003. Multi-spectral Digitisation and 3D Modelling of Paintings and Objects for Image Content Recognition, Image Classification and Multimedia Diffusion. An Ontology Access to the C2RMF Database and Library using the CIDOC-CRM. *International Conference of Museum Digitization, Antiquities, Painting and Calligraphy*, pp. 157-201. National Palace Museum, Taiwan.
- Lawson, C. L. and Hanson, R. J. 1974. Solving Least Squares Problems. *Series in Automatic Computation*. Prentice-Hall, Inc.
- Luo, M. R., Rigg, B. 1987. BFD(1:c) color-difference formula. Part I – development of the formula. *Journal Soc. Dyers & Colorists* **103** pp. 86-94.
- Luo, M. R., Rigg, B. 1987. BFD(1:c) color-difference formula. Part I – performance of the formula. *Journal Soc. Dyers & Colorists* **103** pp. 126-132.
- Mahy, M., van Eycken, L., and Oosterlinck, A. 1994. Evaluation of uniform color spaces developed after the adoption of CIELAB and CIELUV. *Color Research and Application*. **19**(2) pp. 105-121.
- MacDonald L. and Morovic, J. 1995. Assessing the effects of gamut compression in the reproduction of fine art paintings. In proceedings of *Third Color Imaging Conference: Color Science, Systems, and Applications*. pp. 194-200. Scottsdale, Arizona, USA.
- MacDonald L. W., Westland S. and Shaw J. 1999. Color Image Reproduction: Spectral vs Spatial. In proceedings of *International Symposium on Multispectral Imaging and Color Reproduction for Digital Archives*. pp. 81-91.
- MacDonald L. W. and Luo M. R. (edited by). 1999. *Color Imaging. Vision and Technology* John Wiley & Sons, Ltd.
- MacDonald L. Westland S., and Liu D. 2001. Multispectral Image Encoding and Compression. In proceedings of *Ninth Color Imaging Conference: Color Science, Systems, and Applications*. pp. 135-140. Scottsdale, Arizona, USA.
- McLaren, K. 1986. *The Colour Science of Dyes and Pigments*. Second Edition. Hilger, Bristol, UK.
- Merrit J. 2002. Using Fourier Interpolation to Find C^∞ Approximations of a Sampled Function and its Derivatives.

- Neumaier A. 1999. Solving Ill-conditioned and Singular Linear Systems: A Tutorial on Regularization.
- Maître H., Schmitt F., Crettez J., Wu Y., and Hardeberg J.Y. 1996. Spectrophotometric image analysis of fine art paintings. In Proc. *IS&T and SID Fourth Color Imaging Conference*. pp. 50-53. Scottsdale, Arizona, USA.
- Mahy M., Wambacq P., Van Eyken L., and Oosterlinck. A. 1994. Optimal filters for the reconstruction and discrimination of reflectance curves. In Proc. *IS&T and SID Second Color Imaging Conference*. pp. 140-143. Scottsdale, Arizona, USA.
- Ohsawa, K., Fukuda H., Ajito T., Komiya Y., Haneishi H., Yamaguchi M., and Ohyama N. 2003. Six-Band HDTV Camera System for Color Reproduction Based on Spectral Information. *PICS03 The Digital Photography Conference*, pp. 171-176. Rochester, USA.
- Pratt W. K. 1978. *Digital Image Processing*. John Wiley & Sons.
- Pratt W. K., Mancill C. E. 1976. Spectral estimation techniques for the spectral calibration of a color image scanner. *Applied Optics*, 15(1), pp. 73-75.
- Poger S., and Angelopoulou E. 2001. Selecting Components for Building Multispectral Sensors. CVPR.
- Quan S., Ohta N., and Katoh N. 2000. Optimization of Camera Spectral Sensitivities. In proceedings of *Eighth Color Imaging Conference Color Science, Systems, and Applications*. pp. 273-278. Scottsdale, Arizona, USA.
- Ribés A., Schmitt F., and Brettel H. 2001 Reconstructing Spectral Reflectances of Oil Pigments with Neural Networks. In proceedings of *Third International Conference on Multispectral Color Science*. pp. 9-12. Joensuu, Finland.
- Ribés A., Schmitt F. Reconstructing Spectral Reflectances with Mixture Density Networks. 2002. In proceedings of *First European Conference on Colour in Graphics, Imaging and Vision*. pp. 486-491. Poitiers, France.
- Ribés A., and Schmitt F. 2003. A Fully Automatic method for the Reconstruction of Spectral Reflectance Curves by using Mixture Density Networks, *Pattern Recognition Letters*, **24** (11), pp. 1691-1701.
- Ribés A., Brettel H., Schmitt F., Liang H., Cupitt J., Saunders D. 2003. Color and Spectral Imaging with the Crisatel Acquisition System. In proceedings of *PICS'03 The Digital Photography Conference*, pp. 1691-1701. Rochester, USA.
- Ribés A., Brettel H., Schmitt F., Liang H., Cupitt J., Saunders D.. 2003. WP5 - Performance Evaluation of the Acquisition Systems. *Technical report* of the IST-1999-2015 CRISATEL European Project.
- Rosenblatt F. 1962. *Principles of Neurodynamics*. Spartan Books,. New Yor, USA.
- Rumelhart, D. E., and McClelland, J. L.. 1986. *Parallel Distributed Processing: Explorations in the Microstructure of Cognition*. MIT Press, Cambridge, MA.

- Sato T., Nakano Y., Iga T., Nakauchi S. and Usui S. 1999. Color Reproduction Based on Low Dimensional Spectral Reflectance Using the Principal Component Analysis. In proceedings of *International Symposium on Multispectral Imaging and Color Reproduction for Digital Archives*. pp. 185-188. Chiba, Japan.
- Saunders D. and Cupitt J. 1993. Image processing at the National Gallery: The VASARI project, *National Gallery Technical Bulletin* 14 (1993) 72–85.
- Schott J. R. 2003. The Evolution of Spectral Remote Sensing from Color Images to Imaging Spectroscopy. In proceedings of *PICS03: The Digital Photography Conference*. pp. 250-257. Rochester, USA.
- Sève. R. 1996. *Physique de la couleur : de l'apparence colorée à la technique colorimétrique*. Masson.
- Sharma G. and Trussell H. J., 1996. Set Theoretic Estimation in Color Scanner Characterization. *Journal of Electronic Imaging*, 5(4) pp. 479-489.
- Sun Q., and Fairchild M. D. 2003. Image Quality for Visible Spectral Imaging. In proceedings of *PICS03: The Digital Photography Conference*. pp. 210-214. Rochester, USA.
- Tominaga S. 1996. Multichannel vision system for estimating surface and illuminant functions. *Journal of the Optical Society of America*, 13(11) pp. 2163-2173.
- Tominaga S. 1999. Color coordinate conversion via neural networks. Chapter in MacDonald and Luo. pp. 165-178.
- Tikhonov A. N. 1963. Regularization of incorrectly posed problems. *Soviet Mathematics Doklady*, Vol. 4, , pp. 1624-1627.
- Tikhonov A. N. and Arsenin V. Y. 1977. *Solution of ill-posed problems*, Winston-Wiley, New York.
- Tsumura N., Tanaka T., Haneishi H., and Miyake Y. 1998. Optimal design of mosaic color filters for the improvement of image quality in electronic endoscopes. *Optics Communications*, (145)1 pp. 27-32.
- Vrhel, M. J., Gershon, R, and Iwan L. S. 1994. Measurement and analysis of object reflectance spectra. *Color Research and Application*, 19(1), pp. 4-9.
- Vora and Trussell. 1993. Measure of Goodness of a Set of Color-scanning filters. *Journal of the Optical Society of America*.
- Widrow. B., and Hoff M. E. 1960. Adaptive switching circuits. In *IRE WESCOM Convention Record*, pp. 96-104.
- Wyszecki. G., and Stiles W. S. 1982. *Color Science: Concepts and Methods, Quantitative Data and Formulae*. Second Edition. John Wiley & Sons, Inc.
- Youla D. C., and Webb H. 1982. Image Restoration by the Method of Convex Projections: Part 1 – Theory. *IEEE Transactions on Medical Imaging*. 16(1) pp. 81-94.

